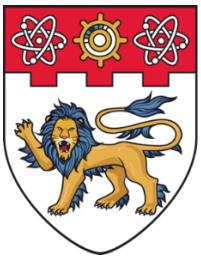

NANYANG TECHNOLOGICAL UNIVERSITY
SINGAPORE

Solid State Nuclear Magnetic Resonance Studies of Functional Materials

Benjamin Elias Griffith

DEPARTMENT OF PHYSICS, UNIVERSITY OF WARWICK

SCHOOL OF MATERIALS SCIENCE AND ENGINEERING, NANYANG TECHNOLOGICAL UNIVERSITY

November 2021

Solid State Nuclear Magnetic Resonance Studies of Functional Materials

Benjamin Elias Griffith

DEPARTMENT OF PHYSICS, UNIVERSITY OF WARWICK

SCHOOL OF MATERIALS SCIENCE AND ENGINEERING, NANYANG TECHNOLOGICAL UNIVERSITY

A thesis submitted to the University of Warwick and the Nanyang Technological University in partial fulfilment of the requirement for the degree of Doctor of Philosophy under the Warwick/NTU Joint PhD Programme

November 2021

Statement of Originality

I hereby certify that the work embodied in this thesis is the result of original research, is free of plagiarized materials, and has not been submitted for a higher degree to any other University or Institution.

21th November 2021

. . . . . .

Date

. .  .

Benjamin Elias Griffith

Supervisor Declaration Statement

We have reviewed the content and presentation style of this thesis and declare it is free of plagiarism and of sufficient grammatical clarity to be examined. To the best of our knowledge, the research and writing are those of the candidate except as acknowledged in the Author Attribution Statement. We confirm that the investigations were conducted in accord with the ethics policies and integrity standards of University of Warwick and Nanyang Technological University, and that the research data are presented honestly and without prejudice.

24th November 2021 . . . . . .
Date

. . . . . .
Prof. John V. Hanna

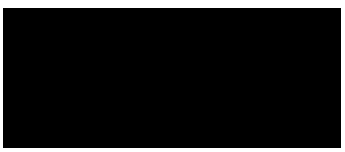

24th November 2021 . . . . . .
Date

. . . . . .
Prof. Timothy J. White

Contents

List of Tables

List of Figures

Acknowledgments

The completion of this PhD would not have been possible without the invaluable contributions of the following people. Firstly, I would like to thank my supervisor Prof. John Hanna, as without his guidance this PhD would not have been possible. Thanks to John I have had the opportunity to study an array of materials (the vast majority of which are not included in this thesis) at both Warwick University and Nanyang Technological University which has greatly enhanced my learning of the field. I am also grateful for all the help supplied by my collaborators, Johnson Matthey. In particular, Dr Gary Evans and Dr Stephen Day who have provided continual support throughout the work on catalysis and were always willing to go out of their way in order to assist me in my studies.

My thanks go to the members Warwick solid state NMR group both past and present who offered invaluable friendships, good humour and respite during stressful periods. Being involved in many activities with my NMR colleagues such as the cake club, board game evenings and climbing made the past 4 years an extremely enjoyable experience. I would like to especially thank Dr Samuel Page who selflessly offered assistance with NMR spectrometer problems as well as entertained my sometimes overly ambitious experimental ideas. In addition, Dr Andrew Howes for providing technical assistance with equipment problems and the frequent chats about Watt bike gym sessions. Likewise, Dr Dinu Iuga for his guidance and assistance for my many uses of the national

facility.

Additionally, I would like to express my gratitude to my colleagues at Nanyang Technological University; Dr Walter Wong, Sai Dintakurti, Dr Parth Vashistha and Dr Tom Hooper for their meaningful discussions, frequent lunches, meals and coffee breaks which made my time in Singapore even more enjoyable and aided my learning and understanding of materials science. I am also grateful to Dr Parth Vashistha for his synthesis of perovskite nanocrystals and PL measurements, Dr Yanan Fang and Prof. Tim White for their expertise in crystallography and A/Prof Albert Bartok for his extensive DFT calculations on perovskite systems which have been integral parts of this thesis.

Finally, I would like to express my appreciation to my close friends and family. In particular my flatmate and friend of 8 years, Mason who often listened to my PhD tribulations and offered escapism through frequent squash sessions despite our constant injuries. Above all, I would like to thank my family for their constant support throughout my academic studies. Especially my parents for giving me the opportunities and experiences which have led to this achievement and for always selflessly encouraging me to pursue my interests often at their own expense.

Declarations

I hereby declare that **Solid State Nuclear Magnetic Resonance of Functional Materials** is an original work and has not been submitted for a degree or diploma or other qualification at any other University.

In Chapter 4, sample synthesis and lability measurements were performed by Dr Gary Evans and Dr Stephen P. Day or myself under the guidance of Dr Gary Evans at Johnson Matthey Technology Centre, UK. STEM measurements were carried out by partners at Johnson Matthey Technology Centre, UK. SAXS data was collected and analysed by Dr Stephen Hubband at the Department of Physics, University of Warwick. PXRD data were collected by myself or partners at Johnson Matthey Technology Centre, UK. All NMR data were collected and analysed by myself.

Chapter 5 is currently being prepared as a manuscript: A Multiple Technique Structural Study on the Effects of Nb^{5+} and Ta^{5+} B-site Doping in $SrTiO_3$ for Uses as High Temperature Thermoelectric Materials. This paper is co-first authored by Yanan Fang and Benjamin E. Griffith. The contributions of authors and co-authors is as follows:

- Sample synthesis, neutron diffraction analysis and XPS analysis were carried out by Dr Yanan Fang at the school of Materials Science and Engineering, Nanyang Technological University.
- All NMR, Raman and IR data were analysed by myself.

- All DFT calculations were performed by A/Prof Albert P. Bartok at the Department of Engineering and Department of Physics, University of Warwick.
- Thermoelectric performance measurements were carried out by partners at the University of New South Wales, Australia.
- Manuscript drafts were written by myself and revised by Prof John V. Hanna.

Chapter 6 has been published as Parth Vashishtha, Benjamin E. Griffith, Albert P. Bartok, Yanan Fang, Ankit Jaiswal, Gautam V. Nutan, Tim White, and John V. Hanna. Elucidation of Structural and Optical Properties of Metal Cation (Na^+, K^+, and Bi^{3+}) Incorporated $Cs_2AgInCl_6$ Double Perovskite Nanocrystals, *Journal of Materials Chemistry A,* ***10****, 3562-3578, 2022.* This paper is co-first authored by Parth Vashishtha and Benjamin E. Griffith. The contributions of authors and co-authors is as follows:

- Samples synthesis, HRTEM and PL measurements were carried out by Dr Parth Vashishtha at the School of Materials Science and Engineering, Nanyang Technological University.
- X-ray diffraction refinements were performed by Dr Yanan Fang school of Materials Science and Engineering, Nanyang Technological University.
- All DFT calculation were carried out by A/Prof Albert Bartok-Partay at the Department of Engineering and Department of Physics, University of Warwick.
- All NMR measurements and analysis were performed by myself.
- Manuscript drafts were prepared by myself and Dr Parth Vashishtha and were revised by Prof John V. Hanna.

Abstract

The functional properties of materials are inherently linked to the structure, and therefore it is imperative that accurate and comprehensive characterisations are accomplished to improve performance. As improvements to materials are often related to a greater morphological complexity through disorder, analytical techniques are required to characterise these structural intricacies. Solid state NMR is excellent at obtaining short range information and has therefore been implemented for structural elucidation in the areas of heterogeneous catalysis, thermoelectric materials and optoelectronic materials.

The large chemical shift range and high sensitivity of ^{17}O solid state NMR allows for minor structural changes to be detected making it an attractive prospective tool in the structural characterisation of platinum group metal (PGM) catalysts. For the first time, ^{17}O solid state NMR spectra for PtO_2, PdO, Rh_2O_3 nanoparticles and bulk RuO_2 are reported and correlated to their structures through the use of PXRD, Raman spectroscopy and TEM. Furthermore, the application of ^{17}O solid state MAS NMR to Pt and Pd supported by the commonly used metal oxide supports; γ-Al_2O_3, SiO_2 and TiO_2 has been explored and complemented by ^{195}Pt, ^{1}H and ^{29}Si solid state NMR. This has allowed for direct observation of catalyst-support bonding which provides new avenues for the structural characterisation of catalytic systems.

A multiple technique approach has been adopted to probe the structure of $Sr_{1-x/2}Ti_{1-x}M_xO_3$ (M = Nb^{5+}, Ta^{5+}) systems for uses as high temperature

thermoelectric materials. The presence of Sr (A) site vacancies were detected for doped $SrTiO_3$ through the use of neutron diffraction, elemental analysis, Raman spectroscopy, and ^{93}Nb and ^{87}Sr solid state MAS NMR data. Comparing ^{93}Nb MAS NMR with calculated NMR parameters generated from materials modelling structural realisations using the GIPAW DFT approach has allowed for the characterisation of three distinct Nb sites; Nb directly substituted into the $SrTiO_3$ cubic lattice, a distorted Nb dimer about a Sr vacancy and disordered niobia nanodomains ($>$ 5 mol% Nb) formed from significant Sr vacancy formation.

^{133}Cs, ^{23}Na and ^{39}K solid state MAS NMR has been implemented to study the structure and mobility of direct band gap Pb-free double perovskite $Cs_2AgIn_xBi_{1-x}Cl_6$, $Cs_2Na_xAg_{1-x}InCl_6$:Bi and $Cs_2K_xAg_{1-x}InCl_6$:Bi nanocrystal systems. The alteration to the optical properties from Bi^{3+}, Na^+ and K^+ incorporation is rationalised in terms of the ^{133}Cs T_1 data and the evolving structural defects comprising each system, whereby a passivation of the defects leads to an enhancement of the photoluminescence quantum yield (PLQY). Materials modelling using the Ab Initio Random Structure Search (AIRSS) method, and the calculation of the NMR parameters emanating from the generated structural realisations using the GIPAW DFT approach, showed that the introduction of K^+ induces significant structural disorder and multi-phase formation as highlighted by the large ^{133}Cs and ^{39}K chemical shift dispersion. The ^{39}K MAS NMR data demonstrates that the PLQY behaviour maps directly with the K^+ incorporation into the cubic $Cs_2K_yAg_{1-y}InCl_6$ phase supporting B site occupancy.

Abbreviations

3Q	Triple Quantum
ATMA	Automated Tuning and Matching
AIRSS	Ab Initio Random Structure Search
CS	Chemical Shift
CSA	Chemical Shift Anisotropy
DFT	Density Functional Theory
DoS	Density of States
DPE	Diphenyl Ether
EDX	Energy Dispersive X-Ray Analysis
EFG	Electric Field Gradient
EPMA	Electron Micro Probe Analyzer
EXAFS	Extended X-ray Absorption Fine Structure
FID	Free Induction Decay
FWHM	Full Width Half Maximum
FTIR	Fourier Transform Infrared Spectroscopy

GIPAW	Gauge Including Projector Augmented Waves
iso	Isotropic
IUPAC	International Union of Pure and Applied Chemistry
LAB	Lab Reference Frame
MAS	Magic Angle Spinning
mol%	Mole percent
MQMAS	Multiple Quantum Magic Angle Spinning
NCs	Nanocrystals
NMR	Nuclear Magnetic Resonance
OAc	Oleic Acid
PAS	Principle Axis System
ppm	Parts Per Million
PGM	Platinum Group Metal
PL	Photoluminescence
PLQY	Photoluminescence Quantum Yield
PXRD	Powder X-Ray Diffraction
Q_{is}	Quadrupolar Induced Shift
RMSE	Root Mean Square Error
ROT	Rotating Frame
rf	Radio Frequency

S/N	Signal-to-Noise
SPS	Spark Plasma Sintering
SQ	Single Quantum
T_1	Spin-Lattice Relaxation Time
T_2	Spin-Spin Relaxation Time
SMSI	Strong Metal-Support Interaction
STMAS	Satellite Transition Magic Angle Spinning
STEM	Scanning Transmission Electron Microscope
STE	Self-Trapped Exciton
TEM	Transmission Electron Microscopy
TPR	Temperature Programmed Reduction
VOCS	Variable Offset Cumulative Spectroscopy
wt%	Percentage by weight
XPS	X-Ray Photoelectron Spectroscopy
XANES	X-ray Absorption Near Edge Structure
ZT	Thermoelectric Figure of Merit

Chapter 1

Introduction

Originally, NMR was developed for use on liquids where detailed and clear data can be achieved due to the averaging of internal nuclear interactions by molecular tumbling. However, the development in the understanding of many nuclear interactions, NMR instrumentation and pulsing techniques have enabled NMR to be applied effectively to solid state materials, providing an array of structural information including chemical speciation, molecular dynamics and disorder. A notable advancement is the progression to radio frequency pulsed NMR methods introduced in 1949 by Erwin Hahn, from continuous wave NMR which resulted in the faster acquisition of data. [2] Furthermore, the development of Magic Angle Spinning (MAS) by Andrew, Bradbury and Eades in 1959 allowed many nuclear interactions to be minimised, enabling higher resolution data to be achieved which nurtured more definitive spectroscopic data. [3] These ameliorations have led to many 1D and 2D NMR techniques used in modern spectroscopic data acquisition, transforming solid state NMR into a powerful analytical tool.

Nuclear Magnetic Resonance (NMR) is a spectroscopic technique which is used to probe the local environments of nuclei allowing for short range structural information to be obtained for nuclear isotopes which possess the intrinsic spin property. However, NMR is rarely used as a complete solution when characterising structures but instead is used in conjunction with other techniques such as diffraction or materials modelling to provide a more complete structural elucidations. Whereas diffraction based techniques pertain to long range periodicity and are generally the first point of call in determining the overall

structure and space group, difficulties arise in detecting and identifying disorder. NMR has the ability to detect such structural intricacies, allowing for a comprehensive structural analysis of materials when these techniques are used cooperatively.

1.1 Motivations

The development of many functional materials is of high importance because of the potential for waste energy saving applications, more efficient catalytic systems and greater electricity generation amongst many others. In order to improve such materials a strong structural understanding is required to elucidate the intricacies contributing to enhancements in materials performance. The motivations of this thesis is to both implement solid state NMR in corroboration with other techniques to correlate the local structure to materials performance as well as develop the NMR techniques used to analyse such materials. These motivations have led to the applications and development of solid state NMR to three main areas of study; first, platinum group metal (PGM) oxides and supported PGMs for uses as heterogeneous catalysis, secondly, doped $SrTiO_3$ for thermoelectric materials applications and finally, metal cation incorporated double perovskites nanocrystals to be employed as optoelectronic materials. Each of these areas requires the detection of subtle changes related to structure, disorder and mobility. Therefore, solid state NMR is the ideal method of analysis for each of these systems.

1.2 Thesis Overview

The background behind NMR theory is explained in Chapter 2, where explanations of internal interactions relevant to the work in this thesis are provided using quantum mechanical Hamiltonian expressions. Afterwards, commonly used practical NMR experimentation are introduced in Chapter 3 which includes the effects of experimental techniques on nuclear interactions.

Initially, ^{17}O enrichment and solid state NMR are utilised in Chapter 4 to investigate the structure of PGM metal catalyst systems. For the first time ^{17}O data has been acquired for PGM oxide metals which was then taken further

by the analysis of PGM impregnated on metal oxide supports. Currently, the ^{17}O enrichment and solid state NMR of PGM materials is an unexplored area of analysis in the development of heterogeneous catalysis, still in many other challenging disordered materials it has proven to be highly sensitive to minor structural changes. Therefore, the viability of enriching PGMs using a direct exchange method and initial identification of PGM oxide ^{17}O NMR spectra are studied.

In Chapter 5, ^{93}Nb and ^{87}Sr solid state MAS NMR are both aligned with diffraction data and materials modelling to provide a full structural understanding of Nb^{5+} and Ta^{5+} doped $SrTiO_3$ systems. Observing a range of doping concentrations allowed structural changes to be correlated to the thermoelectric performance, determined by the dimensionless thermoelectric figure of merit, ZT. Initially, due to the little variation in the long range structure, it was not possible to detect many changes from PXRD measurements. However, the sensitivity of ^{93}Nb solid state NMR to localised environments allowed for multiple accurate analogies to be made, including the effects of octahedral tilting and clustering of disordered niobia. To provide confirmation of these findings, materials modelling techniques were used to correlate extracted quadrupolar NMR parameters with a variety of structural situations.

Finally, ^{133}Cs and ^{23}Na MAS NMR measurements are used to examine metal cation (Na^+, K^+ and Bi^{3+}) doped $Cs_2AgInCl_6$ nanocrystals in Chapter 6. Measurements of the longitudinal relaxation time relating to the cation mobility are correlated to the presence of structural vacancies through the photoluminescence properties, establishing a structure-function relationship from NMR data.

Chapter 2

Theory of Solid State NMR

2.1 Background to Solid State NMR

2.1.1 Spin Angular Momentum

Most nuclei possess the quantised property of nuclear spin (I), originating from an imbalance of proton and neutron spins within a nucleus. The $m = \pm\frac{1}{2}$ spin states of protons and neutrons results in the nuclear spin quantum number being quantised into integer or half-integer values ($I = 0, \frac{1}{2}, 1...$). Nuclei with the intrinsic property of spin will also have a magnetic moment (μ), defined by

$$\hat{\boldsymbol{\mu}} = \gamma\hbar\hat{\boldsymbol{I}}, \tag{2.1}$$

where γ is the gyromagnetic ratio, which has a characteristic value for each nucleus and $\hbar$ is the reduced Planck's constant. [4]

2.1.2 Zeeman Interaction

When a nucleus with spin is placed in an external magnetic field ($\boldsymbol{B}$), Zeeman splitting is induced and the degenerate nuclear spin state evolves into $2I+1$ energy levels (Figure 2.1). The application of a magnetic field along the z axis ($\boldsymbol{B} = (0, 0, B_0)$) will therefore generate a Zeeman Hamiltonian written as:

$$\hat{\mathscr{H}_Z} = -\hat{\boldsymbol{\mu}} \cdot \boldsymbol{B} = -\hat{\mu_z}B_0 = -\gamma\hbar\hat{I}_z B_0. \tag{2.2}$$

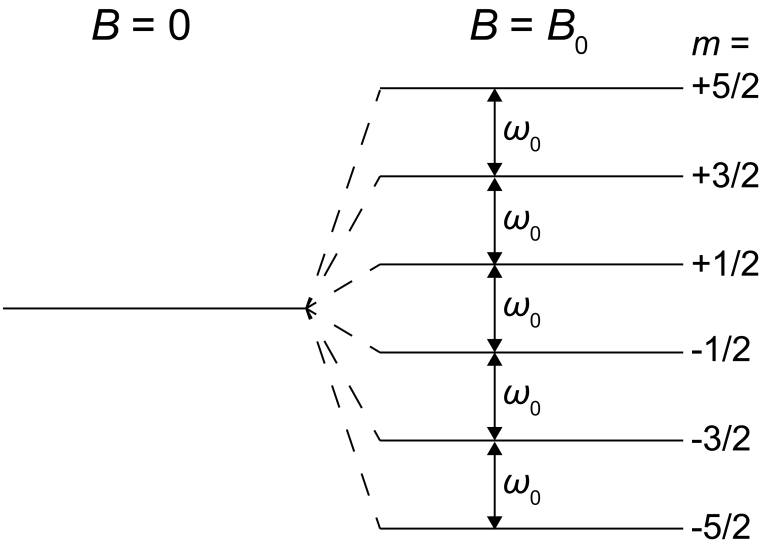

Figure 2.1: Diagram indicating the Zeeman splitting effect taking place for a spin-5/2 nucleus when placed in a magnetic field, B_0.

The separation between energy levels caused by Zeeman splitting is given by the Larmor frequency (ω_0):

$$\omega_0 = -\gamma B_0. \tag{2.3}$$

Nuclear magnetic resonance (NMR) involves the excitation between these energy levels through the use of electromagnetic radiation, followed by the detection of resultant frequencies upon the system's return to equilibrium. Therefore, only nuclei which possess a spin $I>0$ are observable through NMR.

2.2 Internal Interactions

In conjunction with the external Zeeman interaction, a multitude of internal interactions are also present. The overall Hamiltonian experienced by a nucleus can be expressed as the sum of each interaction

$$\hat{\mathscr{H}}_{tot} = \hat{\mathscr{H}}_Z + \hat{\mathscr{H}}_{RF} + \hat{\mathscr{H}}_{CS} + \hat{\mathscr{H}}_D + \hat{\mathscr{H}}_J + \hat{\mathscr{H}}_Q + \hat{\mathscr{H}}_K + \hat{\mathscr{H}}_P. \tag{2.4}$$

The internal interactions associated with each Hamiltonian are namely, chemical shielding ($\hat{\mathscr{H}}_{CS}$), the dipolar interaction ($\hat{\mathscr{H}}_D$), J-coupling ($\hat{\mathscr{H}}_J$), quadrupo-

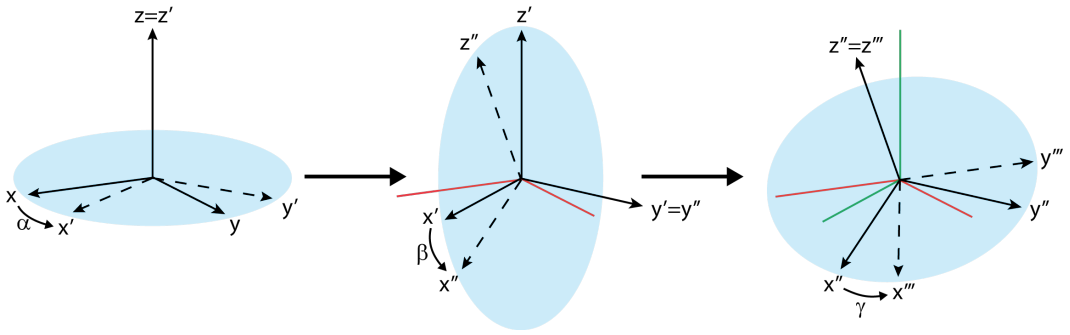

Figure 2.2: A schematic showing the effect of Euler angle transformations.

lar coupling ($\hat{\mathscr{H}}_Q$), Knight shift ($\hat{\mathscr{H}}_K$) and the paramagnetic interaction ($\hat{\mathscr{H}}_P$). [5] Due to the irrelevance of J-coupling to the results in this work, it will not be discussed further here. These internal interactions along with the external radio frequency pulse ($\hat{\mathscr{H}}_{RF}$) can be treated as perturbations to the Zeeman Hamiltonian which change the spin levels for each nuclei. These perturbations provide information about the nuclear environment when detected via NMR.

2.2.1 Coordination Frames

To simplify the explanation of each interaction the introduction of coordination frames and transformations between them is required. Each transformation connecting reference frames can be carried out using the Euler angles α, β and γ coordinates as are ascribed in Figure 2.2. Transformations between the initial frame (x, y, z) and the coordination frame (x", y", z") are achieved through the rotation operators

$$\hat{R}(\alpha, \beta, \gamma) = \hat{R}_z(\alpha)\hat{R}_y(\beta)\hat{R}_z(\alpha). \tag{2.5}$$

The four coordination frames required through this work are shown in Figure 2.3. These include, the laboratory frame (Σ_{LAB}) which has $\boldsymbol{B}$ in the z-direction (Figure 2.3(a)); the principal axis system frame (Σ_{PAS}) describing a frame where the interaction tensor is diagonalised according to α, β and γ (Figure 2.3(b)); the rotating frame (Σ_{ROT}) which describes the rotor rotation about an axis tilted by an angle theta to the z-axis (Figure 2.3(c)); and finally the rf coordination frame (Σ_{RF}) which defines the rotation about the z axis at the

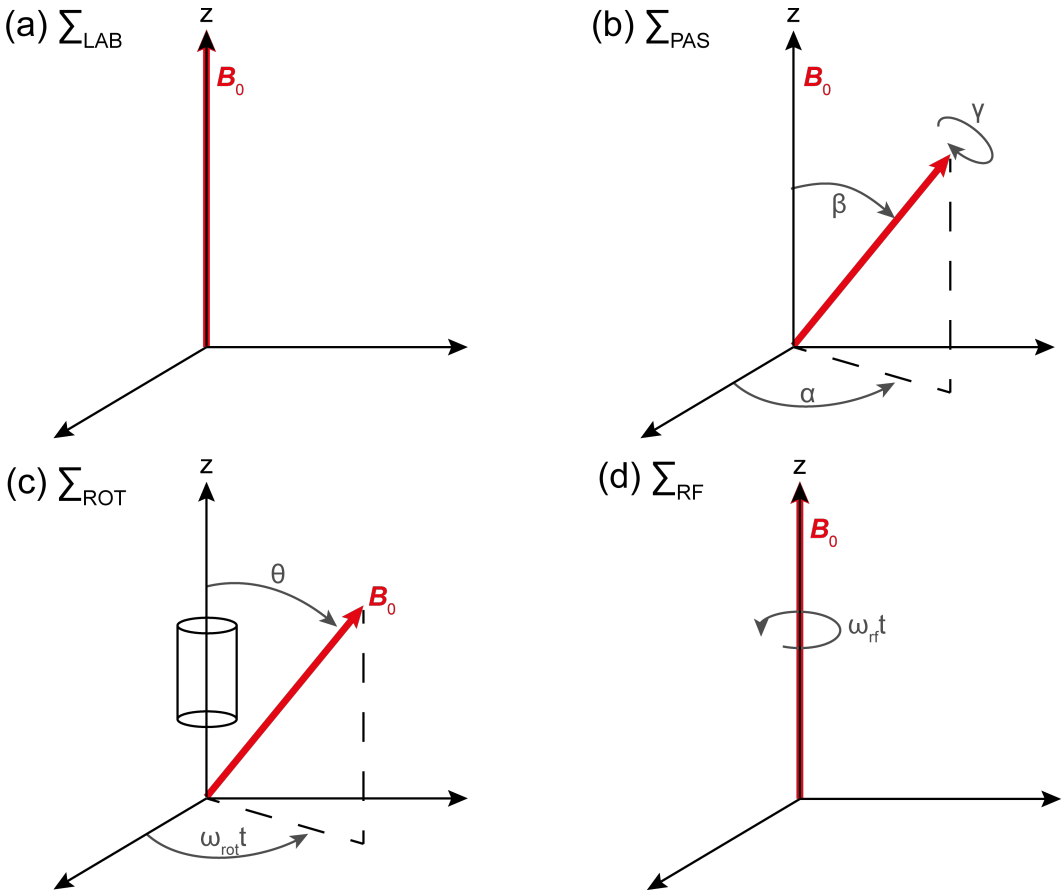

Figure 2.3: Diagrams illustrating the frames of reference; (a) the laboratory frame (Σ_{LAB}), (b) the principal axis system (Σ_{PAS}), (c) the rotating frame (Σ_{ROT}) and the rf coordination frame (Σ_{RF}).

same rate as the rf pulse frequency (Figure 2.3(d)).

2.2.2 Chemical Shielding

When the external strong magnetic field is applied, a current is induced in the electron clouds surrounding the nuclei. This in turn will generate an additional magnetic field which is also 'felt' by the nucleus. This nuclear effect is termed 'chemical shielding'. The direction of the generated field is dependant on the orientation of electronic environment with respect to the external field. The three-dimensional nature of the electron density means magnetic shielding is represented by a second rank tensor, $\boldsymbol{\sigma}$. In the principle axis system (Σ_{PAS}), asymmetric magnetic shielding terms are not observed and $\boldsymbol{\sigma}$ can be given in

the diagonalized form [6, 7]

$$\boldsymbol{\sigma}^{PAS} = \begin{pmatrix} \sigma_{xx} & 0 & 0 \\ 0 & \sigma_{yy} & 0 \\ 0 & 0 & \sigma_{zz} \end{pmatrix}. \tag{2.6}$$

For a magnetic field applied along the z-axis, the resulting chemical shielding Hamiltonian ($\hat{\mathscr{H}}_{CS}$) becomes

$$\hat{\mathscr{H}}_{CS} = \gamma\hbar\hat{\boldsymbol{I}} \cdot \boldsymbol{\sigma} \cdot \boldsymbol{B} \tag{2.7}$$

$$\hat{\mathscr{H}}_{CS} = \gamma\hbar\hat{I}_z\sigma_{zz}B_o, \tag{2.8}$$

and when transformed into the laboratory frame of reference, σ_{zz} becomes

$$\sigma_{zz} = \sigma_{iso} + \frac{\sigma_{aniso}}{2}[(3\cos^2\beta - 1) + \eta_{CS}(\sin^2\beta\cos 2\alpha)], \tag{2.9}$$

where σ_{aniso} and η_{CS} are given in the Haeberlen convention as

$$\sigma_{aniso} = \sigma_{zz} - \sigma_{iso}, \tag{2.10}$$

$$\eta_{CS} = \frac{\sigma_{xx} - \sigma_{yy}}{\sigma_{aniso}}. \tag{2.11}$$

Commonly, the combination of tensorial components in the form of σ_{iso}, σ_{aniso} and η_{CS} are stated in order to reflect the local symmetry about the nucleus. [5, 6] For an NMR spectrum of a fine powder, all crystallite orientations and consequently all possible chemical shielding tensors are observed. The overlap from resonant frequencies produced by each shielding tensor is observed. These characteristic powder patterns are shown in Figure 2.4, with the spectral shape being dependant on σ_{aniso} and η_{CS}. [6]

In order to make the shielding parameter σ_{iso} field independent, the shielding of a sample σ_{sample} is normalised against the known shielding of a reference sample σ_{ref}. The normalised shielding parameter is the isotropic

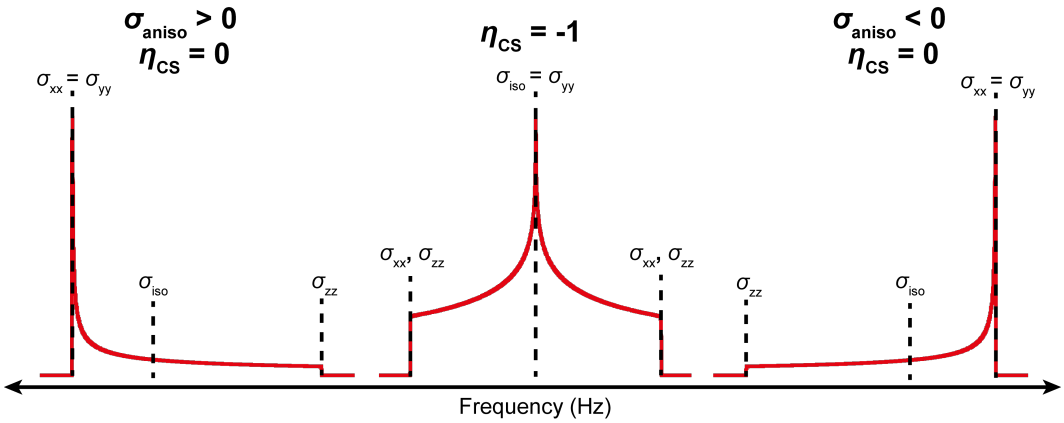

Figure 2.4: Static NMR powder patterns for different values of σ_{iso}, σ_{aniso} and η_{CS}. Powder patterns were simulated using *dmfit*. [8]

chemical shift, δ_{iso}, related by

$$\delta_{iso} = \frac{\nu_{sample} - \nu_{ref}}{\nu_{ref}} \times 10^6 = \frac{\sigma_{ref} - \sigma_{sample}}{1 - \sigma_{ref}}, \tag{2.12}$$

where ν_{sample} and ν_{ref} are the resonant frequencies of the sample and reference, respectively. Due to the relatively small change in chemical shielding between the sample and reference in comparison to the Larmor frequency, the isotropic chemical shift is small and is therefore stated in units of parts per million (ppm). [9]

2.2.3 The Dipolar Interaction

Dipolar coupling originates from the interaction between two magnetic dipoles owing to two nearby nuclear spins. The dipolar Hamiltonian for two interacting nuclear spins, $\hat{\boldsymbol{I}}$ and $\hat{\boldsymbol{S}}$ is given by [6]

$$\hat{\mathscr{H}}_D = \frac{\mu_o \gamma_I \gamma_S \hbar^2}{4\pi r^3} \left(\hat{\boldsymbol{I}} \cdot \hat{\boldsymbol{S}} - \frac{3(\hat{\boldsymbol{I}} \cdot \hat{\boldsymbol{r}})(\hat{\boldsymbol{S}} \cdot \hat{\boldsymbol{r}})}{r^2} \right), \tag{2.13}$$

where r is the distance between two nuclear spins. Written in polar coordinates, the above equation becomes

$$\hat{\mathscr{H}}_D = \frac{\mu_o \gamma_I \gamma_S \hbar^2}{4\pi r^3} (A + B + C + D + E + F), \tag{2.14}$$

where the terms A-F are

$$A = \hat{I}_z \hat{S}_z (3\cos^2\beta - 1), \tag{2.15}$$

$$B = -\frac{1}{4}[\hat{I_+}\hat{S_-} + \hat{I_-}\hat{S_+}](3\cos^2\beta - 1), \tag{2.16}$$

$$C = -\frac{3}{2}[\hat{I_+}\hat{S}_z + \hat{I}_z\hat{S_+}](\sin\beta\cos\beta)e^{-i\alpha}, \tag{2.17}$$

$$D = -\frac{3}{2}[\hat{I_-}\hat{S}_z + \hat{I}_z\hat{S_-}](\sin\beta\cos\beta)e^{+i\alpha}, \tag{2.18}$$

$$E = -\frac{3}{4}[\hat{I_+}\hat{S_+}]\sin^2\beta e^{-2i\alpha}, \tag{2.19}$$

$$F = -\frac{3}{4}[\hat{I_-}\hat{S_-}]\sin^2\beta e^{+2i\alpha}. \tag{2.20}$$

Here β is the angle between a vector connecting the two spins and the magnetic field $\boldsymbol{B}$ aligned along the z axis. $\hat{I_+}$ and $\hat{I_-}$ represent the raising and lowering operators, $\hat{I_+} = \hat{I}_x + i\hat{I}_y$ and $\hat{I_-} = \hat{I}_x - i\hat{I}_y$, respectively.

The terms C-F form the non-secular part of the dipolar hamiltonian and are time-dependant at frequencies ω_0 and $2\omega_0$. The frequency of the time dependence for the non-secular part (C-F) of the Hamiltonian is much higher than the frequency of the secular part (A and B). Therefore, the non-secular terms can be ignored here as they are effectively averaged over time to zero. The spin component of B is referred to as the flip-flop operator because it causes transitions between different spin states of two coupled spins. These transitions are most likely to occur when the process is energy conserving, i.e., between like spins. This leads to the homonuclear dipolar hamiltonian ($\hat{\mathscr{H}}_D^{homo}$) for a set of like spins, I_i and I_j

$$\hat{\mathscr{H}}_D^{homo} = \frac{\mu_o}{4\pi}\frac{\gamma_I^2\hbar^2}{2r_{ij}^3}\left[2\hat{I_{iz}}\hat{I_{jz}} - \frac{1}{2}[\hat{I_{ix}}\hat{I_{jx}} + \hat{I_{iy}}\hat{I_{jy}}]\right](3\cos^2\beta_{ij} - 1). \tag{2.21}$$

For spins of different elements the B term becomes becomes non-secular because the flip-flop process no longer conserves energy. This produces the

heteronuclear dipolar Hamiltonian $\hat{\mathscr{H}}_D^{hetero}$ for spins I and S

$$\hat{\mathscr{H}}_D^{hetero} = -\frac{\mu_o \gamma_I \gamma_S \hbar^2}{4\pi r^3}[\hat{I}_z \hat{S}_z](3\cos^2\beta - 1). \tag{2.22}$$

Due to the angular dependence of the above equations, the dipolar interaction is orientation dependent. In a similar fashion to chemical shielding (Equation 2.9), two-isolated spins form a characteristic lineshape called a pake doublet. [10] However, for more complex powder systems this is broadened into a Gaussian/Lorentzian lineshape.

2.2.4 The Quadrupolar Interaction

For nuclei with $I > \frac{1}{2}$, the quadrupolar interaction is present due to the non-spherical electrical charge distribution in the nucleus giving rise to an electric quadrupole moment eQ. [11] The quadrupolar interaction demonstrates the coupling between eQ and the electric field gradient (EFG). The quadrupolar Hamiltonian is written as

$$\hat{\mathscr{H}}_Q = \frac{eQ}{2I(2I-1)\hbar}\hat{I} \cdot \boldsymbol{V} \cdot \hat{I}, \tag{2.23}$$

where $\boldsymbol{V}$ is a tensor describing the EFG at the nucleus. In Σ_{PAS}, $\boldsymbol{V}$ can be diagonalised such that

$$\boldsymbol{V} = \begin{pmatrix} V_{xx} & 0 & 0 \\ 0 & V_{yy} & 0 \\ 0 & 0 & V_{zz} \end{pmatrix}, \tag{2.24}$$

which results in the conditions $|V_{zz}| \geq |V_{yy}| \geq |V_{xx}|$ and $V_{xx} + V_{yy} + V_{zz} = 0$ being satisfied. Consequently, the EFG can therefore be expressed in the terms of two parameters:

$$eq = V_{zz} \tag{2.25}$$

and

$$\eta_Q = \frac{V_{xx} - V_{yy}}{V_{zz}}, \tag{2.26}$$

which are the principal field gradient and the assymetry parameter respectively. Here the $\hat{\mathscr{H}_Q}$ transformation between Σ_{PAS} and Σ_{LAB} frames is not covered, and instead has been adapted from a report by Man. [12] For further enlightenment, this text should be referred to. According to Man, Equation 2.23 in the PAS frame is determined to be:

$$\hat{\mathscr{H}_Q} = \frac{C_Q\hbar}{4I(2I-1)}[3\hat{I_z}^2 - \hat{I}^2 + \eta_Q(\hat{I_x}^2 - \hat{I_z}^2)], \tag{2.27}$$

where the quadrupolar coupling constant is defined as

$$C_Q = \frac{e^2qQ}{\hbar}. \tag{2.28}$$

In the high field regime ($\hat{\mathscr{H}_Q} << \hat{\mathscr{H}_Z}$) $\hat{\mathscr{H}_Q}$ can be treated as a small perturbation to $\hat{\mathscr{H}_Z}$ and therefore conventional perturbation theory can be applied. The calculated first and second order perturbation terms are

$$\hat{\mathscr{H}_Q^{[1]}} = \frac{C_Q}{4I(2I-1)}[3\hat{I_z}^2 - I(I+1)]\left[\frac{(3\cos^2\beta - 1) + \eta_Q\sin^2\beta\cos 2\alpha}{2}\right], \tag{2.29}$$

and

$$\hat{\mathscr{H}_Q^{[2]}} = -\frac{1}{\omega_0}\left[\frac{eQ}{4I(2I-1)\hbar}\right]^2\begin{Bmatrix} f(\alpha,\beta,\eta_Q)\hat{I}_z[4I(I+1) - 8\hat{I_z}^2 - 1] + \\ 2f'(\alpha,\beta,\eta_Q)\hat{I}_z[2I(I+1) - 2\hat{I_z}^2 - 1] \end{Bmatrix}, \tag{2.30}$$

where $f(\alpha,\beta,\eta_Q)$ and $f'(\alpha,\beta,\eta_Q)$ are functions of the Euler angles α and β as well as the assymetry parameter, η_Q. These first and second order perturbations to $\hat{\mathscr{H}_Z}$ alter the spin energy levels as is shown in Figure 2.5. The effect of these perturbations will also change resonant frequencies. Corresponding frequency shifts due to the first and second order perturbations are given by

$$\omega^{[1]}_{m-1,m} = \frac{3C_Q}{4I(2I-1)}\left[\frac{(3\cos^2\beta - 1) + \eta_Q\sin^2\beta\cos 2\alpha}{2}\right](1-2m), \tag{2.31}$$

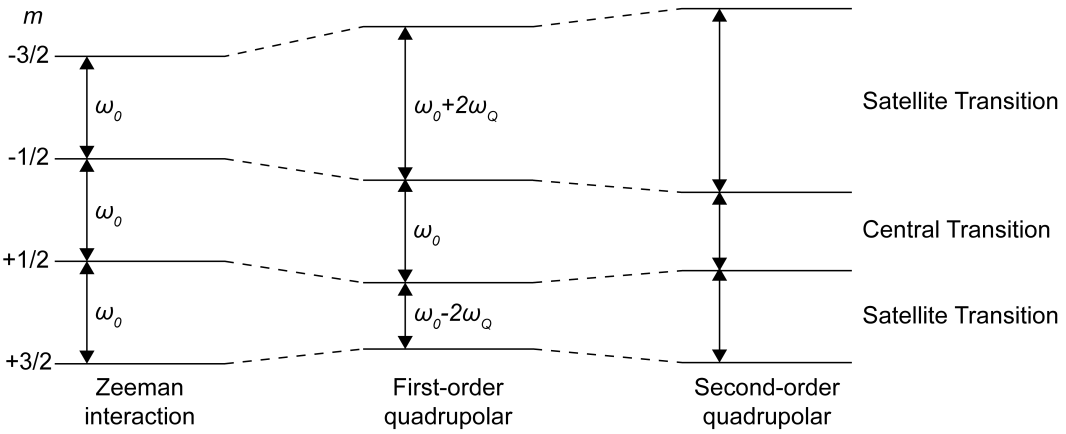

Figure 2.5: Energy level diagram for a spin-$\frac{3}{2}$ nucleus, showing the changes arising from first and second order quadrupolar perturbations.

and

$$\omega^{[2]}_{m-1,m} = -\frac{1}{\omega_0}\left[\frac{eQ}{4I(2I-1)\hbar}\right]^2 \left\{ \begin{matrix} f(\alpha,\beta,\eta_Q)[24m(m-1)-4I(I+1)+9]+ \\ 2f'(\alpha,\beta,\eta_Q)[12m(m-1)-4I(I+1)+6] \end{matrix} \right\}. \tag{2.32}$$

For simplicity the quadrupolar frequency (ω_Q) is ascribed to

$$\omega_Q = \frac{3C_Q}{4I(2I-1)}. \tag{2.33}$$

From Figure 2.5, it can be seen that the central transition (CT) between $m = -\frac{1}{2}$ and $+\frac{1}{2}$ spin states remains constant after first order perturbation effects are applied ($\omega^{[1]}_{-\frac{1}{2},\frac{1}{2}} = 0$). However, the satellite transitions (ST) between $m = -\frac{3}{2}$, $-\frac{1}{2}$ and $m = \frac{1}{2}$, $\frac{3}{2}$ exhibit perturbations in the resonant frequencies to the first order of $+2\omega_Q$ and $-2\omega_Q$, respectively. Furthermore, the first order transition frequencies have a similar dependence on the angles, α and β, which describe the orientation of Σ_{PAS} as for the CSA and dipolar interactions. Therefore, to the first order spin $I > 1/2$ nuclei will produce a powder pattern with contributions from $2I$ non-degenerate transitions as are depicted in Figure 2.6(a). The wide frequency range of a first order quadrupolar powder pattern can make it challenging to observe the spectrum in its entirety even for moderate C_Q values.

Even though the CT is unaffected by first order quadrupolar perturba-

tions, it is altered by second order effects. The shift to the resonant frequency of the CT caused by the second order perturbation is determined from Equation 2.32 to be:

$$\omega^{[2]}_{-\frac{1}{2},\frac{1}{2}} = -\frac{1}{6\omega_0}\left[\frac{3C_Q}{2I(2I-1)}\right]^2\left[I(I+1)-\frac{3}{4}\right]\begin{bmatrix}A(\alpha,\eta_Q)\cos^4\beta\\+B(\alpha,\eta_Q)\cos^2\beta\\+C(\alpha,\eta_Q)\end{bmatrix} \tag{2.34}$$

where

$$A(\alpha,\eta_Q) = -\frac{27}{8}+\frac{9}{4}\eta_Q\cos 2\alpha-\frac{3}{8}(\eta_Q\cos 2\alpha)^2 \tag{2.35}$$

$$B(\alpha,\eta_Q) = \frac{30}{8}-\frac{1}{2}\eta_Q^2-2\eta_Q\cos 2\alpha+\frac{3}{4}(\eta_Q\cos 2\alpha)^2 \tag{2.36}$$

$$C(\alpha,\eta_Q) = -\frac{3}{8}+\frac{1}{3}\eta_Q^2-\frac{1}{4}\eta_Q\cos 2\alpha-\frac{3}{8}(\eta_Q\cos 2\alpha)^2. \tag{2.37}$$

This second order shift to the CT also has an angular dependence which produces the characteristic static quadrupolar patterns where the shape and size of the pattern is dependent on η_Q and C_Q, as is exemplified in Figure 2.6(b) and (c).

2.2.5 The Knight Shift

For a conducting material, the overall magnetism will be affected by the delocalised conduction electrons, not just localised electrons in chemical bonds. The Knight shift (K) is measure of the relative shift in a metallic environment compared to an equivalent non-metallic environment. [13] The characteristics of the Knight shift are analogous to chemical shielding (Section 2.2.2) and can be thus formulated in an equivalent manner. If the Knight shift tensor in Σ_{PAS} is written as

$$\boldsymbol{K} = \begin{pmatrix}K_{xx} & 0 & 0\\ 0 & K_{yy} & 0\\ 0 & 0 & K_{zz}\end{pmatrix}, \tag{2.38}$$

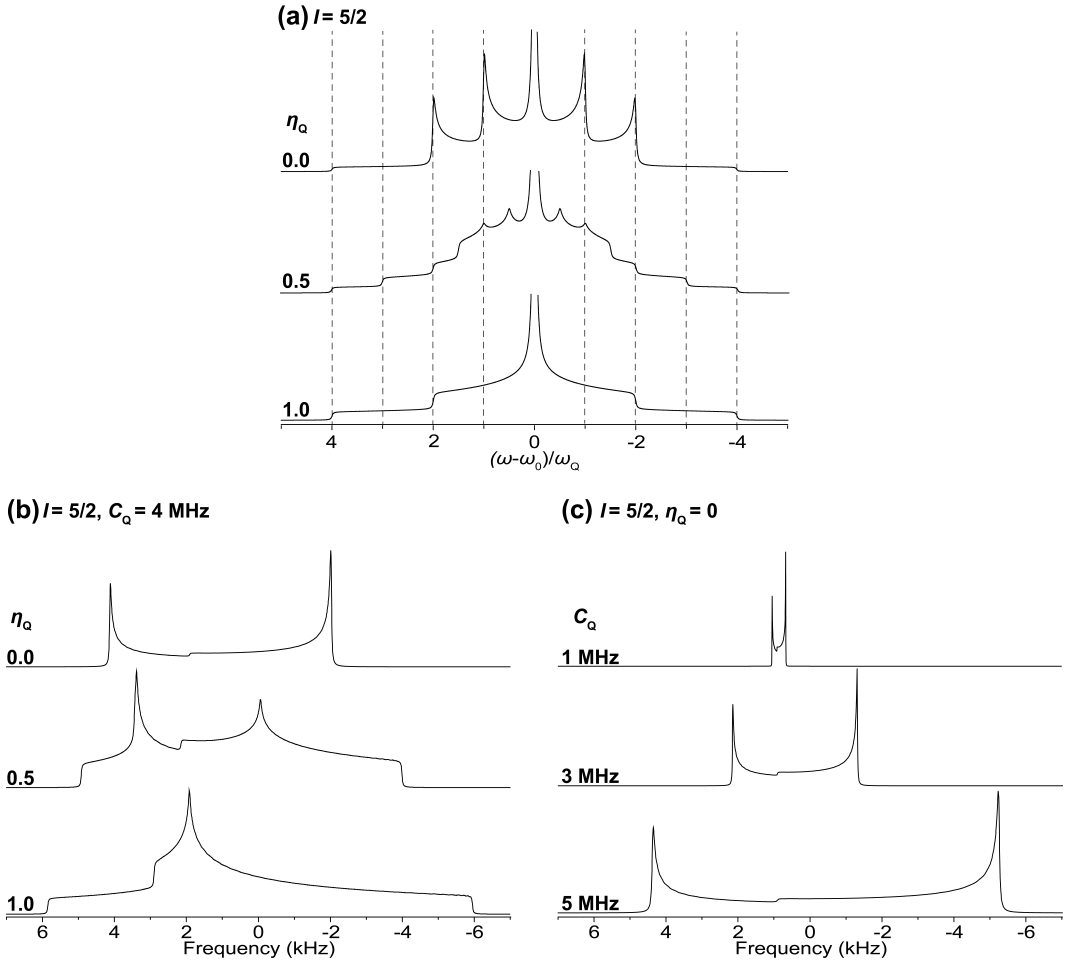

Figure 2.6: Static powder patterns of a spin-$\frac{5}{2}$ nucleus resulting from (a) the first order quadrupolar perturbations showing the ST manifold for varying values of η_Q (the intensity of the CT has been truncated) and the second order perturbations to the central transition at $B_0 = 14.1$ T for different (b) η_Q and (c) C_Q values.

then the frequency shift in Σ_{LAB} is determined to be

$$\omega = -\gamma B_o \left(K_{iso} + K_{aniso} \left[\frac{(3\cos^2\beta - 1) + \eta_K \sin^2\beta \cos 2\alpha}{2} \right] \right) \tag{2.39}$$

where

$$K_{iso} = \frac{K_{xx} + K_{yy} + K_{zz}}{3}, \tag{2.40}$$

$$K_{aniso} = K_{zz} - K_{iso} \tag{2.41}$$

and

$$\eta_{iso} = \frac{K_{xx} - K_{yy}}{K_{aniso}}. \tag{2.42}$$

Usually for metals, the structures are highly symmetrical, therefore $K_{xx} = K_{yy} = K_{zz}$ and only the isotropic component will be relevant. [5]

The total shift in a conducting material is made up of a combination of chemical shifts such that the total shift is: [14]

$$Total\ shift = K + \sigma = K_p + K_{cp} + K_{orb} + \sigma. \tag{2.43}$$

The contact interaction shift (K_p) forms as a result of the Pauli paramagnetic spin susceptibility (χ_p) of the conduction electrons. In a magnetic field, spins of conduction electrons aligned with the field become energetically favourable and will generate an imbalance of electron spin states. This imbalance is 'felt' by the nucleus, giving rise to the contact interaction shift described by

$$K_p = \frac{8\pi}{3} V_0 P_F \chi_p, \tag{2.44}$$

where V_0 is the volume per atom, P_F is an average value of the electron probability density at the nucleus and χ_p is the Pauli susceptibility. As can be seen from Equation 2.43, K_p is dependant on the electron density at the nucleus, hence the shift will be dominated by s-electrons because the direct effect from d-electrons is minimal. However, the d-electrons have an indirect effect called core polarisation (K_{cp}). The field generated by the d-electrons causes a polarisation on the inner s-electrons, producing an additional field which also affects the nucleus. [14] Finally, a contribution to the shift also occurs due to

the orbital magnetic moment of the conduction electrons generated from the application of the external magnetic field (K_{orb}). Problems arise during the characterisation of metals since in experiments only the total shift is observed and not the individual contributions from chemical shielding (σ) and Knight shift (K). A full description of the Knight shift and NMR in metals can be found in the review by Van der Klink and Brom. [14]

2.2.6 The Paramagnetic Interaction

When a material is place in the external magnetic field ($\boldsymbol{B}$), an additional magnetic field in the same direction will be generated if there are localised unpaired electrons present. This is known as the paramagnetic interaction. The paramagnetic Hamiltonian is generated from the sum of two interactions; a through bond Fermi contact interaction, also known as the hyperfine interaction and a through space electron-nuclear dipolar interaction. [15] The Fermi contact interaction is where the unpaired electron polarises the s-orbitals, changing the field experienced by the nucleus. The Hamiltonian for the Fermi-contact interaction for two spins $\hat{I}$ and $\hat{S}$ is expressed as

$$\hat{\mathscr{H}}^C = \frac{\mu_o}{4\pi}\frac{8\pi}{3}\gamma_I\gamma_S\hat{I}\cdot\hat{S}\delta(r), \tag{2.45}$$

where $\delta(r)$ is the Dirac delta function. [16]

The electron-nuclear dipolar interaction can be described analogously to the nuclear-nuclear dipolar interaction (Section 2.2.3) and the Hamiltonian is expressed similarly:

$$\hat{\mathscr{H}}^D = \frac{\hbar\gamma_I}{4\pi r^3}\hat{\boldsymbol{I}}\cdot\boldsymbol{\sigma_p}\cdot\boldsymbol{B} \tag{2.46}$$

where r is the electron-nucleus distance and σ_p is a second rank magnetic susceptibility tensor. [17]

Both the Fermi contact and electron-nuclear dipolar interaction Hamiltonians contribute to chemical shift observed in addition to the chemical shielding. Therefore, the overall observed shift is

$$\delta_{observed} = \delta_{diamagnetic} + \delta_{contact} + \delta_{dipolar}. \tag{2.47}$$

Paramagnetic coupling can be very strong in comparison to other interactions

and therefore the signal can be broadened to a point where it is unobservable. The large resonances produced from paramagnetic materials often makes the acquisition and analysis of solid state NMR spectra challenging. Given the similarity of the electron-nuclear interaction to CSA, paramagnetic resonances will broaden with increasing field and therefore a lower magnetic field will be beneficial for paramagnetic materials.

2.3 Magic Angle Spinning

In many of the interactions defined above, the anisotropic components contain the angular dependence $3\cos^2\beta - 1$, which in powdered samples where multiple crystallite orientations are possible causes lineshapes to broaden. In systems where multiple chemical sites are present, it can be difficult to distinguish spectral features making analysis challenging. To reduce the broadening effects associated with internal interactions, 'magic angle spinning' (MAS) was devised by Andrew, Bradbury and Eades. [3]

If a powdered sample is rotated about the magic angle (θ_r), then the average orientation of an internal interaction's anisotropic component will be the same as the rotation axis. The average angular dependence of the interactions over a rotor period is given by [5]

$$\langle 3\cos^2\theta - 1\rangle = \frac{1}{2}(3\cos^2\theta_r - 1)(3\cos^2\phi - 1) \tag{2.48}$$

where ϕ is the angle between Σ_{PAS} and Σ_{ROT}. The term $3\cos^2\theta - 1$ is the second order Legendre polynomial and is zero if $\theta = 54.74^o$. Therefore, rotating the sample at a magic angle of 54.74^o will minimise first order anisotropic interaction components. However, this is only achieved when the MAS frequency is much greater than the size of the anisotropy. Since it is not always possible to have an infinite rotation speed, residual spectral effects are observed by way of broadening and additional spinning sideband resonances located at multiples of the spinning frequency away from δ_{iso}. [6] Therefore, since dipolar and CSA broadening are described by the second order Legendre polynomials in Σ_{LAB}, sufficiently high spinning frequencies at the magic angle can remove the anisotropic component of their respective Hamiltonians.

2.3.1 The Quadrupolar Interaction under MAS

Even with first order interaction effects minimised, there are still higher order effects that are not fully reduced such as the second order quadrupolar effect. The second order quadrupolar effect also has an angular dependence described by the fourth order Legendre polynomial,

$$P_4(\cos\theta) = 35\cos^4\theta - 30\cos^2\theta + 3, \tag{2.49}$$

which has two solutions $\theta = 30.6^o$ and 70.1^o(Figure 2.7). It is not possible to satisfy both second and fourth order Legendre polynomials using a single MAS angle, resulting in residual second order quadrupolar effects still being observed. The resultant second order frequency shift on the CT is given by [5]

$$\omega^{[2]MAS}_{-\frac{1}{2},\frac{1}{2}} = -\frac{1}{6\omega_0}\left[\frac{3C_Q}{2I(2I-1)}\right]^2\left[I(I+1) - \frac{3}{4}\right]\begin{bmatrix} D(\alpha,\eta_Q)\cos^4\beta \\ + E(\alpha,\eta_Q)\cos^2\beta \\ + F(\alpha,\eta_Q)\end{bmatrix}, \tag{2.50}$$

where

$$D(\alpha,\eta_Q) = \frac{21}{16} - \frac{7}{8}\eta_Q\cos 2\alpha + \frac{7}{48}\eta_Q^2\cos^2 2\alpha, \tag{2.51}$$

$$E(\alpha,\eta_Q) = -\frac{9}{8} + \frac{1}{12}\eta_Q^2 + \eta_Q\cos 2\alpha - \frac{7}{24}\eta_Q^2\cos^2 2\alpha, \tag{2.52}$$

and

$$F(\alpha,\eta_Q) = \frac{5}{16} - \frac{1}{8}\eta_Q\cos 2\alpha + \frac{7}{48}\eta_Q^2\cos^2 2\alpha. \tag{2.53}$$

The orientation dependence of Equation 2.50 means a powder pattern is still observed for quadrupolar nuclei under MAS conditions. Similar to static spectra, the lineshape is characterised by the magnitude of the quadrupolar interaction (C_Q) and the asymmetry (η_Q) as is shown in Figure 2.8(a). It is possible to simulate quadrupolar lineshapes, allowing for NMR spectra to be fitted which in turn will provide experimental values for C_Q and η_Q.

Despite MAS not being able to fully remove second order quadrupolar effects, the lineshape will still be narrowed in comparison to the static conditions. Under fast MAS condition, the breadth of the CT powder pattern is

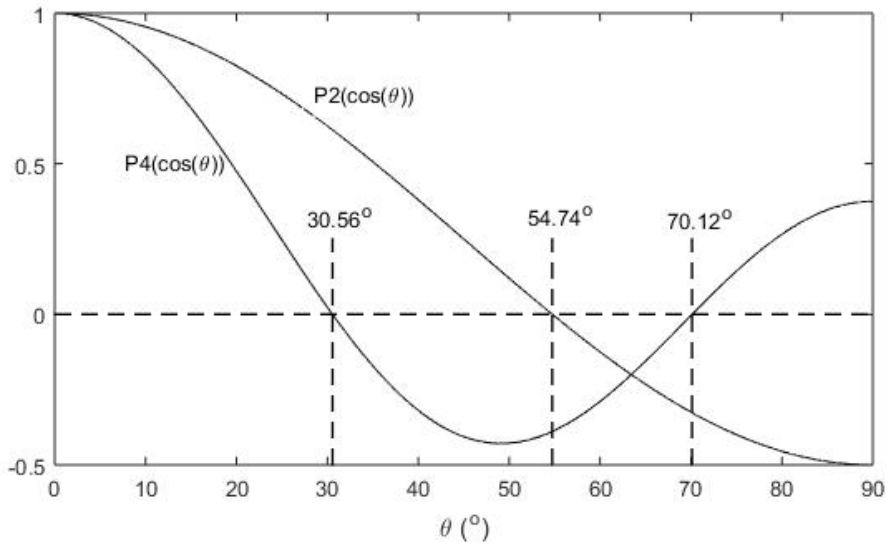

Figure 2.7: Graphical representation of the second- (P2($\cos\theta$)) and fourth order (P4($\cos\theta$)) Legendre polynomials showing the points at which the y-axis is crossed.

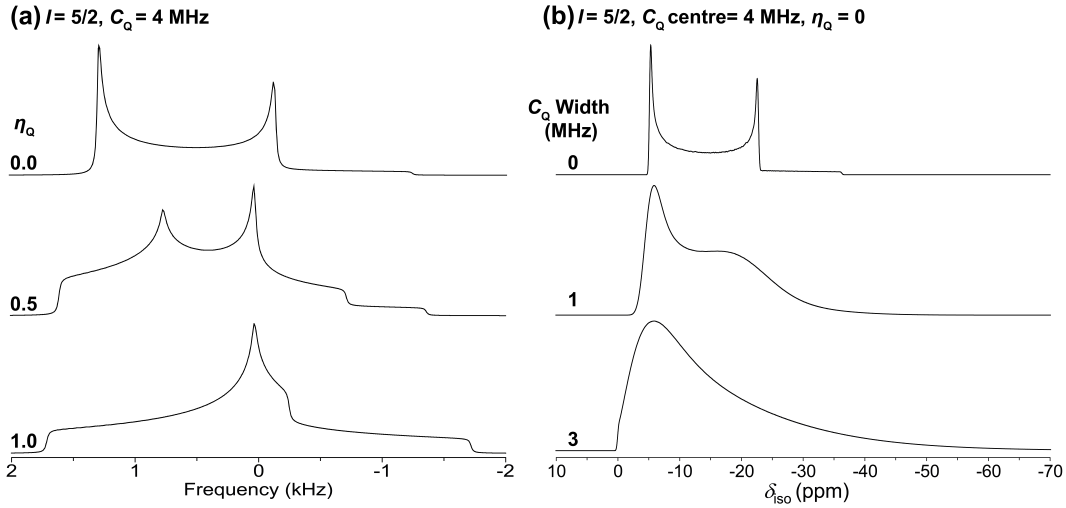

Figure 2.8: (a) Powder pattern spectra (B_0 = 14.1 T) produced for different η_Q values by the second order frequency shift of the CT under the fast MAS regime. (b) Simulated NMR lineshapes of the second order quadrupolar broadened CT for a $I = 5/2$ nucleus with ν_o = 81.341 MHz, $\eta_Q = 0$ and a Gaussian distribution of C_Q defined by the centre and width. Lineshapes were produced using the QuadFit program. [1]

$$\Delta\left(\omega^{[2]}_{-\frac{1}{2},\frac{1}{2}}\right) = \frac{(6+\eta_Q)^2}{504}\left(\frac{\omega_Q^2}{\omega_0}\right)\left[I(I+1)-\frac{3}{4}\right]. \tag{2.54}$$

It should also be noted that the breadth is inversely proportional to ω_0. Therefore, increasing the magnetic field strength (B_0) will reduce the width of quadrupolar lineshapes, potentially giving improved resolution.

Additionally, the centre of gravity of second order quadrupolar lineshapes (δ_{cg}) are dependent on B_0. The chemical shift induced by second order quadrupolar effects on the CT (δ_{QIS}) is given by [12]

$$\delta_{QIS} = -\frac{3\left[I(I+1)-\frac{3}{4}\right]}{40I^2(2I-1)^2}\frac{C_Q^2}{\omega_0^2}\left(1+\frac{\eta_Q^2}{3}\right)\times 10^6. \tag{2.55}$$

Therefore, the total experimental centre of gravity shift (δ_{cg}) is given by

$$\delta_{cg} = \delta_{iso} + \delta_{QIS} = \delta_{iso} - \frac{3}{40}f(I)\left(\frac{P_Q}{\omega_0}\right)^2, \tag{2.56}$$

and the quadrupolar product, P_Q, is defined as

$$P_Q = C_Q\left(1+\frac{\eta_Q^2}{3}\right)^{\frac{1}{2}}, \tag{2.57}$$

and

$$f(I) = \frac{\left[I(I+1)-\frac{3}{4}\right]}{I^2(2I-1)^2}. \tag{2.58}$$

The powder patterns presented in Figure 2.8(a) represent spectra of highly crystalline materials. However, many systems often contain local disorder which is the case for the majority of materials presented in this thesis. Disorder generates a distribution of quadrupolar parameters over the nuclei sites within the material and the resultant spectrum is the sum of each pattern produced for each set of differing parameters. This lineshape can be simulated using a Gaussian distribution of C_Q values, as has been produced using QuadFit in Figure 2.8(b). [1] The disordered pattern is shown to retain the characteristic assymetric quadrupolar lineshape but this becomes broadened as the width of the C_Q distribution increases. At large C_Q distribution widths, the broadening leads to a long tail towards lower frequencies producing

a characteristic Czjzek or GIM (Gaussian Isotropic Model) lineshape. [18]

Chapter 3

Experimental Techniques

3.1 NMR Experimentation

3.1.1 Bulk Magnetisation

Thus far, only interactions concerning individual or a pair of nuclear spins have been considered. In a material there are many spins and therefore for NMR experiments the whole system needs to be considered. The bulk magnetisation is described as the sum of all magnetic moments in a sample. When there is no external magnetic field, the moments in the sample will be randomly oriented resulting in no overall net magnetisation. However, due to the Zeeman interaction (Section 2.1.2) resulting from an applied static magnetic field (B_0), it becomes energetically favourable for moments to align with the field. This results in a net magnetisation (M_0) aligned with the field.

The probability of a single moment being aligned with the field is governed by Boltzmann statistics and is dependent on the temperature and, more importantly, the energy difference between spin-states. In most NMR measurements the high temperature limit ($\gamma\hbar B_0 << k_B T$) can be assumed. [5] Therefore, the average z-component of the magnetic moment is determined to be

$$\langle \hat{\mu_z} \rangle = \frac{(\gamma\hbar)^2 B_0 I(I+1)}{3k_B T}, \tag{3.1}$$

where T is the temperature and k_B is the Boltzmann constant. For N nuclei

within a sample, the resulting magnetisation is therefore

$$M_0 = N\langle\hat{\mu_z}\rangle. \tag{3.2}$$

3.1.2 Radiofrequency Pulse

Perturbation of the magnetisation is achieved through the application of a RF pulse. The use of an EM wave generates a time dependant oscillating magnetic field, $B(t)$, which when applied along the x-axis in Σ_{LAB} can be described by

$$B(t) = 2B_1 cos(\omega_{RF}t + \phi)\hat{x}, \tag{3.3}$$

where $2B_1$ is the field magnitude, ω_{RF} is the oscillation frequency and ϕ is the wave phase. This oscillating EM field will interact with nuclear spins in the static field (B_0) to give a combined Hamiltonian

$$\hat{\mathscr{H}} = \hat{\mathscr{H}_Z} + \hat{\mathscr{H}_{RF}} = -\gamma\hbar(B_0\hat{I}_z + 2B_1\cos(\omega_{RF}t)\hat{I}_x). \tag{3.4}$$

The oscillating magnetic field can be thought of as two counter rotating fields around the z axis at frequencies ω_{RF} and $-\omega_{RF}$. In that case, transforming the Hamiltonian into the Σ_{RF} frame of reference results in only the component rotating in phase with the magnetisation having an effect. Therefore the time dependent part of the Hamiltonian can be removed such that

$$\hat{\mathscr{H}} = (\omega_0 - \omega_{RF})\hbar\hat{I}_z - \gamma\hbar B_1\hat{I}_x. \tag{3.5}$$

If the applied RF pulse oscillates at the same frequency as the Larmor frequency ($\omega_0 = \omega_{RF}$), then only the $\hat{I}_x$ term remains which is of a similar form to the Zeeman Hamiltonian in Chapter 2.1.2. Therefore, just as the magnetisation precesses about B_0 for the Zeeman interaction, when an RF pulse is applied it will precess about the x-axis at the nutation frequency

$$\omega_{nut} = -\gamma B_1. \tag{3.6}$$

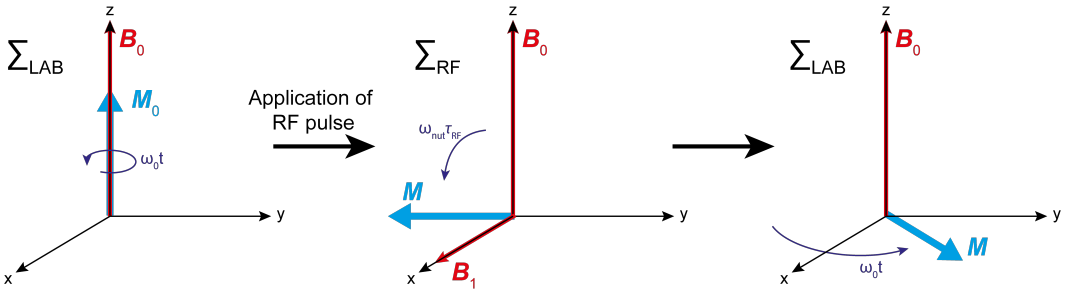

Figure 3.1: The effect of applying a RF pulse to the magnetisation at equilibrium in Σ_{LAB} precessing about B_0 at ω_0. Application of the RF pulse along the x-axis generates transverse magnetisation in Σ_{RF} which sequentially precesses in the x-y plane at a rate of $\omega_0 t$ in Σ_{LAB}.

The angle with which the magnetisation nutates, called the flip angle, during the time τ_{RF} is

$$\theta_{nut} = \omega_{nut}\tau_{RF}. \tag{3.7}$$

Therefore, the application of an RF pulse in the x-direction can rotate the magnetisation along the $-y$-axis such that $\theta_{nut} = \pi/2$, which will subsequently precess at a rate ω_0 in the x-y plane as is depicted in Figure 3.1. Measuring the precession of magnetisation precession in the x-y plane forms the basis of an NMR experiment. [4, 19]

A full review of quadrupolar effects on the nutation is given by Freude and Haase and a summary will be given here. [20] Changes in the nutation can arise when $\hat{\mathscr{H}}_Q \approx \hat{\mathscr{H}}_{RF}$, meaning the quadrupolar Hamiltonian has to be taken into account. [19] Taking into account each Hamiltonian, the nutation frequency for a selective pulse on the central transition $\omega_{nut}^{s,CT}$ is given by

$$\omega_{nut}^{s,CT} = \left(I + \frac{1}{2}\right)\omega_{nut}^{ns} = -\gamma B_1 \left(I + \frac{1}{2}\right), \tag{3.8}$$

where ω_{nut}^{ns} is the non-selective nutation frequency. This also means the pulse duration changes such that

$$\tau_{RF}^{ns} = \left(1 + \frac{1}{2}\right)\tau_{RF}^{s,CT}. \tag{3.9}$$

Consequently, quadrupolar nuclei nutate faster and therefore require shorter

RF pulses to obtain the same flip angle as their spin-1/2 counterparts. For RF pulse calibration of quadrupolar nuclei, these effects need to be taken into account.

Moreover, the magnetisation in the x-y plane after an RF pulse for spin-1/2 resonance and a quadrupolar CT resonance are

$$M_t^{ns} = M_0 \sin \omega_{nut}^{ns} \tau_{RF} \tag{3.10}$$

and

$$M_t^{s,CT} = \frac{M_0}{\left(I + \frac{1}{2}\right)} \sin \left[\left(I \frac{1}{2} \right) \omega_{nut}^{ns} \tau_{RF} \right], \tag{3.11}$$

respectively. If $\omega_{nut}^{ns} \tau_{RF} << \pi$ (i.e. the small angle approximation) then the magnitude of magnetisation for spin-1/2 and quadrupolar nuclei will be equal. Therefore, to minimise differences in transverse magnetisation between resonances for quadrupolar nuclei the condition

$$\left(I + \frac{1}{2} \right) \omega_{nut}^{ns} \tau_{RF} \leq \frac{\pi}{6}, \tag{3.12}$$

needs to be implemented. The small flip angles allow for quantitative interpretations of quadrupolar NMR data. However, this does lead to a significant reduction in the NMR signal obtained and as such the choice of flip angle is usually chosen to be a compromise between the signal and quantitation.

For a single RF pulse experiment, the maximum signal is achieved when $\theta_{nut} = \pi/2$ i.e. when the magnetisation is entirely in the transverse plane. The maximum signal (S) obtainable for such a pulse can be described by the equation:

$$S = V_c \gamma B_0 M = \frac{N V_c \gamma^3 B_0^2 \hbar^2 I(I+1)}{3 k_B T}, \tag{3.13}$$

where V_c is the sample volume. [5] As can be seen from the above equation, an NMR signal can be improved by changing multiple factors such as the magnetic field, volume of sample or even isotopically enriching the sample to contain more NMR active nuclei.

3.1.3 Relaxation

Once the net magnetisation is perturbed from B_0 by an RF pulse it will return back to equilibrium over time. The time it takes the magnetisation component parallel to B_0 ($+z$-direction) to recover is called the longitudinal relaxation (T_1) and the complete decay of magnetisation in the x-y plane is called the transverse relaxation (T_2).

A classical description of magnetisation dynamics in each plane is given by the following Bloch equations: [21]

$$\frac{dM_x}{dt} = \frac{-M_x}{T_2}, \tag{3.14}$$

$$\frac{dM_y}{dt} = \frac{-M_y}{T_2}, \tag{3.15}$$

$$\frac{dM_z}{dt} = \frac{M_0 - M_z}{T_1}, \tag{3.16}$$

where M_0 is the magnetisation at thermal equilibrium. These Bloch equations can be solved in the rotating frame after the application of a 90^o RF pulse ($\theta_{nut} = \pi/2$), to give the exponential build up and decay of the magnetisation:

$$M_x = M_x(0)(e^{-\frac{t}{T_2}}) \tag{3.17}$$

$$M_y = M_y(0)(e^{-\frac{t}{T_2}}) \tag{3.18}$$

$$M_z = M_0(1 - e^{-\frac{t}{T_1}}). \tag{3.19}$$

The relaxation time constants T_1 and T_2 both vary for different systems and nuclei since they are dependent on the strength of local interactions experienced by the nuclei. [22, 23] Hence, it is possible for moments to precess at different rates, depending on the interaction strengths at each nucleus.

When there are multiple nuclei with the same frequency but differing T_1 relaxations (i.e. disordered materials), the longitudinal magnetisation is best

described by a stretched exponential function, written as

$$M_z = M_0 \left(1 - e^{-\left(\frac{t}{T_1^*}\right)^x} \right) \tag{3.20}$$

where T_1^* and x $(0 < x < 1)$ define the probability distribution of relaxation times. This recovery mechanism can also be true for the CT of quadrupolar dominated nuclei where the non-exponential relaxation is due to insufficient excitation of the quadrupolar lineshape. [22, 23]

The spin-lattice relaxation in metals is also different and is dominated by the Fermi contact interaction which induces the Knight shift (2.2.5). The relationship between T_1 and the Knight shift was initially determined by Korringa and is given by

$$T_1 K^2 = \frac{\hbar}{4\pi k_B T} \left(\frac{\gamma_e}{\gamma_n} \right)^2 B, \tag{3.21}$$

where K is the Knight shift, T is the temperature, γ_e and γ_n are the gyromagnetic ratios of the electron and the nucleus, respectively and B is a constant which is equal to one if many body effects are neglected. [24]

In an NMR experiment, T_2 is not always what will be measured. Usually, there will be magnetic field inhomogeneities in B_0 and direct interactions between spins without energy transfer to the lattice which will also contribute to the transverse relaxation time such that T_2^* will be measured instead. This is related to T_2 by [5]

$$\frac{1}{T_2^*} = \frac{1}{T_2} + \frac{1}{T_{2(\Delta B)}}. \tag{3.22}$$

This T_2^* is inversely proportional to the linewidth in an NMR spectrum. Therefore generally, a larger interaction with the nucleus results in a shorter T_2^* which produces a broader lineshape.

3.1.4 Saturation Recovery Experiment

The longitudinal relaxation time (T_1) of a resonance can be ascertained through the use of saturation recovery pulse sequences. Determining the T_1 of a resonance provides beneficial information for materials characterisation because

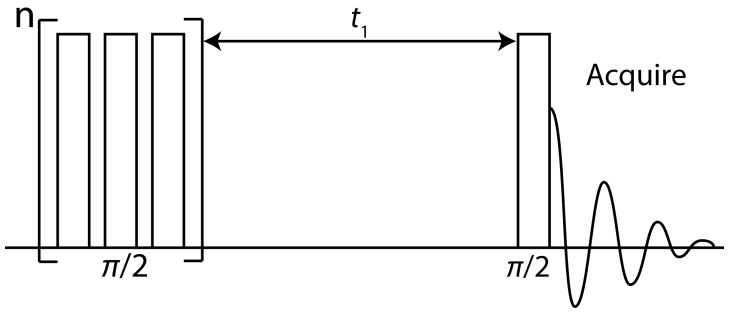

Figure 3.2: A saturation recovery NMR pulse sequence entailing an initial pulse train of n $\pi/2$ pulses followed by a single $\pi/2$ pulse and a variable time t_1 afterwards.

of its correlation to structural surroundings. The saturation recovery pulse sequence is shown in Figure 3.2. A $\pi/2$ pulse train is applied to initially eliminate all longitudinal magnetisation, meaning that the system is not required to relax in order to begin subsequent experiments. Following the pulse train, magnetisation is allowed to recover for a time t_1, at which point a $\pi/2$ pulse will then rotate the recovered magnetisation into the transverse acquisition plane through which it can be detected. By increasing the evolution time (t_1), the resonance intensity will also grow. Fitting recorded intensities for an array of evolution times will therefore determine T_1. [5]

3.1.5 Heteronuclear Decoupling

Even though the majority of hetoronuclear dipolar coupling is removed through MAS conditions, there will still be anisotropic components which remain. These effects become especially noticeable when low abundant nuclei (e.g ^{13}C) are amongst high abundant nuclei (e.g. ^{1}H). A decoupling pulse sequence applied on the abundant nucleus channel whilst acquiring the low abundant nuclei can be applied to minimise these broadening effects. A basic decoupling pulse sequence consists of a high powered RF pulse, however, this can cause sample heating and can be highly demanding on the equipment. Therefore, more efficient sequences have been produced such as SPINAL-64. [25]

3.1.6 Cross Polarisation

The acquisition of NMR nuclei with low sensitivity or a long T_1 can be time consuming and achieve poor signal to noise if acquired through a single pulse experiment. Therefore, cross-polarisation (CP) experiments can be used in conjunction with MAS to offer signal enhancements. Through manipulation of the dipolar interaction between two nuclei, polarisation transfer from a highly sensitive and abundant nucleus (I) to a nucleus with lower sensitivity or abundance. Using CPMAS experiments also allows the T_1 of the more sensitive nucleus to be implemented when calculating the recycle delay between subsequent experiments.

Using ^{1}H as an example of a high abundance nuclei, the ^{1}H magnetisation is first transferred into the x-y plane. Following this, a spin lock pulse is applied to the ^{1}H nuclei whilst a simultaneous matched contact pulse is used on the low abundance nuclei (X). The matching required for a transfer of magnetisation to take place is given by the Hartmann-Hahn condition,

$$\gamma_H B_1(^1\mathrm{H}) = \gamma_X B_1(X) \tag{3.23}$$

where both pulses are to have the same nutation frequencies. [26] Satisfying the above condition generates equal energy gaps between each nuclei's spins, thus allowing for a redistribution of spin states between nuclei resulting in an increase of X spins in the x-y plane. During the acquisition of the X nuclei, decoupling of the ^{1}H nuclei is commonly applied.

The above equations are true when MAS frequencies are low such that the rotor period is much less than the contact period. However, when using fast MAS frequencies (>20 kHz) the matching condition is modified to

$$\gamma_H B_1(^1\mathrm{H}) - \gamma_X B_1(X) = \pm n\omega_r \tag{3.24}$$

where ω_r is the rotor frequency and n is an integer.

The above equations are true when MAS frequencies are low such that the rotor period is much less than the contact period. However, when using

fast MAS frequencies (>20 kHz) the matching condition is modified to

$$\gamma_H B_1(^1\mathrm{H}) - \gamma_X B_1(X) = \pm n\omega_r \tag{3.25}$$

where ω_r is the rotor frequency and n is an integer.

Equation 3.23 is only valid for spin-1/2 nuclei and for quadrupolar systems where C_Q is significant, the Hartmann-Hahn condition needs to be adjust to

$$\gamma_H B_1(^1\mathrm{H}) = \alpha_X \gamma_X B_1(X) \tag{3.26}$$

where $\alpha_X = \sqrt{I(I+1) - m(m-1)}$ for the (m,$m-1$) transition in a quadrupolar nucleus with spin I. [5] For quadrupolar nuclei, a shorter contact time is generally applied to allow for more homogeneous transfer across the spin states.

3.1.7 Hahn Echo Experiment

After a single RF pulse, nuclear spins can become dephased in the acquisition plane due to differing interaction strengths. Erwin Hahn found that through the use of the pulse sequence ($\pi/2 - \tau - \pi/2$) it was possible to refocus the spins which are precessing at different rates. [2] This pulse sequence was later developed into the Hahn echo by Carr and Purcell, where the second pulse is changed to a π pulse ($\pi/2 - \tau - \pi$) which is particularly useful in the refocusing of broad resonances and quadrupolar nuclei. [27] The initial $\pi/2$ acts the same as a single RF pulse transferring the magnetisation into the x-y plane. However, the moments are then allowed to evolve and dephase for a time τ, which for MAS measurements is usually a multiple of the spinning frequency. The subsequent π pulse flips the spins about the x axis (where the RF pulse is applied along the x-axis), allowing the complete refocussing of spins at a time τ later, at which point the FID can be acquired.

It is also possible to use echo experiments to determine T_2' relaxation times. Due to the refocusing of spins in an echo experiment, the inhomogeneities related to T_2^* are removed leaving only T_2' relaxation. Through measurement of the echo peak signal intensity with changing echo delay, Equation 3.17 or 3.18 can be used to determine T_2' noting that the observed T_2' depends in the solid state on experimental parameters such as MAS frequency and,

when decoupling is applied, the nutation frequency and the sequence used for decoupling

3.1.8 Variable Offset Cumulative Spectroscopy

Sometimes a spectral lineshape will cover a broad range of frequencies which is larger than the possible excitation bandwidth of a single pulse and therefore, obtaining the full lineshape is not achievable from a single acquisition. To solve this problem, variable offset cumulative spectroscopy (VOCS) is used, whereby multiple echo experiments are acquired at incremental frequencies across the NMR spectrum. The spectral sum of each frequency will then provide the full lineshape. [28, 29] Uniform excitation is required across the frequency range and therefore pulse profiles must be constant and frequency increments should be less than the pulse excitation bandwidth.

3.1.9 Multiple Quantum MAS (MQMAS)

As was discussed in Section 2.3, spinning at the magic angle (54.74^o) will fully average first order quadrupolar effects and will narrow the spectrum. However, the different angular dependence of second order effects results in the quadrupolar interaction not being fully eliminated. Whilst there are methods such as double rotation (DOR) and dynamic angle spinning (DAS) which will satisfy both angular dependencies, they can be difficult to implement. [30, 31] The 2D MQMAS provides an alternative technique in resolving quadrupolar spectra through the correlation of phase evolutions whilst spinning at the magic angle. [32]

For NMR pulse sequences, it is helpful to describe the echo pathway in terms of the p quantum coherence. It is defined as the superposition of $|m\rangle$ and $|m'\rangle$ states with the multiplicity defined by $p = m - m'$. The most basic MQMAS experiment requires an excitation of the multiple quantum coherence p, an evolution time (t_1) of these coherences, a reconversion of coherences into the observable coherence ($p = -1$) and detection of the resulting echo as a function of teh evolution time t_2. The evolution times t_1 and t_2 are correlated such that the anisotropic components of the quadrupolar interaction

are removed and the isotropic component of the echo t_{2e} will be observed at:

$$t_{2e} = R(I,p)t_1, \tag{3.27}$$

whereby,

$$R(I,p) = \frac{p[36I(I+1) - 17p^2 - 10]}{36I(I+1) - 27}. \tag{3.28}$$

It is common to modify the original two pulse MQMAS sequence experiment with additional pulses by way of a z-filter or split-t_1 experiment to remove the presence of dispersive components that lower the resolution in the spectrum. Figure 3.3(a) shows a typical pulse sequence and coherence pathway for the acquisition of a 3QMAS z-filter experiment for a spin 3/2 nucleus. For a z-filtered MQMAS experiment, the conversion pulse transfers the multiple quantum coherence to a population state ($p = 0$) to ensure that the remaining magnetisation is aligned with B_0. Finally, a selective soft pulse is applied a short delay, τ, after the conversion pulse to transfer the signal into the observable single quantum coherence ($p = -1$). A 2D Fourier transform of the time domain signal results in a correlation spectrum where the axis are the frequencies in single and multiple quantum dimensions represented by F_1 and F_2 respectively and are related by $F_1 = R(I,p)F_2$. Usually, the spectrum is 'sheared' in order to align the F_1 dimension with the isotropic axis (δ_{iso}) and by doing so the F_2 dimension becomes the MAS axis (δ_{MAS}). By convention, two more axis are drawn on a sheared MQMAS spectrum. The first representing a chemical shift axis (CS), signifying the orientation of resonances where the quadrupolar shift is zero. Secondly, the quadrupolar induced shift (QIS) line is drawn to describe the changing quadrupolar induced shift for a constant isotropic chemical shift value. [33]

The phase-modulated split-t_1 MQMAS implements a refocusing π pulse at the end of the sequence to ensure that the entire echo signal is acquired in the time t_2 and ensure dispersive components are removed. An example of this pulse sequence is shown in Figure 3.3(b). This can also be combined with the split-t_1 method proposed by Brown *et. al.* to remove the need to shear fourier transformed spectra. [34] Differently to the pulse sequence in Figure 3.3(a), the time t_1 is split into single quantum coherence ($p = 1$) and multiple quantum coherence evolution periods determined by a ratio of $R(I,p)$, such

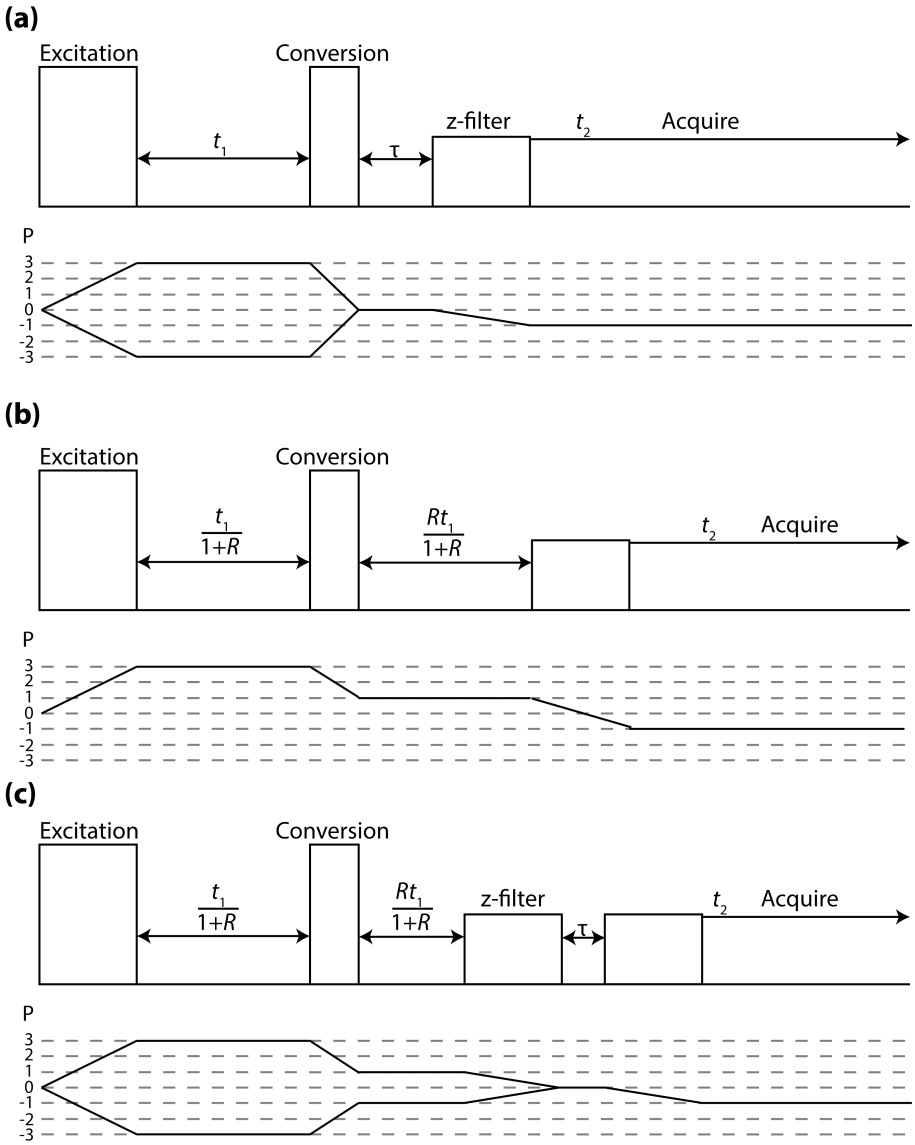

Figure 3.3: Pulse sequence and coherence transfer pathway diagrams for the amplitude modulated MQMAS experiments; (a) z-filter 3QMAS experiment, (b) split-t_1 and (c) a split-t_1 with a z-filter at the end of the t_1 evolution period.

that the fourth rank anisotropic quadrupolar terms are refocused after t_1. In this thesis, a combination of a split-t_1 and z-filter is primarily used as is shown in Figure 3.3(c).

3.2 NMR Simulation Software

3.2.1 DMFit

DMFit is a NMR lineshape fitting software which was developed by D. Massiot. [8] This software has a range of capabilities which take into account many of the interactions described in Section 2 (e.g. quadrupole and CSA broadening), under both static and MAS conditions. Even though DMFit has the ability to fit complex lineshapes, it has primarily been used throughout this thesis to simulate Gaussian/Lorentzian lineshapes of spin 1/2 nuclei or quadrupolar nuclei with small quadrupolar coupling (i.e. $C_Q \sim 0$) under MAS. Since these nuclei experience negligible quadrupolar broadening and the anisotropic broadening is removed by MAS, this method is suitable to extract isotropic shifts and intensities for each lineshape. If given the number of peaks in a spectrum, the program will utilise an iterative technique in order to minimise the differences between experimental data and the simulation providing accurate fitting parameters.

3.2.2 QuadFit

The majority of systems investigated in this thesis contain disorder. As was discussed in Section 2.3.1, disordered quadrupolar NMR lineshapes are broadened, potentially showing featureless assymetric lineshapes. However, the QuadFit package can successfully simulate these disordered lineshapes. Lineshapes are simulated by taking a Gaussian distribution of C_Q and η_Q values which represent a distribution of parameters from multiple slightly different nuclei. The user defines the central C_Q and η_Q values and the width of the distribution. In this work the value of η_Q has not been set to a distribution and instead a constant value since the simulation has been focused on determining C_Q. There are a number of independent variables when fitting these lineshapes

and therefore it was deemed that the C_Q parameter had the greatest influence on disordered lineshapes.

3.3 Powder X-ray Diffraction (PXRD)

In order to determine the crystalline structure of a material, X-ray diffraction (XRD) is commonly used. If the wavelength of an incident X-ray is similar to the lattice spacing then the X-ray will be diffracted. Diffracted rays will undergo both constructive and destructive interference dependant on the phase of the diffracted X-ray beams. However, the detected diffraction pattern will only consist of the constructive interference, which according to Bragg's law occurs when

$$n\lambda = 2d\sin\theta \tag{3.29}$$

where $n\lambda$ are integer multiples of the X-ray wavelength, d is the lattice spacing and θ is the angle between the incident X-ray and the lattice plane.

A XRD experiment consists of a monochromatic X-ray source which is fired at the sample at some angle θ and the diffracted beam intensity is recorded at an angle 2θ away from the source. For powdered samples, there are many crystallite orientations and by scanning over a range of 2θ values every possible diffraction is obtained. The powdered sample is also spun in order to obtain a good powder average. Resultant powder patterns are plotted as intensity versus 2θ where the positions of the peaks are generated based on the size and shape of the unit cell. Therefore, expansion or contraction of the lattice can be quantified by the shift of peak position. The intensity of a diffraction peak is determined by the arrangement of atoms within the unit cell and is given by

$$I_{hkl} \propto \left| \sum_{j=1} N_j f_j e^{[2\pi(hx_j+ky_j+lz_j)]} \right|^2, \tag{3.30}$$

where N_j is the fraction of every equivalent position that is occupied by atom j, f_j is the scattering factor quantifying the efficiency of X-ray scattering at any angle, hkl are the Miller indices defining planes of atoms and x, y and z are the coordinates of atoms on the planes. [35]

The overlap of slightly different reflections in a powder X-ray diffraction (PXRD) experiment makes crystal structure determination difficult. In order to identify a crystal structure from a powder pattern Rietveld refinements can be performed which was a method initially developed by H. Rietveld. [36] The obtained powder pattern is refined against a previously known model and parameters are optimised using a least squares procedure to provide a calculated fit of experimental diffraction peaks. However, since a periodic structure is required for diffraction to occur, disordered or amorphous materials will either not be observed or appear as a broad background signal meaning structure determination of disordered materials is not possible by PXRD. Additionally, the particle size can cause difficulties in structure refinement since smaller particles will broaden diffraction peaks. This is best described using the Scherrer equation which relates the size of sub-micrometre particles in a solid to the broadening of a diffraction peak and is given by

$$\tau = \frac{K\lambda}{\beta \cos\theta}, \tag{3.31}$$

where τ is the particle size, K is a dimensionless shape factor determined by the particle shape and β is the line broadening at half the maximum intensity of the diffraction peak. [37]

Chapter 4

Solid State NMR Studies of PGM oxides and Metal Oxide Supported PGMs

4.1 Introduction

4.1.1 Background

Heterogeneous catalysts play an important role in many industrial processes such as food production, petrochemicals and pharmaceuticals, allowing for greater product yields, improved reaction efficiencies and reduced reaction temperatures and pressures to be achieved. [38–40] Knowledge of a catalyst's structure is of high interest because of the potential improvements in efficiency of industrial processes leading to reduced cost and environmental impact. Platinum, palladium, rhodium, ruthenium, iridium and osmium make up the platinum group metals (PGMs) and are widely used as heterogeneous catalysts in selective oxidation and hydrogenation reactions, most notably in catalytic converters. [41, 42] Their unique properties of high melting temperatures, resistance to oxidation, high chemical stability and good conductivity makes them highly desirable materials. [43] However, annual mining production of PGMs is far less than other precious metals such as gold or silver, and as a result PGMs are expensive. [44] Therefore, it is highly beneficial to use reduced quantities in processes whilst still maintaining similar reaction

efficiencies and conditions.

One such way to improve a catalyst's effectiveness is to disperse the PGM across a support surface, increasing the catalysts active surface area, resulting in efficient use of the precious metal catalyst. [45–47] Knowledge of catalyst-support bonding and interactions are therefore critical in order to understand and improve the performance of these systems and, as a result, they have been the focus of many studies. [48–50] A signifiant early study was by S. J. Tauster et al. (1978) where the term 'strong metal-support interaction' (SMSI) was first introduced to describe the drastic changes in the chemisorption properties of group VIII noble metals when deposited on TiO_2. [51] This discovery was proven to be critical in obtaining high catalytic activity, with the SMSI now being directly linked to the presence of electronic defects on the surface of metal oxide supports. [52,53] The anchoring of precious metal catalysts to electronic defects have proven to be fundamental in determining the dispersion, morphology, and resulting catalytic activity. [54–56]

Some common metal oxide supports used in industrial processes include SiO_2, TiO_2, CeO_2 and γ-Al_2O_3 because of their high porosity allowing for excellent catalyst dispersion. [57–59] A significant amount of studies have focussed on the structure of γ-Al_2O_3 with IR spectroscopy, [60] NMR spectroscopy, [61] diffraction, [62] and materials modelling [63, 64] all being extensively used to characterise the structure. However, the multiple structural variations and presence of complex local disorder at each of the tetrahedrally (AlO(IV)), pentahedrally (AlO(V)) and octahedrally (AlO(VI)) coordinated Al sites makes structures of γ-Al_2O_3 difficult to determine. Many studies have suggested a preference for vacancies located at octahedral Al sites, [65, 66] whereas other studies have demonstrated that vacancies are also present on tetrahedrally coordinated sites. [67, 68] The presence of pentahedrally coordinated Al cations has been found in small quantities on the surface of γ-Al_2O_3, although the amount varies on modification of the structure. [69] An important study on Pt bonding to γ-Al_2O_3 was carried out by D. Dou *et. al.* (2001), where x-ray absorption near edge spectroscopy (XANES), extended x-ray absorption fine structures (EXAFS) and temperature programmed reduction (TPR) were all used to look at the coordination and bond distance of Pt to oxygen atoms both before and after calcination. [70] From this work,

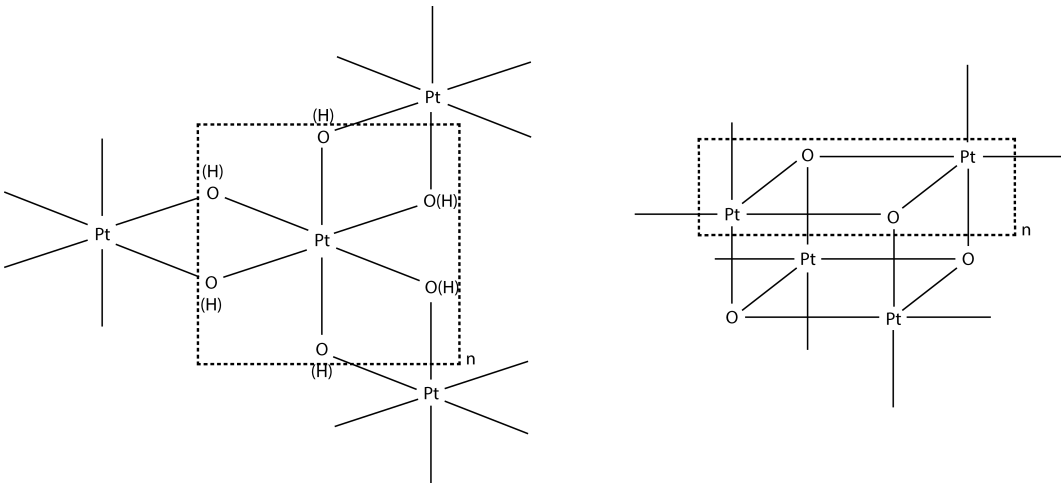

Figure 4.1: Possible oligomeric structures formed from an aqueous platinum precursor in solution as suggested by D. Dou *et. al.* (2009). [70]

it was suggested that Pt remains in the +4 oxidation state with an average oxygen coordination number of 5.4 post calcination. It was also proposed that the aqueous $Pt(NO_3)_4$ precursor solution is made up of multiple differing oligomeric structures which are then deposited onto the γ-Al_2O_3 surface. Examples of these structures are shown in Figure 4.1.

Mesoporous silica has typically been used as a catalyst support for Ni, Pd or Pt catalysts in hydrogenation reactions. [71, 72] The tunability of mesoporous silica allows for the pore diameter, surface area and pore volume to be easily adjusted allowing for great versatility. [73] In addition, the pH adjustment of catalyst salt precursors has been found to improve the catalyst dispersion on silica, silica-alumina and alumina supports. [74] Silica has a hydrophilic nature and therefore the surface is covered by hydroxyl groups and water which facilitates a greater catalyst immobilisation on the surface upon impregnation. [75] In addition to mesoporous SiO_2, TiO_2 is widely used as a heterogeneous catalyst support primarily in fuel processing because of its tunable porous surface, high thermal stability and mechanical strength. [76] Amongst the TiO_2 polymorphs, anatase is commonly used as a catalyst support because it usually exhibits higher catalytic activity due to its larger surface area and strong interaction with metal nanoparticles than its rutile counterpart. [77, 78] However, rutile's high crystallinity and thermal stability means it is favoured as a model support in studies of the support surface. [79]

Therefore, there are many TiO_2 supports which utilise mixed phases of both anatase and rutile phases.

Here the structure of PGM oxides on the surface of the inorganic metal oxide supports, γ-Al_2O_3, TiO_2 and SiO_2, are investigated by solid state NMR. Whereas many forms of these metal oxide supports exist, the specific forms SCFa-140 (γ-Al_2O_3), Degussa-P25 (TiO_2) and Grace-P432 (SiO_2) are used because of their high porosity and common utilisation in industry.

4.1.2 Solid State NMR in Heterogeneous Catalysis

Given the highly disordered nature of PGM bonding to the metal oxide support surface, techniques pertaining to short range localised structures are required in order to fully characterise systems. Therefore, the implementation of solid state NMR can probe the structure of PGMs and their anchoring to supports due to its sensitivity to short range chemical environments and speciation. However, there has not been many reported studies that look directly at PGM materials using solid state nuclear magnetic resonance (NMR) due to the lack of easily observable NMR nuclei associated with the systems.

Early static ^{195}Pt solid state NMR was used to identify the presence of both diamagnetic and metallic Pt. [80–82] However, despite being spin-1/2, the ^{195}Pt nucleus is subjected to large Knight shifts which leads to enormous lineshapes (>3 MHz) making the acquisition of such spectra challenging and time consuming. More recent ^{195}Pt NMR studies by G. Rees *et al.* (2013) have used the variable offset cumulative spectroscopy (VOCS) technique to acquire spectra in order to explore Pt metal nanoparticles and bimetallic systems. [83] From this, it was possible to identify different sub-core nanoparticle sizes due to differing Knight shifts causing varied chemical shifts and broadenings for each nanoparticle shell layer. It was also found that the number of atoms in each nanoparticle layer could be estimated from its respective ^{195}Pt spectrum. With even fewer reports, observing the ^{105}Pd nucleus poses a greater challenge due to its very small gyromagnetic ratio ($\gamma \sim 1.948$ MHzT^{-1}), low sensitivity and large quadrupolar moment ($Q \sim 66.0$ x10^{-30}m^2) meaning lineshapes are very broad. However, the use of ^{105}Pd solid state NMR was recently reported by T. J. N. Hooper *et al.* (2018) which allowed small structural changes to

be identified from the drastic chemical shift and lineshape changes caused by the large varying quadrupolar couplings. [84] Moderate success has been achieved through ^{99,101}Ru solid state NMR despite both nuclei having small gyromagnetic ratios, relatively large quadrupolar moments and low natural abundances making both nuclei undesirable isotopes for NMR investigations. Despite this, it has been possible to observe both metallic and a number of diamagnetic Ru complexes. [85, 86]

Previous studies by J. H. Kwak *et al.* have implemented solid state NMR to investigate catalyst support bonding where ultra high field (21.1 T) ^{27}Al measurements were utilised to investigate the anchoring of BaO and PtO to γ-Al_2O_3. [87, 88] Their findings indicated that low Ba or Pt loadings preferentially bond to the small amount of AlO(V) sites located on the surface. Solid state NMR has also been commonly used to investigate silica based supports, where ^{29}Si and ^{1}H have been carried out to characterise the surface speciation of mesoporous silicas. [89, 90] Notable, E. Raine *et al.* (2018) implemented ^{29}Si and ^{1}H NMR to identify the coordination of SBA-15 upon impregnation with Pt capped Zn and also used ^{195}Pt to show that both oxide and metallic nanoparticles were present. [91]

Out of the three stable oxygen isotopes, ^{16}O, ^{17}O and ^{18}O only ^{17}O has nuclear spin (I = 5/2) and therefore is the only observable oxygen nucleus by solid state NMR. Given that many heterogeneous catalysts and their supports are oxide based, ^{17}O solid state NMR is an exciting prospect for investigating the structure and characterising PGM catalyst systems. However, the low natural abundance of this nucleus (0.0373 %) means that enrichment is necessary in order to obtain sufficient signal to noise. Enrichment has been previously achieved through a variety of methods such as chemisorption, hydrothermal, ionothermal and ball milling. [92–95] Problems can arise when using these methods since high temperatures are required for exchange to take place, potentially causing a reduction or phase transition in the sample. Despite this, the wide chemical shift range and sensitivity of ^{17}O NMR to minor structural changes has provided insight into catalytic systems. M. Wang *et al.* (2015) has shown that it is possible to observe different surface, sub-surface and bulk layers in CeO_2 nanoparticles using ^{17}O solid state NMR. [96] It was also possible to detect defect sites in CeO_2 through longitudinal (T_1) relax-

ation measurements. Furthermore, the enrichment and observation of V_2O_5 on Al_2O_3, TiO_2 and SiO_2 supports was achieved by C. A. Klug *et al.* (2009), where catalyst-support bonding was directly observed. [97]

Even with the numerous studies ^{17}O solid state NMR, there has been no investigations into the ^{17}O enrichment and observation of PGM materials. This offers an exciting, yet unexplored new avenue for characterising PGM containing materials in catalysis. Given the effectiveness shown by many other previously reported ^{17}O NMR studies, the viability of ^{17}O enrichment and NMR of PGM oxides and supported PGMs are investigated.

4.2 Experimental

4.2.1 Synthesis

Both PtO_2 and PdO samples were supplied by Johnson Matthey whereas Rh_2O_3 (99.9 %), RuO_2 (99.9 %) and IrO_2 (99 %) were obtained from Alfa Aesar. All PGM oxide materials were used as prepared by Johnson Matthey or Alfa Aesar. Synthesis of all supported PGM samples were performed at Johnson Matthey Technology Centre. Initial Pt/γ-Al_2O_3 (SCFa-140), Pt/SiO_2 (Grace-P432), Pt/TiO_2 (Degussa-P25) and Ni/γ-Al_2O_3 (scfa-140) catalyst-support materials were prepared using $Pt(NO_3)_4$ and $Ni(NO_3)_2$ precursor solutions provided by Johnson Matthey and impregnated onto the oxide supports using an incipient wetness technique. [98] Subsequent Pt/γ-Al_2O_3 and Pd/γ-Al_2O_3 samples were prepared at 1 and 10 wt% Pt and Pd using $Pt(NH_3)_4(HCO_3)_2$ and $Pd(NO_3)_2$ precursors, respectively. Precursors were deposited onto γ-Al_2O_3 supports through deposition precipitation followed by filtration and then drying of the precipitate. [98] All pre-catalyst support materials were calcined in air at 500 ^{o}C for 2 hours.

4.2.2 Lability

All lability experiments were performed using a Quantachrome Autisorb-iQ-C Analyzer. For each sample, ^{18}O gas was passed through the sample in a sealed vessel whilst heating the powder in a furnace at a rate of 4 ^{o}C/min.

The resultant gas product was then put through a mass spectrometer and the counts of mass-34 ($^{16}O +^{18} O$) were recorded.

4.2.3 ^{17}O Enrichment

All Oxygen-17 enrichments were carried out through a chemisorption technique using 99% ^{17}O enriched oxygen gas acquired from Cortecnet. A Quantachrome Autisorb-iQ-C Analyzer was used to perform the chemisorption where an initial heating at 500 ^{o}C under vacuum conditions was used to remove contaminants. The sample was then cooled to room temperature and ^{17}O gas injected before the temperature was increased at a rate of 25 ^{o}C/min to the exchange temperature which was predetermined from ^{18}O lability experiments. Samples were kept at the exchange temperature for 2 hours before being cooled.

4.2.4 PXRD and SAXS Measurements

Initial Powder X-ray diffraction patterns (PXRD) of PGM oxides prior to enrichment were collected with a Bruker D8 Advance using Cu-K$_\alpha$ radiation (λ = 1.5406 Å) and operating at 40 kV and 40 mA using Bragg-Brentano geometry. A slit width of 1.4 cm^{-1} was used and the samples were spun during acquisition at a rate of 1 rev.s^{-1}. Patterns were collected between 10^o and 130^o using a step size of 0.044^o and a scan rate of 0.7 ^{o}/min. Subsequent measurements on enriched PGM oxides and TiO_2 samples were achieved using a Panalytical Empyrean using Cu-K$_\alpha$ radiation (λ = 1.5406 Å) operating at 45 kV and 40 mA implementing Bragg-Brentano geometry. A slit width of 1.4 cm^{-1} was used along with a sample spin rate of 0.5 rev.s^{-1}. Diffraction patterns were collected between 10^o and 120^o using a step size of 0.026^o and a scan rate of 1.2 ^{o}/min.

Small Angle X-ray Scattering (SAXS) measurements were performed using a Xenocs Xeuss 2.0 equipped with a Pilatus 300K hybrid photon counting detector. The X-ray source used was Cu-K$_\alpha$ radiation (λ = 1.5418 Å) along with an exposure time of 1200 s. Data were collected in the q range from 0.004 to 0.16 Å^{-1} and relative instrumental correction was taken into account when fitting the data. All particles were assumed to have a spherical form with different size distributions.

4.2.5 TEM

All samples were deposited with the help of a micromanipulator on to a carbon-coated finder Cu grid. The samples were first examined as they are, then they were dehydrogenated at 300 ^{o}C at nitrogen 5 mbar atmosphere for 90 mins and as the last treatment they were re-hydrogenated again at 300 ^{o}C under 10 % hydrogen atmosphere for 90 mins. The samples were examined with a JEM 2800 (Scanning) Transmission Electron Microscope using the following instrumental conditions: Voltage (kV) 200; C2 aperture (μm) 70 and 40; dark-field (Z-contrast) imaging in scanning mode using an off-axis annular detector. The secondary electron signal was acquired simultaneously with the other Scanning Transmission Electron Microscope (STEM) images providing topological information of the sample.

4.2.6 Raman Spectroscopy

Raman spectra were recorded using a Renishaw inVia Reflex Raman Microsope with a Renishaw CCD detector. All spectra were acquired using a diode pumped solid state (DPSS) laser operating at a wavelength of 532 nm. A grating of 1800 l/mm with 10 % of 2 MW laser power being used per acquisition. The exposure time was set to 2 s and a total of 10 accumulations were acquired per spectrum.

4.2.7 Solid State NMR

Solid State ^{27}Al MAS NMR spectra were acquired at multiple magnetic fields strengths: 4.7, 14.1, 16.4 T using Bruker Avance III HD (4.7 and 16.4 T), and Bruker Avance Neo (14.1 T) spectrometers operating at Larmor frequencies (ν_o) of 52.1, 104.2 and 181.9 MHz, respectively. All ^{27}Al experiments were executed using a Bruker HXY 3.2 mm probe which allowed a spinning frequency of 20 kHz. Pulse calibration was achieved using a 1.1 M solution of $Al(NO_3)_3$ where a non-selective $\pi/2$ solution pulse of 18 μs was achieved leading to a selective solid pulse of 1 μs ($\pi/6$ flip angle) to be implemented for quantitative measurements to be achieved. An optimised recycle delay of 1 s was used for between 1000 - 10000 transients per spectrum. 2D ^{27}Al 3QMAS z-filter

experiments were acquired at Larmor frequencies (ν_o) of 52.1, 104.2, 181.9 MHz using Bruker Avance III HD (4.7 and 16.4 T), and Bruker Avance Neo (14.1 T) spectrometers. A 4-pulse split-t_1 with z-filter 3QMAS pulse sequence (excitation-conversion-$\pi/2$-$\pi/2$-acquire) was implemented. Pulse calibration of the 'hard' excitation (7.8 μs) and conversion (2 μs) and 'soft' z-filter pulses (12 μs) were optimized using the γ-Al_2O_3 parent sample. More than 64 slices were acquired per spectrum and between 96-1920 transients were coadded for each t_1 FID. All resultant 2D MQMAS spectra were sheared. ^{1}H-^{27}Al cross polarisation MAS experiments were performed at 14.1 T (ν_o = 156.3 MHz) using a Bruker Avance Neo spectrometer. Pulse calibration was achieved using $Al(acac)_3$ where a ^{1}H $\pi/2$ pulse of 3 μs was measured. A contact time of 0.3 ms with no ramp was utilised along with a recycle delay of 5 s. All ^{27}Al chemical shift referencing was carried out using the IUPAC primary reference of 1.1 M $Al(NO_3)_3$ solution (δ_{iso} = 0.0 ppm). [9]

All solid state ^{1}H MAS NMR data were acquired at a magnetic field of 11.7 T (ν_o = 500.0 MHz) using a Bruker Avance III spectrometer. Spectra were acquired using a Bruker HXY 1.3 mm probe, utilising a spinning frequency of 55 kHz. A single pulse experiment was implemented for the acquisition of each spectrum using a 2.5 μs $\pi/2$ pulse along with a 1 s recycle delay between subsequent FIDs. A total of 600 transients were acquired for each spectrum. Shift referencing and pulse calibration was carried out using a solid α-alanine secondary reference (CH_3 resonance at δ_{iso} = 1.1 ppm), reported against the IUPAC recommended primary reference of Me_4Si (δ_{iso} = 0.0 ppm). [9]

All ^{195}Pt static solid state NMR experiments were performed on a Bruker Avance HD spectrometer operating at a magnetic field strength of 7.1 T (ν_o = 64.496 MHz). Spectra were acquired using a novel Bruker 7.5 mm static solids auto-tuning (ATMA) probe, implementing a variable offset cumulative spectra (VOCS) technique. The automatic tuning probe stepped through the ^{195}Pt spectral range at 50 kHz frequency intervals and applied a solid echo ($\pi/2$ - τ - $\pi/2$ - acquire) experiments which employed a 4 μs $\pi/2$ and a 8 μs π pulse for data acquisition at each frequency step. A total of 250,000 transients were acquired at each frequency whilst using a recycle delay of 7 s between subsequent scans. Pulse time calibration and the ^{195}Pt shift referencing was performed on a Pt metal sample which served as secondary

reference ($\delta_{iso} = -35{,}350$ ppm) against the primary IUPAC reference of 1.2 M Na_2PtCl_6(aq) ($\delta_{iso} = 0.0$ ppm). [9]

All ^{29}Si MAS NMR measurements were performed at 7.05 T using a Varian/Chemagnetics InfinityPlus spectrometer operating at a Larmor frequency (ν_o) of 59.6 MHz. These experiments were performed using a Bruker 7 mm HX probe, enabling a MAS frequency of 5 kHz. Pulse calibration was achieved using kaolinite$_{(s)}$ where a $\pi/2$ pulse time of 4.25 μs was measured. All measurements were undertaken with a $\pi/2$ flip angle along with a delay between subsequent pulses of 240 s. For the analogous cross polarisation MAS (CPMAS) experiments, a 4 μs $\pi/2$ pulse, a 4 ms contact time and a ramp from 75 % and 100 % was used. A 2.5 s recycle delay was used. For both single pulsed and CPMAS experiments, continuous wave (CW) heteronuclear decoupling was applied on the ^{1}H channel at a frequency of 300.01 MHz during collection of the FID. All ^{29}Si shifts were reported against the IUPAC recommended primary reference of Me_4Si ($\delta_{iso} = 0.0$ ppm), via a kaolinite secondary reference ($\delta_{iso} = -92$ ppm). [9]

^{17}O MAS NMR measurements were carried out at 7.1, 9.4, 14.1 and 16.4 T magnetic fields strengths using Bruker Avance III HD 7.1, 9.4 and 16.4 T and Bruker Avance Neo (14.1 T) spectrometers operating at the Larmor frequencies (ν_o) 40.7, 54.2, 81.3 and 94.7 MHz, respectively. Bruker 3.2 mm HX, Bruker 4 mm HXY and Bruker 1.3 mm HXY probheads were used allowing for spinning frequencies between 7 and 55 kHz to be implemented. For the 1D spectra both single pulse and Hahn echo ($\pi/2$ - τ - π - acquire) experiments were carried out depending on the enrichment level of the sample. Pulse calibration was carried out using D_2O (heavy water) for a $\pi/2$ 'solution' pulse of 7 μs; invoking a semi-quantative 'solids' pulse of 1 μs to be used. Recycle delays between 0.5 and 10 s was used for between 64,000 and 600,000 FIDs per spectrum. 2D ^{17}O experiments also used a 4 pulse 3QMAS split-t_1 with a z-filter. Optimisation of the hard and soft pulses were achieved using the sample obtaining a 'hard' excitation and conversion pulses of 5.4 and 2.2 μs, respectively. This was combined with 'soft' $\pi/2$ pulses of 12.5 μs. A total of 672 transients were coadded for each t_1 FID. Corresponding T_1 measurements were carried out using a saturation recovery experiment which used a pulse train of 100 2 μs pulses with a delay of 0.1 ms between each pulse. A variable τ delay between

0.001 and 5 s was implemented and 1000 transients were acquired per delay. All ^{17}O spectra are referenced to the IUPAC primary reference D_2O (δ_{iso} = 0.0 ppm). [9]

4.3 ^{17}O Solid State NMR of PGM Oxides

4.3.1 Platinum group metal oxides

Initial investigations focussed on the ^{17}O enrichment and solid state NMR of PGM oxide materials (i.e. PtO_2, PdO, IrO_2, RuO_2 and Rh_2O_3) as a basis for further exploration into the supported structures. A direct exchange chemisorption technique using ^{17}O gas was adopted to enrich samples. In order to establish the temperature at which direct exchange of oxygen occurs, lability curves were measured for each oxide shown in Figure 4.2. The highly stable structure of PtO_2 has the largest exchange temperature between ∼500-560 ^oC. An additional secondary component is observed at ∼525 ^oC for PtO_2 which is thought to be caused by absorbed water within the structure which will induce an exchange at lower temperatures. A multiple component curve is also seen for Rh_2O_3 which peaks at ∼285 ^oC. Both PdO and IrO_2 show a single component growth curve indicating exchange occurs at temperatures between ∼225-275 ^oC and ∼350-500 ^oC, respectively. Interestingly, RuO_2 has two distinct uptakes of ^{18}O gas at ∼160 and ∼260 ^oC which is possibly caused by the previously reported phase transition from tetragonal ($P4_2/mnm$) to orthorhombic (Pnnm) at high temperatures. [99]

PXRD patterns for each PGM oxide as procured from Johnson Matthey or Alfa Aesar and after ^{17}O enrichment are shown in Figures 4.3(a) and (b), respectively. Prior to enrichment, PtO_2 exhibits broad diffraction peaks suggesting the presence of PtO_2 nanoparticles within the sample. The diffraction pattern found here does not exactly correspond to any previously reported platinum oxide structure. However, it loosely correlates to a trigonal ($P4_2/mmc$) $\alpha - PtO_2$ phase. The disparity between diffraction peaks could be caused by labile water species within the structure as is suggested by the multiple component curve found in the lability measurement (Figure 4.2). After enrichment, the sharp diffraction peaks indicate significant amounts of bulk

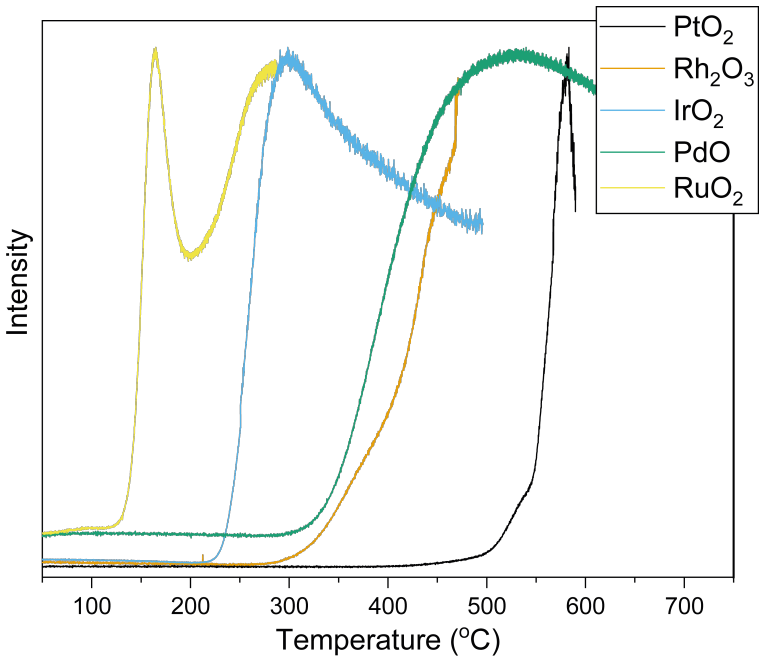

Figure 4.2: ^{18}O lability curves showing the counts of resultant mass-34 detected from a mass spectrometer across the temperature range 50-700^{o}C for ^{18}O gas passed through PtO_2, PdO, RuO_2, Rh_2O_3 and IrO_2.

Pt metal are present, formed by reduction of PtO_2. Despite reduction taking place, a small amount of the original PtO_2 phase is still present. This is further confirmed by Raman spectroscopy data shown in Figure 4.4, where A_{1g} (∼500 cm^{-1}) and E_g (∼550 cm^{-1}) PtO_2 vibrational modes are present. Additional modes assigned to A_{1g} (∼450 cm^{-1}) and E_g (∼550 cm^{-1}) modes of PtO are also detected indicating a partial reduction to PtO also arises. Pt metal is not observed since it is not Raman active. Furthermore, H_2O is detected in both samples which provides additional evidence for the presence of physisorbed water within the structure.

Additional characterisation of PtO_2 before and after enrichment was also achieved from static ^{195}Pt wideline VOCS NMR data shown in Figure 4.5 and the corresponding fit parameters specified in Table 4.1. The combination of a large CSA and Knight shift interactions in ^{195}Pt nuclei leads to extremely broad resonances and an enormous chemical shift range (∼30 MHz). Therefore, all spectra were acquired using a frequency stepping variable offset cumulative spectroscopy technique (VOCS) using the novel automated tuning

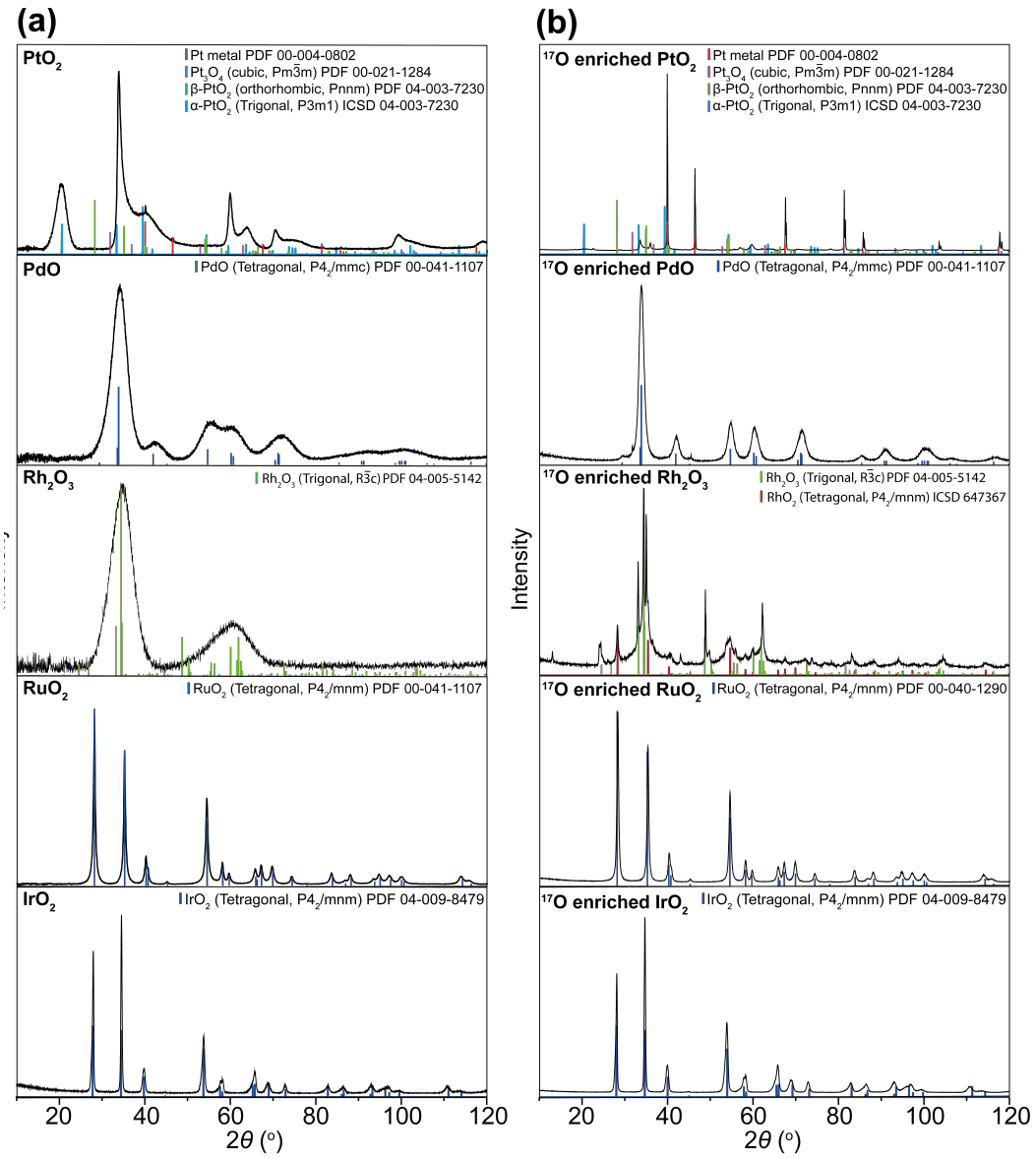

Figure 4.3: Powder X-ray diffraction patterns of PtO_2, PdO, RuO_2, Rh_2O_3 and IrO_2 (a) prior to ^{17}O enrichment and (b) after ^{17}O enrichment. All diffraction patterns are shown compared to the patterns of previously reported structures.

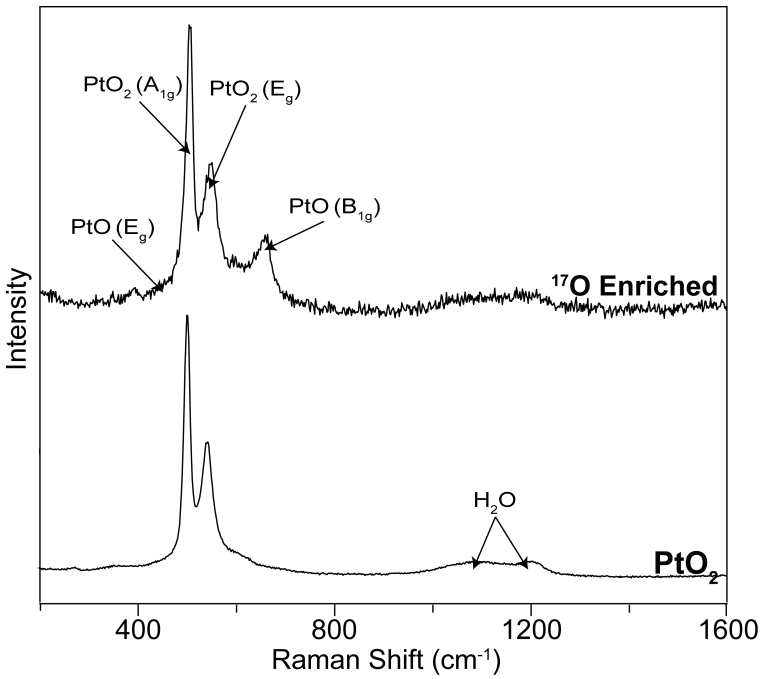

Figure 4.4: Raman spectra of PtO_2 procured from Johnson Matthey and ^{17}O enriched PtO_2 using a chemisorption temperature of 500 ^oC. Spectra were acquired using a laser wavelength of 532 nm.

and matching (ATMA) probe. It is well known that metallic Pt species are largely Knight shifted towards negative chemical shifts ($\delta\sim$-35,380 ppm) and therefore diamagnetic and metallic Pt species are easily distinguishable. [83] The ^{195}Pt static spectrum of PtO_2 shows a single axially symmetric Pt site ($\eta_{CS} = 0$) in the diamagnetic region consistent with the trigonal ($P4_2/mmc$) PtO_2 structure. The corresponding ^{17}O enriched PtO_2 exhibits three distinct Pt species as has been identified from PXRD and Raman spectroscopy; PtO_2, PtO and Pt metal. In the diamagnetic region ($\delta\sim$0-10,000 ppm), both PtO_2 and PtO species are present. Since PtO primarily forms as a surface species, it is represented by a broad gaussian resonance centred at $\delta\sim$670 ppm. An axially symmetric ($\eta_{cs} = 0$) PtO_2 resonance comparable to the original un-enriched PtO_2 spectrum is observed. However, a reduction in both δ_{cs} from 2820 to 2080 ppm and δ from 3630 to 3290 ppm allude to a more symmetric electron density about the Pt nucleus which could be attributed to the removal of labile water molecules. Furthermore, the quantative nature of ^{195}Pt experiments conducted allows for relative amounts of Pt species to be quantified as

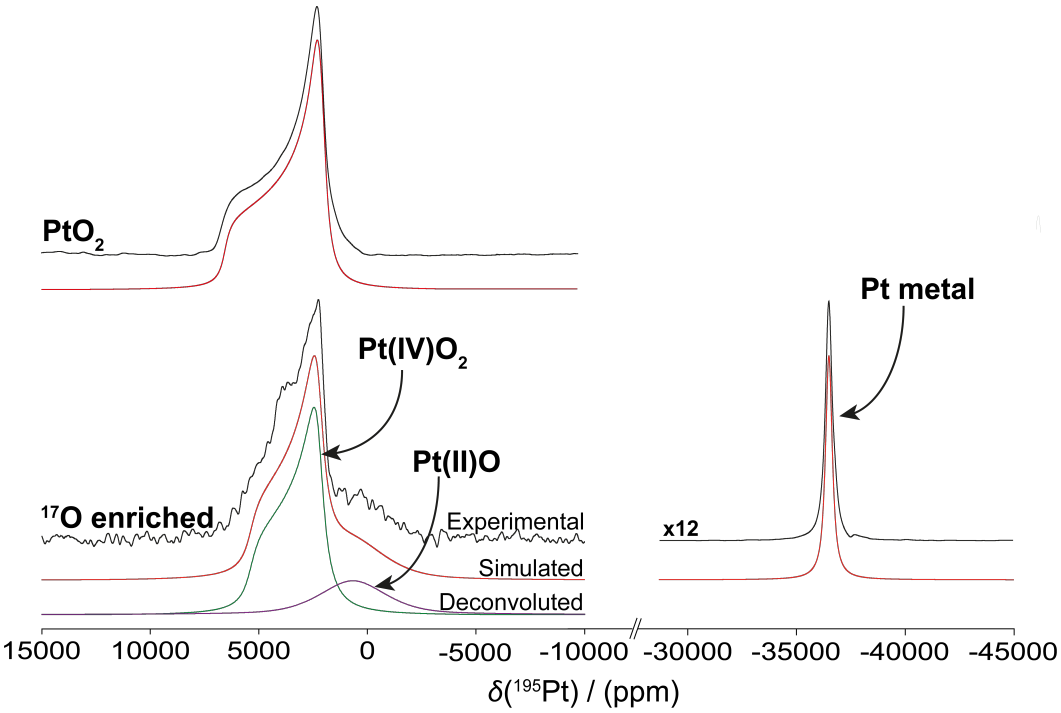

Figure 4.5: Static wideline ^{195}Pt spectra (B_0=7.1 T) of PtO_2 and ^{17}O enriched PtO_2, acquired through a frequency stepping VOCS method using the novel ATMA probe.

~70 % Pt metal, ~7 % PtO and ~23 % remains as PtO_2.

Despite 70 % of PtO_2 undergoing a reduction to Pt metal, it was still possible to obtain ^{17}O MAS solid state NMR data which is presented in Figure 4.6(a) and the corresponding fitting parameters are given in Table 4.2. The substantial reduction to Pt metal results in S/N which is only a marginal improvement on the natural abundance signal obtained from the zirconia rotor resonance located at δ ~387 ppm. It should also be noted that the presence of Pt metal resulted in difficulties spinning, limiting MAS rates (10-16 kHz) and causing significant sideband overlap. Both PtO_2 and PtO species are distinguishable from the spectral deconvolutions. Similarly to the ^{195}Pt static NMR measurements, PtO (blue) is present as a broad gaussian resonance emanating from the aforementioned disordered nature associated with the surface species. The resonance assigned to PtO_2 (green) exhibits a narrower quadrupolar lineshape alluding to a high point symmetry. In order to extract meaningful NMR parameters, the centre of gravity shift (δ_{cg}) is plotted against $1/\nu_o^2$ as is shown

Table 4.1: Static ^{195}Pt solid state NMR parameters used to fit characteristic CSA lineshapes for PtO_2 and ^{17}O enriched PtO_2 in Figure 4.5.

Sample	Site	δ (ppm)	δ_{cs} (ppm)	η_{cs} ($\pm$ 0.1)	Rel. Int. ($\pm$ 5%)
PtO_2	PtO_2	3630 $\pm$ 20	2820 $\pm$ 20	0	100
^{17}O enriched	PtO_2	3290 $\pm$ 50	2080 $\pm$ 50	0	23
	PtO	670 $\pm$ 50	-	-	7
	Pt metal	$-$36580 $\pm$ 20	-	-	70

Table 4.2: ^{17}O solid state quadrupolar parameters extracted from PtO and PtO_2 multi-field data using both simulated quadrupolar fits (Figure 4.6(a)) and linear graphical fits (Figure 4.6(b)).

Site	Simulated Fit			Linear Fit	
	δ_{iso} (ppm)	C_Q (MHz)	η_Q ($\pm$ 0.1)	δ_{iso} (ppm)	P_Q (MHz)
Pt(IV)O_2	$-$85 $\pm$ 3	6 $\pm$ 2	0.1	$-$102 $\pm$ 5	4 $\pm$ 1
Pt(II)O	-	-	-	$-$110 $\pm$ 10	6.4 $\pm$ 0.9

in Figure 4.6(b). Using Equation 2.57, the y-axis intercept and the gradient allow for accurate determination of δ_{iso} and P_Q. Both PtO_2 and PtO exhibit similar δ_{iso} shift values at $-$102 and $-$110 ppm, respectively. Interestingly, both resonances show a negative δ_{iso} located between $\sim$-85 and $\sim$-110 ppm which is outside the known ^{17}O chemical shift range for inorganic materials (0 $\sim$ 800 ppm). The negative shift in both sites is attributed to the large Knight shift interaction of Pt metal, thought to be in close proximity to the oxide species thus shifting the resonances towards lower frequencies. PtO is observed to have a larger P_Q ($\sim$6.4 MHz) compared to PtO_2 ($\sim$4 MHz) indicating a lower point symmetry. These extracted linear fit parameters were also used to simulate the ^{17}O lineshape, allowing for $C_Q\sim$6 MHz and $\eta_Q\sim$0.1 to be determined for PtO_2.

Initial PXRD data of PdO prior to the enrichment (Figure 4.3(a)) show broad reflections due to the presence of small PdO nanoparticles in a tetragonal ($P4_2/mmc$) phase. However, after enrichment at 500 ^{o}C, these peaks narrow, suggesting agglomeration into larger nanoparticles occurs. Furthermore, the original tetragonal structure is maintained and there is no indication of a reduction to Pd metal. Nanoparticle sizes post enrichment were determined

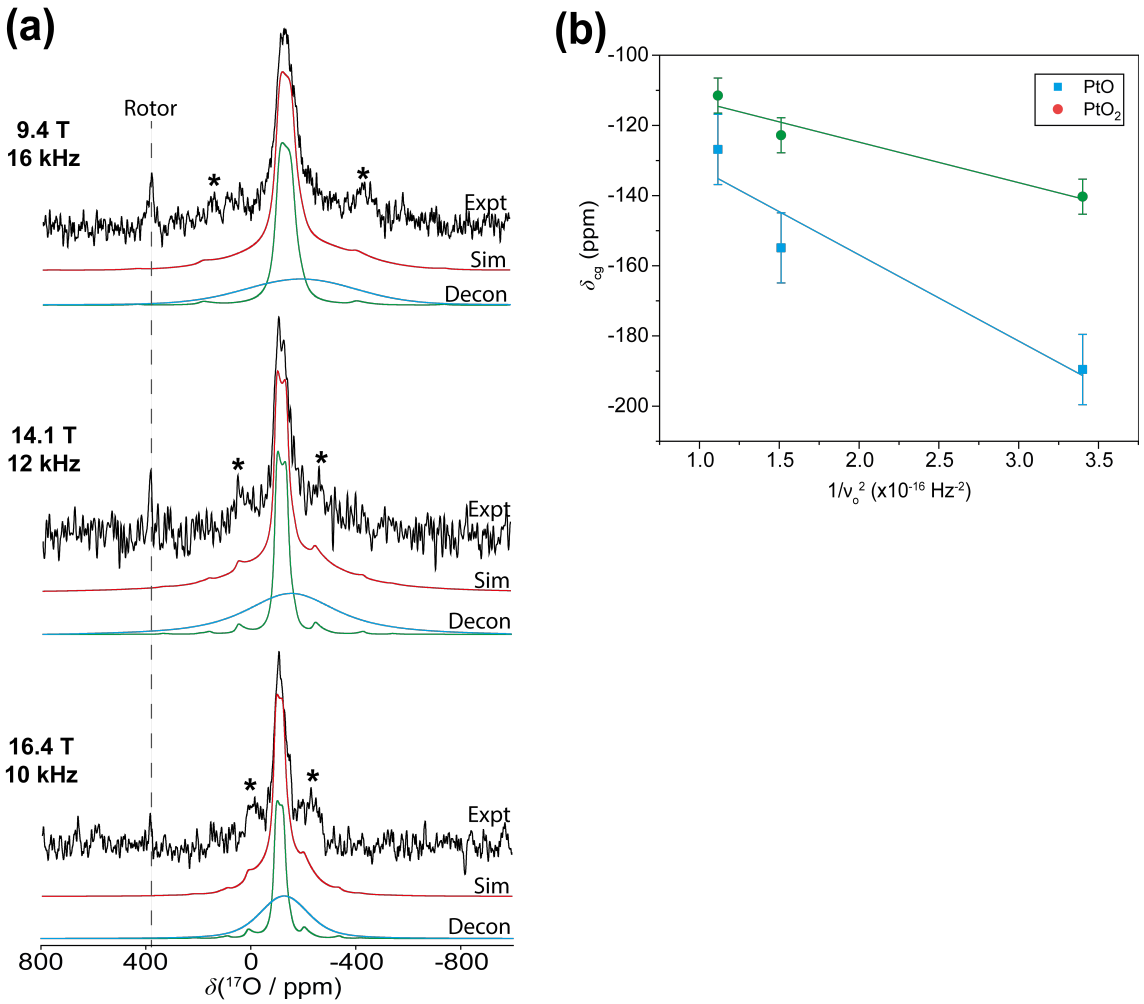

Figure 4.6: (a) Solid state ^{17}O MAS NMR of ^{17}O enriched PtO_2 acquired at three field strengths (B_0 = 9.4, 14.1 and 16.4 T) using spinning frequencies between 10 and 16 kHz. (b) Linear fit plots of δ_{cg} against $1/\nu_o^2$ for PtO and PtO_2 species.

from STEM and SAXS data presented in Figures 4.7(a) and (b) where an average particle diameter of ∼6 nm was determined.

Despite the changing PdO speciation, excellent ^{17}O enrichment is achieved and demonstrated by the exceptional S/N obtained in the ^{17}O MAS NMR data shown in Figure 4.7(g). This has facilitated higher MAS spinning rates to be implemented, thus allowing for higher resolution spectra to be collected. The fast spinning ^{17}O NMR data for PdO nanoparticles is shown in Figure 4.8(a) and the corresponding calculated NMR parameters are specified in Table 4.3. Similarly to PtO_2, the ^{17}O MAS NMR of PdO nanoparticles exhibit atypical large negative chemical shifts ($\delta\sim-237$--412). From previously reported ^{105}Pd NMR studies by Hooper *et. al.*, it was shown that the ^{105}Pd nucleus generates enormous Knight shifts for metallic Pd species. [84] These effects will also be experienced by the ^{17}O nuclei shifting NMR resonances towards lower frequencies. Furthermore, the ^{17}O spectrum here shows comparable results to the static ^{195}Pt NMR performed by Rees *et. al.* (2013) on 5 nm Pt nanoparticles. [83] Their results consisted of broad resonances corresponding to nanoparticle layers exhibiting a range of Knight shifts. Resonances were assigned according to a core-shell model (Figure 4.8(e)), where the Pt nanoparticle core exhibited a Knight shift similar to bulk Pt metal and subsurface layers showed reduced Knight shifts, the closer they were to the surface. A core-shell nanoparticle model has therefore been adopted to deconvolute the ^{17}O PdO spectrum. The four resonances located at $\delta\sim-412$, -408, -307 and -237 ppm are assigned to core, inner sub-surface (1), outer sub-surface (2) and surface nanoparticles layers. The broadness of each resonance increases with the nucleus' proximity to the nanoparticle surface due to the increased disorder exhibiting a larger range of Knight and chemical shifts. Further evidence for the distribution in chemical shifts is provided by the orientation of core and sub-surface 1 resonances along the chemical shift axis in the corresponding ^{17}O 3QMAS spectra shown in Figure 4.8(d). It was not possible to excite the sub-surface 2 and surface sites in the 3QMAS spectra due to their low intensities, although it is expected they would show similar characteristics to the core and inner sub-surface species. The effects of nanoparticle surface proximity are also apparent in the corresponding P_Q and T_1 parameters. For the core site, approximately no quadrupolar coupling is observed due to the high symmetry,

Table 4.3: Extracted solid state ^{17}O NMR parameters obtained from linear fit plots for ^{17}O enriched PdO using 500, 400 and 300 ^{o}C exchange temperatures. The measured spin-lattice (T_1) relaxation times for core and sub-surface 1 sites are also given.

Exchange Temp. (^{o}C)	Peak	δ (ppm)	P_Q (MHz)	T_1 ($\pm$0.3 s)	Rel. Int ($\pm$3 %)
500	Core	-412 ± 1	$\sim 0 \pm 0.1$	1.4	20
	Sub-surface 1	-408 ± 2	1.1 ± 0.2	0.8	63
	Sub-surface 2	-307 ± 4	1.5 ± 0.5	-	10
	Surface	-237 ± 4	2.0 ± 0.5	-	7
400	PdO	-409 ± 1	-	-	-
300	PdO	-409 ± 1	-	-	-

however, it should be noted that the C_Q is non-zero because the core resonance is observed in the 3QMAS spectra. Following the core, each subsequent layer exhibits an increasing quadrupolar coupling up to $P_Q \sim 2$ MHz for surface species owing to the increased local disorder within surface layers. A decrease in the longitudinal relaxation time between the core and sub-surface 1 layer is also attributed to the increased disorder, providing further evidence for the core-shell model.

Lower chemisorption temperatures of 300°C and 400°C were also implemented in order to further understand the changes occuring throughout the enrichment process. The STEM micrographs and SAXS analysis for ^{17}O enriched PdO at 300 and 400°C are shown in Figures 4.7(c-f). Both enrichment temperatures show agglomerations of particles with a broad range of different particle sizes (diameter$\sim$5-50nm) centred about a $\sim$12 nm diameter. The larger particle size prevents layered nanoparticle effects from appearing in the corresponding ^{17}O MAS NMR spectra (Figure 4.7(g)). Instead, a single ^{17}O resonance at $\delta \sim -409$ ppm is observed and assigned as bulk PdO. It should also be noted that the bulk PdO resonance is comparable to that assigned to the PdO nanoparticle core resonance.

Prior to enrichment, nanoparticles were also detected for Rh_2O_3 from PXRD data (Figure 4.3(a)) where a trigonal ($R\bar{3}c$) is identified. However, upon enrichment significant changes occur. The original Rh_2O_3 structure is still present, however the far narrower reflections suggest the nanoparticles have agglomerated into a bulk crystalline phase. Furthermore, the presence

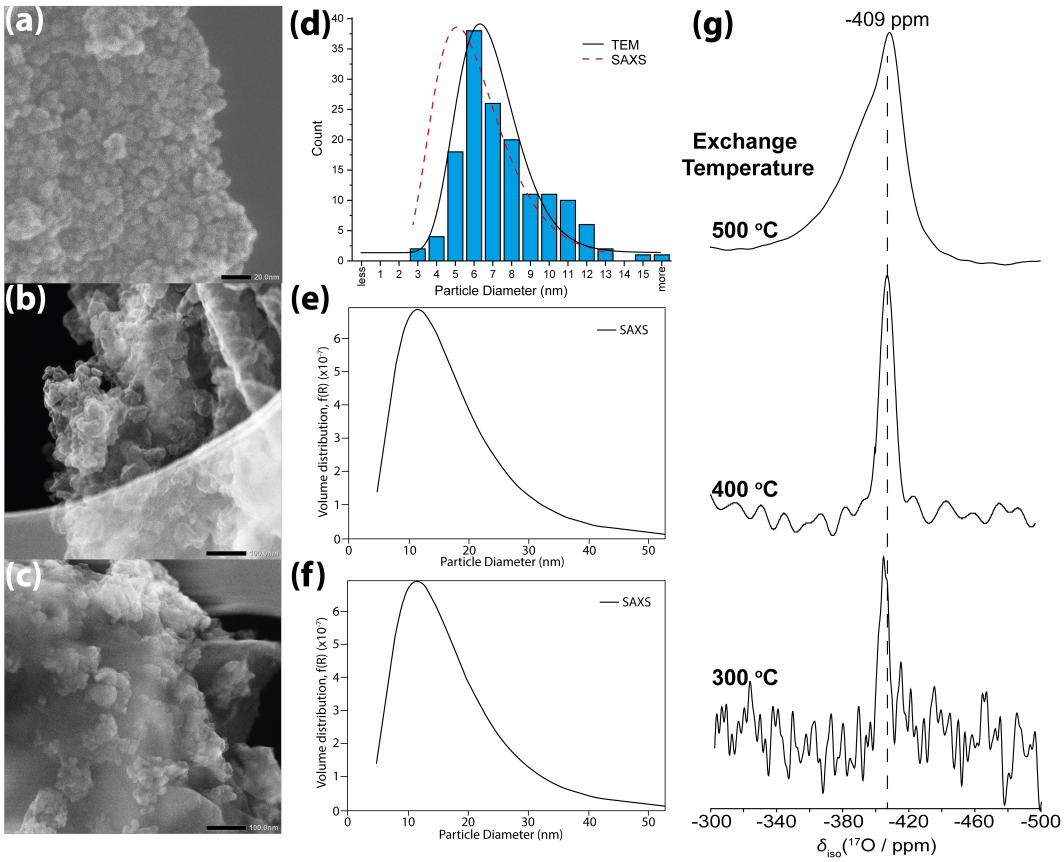

Figure 4.7: STEM micrograph images of ^{17}O enriched PdO samples at the exchange temperatures (a) 500°C, (b) 400°C and (c) 300°C. The analogous log normal distributions of particle sizes obtained from SAXS diffraction patterns for enrichments at (d) 300°C and (e) 400°C and (f) 500°C. For 500°C enrichment, particle size distributions obtained from STEM are also shown. (g) ^{17}O solid state MAS NMR (B_0 = 14.1 T, ν_r = 12 kHz) spectra of ^{17}O enriched Pd(II)O for the different chemisorption exchange temperatures of 300°C, 400°C and 500°C.

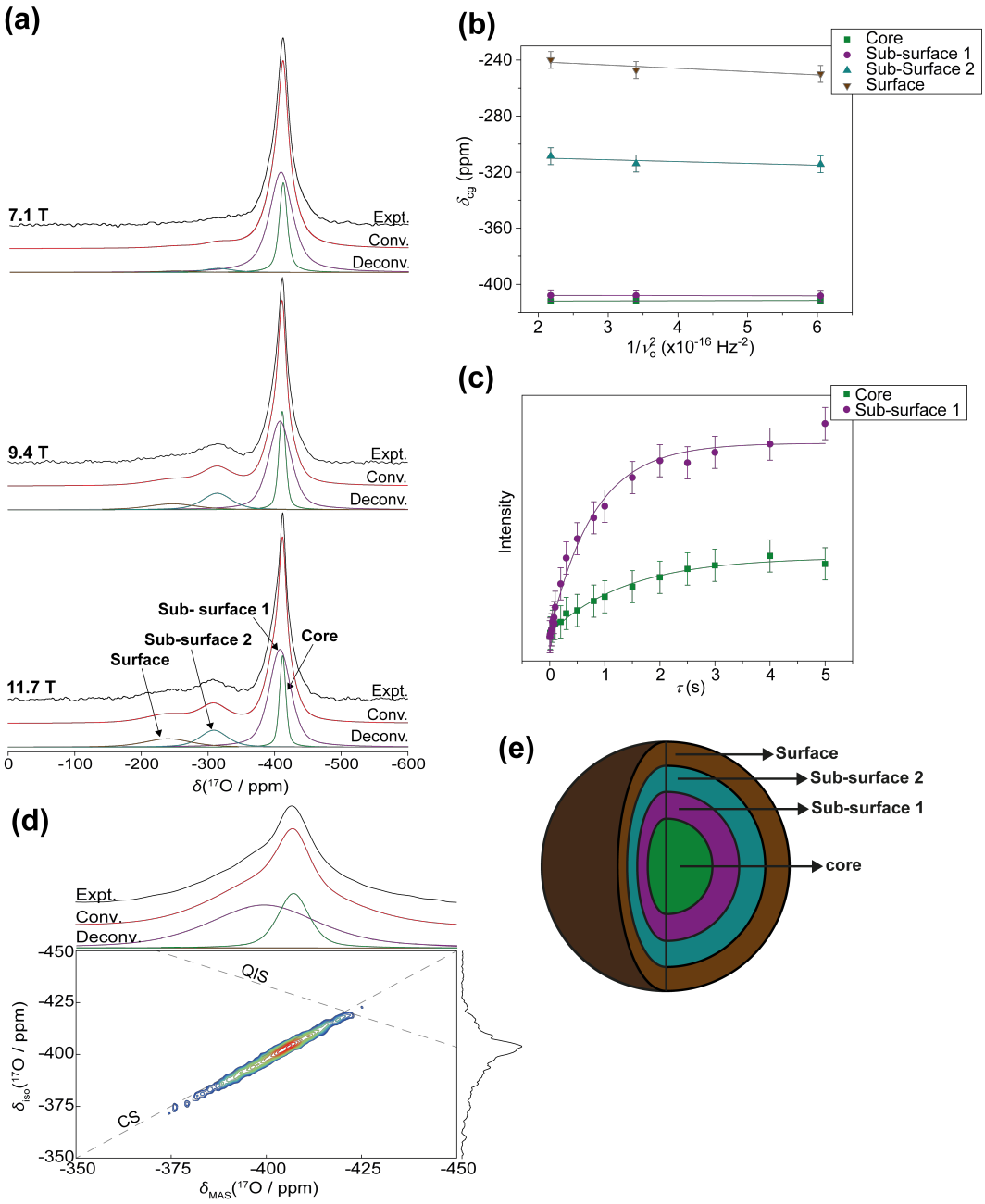

Figure 4.8: (a) Solid state ^{17}O MAS NMR ($\nu_r = 50$ kHz) of ^{17}O enriched PdO acquired at the magnetic fields, 7.1, 9.4 and 11.7 T. (b) Multi-field graphical linear fits of δ_{cg} against $1/\nu_o^2$ for each deconvoluted gaussian peak. (c) Corresponding T_1 exponential build up curves for core and sub-surface 1 resonances determined from saturation recovery experiments. (d) A two dimensional ^{17}O multiple quantum MAS spectrum ($B_0 = 9.4$ T, $\nu_r = 20$ kHz) of PdO enriched at 500 ^{o}C. (e) A schematic of the core shell model used to describe ^{17}O spectra of PdO.

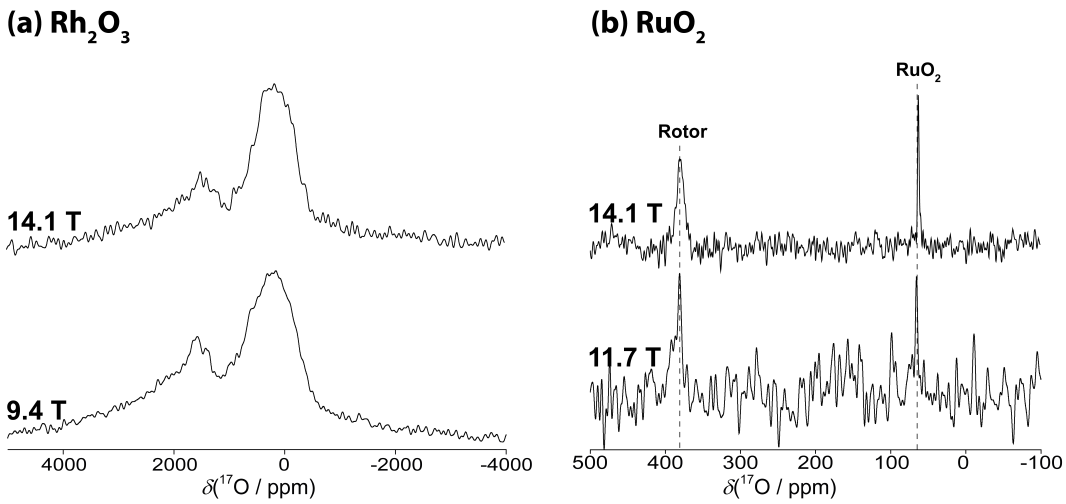

Figure 4.9: Static solid state ^{17}O NMR spectra of (a) Rh_2O_3 (B_0=9.4 and 14.1 T) and ^{17}O MAS NMR spectra of (b) RuO_2 (B_0=11.7 and 14.1 T, ν_r=7 kHz) enriched at 350 ^{o}C.

of tetragonal ($P4_2/mnm$) RhO_2 is found where the Rh oxidation state has changed from +3 to +4. Both of these phases are also identified in the corresponding ^{17}O MAS NMR data presented in Figure 4.9(a) where two resonances are present. However, each resonance exhibits an enormous broad lineshape spanning ∼500 kHz and therefore static VOCS spectra were acquired. This broadening is caused by the paramagnetic interaction associated with the Rh_2O_3 phase which has a known magnetic susceptibility of χ_m∼+104.0x10^{-6} cm^{3}mol^{-1}. [100] However, it was not possible to detect these paramagnetic effects through EPR because of the highly conductive nature of Rh_2O_3.

RuO_2 and IrO_2 PXRD diffraction patterns (Figure 4.3(a)) indicate highly crystalline bulk phases of the tetragonal structures ($P4_2/mnm$). These tetragonal structures are also retained after the enrichment process where there is no change in the PXRD pattern (Figure 4.3(b)). Figures 4.9(b) shows the ^{17}O solid state NMR data for RuO_2. A single narrow peak at ∼63 ppm is observed for RuO_2 which is invariant upon changing the magnetic field, signifying a small quadrupole moment. Comparing this resonance to the zirconia rotor peak at ∼380 ppm, it is clear that little enrichment has taken place within the material. Additionally, for IrO_2 it was not possible to obtain an ^{17}O NMR signal because of the low enrichment levels achieved. It is possible that the reduced enrichment of RuO_2 and IrO_2 is caused by the reduced surface area

of the bulk species, whereas for PtO_2, PdO and Rh_2O_3 the nanoparticles had a greater surface area for oxygen exchange to occur.

4.4 PGM Catalysts on Metal Oxide Supports

It has been shown that it is possible to ^{17}O enrich PtO_2 and PdO and the spectra provide sufficient resolution in order to provide meaningful structural information. Therefore, a logical progression has been made to ^{17}O enrich and observe PtO_2 and PdO nanoparticles supported on the common industrial metal oxide supports; γ-Al_2O_3 (SCFa-140), SiO_2 (Grace-P432) and TiO_2 (Degussa-P25). Additionally, Ni/γ-Al_2O_3 has been studied as Ni is looked at as a potentially cheaper alternative catalyst to PGMs, however this is usually counteracted by a reduction in catalytic performance. The ^{18}O lability curves for each of the supported precious metals studied here are shown in Figure 4.10. The exchange temperatures for Pd, Pt and Ni supported on γ-Al_2O_3 occur at $\sim$350, 400 and 480 ^oC, respectively. The large differences in temperatures between these species emanates from Ni retarding oxygen from exchanging with the bulk alumina support, whereas for Pt and Pd the oxygen will exchange more readily. The analogous 10 % Pt/TiO_2 indicates a similar temperature of $\sim$360 ^oC to its γ-Al_2O_3 counterpart. However, 10 % Pt/SiO_2 exhibits a gradual increase in intensity across the temperature range $\sim$250-500 ^oC. This is likely caused by the large abundance of physisorbed water and hydroxyls on the surface of the SiO_2 support which results in a gradual emission of ^{16}O. From consideration of the ^{18}O lability curves in both Figure 4.2 and Figure 4.10, an enrichment temperature of 500 ^oC was used for Pt and Ni containing samples and both 400 and 500 ^oC was utilised for Pd containing samples.

4.4.1 Pt, Ni & Pd Supported γ-Al_2O_3

Pt, Pd and Ni supported on γ-Al_2O_3 samples were initially prepared using an incipient wetness impregnation method, commonly used in industrial preparation methods. [98] Figure 4.11(a) and (b) show the ^{27}Al and ^{1}H MAS NMR, respectively. The ^{27}Al NMR spectra for each catalyst shows an unchanged γ-Al_2O_3 spectra where a characteristic Czjzek (also known as the Gaussian

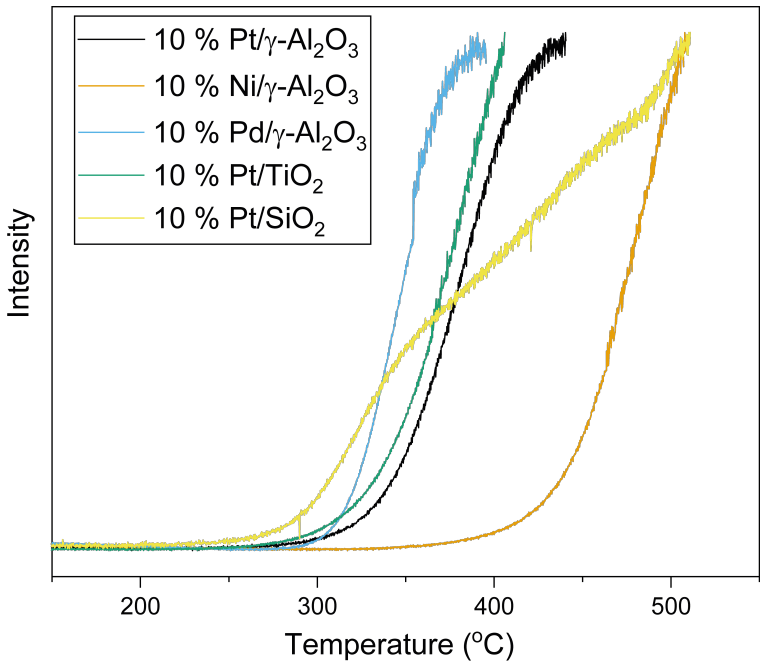

Figure 4.10: ^{18}O lability curves showing the counts of mass-34 with temperature when ^{18}O gas is passed through each of the materials Pt/γ-Al_2O_3, Pd/γ-Al_2O_3, Ni/γ-Al_2O_3, Pt/SiO_2 and Pt/TiO_2. The temperature at which a direct exchange occurs is indicated by the sharp rise in mass-34 counts.

Isotropic Model) disordered quadrupolar lineshape is seen for both tetrahedrally (AlO_4) and octahedrally (AlO_6) coordinated Al sites centred at ~65 and 10 ppm, respectively. [18] It is has also been previously shown that a small amount of pentahedrally coordinated (AlO_5) Al species are present on the surface of γ-Al_2O_3, however this cannot be clearly identified from Figure 4.11(a) due to its low abundance within the structure. [87, 88]

In contrast, the corresponding ^1H MAS NMR spectra (Figure 4.11(b) and Table 4.4) show considerable differences in speciation between the supported catalyst and the γ-Al_2O_3 support. Spectral assignments have been achieved from previous ^1H MAS NMR reports on γ-Al_2O_3 which show similar spectra. [101, 102] Four species are identified from the ^1H MAS data; isolated terminal μ^1-OH (δ_{iso}~0.7-1.0 ppm), doubly bridging μ^2-OH (δ_{iso}~1.9 ppm) and triply bridging μ^3-OH (δ_{iso}~3.6-3.8 ppm) hydroxyl species, in addition to H_2O (δ_{iso}~4.0-5.0 ppm). For γ-Al_2O_3, the predominant hydroxyl groups present are terminal species with a small amount of μ^3-OH. Upon Pt impreg-

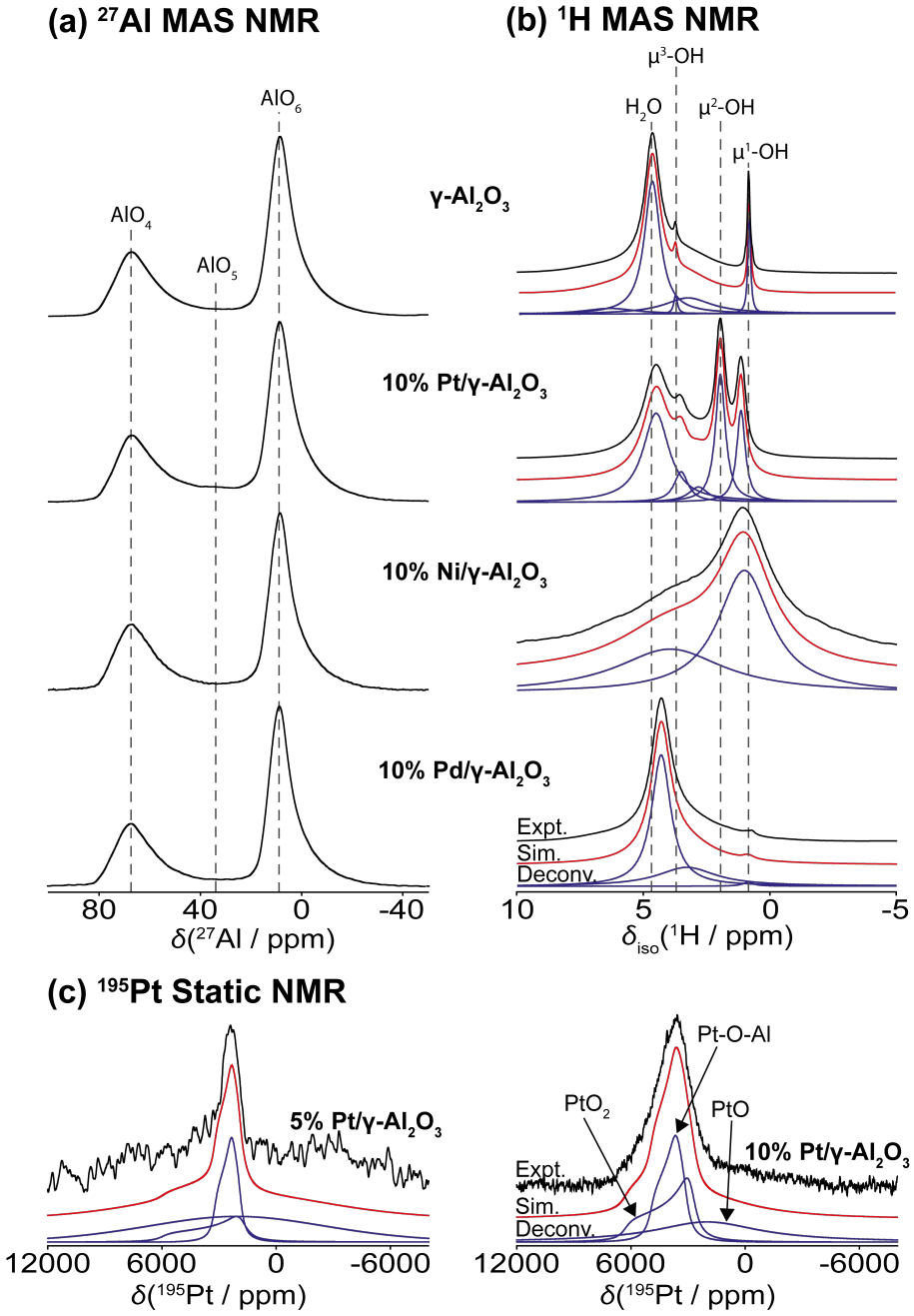

Figure 4.11: Solid state (a) ^{27}Al ($B_0 = 14.1$ T, $\nu_r = 20$ kHz) and (b) ^{1}H ($B_0 = 11.7$ T, $\nu_r = 60$ kHz) MAS NMR spectra of γ-Al_2O_3, 10 % Pt/γ-Al_2O_3, 10 % Ni/γ-Al_2O_3 and 10 % Pd/γ-Al_2O_3 prepared using an incipient wetness impregnation. (c) Static solid state ^{195}Pt NMR spectra of 5 and 10 % Pt/γ-Al_2O_3 acquired using a frequency sweep VOCS technique. Resonance assignments along with ^{1}H and ^{195}Pt spectral deconvolutions are shown.

Table 4.4: Solid state ^{1}H MAS NMR parameters and site assignments from spectral deconvolutions of γ-Al_2O_3, 10 wt% Pt and Ni/γ-Al_2O_3 synthesised using an incipient wetness method and 10 wt% Pt and Pd/γ-Al_2O_3 and 1 wt% Pt/γ-Al_2O_3 samples synthesised from a precipitation technique.

Sample	δ_{iso} (±0.1 ppm)	Rel. Int. (±1 %)		Assignment
γ-Al_2O_3	0.7	8	80	μ^1-OH
	3.6	2	20	μ^3-OH
	4.5	90		H_2O
10 % Pt/γ-Al_2O_3	0.9	15	31	μ^1-OH
	1.9	25	52	μ^2-OH
	3.8	8	17	μ^3-OH
	5.0	51		H_2O
10 % Ni/γ-Al_2O_3	1.0	59	100	-OH
	4.0	41		H_2O
10 % Pd/γ-Al_2O_3	0.9	1	100	μ^1-OH
	4.4	99		H_2O
1 % Pt/γ-Al_2O_3 precipitated	0.8	4	57	μ^1-OH
	1.8	1	14	μ^2-OH
	3.6	2	29	μ^3-OH
	4.3	93		H_2O
10 % Pt/γ-Al_2O_3 precipitated	0.9	1	20	μ^1-OH
	1.9	4	80	μ^2-OH
	4.5	95		H_2O

nation onto the surface, a significant amount of μ^2-OH species become present which is accompanied by a decrease in the relative intensity of μ^1-OH from 80 % to 31 %. This implies that Pt impregnation through the incipient wetness process disrupts -OH bonding to AlO groups. Similarly, Pd impregnation results in a reduction of μ^1-OH groups. Furthermore, two resonances are observed for Ni, which can be attributed to H_2O and -OH species; however, the broadness which is likely caused by clustering of these groups does not allow for specific -OH speciation to be identified.

Figure 4.11(c) shows ^{195}Pt static NMR spectra for 5 wt% and 10 wt% Pt/γ-Al_2O_3 and the corresponding parameters obtained from spectral simulations are given in Table 4.5. Comparing to the ^{195}Pt NMR spectrum of PtO_2 (Figure 4.5), a similar PtO_2 lineshape is identified which has comparable δ_{CS} and η_{CS} values. For industrial processes, only small amounts of the

Table 4.5: Solid state static ^{195}Pt NMR parameters obtained from simulated wideline VOCS NMR data of PtO_2, 5 wt% Pt/γ-Al_2O_3, 10 wt% Pt/γ-Al_2O_3, 10 wt% Pt/SiO_2 and 10 wt% Pt/TiO_2.

Sample	Site	δ (± 100 ppm)	δ_{CS} (± 100 ppm)	η_{CS} (± 0.2)	Rel. Int. (± 5 %)
PtO_2	PtO_2	3600	2800	0.0	100
5 % Pt/γ-Al_2O_3	PtO_2	3200	2800	0.1	16
	Pt-O-Al	2500	800	0.6	25
	PtO	2100	-	-	59
10 % Pt/γ-Al_2O_3	PtO_2	4000	2300	0.1	33
	Pt-O-Al	3900	1000	0.5	34
	PtO	2000	-	-	33
10 % Pt/SiO_2	PtO_2	3500	2800	0	32
	Pt-O-Si	2600	1300	0.5	28
	PtO	1500	-	-	40
10 % Pt/TiO_2	PtO_2	3600	2500	0.1	38
	Pt-O-Ti	2800	1400	0.6	41
	PtO	1900	-	-	21

precious metal are used (<5 wt%) and, by using a high Pt loading, PtO_2 agglomerations will occur, thus producing the PtO_2 resonance. Reducing the Pt loadings from 10 wt% to 5 wt% results in a concomitant decrease in the relative intensity from 33 % to 16 %, providing further evidence that the PtO_2-like resonance eludes to agglomerated nanoparticles. From Figure 4.5, a broad disordered PtO species centred at δ∼2000 ppm is also identified which increases in relative intensity for a decrease in Pt loading. Given the propensity for PtO to form as a surface species, it is likely PtO is present on the γ-Al_2O_3 surface. A third resonance is attributed to the oligomeric PtO_2 structures (Figure 4.1) originally proposed by Dou *et. al.* (2001) which are also bonded to the alumina surface. The asymetry parameter of η_{CS}=0.5 demonstrates the non-axial symmetry of the site caused by Al-O-Pt bonding. Furthermore, the δ_{CS} is considerably lower than PtO_2 showing the preferential orientation of the ^{195}Pt nucleus when bonding to the γ-Al_2O_3 support.

The ^{17}O enrichment for γ-Al_2O_3, 10 % Pt/γ-Al_2O_3 and 10 % Ni/γ-Al_2O_3 were carried out at an exchange temperature of 500 ^{o}C according to the lability curves in Figures 4.2 and 4.10. Figure 4.12 shows the resultant ^{17}O MAS NMR spectra at three fields (B_0 = 9.4 T, 14.1 T and 16.4 T). The ^{17}O MAS

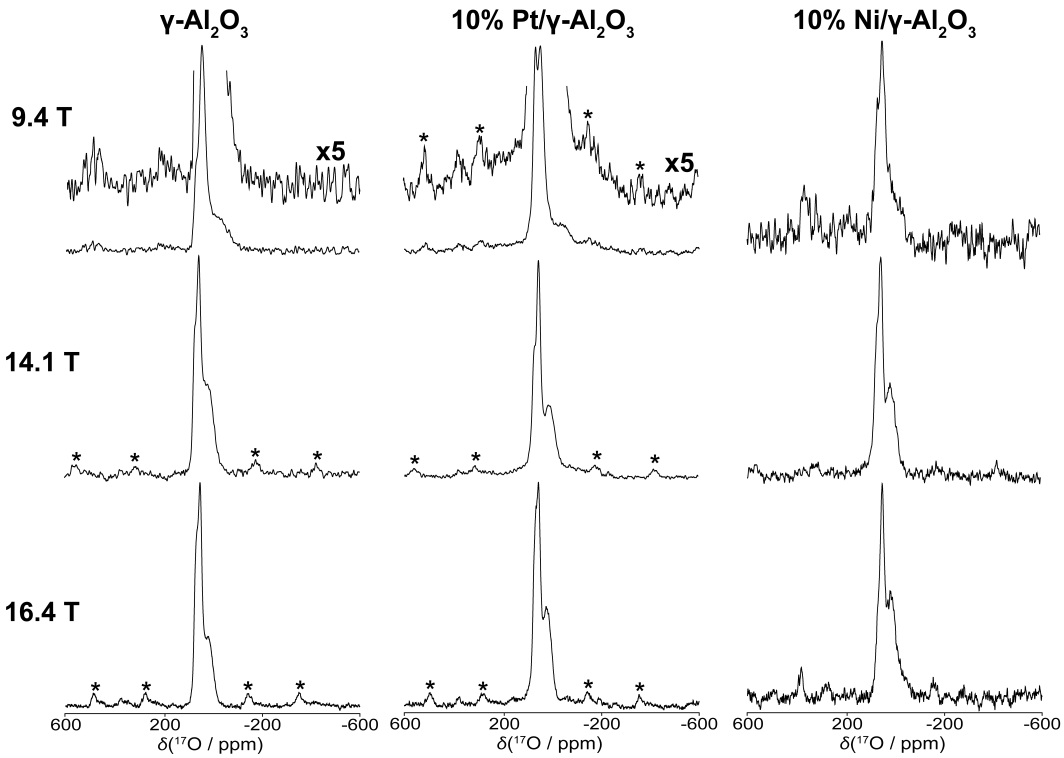

Figure 4.12: Solid state ^{17}O MAS NMR spectra (ν_r = 12 kHz) of ^{17}O enriched γ-Al_2O_3, 10 wt% Pt/γ-Al_2O_3 and 10 wt% Ni/γ-Al_2O_3 synthesised via an incipient wetness technique acquired at three field strengths, 9.4, 14.1 and 16.4 T. Spinning sidebands are indicated with an $*$.

NMR sectra of γ-Al_2O_3 is well documented and consists of a OAl_4 site centred at $\delta\sim$70 ppm, a OAl_3 at $\delta\sim$50 ppm and Al_xOH species at $\delta\sim$10 ppm. [95, 103]

No observable change in these sites occurs from catalyst inclusion across each field strength. However, for 10 wt% Pt/γ-Al_2O_3, an additional broad resonance beneath the bulk γ-Al_2O_3 sites spanning a $\sim$700 ppm range is detected and assigned to Pt-O-Al linkages, where the broadness is caused by the disordered surface structure. A similar broad resonance has been observed in a previous study by Klug *et. al* (2009), where a V_2O_5 catalyst was deposited on the surface of γ-Al_2O_3 and was attributed to a vanadia surface species. [97] The presence of this same broad resonance is not clear in the ^{17}O spectra of 10 % Ni/γ-Al_2O_3 because of the inferior enrichment achieved resulting in lower S/N. As suggested earlier, this is likely caused by Ni retarding the exchange of ^{17}O during the enrichment process.

It has been shown previously that the Pt dispersion on supports can be enhanced by a decrease in catalyst agglomeration occurring when synthesised through co-precipitation. [104] Therefore, 1 and 10 wt% Pt/γ-Al_2O_3 samples were synthesised using a precipitation method in an attempt to enhance the structural changes observed thus far. Energy dispersive X-ray analysis (EDX) analysis along with the corresponding STEM images and particle size distributions for co-precipitated 1 and 10 wt% Pt/γ-Al_2O_3 are illustrated in Figures 4.13(a)-(d) and Figure A.2(a) and (b). The EDX image and the particle size distribution for 1 wt% Pt show a high level of dispersion across the γ-Al_2O_3 surface with an average particle diameter of $\sim$2 nm. However for 10 wt% Pt, agglomerations are seen which is reflected in the larger average particle size of $\sim$3.2 nm. A ^{17}O MAS NMR spectrum of 1 wt% Pt/γ-Al_2O_3 is shown in Figure 4.13(e). Due to the higher catalyst dispersion on the γ-Al_2O_3 surface, the broad resonance assigned to Al-O-Pt linkages is more prominent.

Similarly to samples prepared via incipient wetness impregnation, no change from γ-Al_2O_3 is identified in ^{27}Al data or the associated 3QMAS data (Figure A.1) for the precipitated samples. However, changes in the hydroxyl surface speciation are detected in ^{1}H-^{27}Al CPMAS and ^{1}H data shown in Figures 4.14(a) and (b), respectively. From the CPMAS data, the three Al sites can be identified in the spectrum of γ-Al_2O_3; AlO_4, AlO_5 and AlO_6. The presence of the AlO_5 resonance disappears for 1 % and 10 % Pt loadings implying -OH groups associated with this site are removed due to preferential bonding of Pt species to AlO_5 surface species. The corresponding ^{1}H MAS data shows a systematic decrease in the relative intensity for isolated μ^1-OH species when the Pt loading is increased. Earlier studies by Taoufik *et. al.* (2014) reported that μ^1-OH species are primarily associated with AlO_4 sites. [101] Therefore, the decrease in μ^1-OH species suggests Pt bonding to surface AlO_4 sites in addition to AlO_5. The presence of μ^2-OH species is observed at 10 % Pt which could be a result of the Pt species disrupting the connectivity of bridging hydroxyl groups.

The ^{17}O MAS NMR spectra of 1 and 10% Pd/γ-Al_2O_3 enriched at 400 and 500 ^{o}C are illustrated in Figure 4.15(a). Given the lower ^{18}O exchange temperature for Pd/γ-Al_2O_3 compared to the Pt/γ-Al_2O_3 and Ni/γ-Al_2O_3 counterparts, 400 ^{o}C was initially used as the enrichment temperature. The

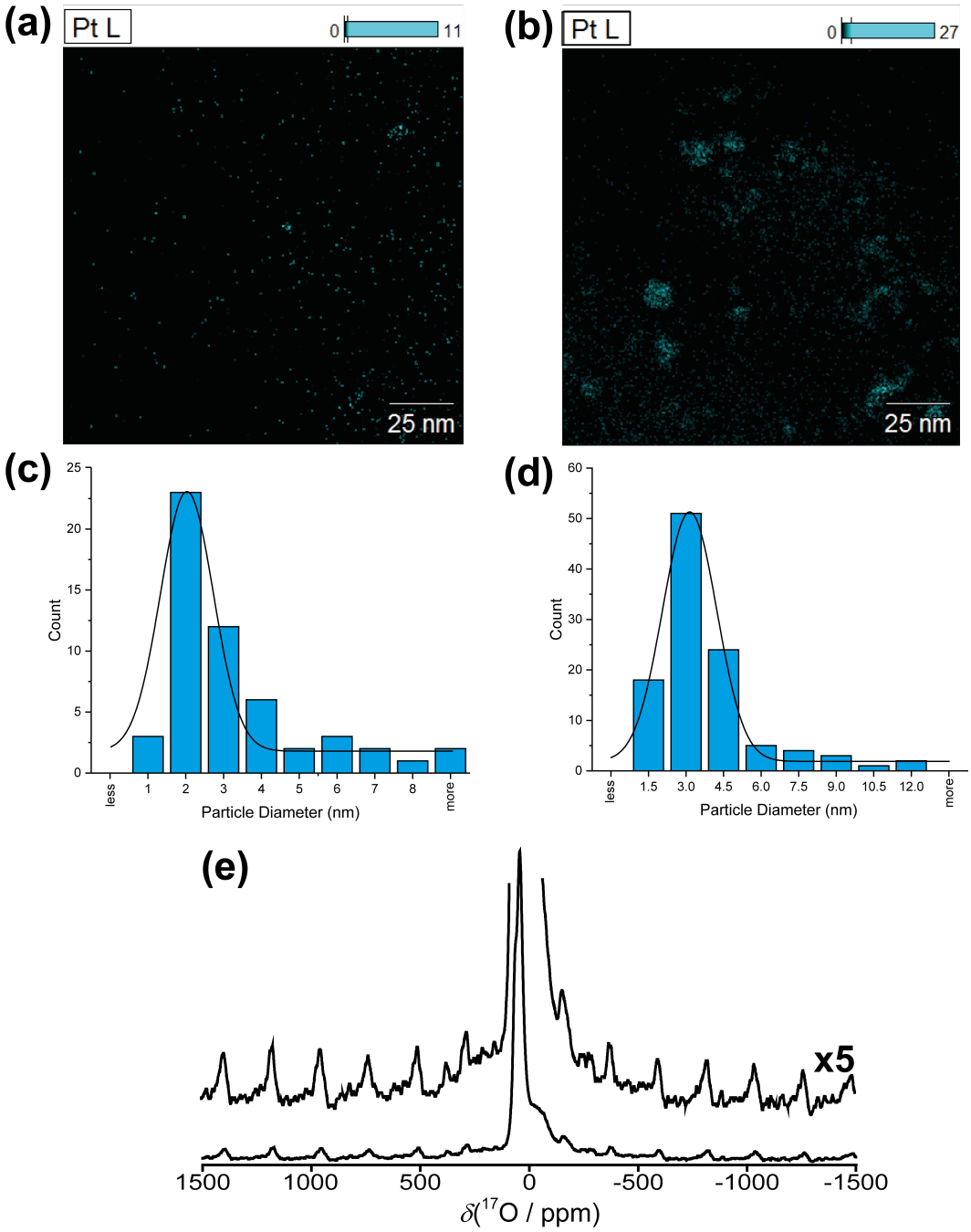

Figure 4.13: Pt EDX analysis of (a) 1 wt% and (b) 10 wt% Pt/γ-Al_2O_3 synthesised using the precipitation method and calcined at 500 ^{o}C. Histogram plots of particle size distribution for (c) 1 % and (d) 10 wt% Pt/γ-Al_2O_3 obtained from STEM analyses. (e) A ^{17}O solid state MAS Hahn echo NMR spectrum (B_0 = 9.4 T, ν_r = 12 kHz) of enriched 1 wt% Pt/γ-Al_2O_3 shown with a magnification of the baseline.

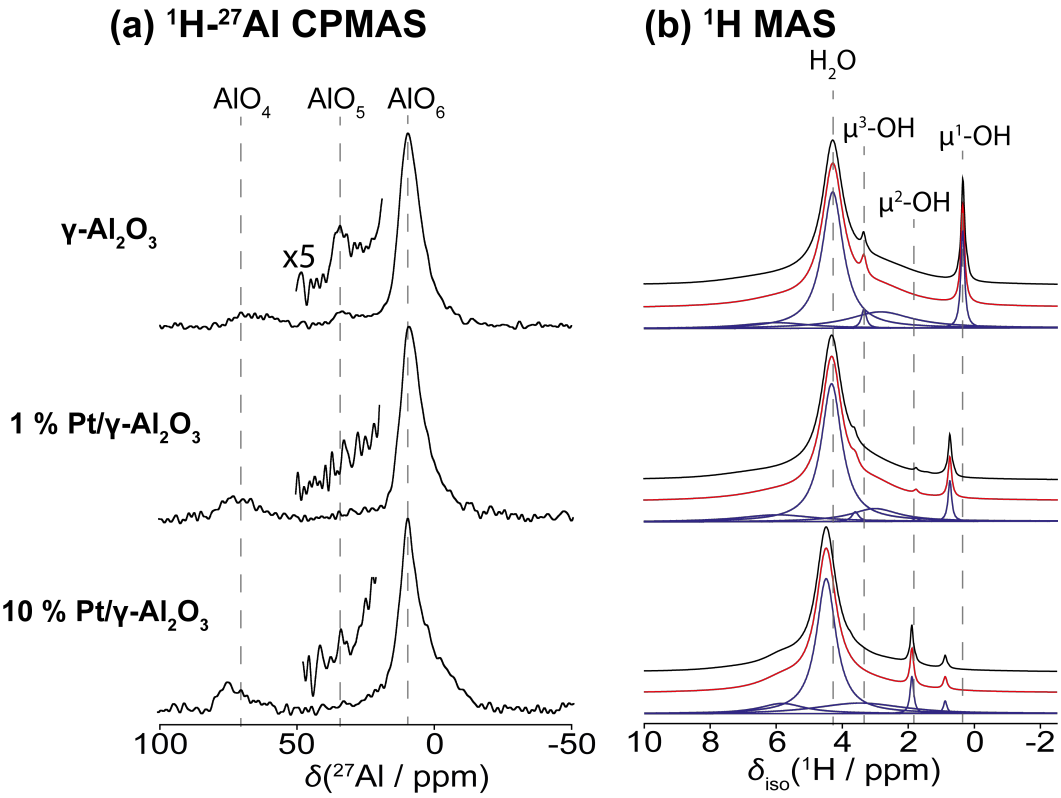

Figure 4.14: (b) ^{1}H-^{27}Al cross polarisation MAS NMR spectra (B_0 = 14.1 T, ν_r = 20 kHz, contact time = 0.3 ms) and (c) ^{1}H single pulse MAS NMR spectra (B_0 = 14.1 T, ν_r = 55 kHz) of γ-Al_2O_3, 1 and 10 wt% Pt/γ-Al_2O_3 synthesised via co-precipitation which have been subsequently oxidised at 500 ^{o}C.

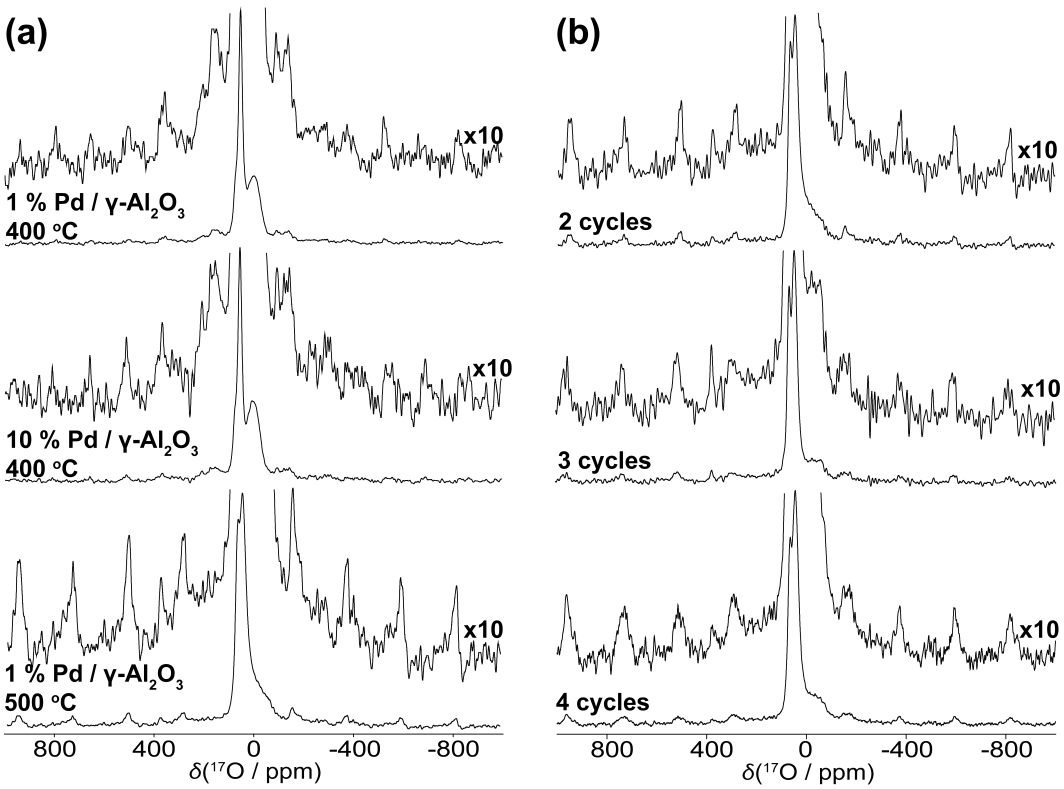

Figure 4.15: (a) Solid state ^{17}O MAS NMR (B_0 = 14.1 T, ν_r = 12 kHz) spectra of ^{17}O enriched 1 wt% and 10 wt% Pd/γ-Al_2O_3 using chemisorption temperatures 400 and 500 ^{o}C. (b) ^{17}O MAS NMR spectra of 10 % Pd/γ-Al_2O_3 cycled through 2, 3 and 4 ^{17}O enrichments at 500 ^{o}C. A 10x magnification of the baseline is also shown.

broad resonance previously detected for Pt/γ-Al_2O_3 samples was also observed at both 1 and 10 % loadings. Similarly to Pt samples, there was no change to the bulk alumina sites. Since the enrichment of PdO at 500 ^{o}C resulted in excellent S/N of PdO sites and the detection of a core shell model, 1 % Pd/γ-Al_2O_3 was also enriched at 500 ^{o}C. However, no additional PdO species were observed. Furthermore, 2, 3 and 4 cycles of enrichment were also implemented in an attempt to saturate the bulk γ-Al_2O_3 oxygen species and enrich sites related to Pd. This also resulted in no additional resonances being observed.

4.4.2 Pt Supported SiO_2

Silica is commonly used as a support for many precious metals due to its high porosity and tunable properties allowing for it to be used in many industrial processes. [73] However, the amorphous nature of common silicas used in industry makes insights into the structure and bonding difficult to detect through conventional diffraction techniques. Whereas ^{29}Si and ^{1}H solid state NMR have been widely used to study the catalyst surface bonding to SiO_2, there are few studies which have utilised ^{17}O NMR. [89–91] Therefore, SiO_2 and 10 wt% Pt/SiO_2 structures have been investigated using ^{17}O solid state NMR.

Initial characterisation was achieved using ^{29}Si single pulse (with ^{1}H decoupling) and CPMAS NMR as well as ^{1}H MAS data shown in Figure 4.16(a), (b) and (c), respectively and the corresponding fit parameters are given in Table 4.6. The ^{29}Si isotropic chemical shifts over the range $\sim$−85-−120 ppm clearly demonstrate that the silica network is defined by the characteristic Q^n tetrahedrally coordinated ^{29}Si speciation, whereby n is described by $Si(OSi)_nO(R)_{4-n}$ (with R = Pt, H). [105] In such systems, the network connectivity (N.C.) is commonly used to elucidate the network alteration upon incorporation of network modifying cations and is defined by

$$\text{N.C.} = \frac{[(Q^1/\%) + 2(Q^2/\%) + 3(Q^3/\%) + 4(Q^4/\%)]}{100}, \tag{4.1}$$

where the intensities of each Q^n species are used. [105, 106] For SiO_2 single pulse data, Q^2, Q^3 and Q^4 species are present at −101, −109 and −114 ppm, respectively, giving a N.C. of 3.1. This is indicative of a high network connectivity since Si is primarily bonded to three (Q^3) and four (Q^4) neighbouring Si. The formation of Q^2 and Q^3 units is attributed to the presence of surface and bulk -OH and H_2O groups present on the support surface. These Q^n species are also identified in the corresponding ^{29}Si CPMAS data in addition to a small amount of Q^1 species. Upon impregnation with Pt, significant changes to the Si network become apparent. A large increase in the relative amount of Q^1 and Q^2 species is observed which is facilitated by a significant decrease in Q^3 units from $\sim$42 % to $\sim$29 % resulting in a reduction of N.C. from 3.1 to 2.7. The loss in network connectivity alludes to Pt disrupting the silica

Table 4.6: Solid state NMR parameters obtained for SiO_2 and 10 % Pt/SiO_2 from ^{29}Si and ^{1}H MAS NMR spectral data. The isotropic chemical shift (δ_{iso}), relative intensities and Si network connectivity (N.C.) are shown.

Sample	Site	^{29}Si MAS NMR δ_{iso} (±2 ppm)	^{29}Si MAS NMR Rel. Int. (±5 %)	N.C.	^{1}H MAS NMR δ_{iso} (±0.1 ppm)	^{1}H MAS NMR Rel. Int. (±5 %)
SiO_2	Q^2	−101	23	3.1	0.7	17
	Q^3	−109	42		1.6	8
	Q^4	−114	35		2.5	36
					3.6	3
					4.3	19
					6.4	17
10% Pt/SiO_2	Q^1	−91	13	2.7	3.1	35
	Q^2	−101	29		3.6	53
	Q^3	−109	29		6.3	13
	Q^4	−114	29			

network by forming Si-O-Pt-O-Si bonding, thus lowering the Q speciation.

The corresponding ^{1}H MAS data exhibits large changes upon Pt impregnation to -OH species on the SiO_2 surface. Although the ^{1}H speciation in silica materials is complex, the spectra show similarities to previously reported silica ^{1}H data and therefore sites can be assigned accordingly. [91,107] The two resolved resonances at $\delta\sim$0.7 and 1.6 ppm for SiO_2 represent isolated surface silanol groups (Si-OH) which have no nearby ^{1}H species to promote H-bonding, thus resulting in lower shifts and narrower resonances. While it is possible to resolve narrower resonances in the parent SiO_2, these are not present upon Pt incorporation indicating Pt replaces H species in isolated hydroxyl groups when bonding to the support. The broader ^{1}H species located at $\delta\sim$3.6 and 6.3 ppm represent surface hydroxyl groups which are subject to H-bonding/in close proximity to non-bridging O components and physisorbed H_2O or a cluster of H_2O molecules, respectively. These species appear to remain largely unaffected as Pt is introduced, suggesting they could be bulk species. Figure 4.16(d) shows the static ^{195}Pt NMR spectrum for 10 wt% Pt/SiO_2. Similarly to 5 and 10 wt% Pt/γ-Al_2O_3, three Pt sites can be identified attributed to PtO_2 agglomerations, PtO_2 oligomeric structures and surface PtO species. Whereas the PtO_2 agglomerations and PtO surface resonances show compa-

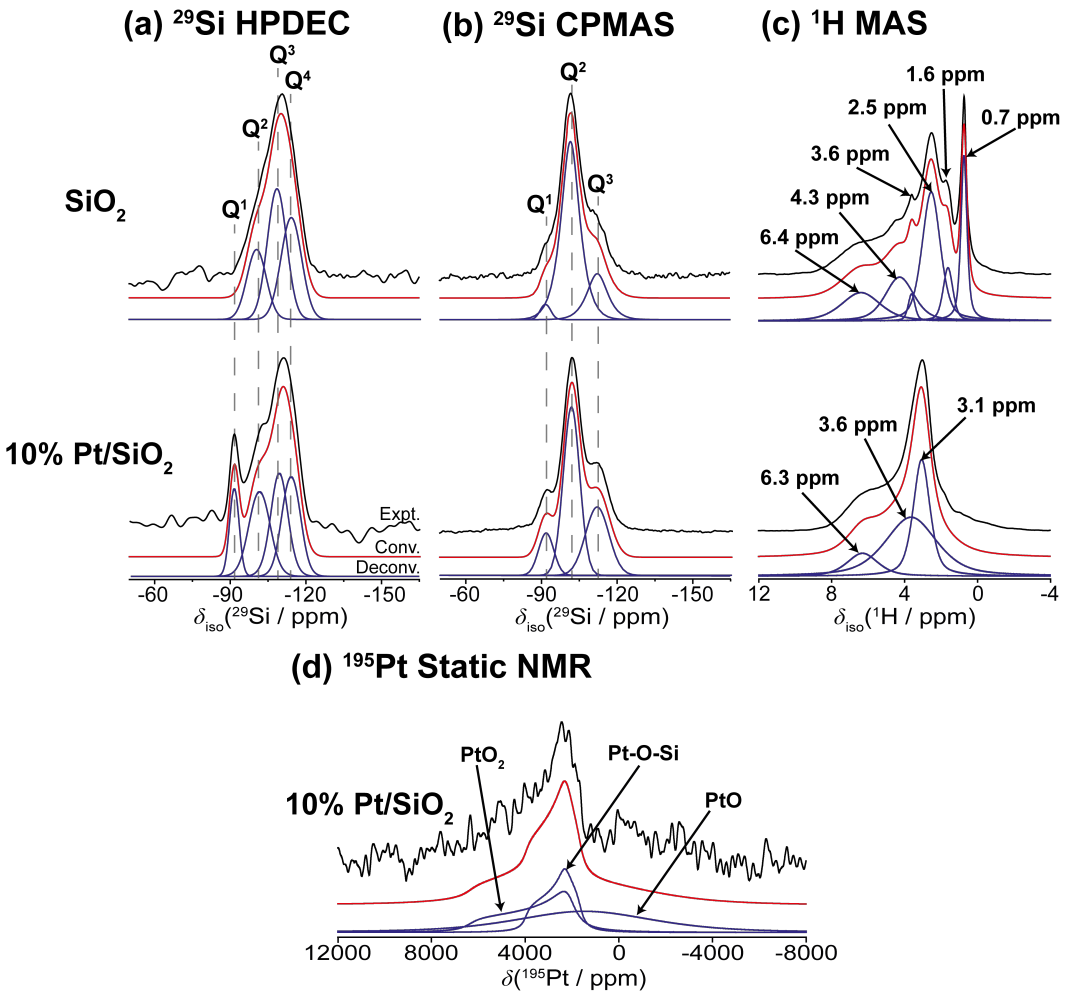

Figure 4.16: ^{29}Si, ^{1}H and ^{195}Pt NMR spectra from SiO_2 (Grace) and 10 % Pt/SiO_2 showing; (a) ^{29}Si MAS single pulse with ^{1}H decoupling (B_0 = 7.1 T, ν_r = 5 kHz, contact time = 4 ms), (b) ^{1}H-^{29}Si cross-polarisation MAS (B_0 = 7.1 T, ν_r = 5 kHz), (c) ^{1}H MAS single pulse (B_0 = 11.7 T, ν_r = 55 kHz) and (d) ^{195}Pt static frequency sweep VOCS spectra. All spectra are shown with their corresponding deconvoluted and simulated spectra along with resonance assignments.

Table 4.7: ^{17}O solid state MAS NMR parameters determined from disordered quadrupolar lineshape fits of SiO_2 and 10 wt% Pt/SiO_2.

Sample	Site	δ_{iso} (± 2 ppm)	C_Q (± 0.2 MHz)	C_Q dist. (± 0.1 MHz)	η_Q (± 0.05)
SiO_2	SiOSi	41	5.4	1.2	0.17
10% Pt/SiO_2	SiOSi	40	5.4	1.0	0.16
	SiOH	-13	-	-	-

rable parameters to 10 wt% Pt/γ-Al_2O_3, the site corresponding to oligomeric structures exhibits a lower chemical shift ($\delta\sim$2600 ppm) and higher anisotropic shift ($\delta_{CS}\sim$1300 ppm). Changing the support will alter the strength of the strong metal support interaction and thus alters the polarisation of electrons surrounding Pt species associated with the oligomeric structures and will lead to differences in the anisotropic chemical shift parameters.

Figure 4.17(a) shows ^{17}O MAS NMR spectra for enriched SiO_2 and 10 wt% Pt/SiO_2 at three fields; 9.4, 14.1 and 16.4 T. The corresponding 2D 3QMAS z-filter experiment for SiO_2 is illustrated in Figure 4.17(b) indicating a single site. Therefore, the MAS spectra are fitted to a quadrupolar lineshape with a distribution in quadrupolar parameters to represent the apparent disorder in the system; fitting parameters are given in Table 4.7. The fitting parameters obtained here show characteristic quadrupolar parameters for siloxanes. [95,108] For 10 wt% Pt/SiO_2, an additional resonance is detected at $\delta\sim-13$ ppm in the 2D 3QMAS spectrum which can also be resolved at 16.4 T. This site is assigned to a minor amount of silanol groups, which have been detected in previous silica studies. [108] Despite observation of these ^{17}O resonances, there is not a significant change in the fit parameters upon Pt loading and therefore there is no detection of catalyst-support bonding. This could be due to preferential enrichment of bulk silica species over PtO_2 or -OH species using this chemisorption enrichment method.

4.4.3 Pt Supported TiO_2

TiO_2 was the first catalyst support material where strong metal-support interactions were detected, making it of significant interest during the early developments of catalysis research. [51] Despite many other metal oxide supports

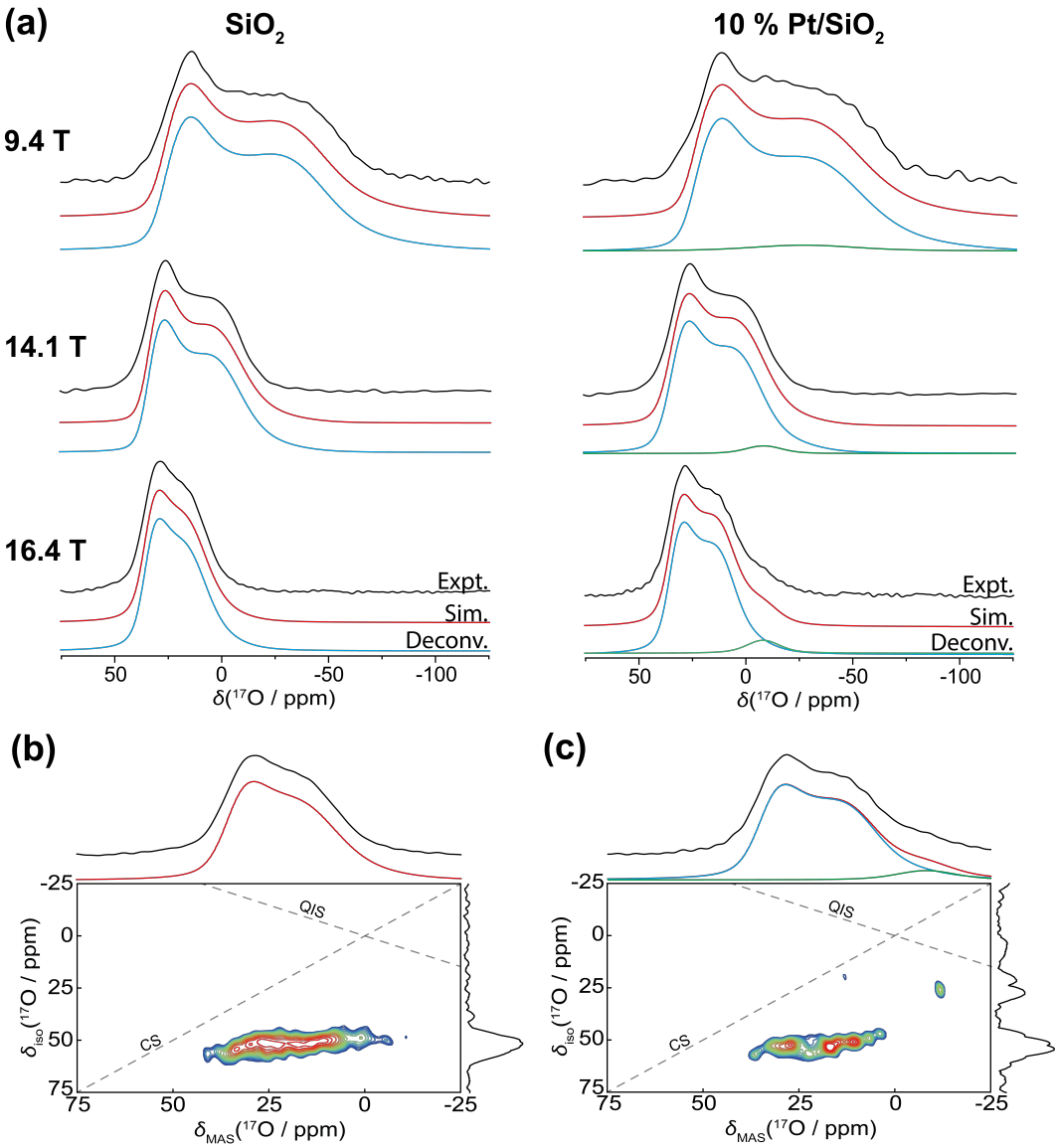

Figure 4.17: (a) ^{17}O MAS NMR spectra (ν_r = 20 kHz) for SiO_2 and 10 % Pt/SiO_2 acquired at the magnetic fields; 9.4 T, 14.1 T and 16.4 T. Spectra are shown with their respective deconvolutions and simulated fits. Corresponding ^{17}O 3QMAS z-filter NMR spectra (B_0 = 16.4 T, ν_r = 20 kHz) of (b) SiO_2 and (c) 10 wt% Pt/SiO_2.

showing similar properties, TiO_2 is still used in many industrial processes, however, the structure has been adapted from its early stages in order to generate a more porous material. Here, the common industrial TiO_2 Degussa-P25 material is studied as a metal oxide support, consisting of a mixed phase of the TiO_2 polymorphs anatase (A) and rutile (R).

Initial characterisation of TiO_2 and 10 wt% Pt/TiO_2 was achieved using PXRD shown in Figure A.3(a) and (b), respectively. No overall change is indicated to the bulk rutile and anatase phases upon Pt incorperation onto the surface. However, a broad reflection appears for 10 wt% Pt/TiO_2 at $\sim 35^o$ caused by agglomerations of PtO_2 species.

Solid state ^{195}Pt static and ^{1}H MAS NMR measurements were employed to probe the local structures of Pt bonding to TiO_2. Figure 4.18(a) shows a static ^{195}Pt VOCS spectrum for 10 wt% Pt/TiO_2, where similarities to data acquired for Pt/γ-Al_2O_3 (Figure 4.11(c)) and Pt/SiO_2 (Figure 4.16(c)) can be drawn. A PtO_2 CSA lineshape can be seen at $\sim$3600 ppm, however compared to pure PtO_2 the lineshape is significantly broadened indicative of greater disorder within the structure. As was observed for 10 wt% Pt/γ-Al_2O_3 and SiO_2, the large Pt loading used here cause agglomerations of PtO_2 particles giving a ^{195}Pt PtO_2-like lineshape. An additional ^{195}Pt CSA lineshape assigned to the oligomeric structures on the surface is also present at $\sim$2800 ppm which is significantly shifted compared to γ-Al_2O_3 supported species possible, due to the differences in the strong metal support interaction. Furthermore, the site assigned to a surface PtO species is also present for TiO_2 supports.

Corresponding ^{1}H MAS NMR data for TiO_2 and 10 wt% Pt/TiO_2 are depicted in Figure 4.18(b). Each spectrum displays three resonances which can be assigned according to previous ^{1}H NMR studies of anatase and rutile based materials. [109, 110] For TiO_2, the predominant resonance is located at $\delta_{iso}\sim$1 ppm, representative of a non-bridging isolated -OH group coordinated to a single titanium atom (i.e. little to no H-bonding). The peaks present towards higher chemical shifts ($\delta_{iso}\sim$5.7-6.3 ppm) are attributed to bridging -OH groups coordinated to multiple titania atoms and subjected to greater H-bonding. The relative amount of bridging hydroxyls significantly increases and contrastingly the amount of non-bridging hydroxyls decreases as a result of Pt impregnation onto the TiO_2 surface. Similarly to the ^{1}H data obtained

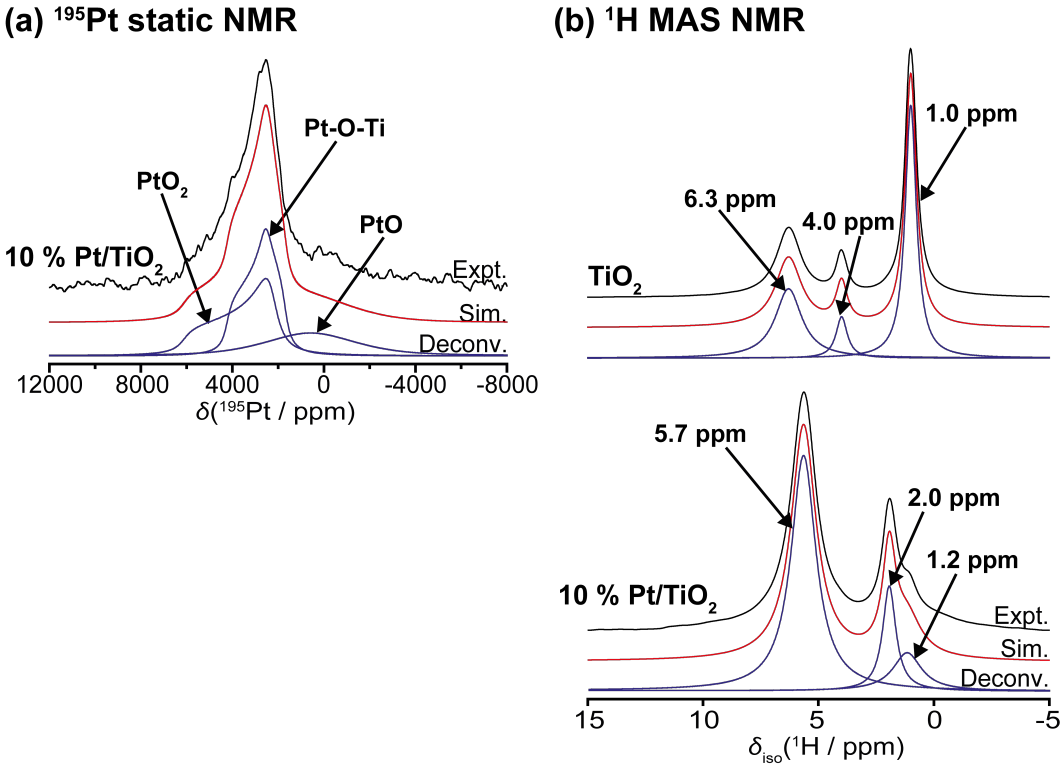

Figure 4.18: (a) Static ^{195}Pt solid state wideline VOCS NMR spectra (B_0 = 7.1 T)of 10 wt% Pt/TiO_2 showing the simulated lineshapes and assigned deconvoluted spectra. (b) ^{1}H MAS NMR data (B_0 = 11.7 T, ν_r = 55 kHz) of TiO_2 and 10 wt% Pt/TiO_2 along with simulated and deconvoluted spectra.

for SiO_2, the reduction in isolated surface hydroxyls in TiO_2 suggests the Pt catalyst anchors to the support surface through these isolated -OH groups.

Figure 4.19 shows ^{17}O solid state MAS NMR data for TiO_2 and 10 % Pt/TiO_2 acquired at three fields; 9.4, 14.1 and 16.4 T. Resonance assignments and spectral deconvolutions have been accomplished similarly to a previous ^{17}O NMR study on Degussa-P25 by Sun *et. al.* (2014) where spectral simulations were achieved based on parameters obtained from previous characterisations of TiO_2-based materials. [111,112] Five distinctive resonances at the chemical shifts δ∼520, 547, 562, 577 and 600 ppm are identified and the corresponding spectral simulations led to comparable quadrupolar parameters (C_Q and η_Q) to those previously reported. A study by Bastow *et. al.* (1993) has shown the OTi_3 sites of anatase and rutile to be situated at ∼562 and 600 ppm which are assigned accordingly in Figure 4.19. [112] The sites at ∼520 and 547 ppm

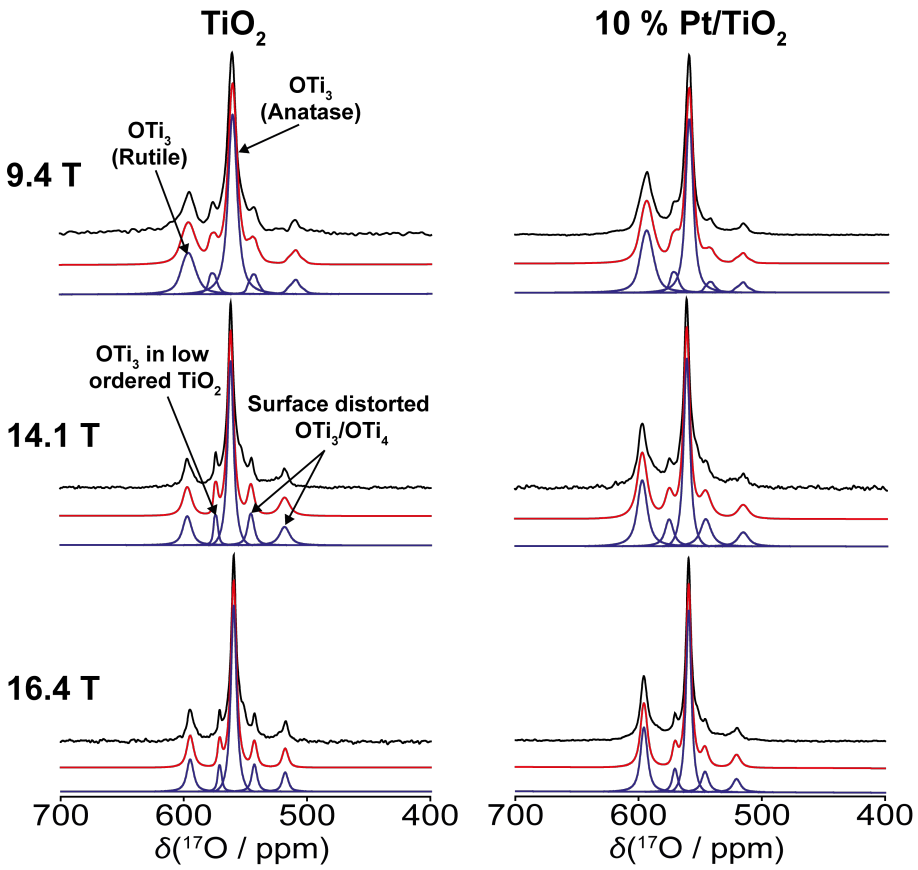

Figure 4.19: Solid State ^{17}O MAS NMR ($\nu_r = 20$ kHz) spectra of ^{17}O enriched TiO_2 (Degussa-P25) and 10 % Pt/TiO_2 acquired at multiple fields, 9.4, 14.1 and 16.4 T. Simulated quadrupolar fits are shown for each spectrum.

arise from distorted OTi_3 and/or TiO_4 sites located near the surface of the predominant anatase phase, while the site at ~577 ppm is attributed to a OTi_3 in a low-ordered TiO_2 phase. [97, 113] The calculated relative intensity of OTi_3 (rutile) increases with the introduction of Pt in addition to a concomitant decrease in the amount of OTi_3 (anatase). The presence of Pt is thought to facilitate a phase change from anatase to rutile under the enrichment conditions. Nevertheless, as can be seen from Table A.2 the δ_{iso}, C_Q and η_Q of the OTi_3 bulk anatase and rutile species remain unaffected. Furthermore, minor changes are observed in the distorted OTi_3/surface OTi_4 species possibly due to the preferential Pt bonding to these surface sites. However, these differences are within experimental error and therefore do not give a clear indication.

4.5 Conclusions

^{17}O enrichment by chemisorption and characterisation by ^{17}O solid state NMR of PGM oxide materials have been achieved for the first time. Initial structural characterisation using PXRD showed that PtO_2, PdO and Rh_2O_3 samples contained nanoparticle forms. However, both RuO_2 and IrO_2 indicated highly crystalline tetragonal structures. After enrichment, PtO_2 reduced primarily to Pt metal, however PtO_2 and PtO phases still remained, PdO nanoparticles agglomerated into larger particles and Rh_2O_3 produced crystalline phases of Rh_2O_3 and RhO_2. Both IrO_2 and RuO_2 remain unchanged.

PtO_2 and PtO phases were both identified and characterised through ^{195}Pt and ^{17}O solid state NMR. Furthermore, a core shell model was used to deconvolute the ^{17}O MAS NMR spectra of PdO nanoparticles where each nanoparticle layer is distinguishable because of differing Knight shift interaction strengths. For Rh_2O_3, two ^{17}O resonances which were significantly broadened by the paramagnetic Rh_2O_3 species are seen and were assigned to Rh_2O_3 and RuO_2 phases. A single narrow resonance was observed for RuO_2 attributed to a single oxygen environment within the tetragonal structure. However, poor enrichment was achieved for both RuO_2 and IrO_2 samples leading to no observable signal for IrO_2.

Further investigations into the ^{17}O solid state NMR of Pt and Pd on γ-Al_2O_3 lead to the observation of catalyst bonding to the metal oxide support. However, this was not observed for SiO_2 and TiO_2 supports, where little change was seen upon catalyst impregnation. However, static ^{195}Pt solid state NMR measurements showed evidence of PtO and PtO_2 bonding to the support surface and it is also suggested that PtO_2 forms oligomeric structures indicated by an increase in assymetry of the Pt nucleus compared to bulk PtO_2 species. ^{1}H MAS NMR data of metal oxide supports suggested catalyst bonding to isolated surface hydroxyl species.

Overall, it has been shown that ^{17}O solid state NMR is an excellent tool to study the local structures of PGM oxide nanoparticles. However, further studies such as correlating ^{17}O solid state NMR spectra to catalytic activity or looking at the changes in ^{17}O spectra for different particle sizes are still required in order to elucidate improvements to the design of supported PGM

catalysts.

Chapter 5

Quadrupolar Solid State NMR Investigations of High Temperature Thermoelectric Materials

5.1 Introduction

5.1.1 Background

Thermoelectric materials can directly convert heat into electrical energy and are widely looked at as favourable materials to be used in waste heat recovery and electronic cooling. [114, 115] Due to the attractive energy saving benefits, there has been a growing amount of interest in the development of thermoelectric materials with the primary focuses being on enhancing stability and performance. [116,117] The performance of such materials can be characterised using the dimensionless thermoelectric figure of merit, ZT, determined via

$$ZT = \sigma S^2/\kappa, \tag{5.1}$$

where S is the Seebeck coefficient, σ is electrical conductivity and κ is thermal conductivity. [118] Currently, the best performing thermoelectric materials are chalcogenides which have $ZT{\sim}1$ across the typical operational tem-

perature range. [119] However, for thermoelectric materials to compete with conventional generators, $ZT \geq 3$ is required, leading to an energy conversion efficiency of ∼30%. [120] Challenges arise in improving ZT because S, σ, and κ are interdependent; changing one will alter the others, making optimisation extremely difficult. Moreover, materials which are stable across a large temperature range, non-toxic, have a high electrical conductivity and low thermal conductivity are necessary for thermoelectric materials to be implemented in industrial and commercial settings. [121]

High-performance thermoelectric materials ($ZT \geq 1$) such as Bi_2Te_3, [122] PbTe [123], SnSe [124], GeTe [125] and Cu_2Se [126] are usually intermetallic alloys, but despite showing high figure of merits they are generally less stable, decomposing when used at high temperatures. In contrast, a multitude of different oxide based perovskite materials have been studied due to their robust stability across large temperature ranges and reduced toxicity. [127] Despite the relatively lower performance, many promising oxide based materials have been developed, including Na_2CoO_4, [128] $SrCrO_3$, [129] $Ca_3Co_4O_9$, [130, 131] $CaMnO_3$ [132] and ZnO. [133] As well as these, $SrTiO_3$ based materials have been of significant interest for a long time due to their good thermal stability at high temperatures and relatively high Seebeck coefficient generated by the six-fold degeneracy of the $Ti^{3d}{}_{-t2g}$ conduction bands. [134] However, these $SrTiO_3$ based materials usually exhibit comparatively lower ZT factors because of their very high thermal conductivity when compared to intermetallic materials. [135]

Using heavy metals dopants which directly substitute onto the 'Sr^{2+}' A and/or the 'Ti^{4+}' B sites (Figure 5.1) within the simple cubic structure of $SrTiO_3$ can tune the electronic transport properties, allowing for larger ZT values to be achieved whilst leaving the structural stability largely unaffected. [146] Common heavy metal dopants include La^{3+} [143,147], Dy^{3+} [126], Nd^{3+} [140] for the A site and Nb^{5+} [138], Ta^{5+} [148] and Sn^{5+} [149] as B site dopants. Table 5.1 summarises the maximum ZT values obtained for several $SrTiO_3$ based thermoelectric materials. Donor doped perovskites will have a higher cationic charge than the host cation that it replaces leading to an excess cationic charge which must be balanced by either increasing the amount of oxide ions, formation of vacancies or a reduction in cation oxidation state. [150]

Table 5.1: The highest reported thermoelectric figure of merit (ZT) for different compositions of $SrTiO_3$ based thermoelectric materials and the temperature at which the ZT value was achieved.

Composition	Temperature (K)	ZT	Ref.
$SrTi_{0.9}Ta_{0.1}O_3$	725	0.17	[136]
$SrTi_{0.85}Nb_{0.15}O_3$ with YSZ	900	0.21	[137]
$SrTi_{0.80}Nb_{0.20}O_3$ epitaxial film	1000	0.37	[134]
$Sr_{0.92}La_{0.08}TiO_3$	1045	0.22	[138]
$Sr_{0.85}Pr_{0.15}TiO_3$	773	0.35	[139]
$Sr_{0.90}Nd_{0.10}TiO_3$	873	0.28	[140]
$Sr_{0.8}La_{0.13}Ti_{0.95}Nb_{0.05}O_3$	1000	0.30	[141]
$Sr_{0.8}La_{0.08}Dy_{0.12}TiO_3$	1076	0.36	[142]
$Sr_{0.775}La_{0.15}TiO_3$	973	0.41	[143]
$Sr_{0.95}Ti_{0.9}Ta_{0.1}O_3$	1230	0.37	[144]
$Sr_{0.97}Ti_{0.8}Nb_{0.17}W_{0.03}O_3$	1270	0.28	[145]

However, it has been shown that only 'A site' Sr vacancies are formed when doping with heavy metal A site dopants, leading to improved electronic transport properties. [151–153] Using La as an A site dopant, it has been shown that octahedral tilting of the TiO_6 octahedra takes place about a formed Sr vacancy, leading to distortions in the cubic lattice. [143] It has also been suggested from theoretical models that increasing the tilt angle in the out of phase $a^-a^-a^-$ tilt system (Glazer notation) in $SrTiO_3$ leads to improvements in the Seebeck coefficient due to a greater overlap between the atomic orbitals. [154]

The addition of different heavy metal dopants on either the A/B site do not always have systematic effects on the thermal conductivity, electrical conductivity and the Seebeck coefficient. For example, Nb addition into the $SrTiO_3$ lattice has been observed to increase the electrical conductivity with a constant or lower Seebeck constant. [155–158] However, reported effects of Nb inclusion on the thermal conductivity is varied and has been seen to increase, [158] decrease [134] and remain constant [155, 156]. On the other hand, the inclusion of La will increase both the electrical conductivity and Seebeck coefficient with only minor changes exhibited for the thermal conductivity. [140, 155, 159] Furthermore, coinclusion of La and Dy on the Sr (A) site has led to increases in Seebeck coefficient and electrical conductivity with a decrease in thermal conductivity leading to excellent improvements

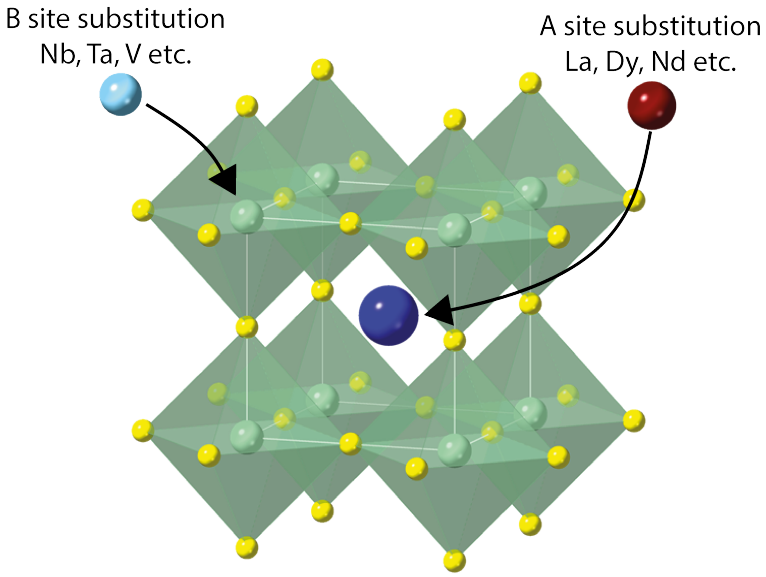

Figure 5.1: Diagram showing metal cation substitution onto the Sr 'A' and Ti 'B' site dopants within the cubic $SrTiO_3$ structure.

in ZT. [160, 161] However, if the Dy replaces La in the lattice, a decrease in electrical conductivity and Seebeck coefficient is observed. [142] In order to attribute these varied changes in cation doping to the thermoelectric performance, a full structural characterisation is needed where localised changes contributing to thermoelectric parameters can be identified.

Here, a multiple technique approach has been undertaken to determine the structural intricacies associated with the B-site doping of $SrTiO_3$ through the inclusion of Nb^{5+} and Ta^{5+}. Diffraction based methods have been implemented to observe structural evolutions associated with the long-range periodicity and strain of the lattice. Moreover, solid state NMR measurements have been carried out for the first time to analyse oxide based thermoelectric materials in order to observe short range local structural changes. These characterisation techniques have been complemented by the use of structural modelling to offer structural confirmation leading to a thorough understanding of doped $SrTiO_3$ systems.

5.2 Experimental

5.2.1 Synthesis

Stoichiometric amounts of $SrCO_3$ (Merck), TiO_2 (Merck), Nb_2O_5 (Merck), and Ta_2O_5 (Merck) were mixed and fired at 1350 ^oC for 20 h. Samples were then ground and subsequently heated at 1350 ^oC in air with intermediate regrinding every 10 hrs until a single phase perovskite was achieved.

5.2.2 PXRD, Neutron diffraction and XPS Measurements

Powder X-ray diffraction experiments were performed using a Bruker D8 Advance diffractometer equipped with a Cu Kα X-ray tube operating at 40 kV and 40 mA. The data was collected from 10^o to 100^o with a 0.01^o step size and a count time of 5 s per step. Rietveld refinements of collected XRD data was performed using the Topas 3 software. [162]

Powder neutron diffraction measurements were acquired on the High Resolution Powder Diffractometer at the Open Pool Australian Lightwater (OPAL) reactor at Australian Nuclear Science and Technology Organization (ANSTO) facility. Approximately 2 g of sample was loaded into a 6 mm diameter vanadium can that was rotated during collection. The vanadium can was covered with Cu foil for high temperature diffraction experiments. Diffraction data was collected at both ambient (300 K) and high temperatures (700 K) using a neutron wavelength of 1.622 $\AA$ from 2.75^o to 163.95^o 2θ with a step size of 0.05^o. The Topas 3 program was utilized for the Rietveld refinement. A cylindrical absorption correction was employed for the neutron data refinement.

X-ray photoelectron spectroscopy was performed using a Kratos AXIS Supra spectrometer with a monochromatic Al Kα source (15 mA, 15 kV). The XPS spectra were collected with solid powder samples pressed on carbon tape. A 3.1-volt bias was applied to the sample to neutralize charge build up on the sample surface. Individual core levels were measured with a pass energy of 20 eV. The spectra were calibrated by setting the adventitious carbon 1 s peak to 284.8 eV.

5.2.3 Raman and IR Spectroscopy

Raman spectra were recorded at room temperature using a Renishaw InVia spectrometer using 514.5 nm radiation from an Ar^+ laser for excitation. A grating of 1800 l/mm was used along with 10 % of the 2 mW laser power. The collection time was set to 5 s for the acquisition of 6 accumulations.

FTIR spectra were undertaken using a ThermoFischer Nicolet iN10 spectrometer equipped with a LN2 cooled MCT/A detector. Spectra were acquired over the 675-3999.8 cm^{-1} range achieving a resolution of 4 cm^{-1}. A total of 128 scans were acquired per spectrum.

5.2.4 Electron Probe Microanalysis

The chemical compositions of the samples were examined by electron probe microanalysis (EPMA) using JEOL JXA-8200 at 20 kV, with a beam current of 20 nA, beam diameter of 2.5 μm and peak counting times of 40 s for all elements (both peak and background). The standards used were a natural single crystal of $SrTiO_3$(Sr, Ti and O), niobium oxide (Nb) and tantalum oxide (Ta). An atomic number (Z) effect, absorption (A) effect, and fluorescence excitation (F) effect correction procedure was applied to all analyses.

5.2.5 Solid State NMR

One dimensional solid state ^{93}Nb MAS NMR data were acquired at 14.1, 16.4 and 20.0 T using a Bruker Avance Neo-600, Bruker Avance III HD-700 and Bruker Avance Neo-850 spectrometer, operating at ^{93}Nb Larmor frequencies (ν_o) of 146.7, 170.7 and 207.8 MHz, respectively. Measurements were undertaken using a Bruker 1.3 mm HXY MAS probe which enabled a MAS frequency (ν_r) of 55 kHz. A 'non-selective' ^{93}Nb (solution) $\pi/2$ pulse length of 15 μs was calibrated using a $H(NbCl_6).CH_3CN$ saturated solution from which a 'selective' (solids) $\pi/2$ pulse length of 3 μs was determined for the ^{93}Nb ($I = 9/2$) nucleus. Data was collected using a rotor synchronised Hahn-echo pulse sequence ($\pi/2$-τ-π-τ-acquire) implementing a $\pi/6$ flip angle of 1 μs duration, acquiring between 32,000 and 256,000 transients per spectra. Three pulse two dimensional ^{93}Nb 3QMAS z-filter measurements were acquired at

14.1 and 20.0 T (ν_o = 146.7 and 207.8 MHz) using MAS frequencies of 38 and 55 kHz, respectively. A 2 μs 'non-selective' triple quantum excitation pulse was implemented followed by a 0.4 μs 'non-selective' conversion pulse and a 'selective' 10 μs z-filter pulse. A total of 96 slices were used, acquiring 3840 scans per slice and using a delay increment of 18.2 μs. A measured recycle delay of 0.5 s was used between subsequent slices. All ^{93}Nb spectra and all chemical shifts were externally referenced against the IUPAC primary reference of K($NbCl_6$).CH_3CN (sat.) solution (δ_{iso} = 0 ppm) via the secondary H($NbCl_6$).CH_3CN (sat.) solution reference (δ_{iso} = 0 ppm). [9]

1D solid state ^{87}Sr MAS NMR data were acquired at 11.7, 14.1 and 20.0 T using a Bruker Avance III-500, Bruker Avance Neo-600, and Bruker Avance Neo-850 spectrometer operating at the ^{87}Sr Larmor frequencies (ν_o) 21.7, 26.0 and 36.8 MHz, respectively. Measurements were undertaken using both a Chemagnetics 9.5 mm XY MAS probe and Bruker 7 mm HX MAS probe, allowing a MAS frequency (ν_r) of 3 kHz to be implemented. Acquisition of the data was achieved using a rotor synchronised Hahn-echo pulse sequence ($\pi/2$-τ-π-τ-acquire), where a $\pi/6$ flip angle of between 2.4 and 3 μs duration was used. A recycle delay of 0.5 s was used for all acquisitions with more than 69,000 transients per spectrum. Pulse optimisation and ^{87}Sr chemical shift referencing were executed via an external secondary $SrTiO_3$ solid reference (δ_{iso} = 0 ppm) against the IUPAC primary reference of $SrCl_2$ (aq) solution (δ_{iso} = 0 ppm). [9] All ^{93}Nb and ^{87}Sr MAS NMR data were simulated using the Quadfit program. [1]

5.2.6 DFT Calculations and Materials Modelling

Ab initio calculations were performed using the CASTEP [163] density functional theory (DFT) package, which employs a planewave basis set and ultrasoft pseudopotentials. Input files were generated using the cif2cell [164] package and the Atomic Simulation Environment. [165] The regularised SCAN exchange-correlation functional [166] has been used throughout with consistent, on-the-fly generated ultrasoft pseudopotentials. [167] SCAN has been shown to accurately describe the electronic and geometrical structure of perovskite materials. [168]

A charge model of Nb-doped $SrTiO_3$ was parametrised. First, a set of random unrelaxed structures were generated for which the ab initio energies were computed using DFT. In a 4x4x4 supercell, 4 randomly selected Ti atoms were replaced by Nb atoms, and two random Sr atoms were removed. Across these configurations, the nearest-neighbour chemical environments are equivalent, therefore we attributed the difference in energetics to the difference in the Coulomb interactions. Rather coarse settings were used in the DFT calculations: QC5 pseudopotentials with the FINE setting for the plane-wave cutoff, corresponding to 408 eV and only the Γ-point was included from the Brillouin zone. Using a least-square fitting procedure, partial charges (Ti = 1.83, Sr = 0.89, Nb = 2.30) were assigned to each metal ion. The charge associated with O atoms were adjusted for each different composition to achieve overall charge neutrality.

A simple charge model was used to generate energetically favourable initial configurations of defected but unrelaxed cubic $SrTiO_3$ structures. Adapting the nested sample method [169] found a series of low-energy, unrelaxed configurations at different doping levels, in which the atomic positions were relaxed using DFT to analyse the ab initio energetics. On the relaxed structures NMR parameters were calculated using the GIPAW method. [170, 171] Geometry relaxations and NMR parameter calculations were performed using k-point grids corresponding to approximately 30 $\mathring{A}$ lattice parameters. While the geometry relaxations used the QC5 pseudopotential set and a 408 eV plane-wave cutoff, the more accurate C19 pseudopotential set with a 700 eV plane-wave cutoff were used for the NMR calculations. It was established that even with the more accurate settings in the NMR calculations, atomic forces were less than 0.07 eV/$\mathring{A}$ on individual atoms and the force Root Mean Square Error (RMSE) was 0.01 eV/$\mathring{A}$. Due to the lack of suitable calibration compounds, Nb shifts were referenced to the 'isolated' Nb defect's chemical shielding.

5.2.7 Spark Plasma Sintering Synthesis (SPS) and Thermoelectric Properties

Spark Plasma Sintering (SPS) was used to synthesize the bulk perovskites samples for thermoelectric properties tests. The doped perovksite powders were filled in a cylindrical graphite die and heated up to 1200 K for 2-3 min in vacuum. The obtained disk samples were cut into a rectangular pellet for Seebeck coefficient measurements and the thermal diffusivity studies. The Seebeck coefficient and electrical resistivity were measured simultaneously from room temperature to 973 K, in low-pressure helium using an ULVAC-RIKO ZEM3 system. Thermal conductivity was calculated using the formula $\kappa = \alpha\rho C_p$, where α, ρ, and C_p represent thermal diffusivity, density and specific heat, respectively. The specific heat was calculated from the measured DSC data on a NETZSCH STA (499F1 Jupiter), and thermal diffusivity was measured in a NETZSCH LFA-427 instrument. The density measurement was carried out by a Micromeritics OccuPyc II 1340 Gas Pycnometer.

5.3 Results and Discussion

5.3.1 Initial Characterisation

To investigate the crystal structure of $Sr_{1-x/2}M_xTi_{1-x}O_3$ (M = Nb, Ta) over the compositional range x = 0, 0.01, 0.05, 0.1, 0.2, room temperature PXRD data were collected and are shown in Figure 5.2. The PXRD results of all inclusions of Nb^{5+} or Ta^{5+} show excellent crystallinity, and the indexed original cubic $SrTiO_3$ ($Pm\bar{3}m$) structure. Rietveld refinements of $Sr_{(1-x/2)}Ti_{(1-x)}M_xO_3$ (x = 0.05, 0.1 and 0.2) of the corresponding neutron powder diffraction patterns are presented in Figure B.1 and the resultant plot of the refined lattice parameter, a, against x is shown in Figure 5.3. The refined lattice parameter (a) increases systematically from 3.9058(3) $\mathring{A}$ to the maxima 3.9195(2) $\mathring{A}$ and 3.9185(3) $\mathring{A}$ for x = 0.2 concentrations of Nb^{5+} and Ta^{5+}, respectively. The unit cell expansion follows Vegard's law, where the replacement of Ti^{4+} ions (0.61 $\mathring{A}$) by the larger Nb^{5+} and Ta^{5+} ions (0.64 $\mathring{A}$) causes a linear expansion of the lattice (Figure 5.3(a)). In order to balance the excess cationic charge generated from Nb^{5+} and Ta^{5+} inclusion, vacancies are formed at the Sr (A)

Table 5.2: Calculated Nb and Ta occupancies and the associated Sr vacancies determined from neutron diffraction data.

Ideal	$Sr_{(1-x/2)}Ti_{(1-x)}Nb_xO_3$		$Sr_{(1-x/2)}Ti_{(1-x)}Ta_xO_3$	
x	Refined x	A site vacancies (%)	Refined x	A site vacancies (%)
0	0.0	0.0	0.0	0.0
0.05	0.029(1)	1.47	0.04(1)	2.1
0.10	0.096(1)	4.8	0.094(1)	4.7
0.20	0.212(2)	10.6	0.181(2)	9.1

site (1a (0, 0, 0)). The relationship between M^{5+} dopants and cation vacancies can be expressed through the following equation:

$$xM^{5+} + \frac{x}{2}Vac(Sr) \rightarrow xTi^{4+} + \frac{x}{2}Sr^{2+}. \tag{5.2}$$

Using the above equation, refined values for Nb and Ta occupancies enable the accurate determination of the Sr (A site) vacancies summarised in Table 5.2. The refined occupancies are close to the ideal values. Stoichiometries of Nb and Ta determined from elemental analysis of EPMA data are also suggestive of Sr (A) site vacancies, due to the unmatched atomic ratios between the A and B site elements (Table 5.3). Furthermore, the amount of A site vacancies determined from elemental analysis closely correlate with those determined from refinements of the neutron diffraction data.

Validation of cation oxidation states was achieved from Ti, Nb and Ta X-ray photoelectron spectroscopy (XPS) data shown in Figure 5.3(b)-(d), where a characteristic doublet peak is observed for each cation. The dominant Ti binding energies at approximately 458.9 and 464.8 eV are assigned to Ti $2p_{3/2}$ and Ti $2p_{1/2}$ peaks, respectively. A separation between these peaks of 5.9 eV indicates that the predominant oxidation state is Ti^{4+} and no Ti^{3+} is present. Figure 5.3(c) and (d) show the deconvoluted Nb 3d and Ta 4f doublet peaks corresponding to oxidation states of Nb^{5+} and Ta^{5+}, respectively. Similarly to Ti, no reduction to Nb^{4+} or Ta^{4+} species is observed, providing further evidence for the generation of Sr (A) site vacancies to balance the overabundant cationic charge.

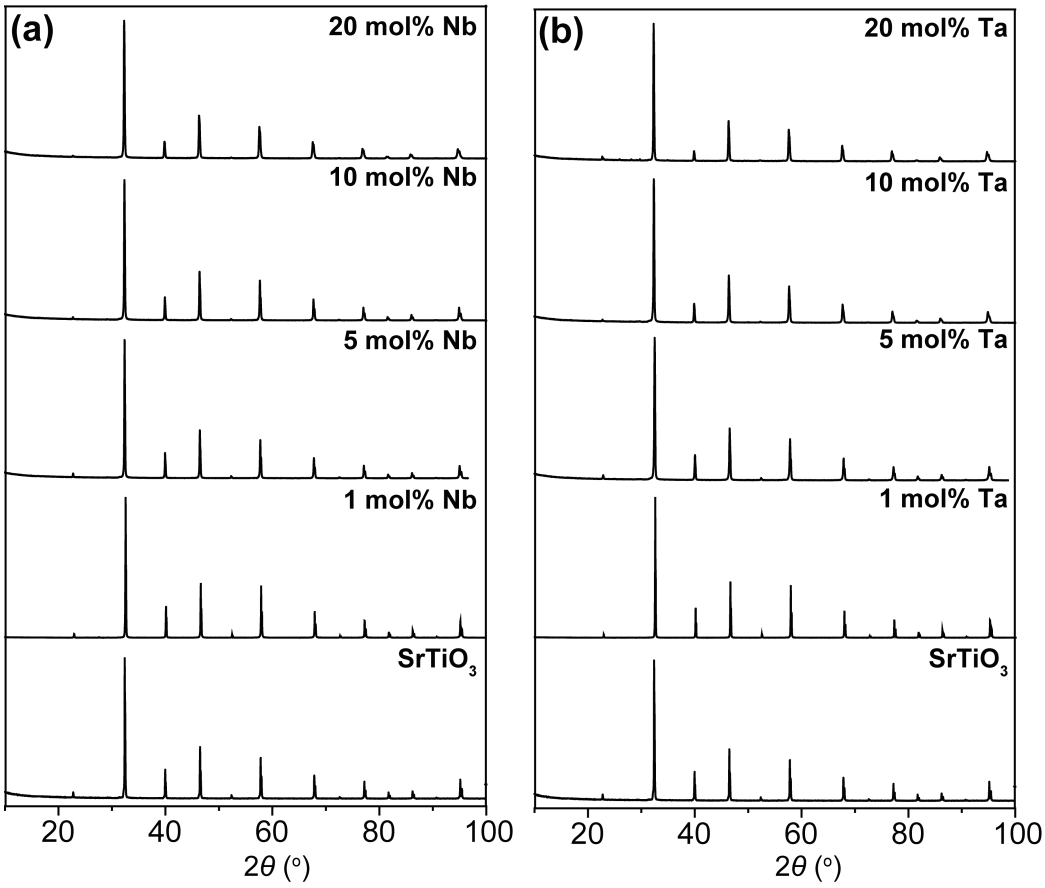

Figure 5.2: Powder X-ray diffraction patterns for (a) $Sr_{(1-x/2)}Ti_{(1-x)}Nb_xO_3$ and (b) $Sr_{(1-x/2)}Ti_{(1-x)}Ta_xO_3$ at x concentrations 0, 0.01, 0.05, 0.1 and 0.2.

5.3.2 Raman and IR Spectroscopy

Raman spectroscopy was utilised to study the lattice dynamics of Nb/Ta doped $SrTiO_3$, because of its sensitivity to short range structural distortions arising from microstructural defects. The parent cubic ($Pm\bar{3}m$) perovskite structure of $SrTiO_3$ generates odd symmetry zone-centered optical phonons; therefore the Raman spectrum will be dominated by second order scattering. This can be seen in Figure 5.4, where the $SrTiO_3$ spectra consists of two second-order broad bands over the regions of 200-400 cm^{-1} and 600-800 cm^{-1}. However, upon inclusion of Nb and Ta, several additional features beyond these second-order bands are detected. For Nb doped $SrTiO_3$, four additional peaks are seen at 127 cm^{-1}, 529 cm^{-1}, 802 cm^{-1} and 864 cm^{-1}, each showing increasing

Table 5.3: Mean compositions of Nb and Ta doped $SrTiO_3$ as determined by EPMA data along with the calculated percentage of Sr vacancies.

Ideal	$Sr_{(1-x/2)}Ti_{(1-x)}Nb_xO_3$*				$Sr_{(1-x/2)}Ti_{(1-x)}Ta_xO_3$*			
x	Sr	Ti	Nb	A site vacancies (%)	Sr	Ti	Ta	A site vacancies (%)
0	0.998	1.004	-	0.2	0.998	1.004	-	0.2
0.05	0.985	0.943	0.052	1.5	0.980	0.959	0.040	2.0
0.10	0.954	0.901	0.098	4.6	0.953	0.900	0.100	4.7
0.20	0.909	0.785	0.208	9.1	0.998	1.004	0.180	9.0

*Atomic ratios were calculated from EPMA data basis of 3 oxygen atoms per formula unit (afpu). For each composition, 10 EPMA analyses were made.

intensity with greater Nb inclusion (Figure 5.4(a)). In a similar fashion, Ta doped samples exhibit three additional peaks at 130 cm^{-1}, 525 cm^{-1} and 800 cm^{-1} (Figure 5.4(b)). The peaks at ∼130, 525, and 800 cm^{-1} are identified as TO_1, TO_4 and LO_4 phonons, respectively, which arise from first-order Raman scattering of $Sr_{(1-x/2)}Ti_{(1-x)}M_xO_3$ vibrational modes. The appearance of first-order Raman scattering, where the bulk crystalline structure is cubic suggests a local loss of inversion symmetry caused by point defects such as impurities and vacancies commonly seen in perovskites. [172] Here, it is thought to be caused by the formation of Sr (A) site vacancies, confirmed earlier from neutron diffraction data and elemental analysis. As the presence of Sr vacancies increases in the structures, the intensities of the first-order peaks become greater, further suggesting that these forbidden modes are associated with the apparent vacancy formation.

Analogous FTIR spectra carried out over the 700-4000 cm^{-1} range for $Sr_{(1-x/2)}Ti_{(1-x)}M_xO_3$ (M = Nb^{5+}, Ta^{5+}) are shown in Figure 5.4(c) and (d). The broad peaks spanning 2700-3700 cm^{-1} and 750-1200 cm^{-1} are attributed to O-H bonds in physisorbed water and the Ti-O bonds of $SrTiO_3$, respectively. For both Nb and Ta based systems a decrease in intensity is seen for peaks at 1457 and 1508 cm^{-1} which are tentatively assigned to Sr-O bonds from previous $SrTiO_3$ based IR studies. [173] The reduction in peak intensities are thus caused by the development of Sr vacancies.

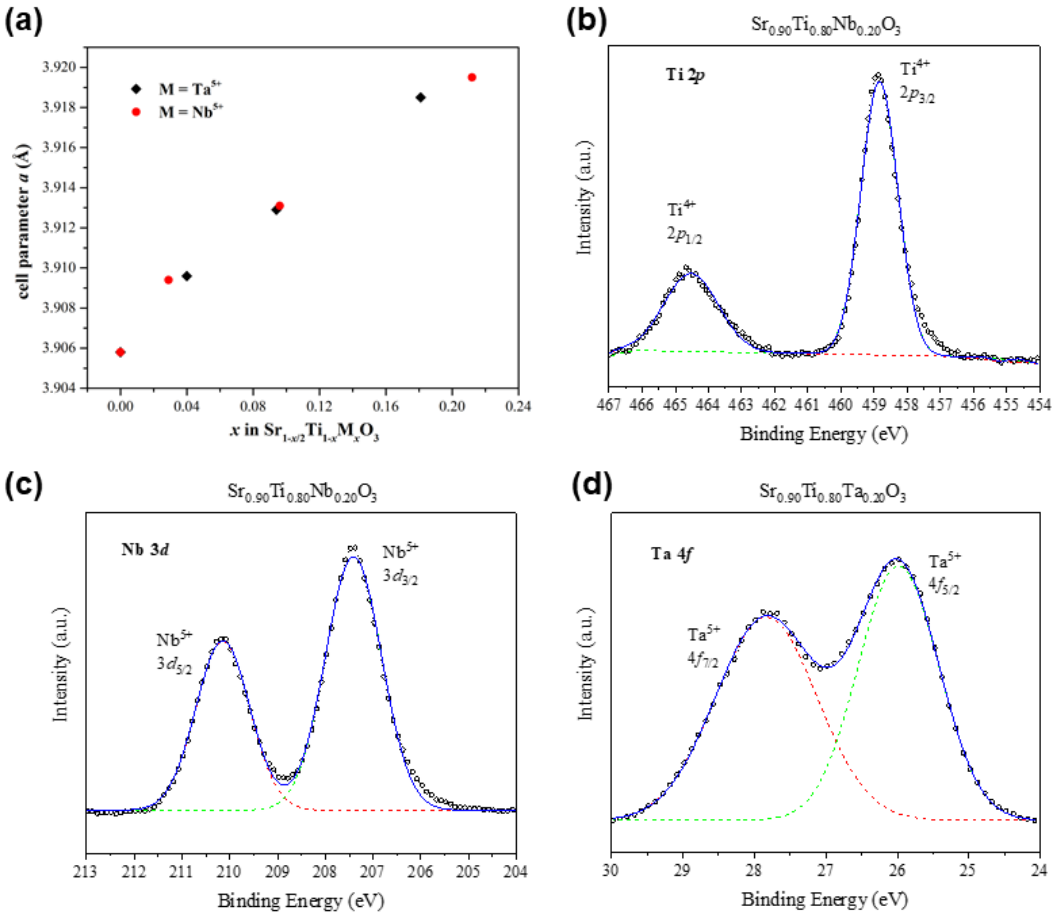

Figure 5.3: (a) A plot of the lattice parameter (a) obtained from neutron diffraction refinements against the metal cation dopant concentration (x) for $Sr_{1-x/2}Ti_{1-x}M_xO_3$ (M = Nb, Ta). Characteristic XPS doublet peaks obtained for (b) Ti 2p and (c) Nb 3d from $Sr_{0.90}Ti_{0.80}Nb_{0.20}O_3$ and (d) Ta 4f from $Sr_{0.90}Ti_{0.80}Nb_{0.20}O_3$.

5.3.3 ^{93}Nb and ^{87}Sr Solid state NMR and Materials Modelling

Both ^{87}Sr and ^{93}Nb solid state MAS NMR were implemented to provide further enlightenment to the local structures evidenced by neutron diffraction and Raman spectroscopy techniques. The high spin ($I = 9/2$) and relatively large quadrupolar couplings ($Q(^{93}\text{Nb}) \sim 32$ x10^{-30} m^2, $Q(^{87}\text{Sr}) \sim 33.5$ x10^{-30} m^2) of both nuclei means that even minor structural distortions will be observable. As well as large second order quadrupolar contributions, previous

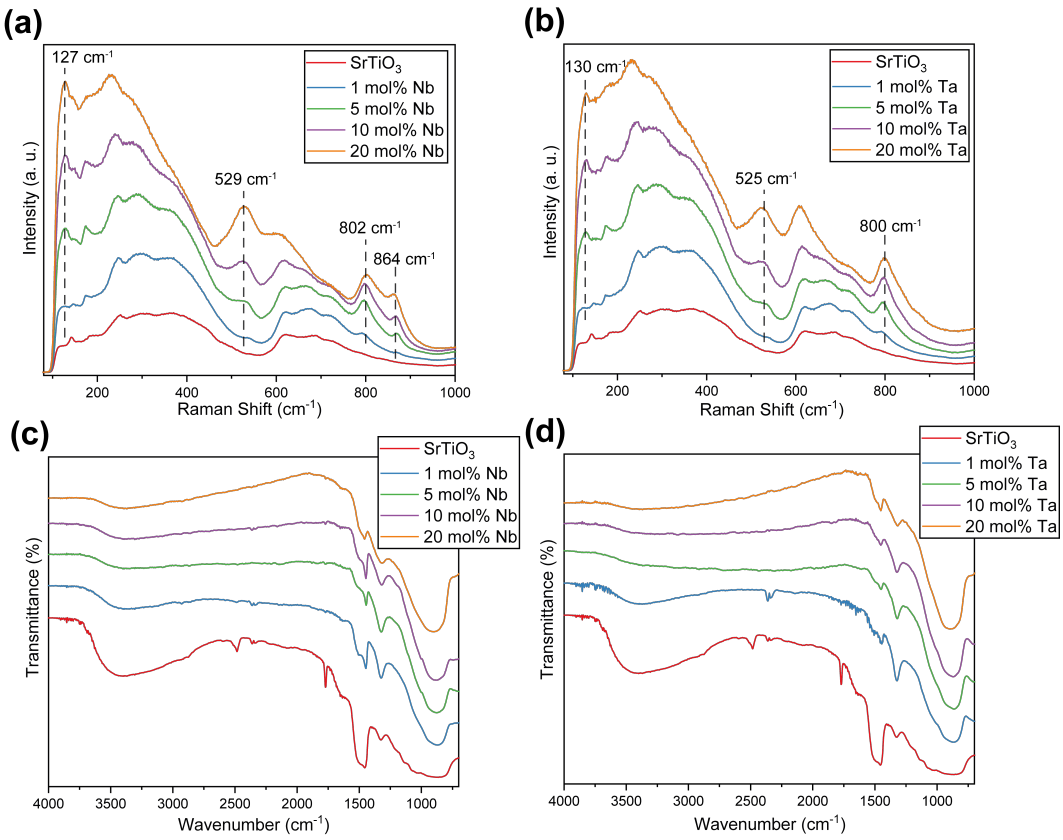

Figure 5.4: Raman spectra of (a) $Sr_{(1-x/2)}Ti_{(1-x)}Nb_xO_3$ and (b) $Sr_{(1-x/2)}Ti_{(1-x)}Ta_xO_3$ for the doping concentrations x = 0, 0.01, 0.05, 0.1 and 0.2. Corresponding FTIR spectra of (c) $Sr_{(1-x/2)}Ti_{(1-x)}Nb_xO_3$ and (d) $Sr_{(1-x/2)}Ti_{(1-x)}Ta_xO_3$.

studies have shown that both nuclei experience comparatively large chemical shift anisotropies (CSA) owing to the electronic environment around each nuclei. [174, 175] Significant contributions from each interaction lead to complex line shapes, which require a multiple field study to obtain meaningful structural parameters because of the opposing dependencies of each interaction with magnetic field strength ($\mathscr{H}_{CSA} \sim B_0$ and $\mathscr{H}_Q \sim 1/B_0$).

Figure 5.5 shows the solid state ^{93}Nb MAS NMR spectra for $Sr_{(1-x/2)}Ti_(1-x)Nb_xO_3$ (x = 0.01, 0.05, 0.10 and 0.20) at three field strengths (B_0 = 14.1, 16.4 and 20.0 T) and the corresponding quadrupolar parameters extracted from spectral deconvolutions and graphical linear fits (Figure 5.6) are presented in Table 5.4. Previous studies by Hanna *et. al.* have correlated the isotropic chemical shift (δ_{iso}) of ^{93}Nb resonances to the Nb coordination

with the shifts between −900 and −1300 ppm found being attributed to six-coordinated Nb^{5+} sites. [176] This further corroborates findings from XPS data. Three distinct Nb environments are identified, pertaining to multiple different Nb structural realisation as determined by CASTEP DFT calculations which are depicted in Figure 5.7. The dominant resonance at 1 mol% Nb doping (site 1), located at $\delta\sim-1040$ ppm exhibits a narrow resonance which systematically decreases in relative intensity as the Nb content increases. This site is attributed to the direct substitution of the Nb^{5+} cation onto the Ti^{4+} B site, whilst preserving the high point symmetry of the cubic ($Pm\bar{3}m$) $SrTiO_3$ structure, as is depicted as the initial structure in Figure 5.7. This resonance also broadens as the doping level increases, alluding to a greater distribution in chemical shifts and therefore local environments. The nature of disorder is confirmed from z-filter 3QMAS experiments shown in Figure 5.8(a-c) by the orientation of this site along the chemical shift axis at each Nb concentration. The larger distribution in chemical shifts is caused by the greater variation not only in the immediate Nb environment but also in the next nearest neighbours surrounding the observed Nb site. However, the chemical shift distribution and featureless lineshape makes simulated quadrupolar lineshape fitting challenging for this site. Therefore, in order to extract accurate readings for δ_{iso} and quadrupolar parameters, graphical linear fits were undertaken using Eqn 2.57. Figure 5.6(a-d) shows the ^{93}Nb graphical linear fit plots of site 1 at Nb concentration levels 1, 5, 10 and 20 mol% and the corresponding extracted parameters are given in Table 5.4. It should be noted that site 1 exhibits an unexpectedly large P_Q ($\sim$4 – 18 MHz), which is consistent with the DFT calculated ^{93}Nb NMR parameter of 9 MHz (see Table 5.5) for the octahedral Nb position. This suggests that the Sr vacancy formation is within close enough proximity (i.e. next nearest neighbour) to the substituted Nb^{5+} cation in order to slightly perturb the pristine cubic $SrTiO_3$ structure.

The site denoted peak 2 located at $\delta \sim -1070$ ppm is present at all Nb concentrations and exhibits a characteristic second order quadrupolar lineshape, particularly noticeable at lower niobium contents where reduced disorder allows for accurate identification of quadrupolar features. From spectral simulations, a constant quadrupolar coupling parameter (C_Q) of $\sim$22 MHz is found across the doping range. However, increasing the Nb content results

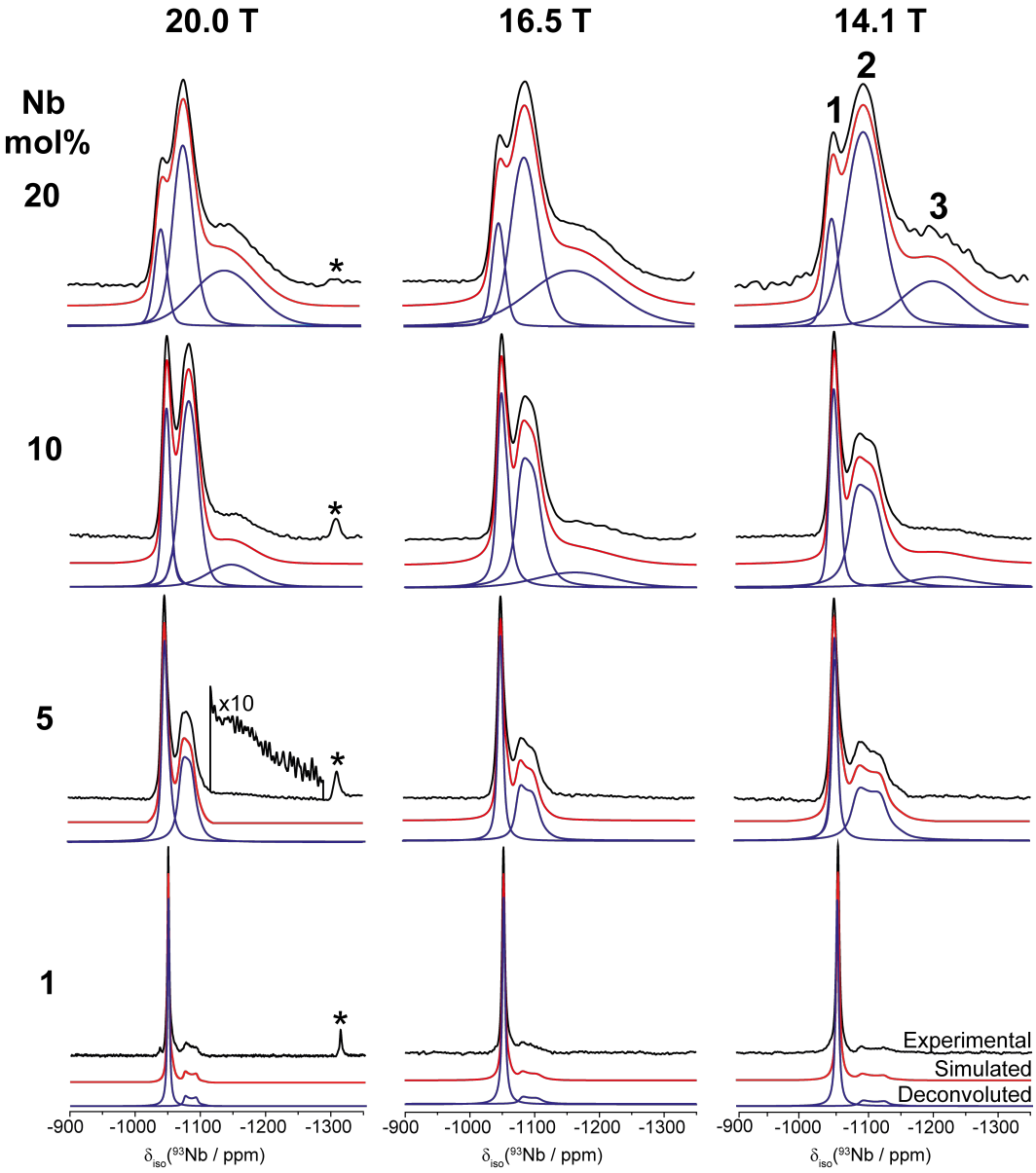

Figure 5.5: Solid state ^{93}Nb MAS NMR spectra (ν_r = 55 kHz) of $Sr_{(1-x/2)}Ti_{(1-x)}Nb_xO_3$ for $x = 0.01$, 0.05, 0.1 and 0.2 acquired at the magnetic fields 14.1, 16.5 and 20.0 T. Spectra are shown together with their simulated spectra (red) and deconvolution (blue), modelled using the parameters found in Table 5.4. Spinning sidebands are indicated with the use of $*$.

in a concomitant increase in the assymetry parameter (η_Q) from ∼0 to 0.25 across the compositional range, indicative of a progressive loss in point symmetry. From materials modelling DFT calculations, this site corresponds to NbO_6 dimers positioned about a Sr vacancy where the Nb^{5+} cations are moved closer towards the vacancy and the O^{2-} anions are distorted away from the vacancy (see Figure 5.7). Calculated NMR parameters for dimers positioned along <100>, <110> and <111> unit cell planes are given in Table 5.5. Comparing the C_Q of each dimer with the experimental value (C_Q∼22 MHz), it can be inferred that Nb dimers do not form along the <100> planes due to the much lower C_Q of 9 MHz. Instead, Nb dimers will form along <110> and <111> unit cell planes. It should also be noted that <110> and <111> (relative energy ∼−326 and −311 meV, respectively) dimers are far more energetically favourable than <100> (relative energy ∼−15 meV). Furthermore, at the 1 mol% Nb dopant level, an η_Q of 0 is observed corresponding to the <111> dimer, indicating the preferential formation of this dimer. At higher Nb concentrations (≥5 mol% Nb), the η_Q increases due to the additional formation of <110> dimers and greater structural disorder (Figure 5.7). Further evidence for the presence of these two dimers is established from $\Delta\delta_{iso}$ parameters which represents the change in isotropic shifts relative to δ_{iso} for an individual Nb^{5+} placed in the cubic SrTiO3 structure (i.e. site 1 in the NMR spectrum). Experimentally, the difference in δ_{iso} between site 1 and 2 is in the range ∼−21-−33 ppm which is within experimental error of the theoretical shifts calculated for <110> or <111> dimers. The ^{93}Nb 2D 3QMAS z-filter spectra shown in Figure 5.8(a-c) indicates that the disorder associated with this site is manifested as a combination of both distributions in chemical shifts and quadrupolar couplings. Moreover, the site loses its quadrupolar features at 20 mol% Nb due to the increased broadening of the lineshape caused by the significant formation of Sr vacancies and complex dimer formation ensuing greater local disorder. This is mirrored by the increased breadth of C_Q distribution (Table 5.4).

The final ^{93}Nb resonance is observed at comparatively lower chemical shifts to sites 1 and 2, but is only seen at Nb inclusions ≥5 mol%, with only a minor amount being observed at 20.0 T at 5 mol% Nb. Given the broad nature of this resonance, linear graphical fit plots (Figure 5.6) were deemed to

Table 5.4: Solid state ^{93}Nb NMR quadrupolar parameters obtained from quadrupolar spectral simulations and graphical linear fits of corresponding ^{93}Nb MAS NMR data.

Nb (mol%)	Peak	δ_{iso} (ppm)	C_Q (MHz)	C_Q dist. (MHz)	η_Q (±0.05)	P_Q (MHz)	R.I. (± 5 %)
1	1	-1040 ± 2	-	-	-	17 ± 2	84
	2	-1072 ± 1	22.2 ± 0.3	1.3 ± 0.5	0.00	22.2 ± 0.3	16
5	1	-1036 ± 3	-	-	-	18 ± 3	51
	2	-1069 ± 1	22.2 ± 0.5	2.6 ± 0.8	0.10	22.0 ± 0.5	49
10	1	-1047 ± 5	-	-	-	4 ± 3	30
	2	-1068 ± 1	22 ± 1	3 ± 1	0.20	22 ± 1	52
	3	-1109 ± 8	-	-	-	40 ± 8	18
20	1	-1037 ± 7	-	-	-	13 ± 5	15
	2	-1063 ± 4	22 ± 2	5 ± 2	0.25	22 ± 2	50
	3	-1077 ± 10	-	-	-	44 ± 10	35

Table 5.5: Theoretical ^{93}Nb NMR parameters and corresponding relative energies obtained from GIPAW CASTEP DFT calculations of different structural realisations for Nb substitutions within the $SrTiO_3$ lattice. The parameter $\Delta\delta_{iso}$ is the isotropic chemical shift relative to that of an individual Nb site within the relaxed cubic $SrTiO_3$ structure.

Arrangement	$\Delta\delta_{iso}$ (ppm)	C_Q (MHz)	η_Q	P_Q (MHz)	Relative Energy (meV)
Individual Nb	0	9	0.01	9	0
100 Nb-vac-Nb	−8	9	0	9	−15
110 Nb-vac-Nb	−18	21	0.08	22	−326
111 Nb-vac-Nb	−16	21	0	21	−311
$cluster_1$	−55	39	0.29	40	
$cluster_1$	−49	35	0.26	36	−314
$cluster_1$	−14	21	0.56	22	
$cluster_2$	−40	47	0.57	49	
$cluster_2$	−16	21	0.27	22	−292
$cluster_2$	−51	43	0.80	47	
$cluster_2$	−2	25	0.33	25	

give a more accurate representation of the quadrupolar parameters. A large quadrupolar coupling of ∼42 MHz is determined, demonstrating a significant loss in point symmetry with this site. This is clear from the 3QMAS z-filter spectrum of $Sr_{0.9}Ti_{0.8}Nb_{0.2}O_3$ (Figure 5.8(c)), indicating a disorder where there is large distribution in both chemical shifts and quadrupolar couplings contributing to the lineshape. Given the substantial formation of A site vacancies, as determined from neutron diffraction and elemental analysis, disordered niobia nanodomains form through a clustering of NbO_6 octahedra (see Figure 5.7). Structural modelling of niobia clustering achieved a distribution of Nb environments all with comparable relative formation energies to the <110> or <111> NbO_6. The corresponding ^{93}Nb theoretical NMR parameters for each of the NbO_6 clusters depicted in Figure 5.7 are given in Table 5.4. Taking the average of the seven clustering Nb environments produces a $\Delta\delta_{iso}$ ∼ -32 ppm which is within experimental error of the 20 mol% Nb experimental data of $\Delta\delta_{iso}$ 40 ppm. Moreover, a calculated average P_Q value of ∼34 MHz is determined, again this is consistent with the experimentally determined values of 40 and 44 MHz.

^{87}Sr solid state MAS NMR spectra for $Sr_{(1-x/2)}Ti_{(1-x)}Nb_xO_3$ and

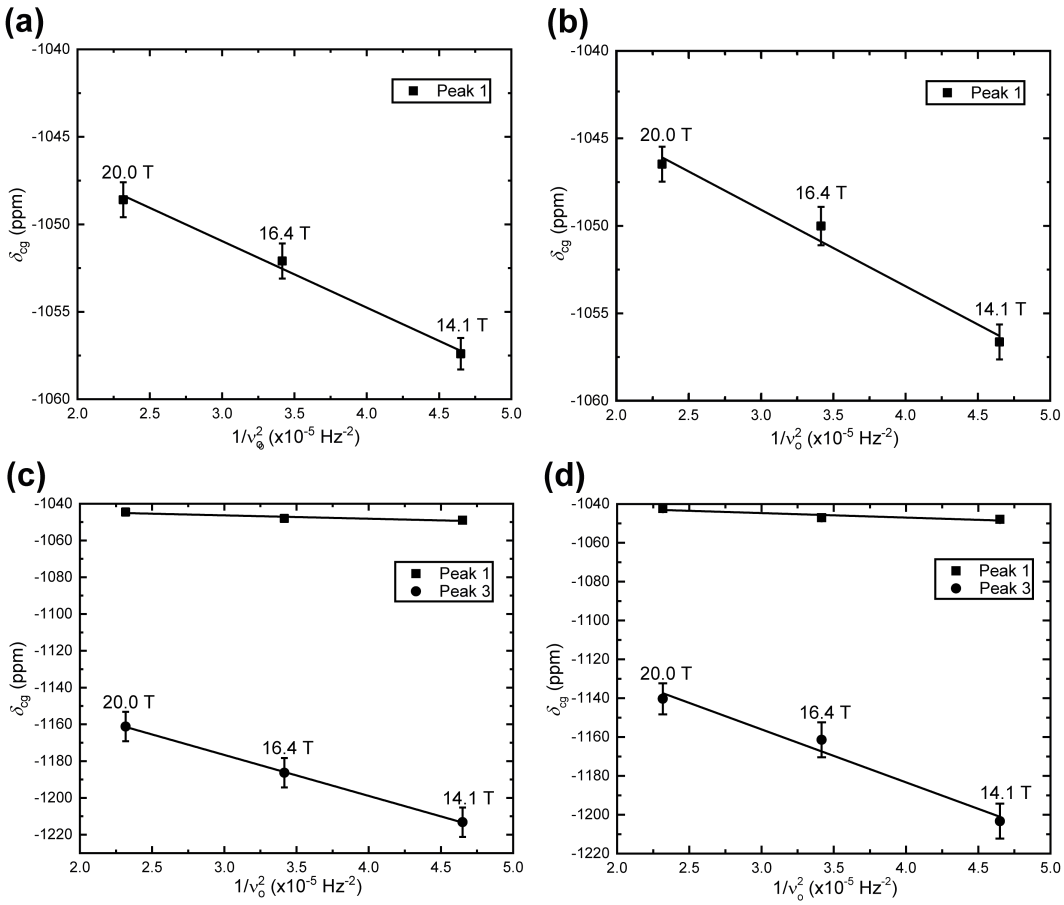

Figure 5.6: Centre of gravity chemical shifts plotted against the $1/\nu_o^2$ for peaks 1 and 3 from the corresponding ^{93}Nb MAS NMR data (see Figure 5.5). The linear fits for Nb concentrations of (a) 1, (b) 5, (c) 10 and (d) 20 mol% are shown and used to calculate the respective isotropic chemical shifts, δ_{iso} and quadrupolar parameter, P_Q.

$Sr_{(1-x/2)}Ti_{(1-x)}Ta_xO_3$ are presented in Figure 5.9 and Figure B.2, respectively, along with the corresponding fit parameters in Table B.1. As anticipated, with no metal dopant, $SrTiO_3$ shows a single narrow gaussian lineshape with minimal quadrupolar coupling; this is consistent with the single highly symmetric Sr environment present in the cubic phase. Doping the structure with either Ta^{5+} or Nb^{5+} leads to large asymetric broadening as a result of local structural distortions associated with B site doping. The low Larmor frequency of the ^{87}Sr nucleus gives rise to little separation between resonances making it difficult to resolve spectra. However, acquiring data at the lower magnetic field of

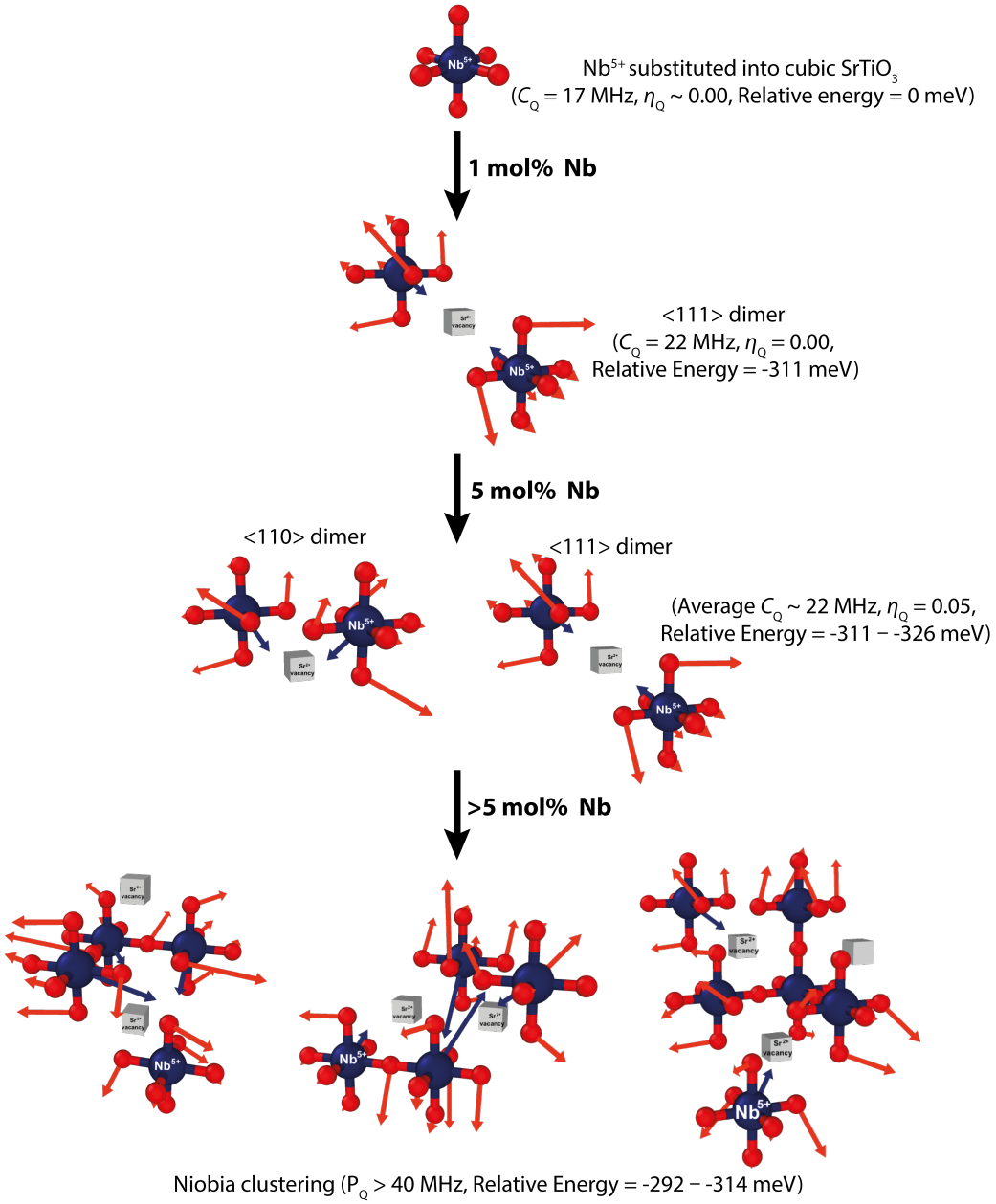

Figure 5.7: Structural realisations determined from CASTEP DFT calculations for different Nb substitutions in $SrTiO_3$ showing: an 'isolated' Nb cubic $SrTiO_3$ lattice, the formation of NbO_6 dimers along the <110> and <111> planes about a Sr vacancy and a clustering of NbO_6 after significant Sr vacancy formation. The movement of atoms relative to the parent $SrTiO_3$ cubic structure are represented by arrows and the calculated NMR parameters and relative energies for each structure are given. Arrows indicate the relative movement of Nb^{5+} and O^{2-} ions compared to the parent $SrTiO_3$ cubic lattice.

11.7 T has allowed for the identification of two distinct Sr sites present in all samples. Both sites exhibit a characteristic Czjzek lineshape, commonly observed for disordered quadrupolar nuclei. [18] The narrower site represents Sr in the octahedral environment as seen for undoped $SrTiO_3$, although the site broadens as the amount of Nb or Ta increases caused by the greater variation in neighbouring octahedra. The broader second Sr site shows considerably more disorder eluding to a Sr nucleus which is nearby to multiple Sr (A) site vacancies. Two approaches were undertaken in extracting quadrupolar parameters; both through quadrupolar simulations (Figure 5.9 and B.2) and graphical linear fits (Figure B.3). As can be seen from Table B.1, discernable differences are encountered between parameters determined via the two methods, largely caused by considerable CSA interaction contributions to the lineshape. As a result, an over compensation of quadrupolar coupling constants occur when fitting the lineshape using the QuadFit simulation package. A systematic decrease in δ_{iso} for both sites is observed as the amount of Nb/Ta is increased, eluding to the expansion of the lattice as indicated from diffraction based methods. This is also complemented by an increase in P_Q due to the loss in point symmetry of both the Sr sites as was also evident in ^{93}Nb MAS NMR data.

5.3.4 Thermoelectric Performance

Measurements of the electrical resistivity, Seebeck coefficient, power factor, thermal conductivity and the resultant ZT values with respect to temperature are all shown in Figure 5.10(a-d). The electrical conductivity of the parent undoped $SrTiO_3$ is too small to measure and therefore it is not discussed hereinafter. The electrical resistivity values of all samples show a similar temperature dependence with a broad dip around 450 K, relating to a semiconductor-like nature at low temperatures which suggests that some of the excess electrons tend to be localized and can be thermally excited. This phenomenon is caused by the distortion of local structures dependent on the Nb/Ta dopant concentrations as was shown from solid state NMR and materials modelling. When the temperature exceeds 450 K, the electron concentration is temperature independent because at this temperature, excess electrons

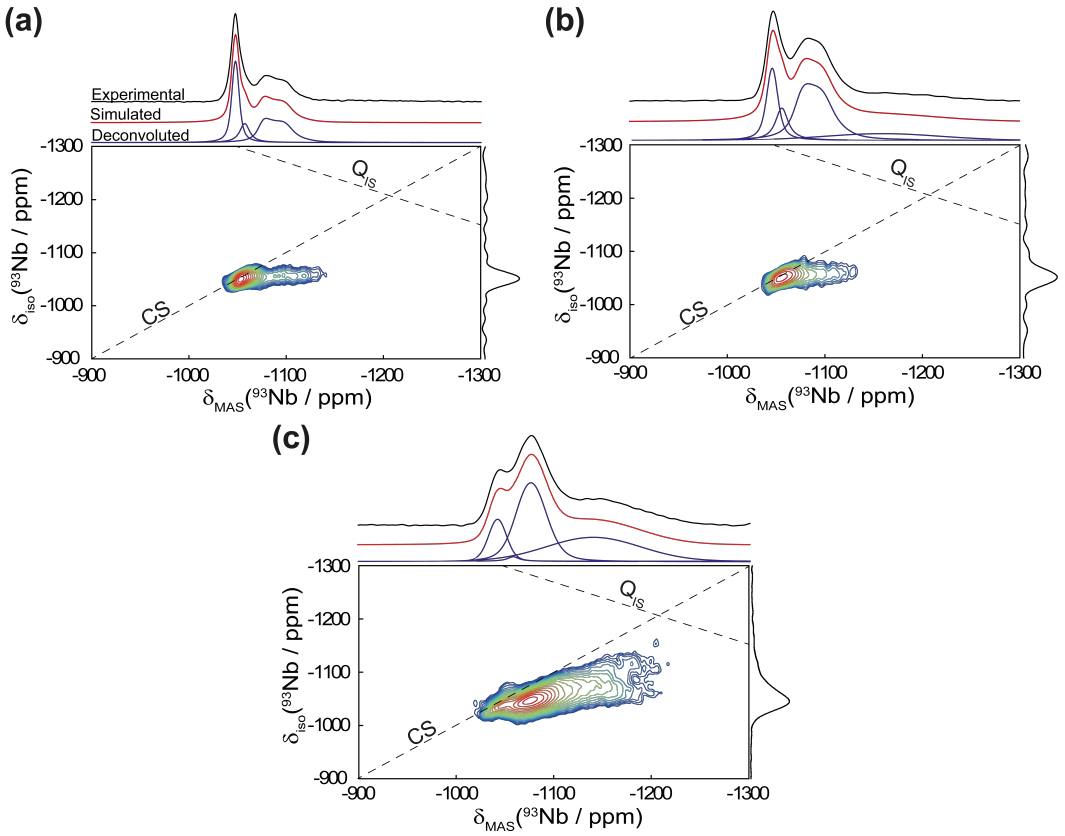

Figure 5.8: Solid state ^{93}Nb 2D z-filter multiple quantum MAS NMR spectra of $Sr_{(1-x/2)}Ti_{(1-x)}Nb_xO_3$ for Nb concentrations (a) 5 mol% (B_0 = 14.1 T, ν_r = 38 kHz), (b) 10 mol% (B_0 = 14.1 T, ν_r = 38 kHz) and (c) 20 mol% (B_0 = 20.0 T, ν_r = 55 kHz).

are in an excited state. As a result, the electrical resistivity increases for all doping levels. In the high temperature regime (>500 K), the electrical resistivity decreases with increasing Nb doping level, in particular at 20 mol% Nb, due to significant formation of <110> and <111> NbO_6 dimers resulting in minor distortions from the original cubic $SrTiO_3$ structure, generating a greater overlap of electronic orbitals which has been suggested previously by Lu *et. al.*. [143] The high electrical conductivity of 20 mol% Nb sample is maintained up to 960 K. In contrast, the electrical conductivity decreases with increasing Ta content despite formation of a similar amount of A site vacancies. It is possible that the formation of TaO_6 dimers distorts the lattice differently to NbO_6 which could result in lesser overlap of electronic orbitals. Furthermore, for 20 mol% Ta incorporation, the value is beyond the detectable limit and

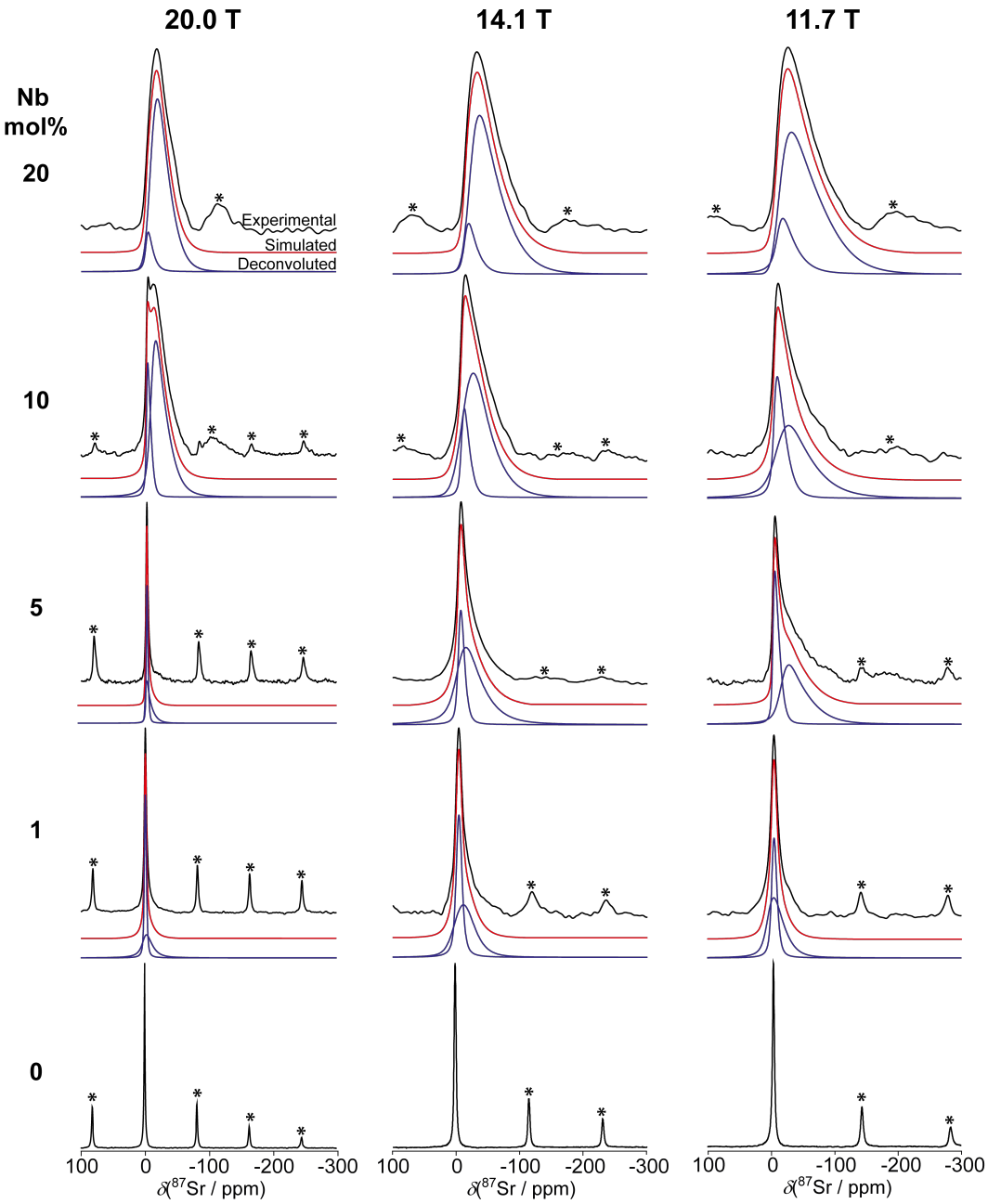

Figure 5.9: Solid state ^{87}Sr MAS NMR spectra (ν_r = 3 kHz) of $Sr_{(1-x/2)}Ti_{(1-x)}Nb_xO_3$ for x = 0.00, 0.01, 0.05, 0.10 and 0.20. Spectra are shown at three field strengths, 20.0, 14.1 and 11.7 T and are shown together with their simulated spectra (red) and deconvolution (blue)(see Table B.1). Spinning sidebands are indicated using an $*$.

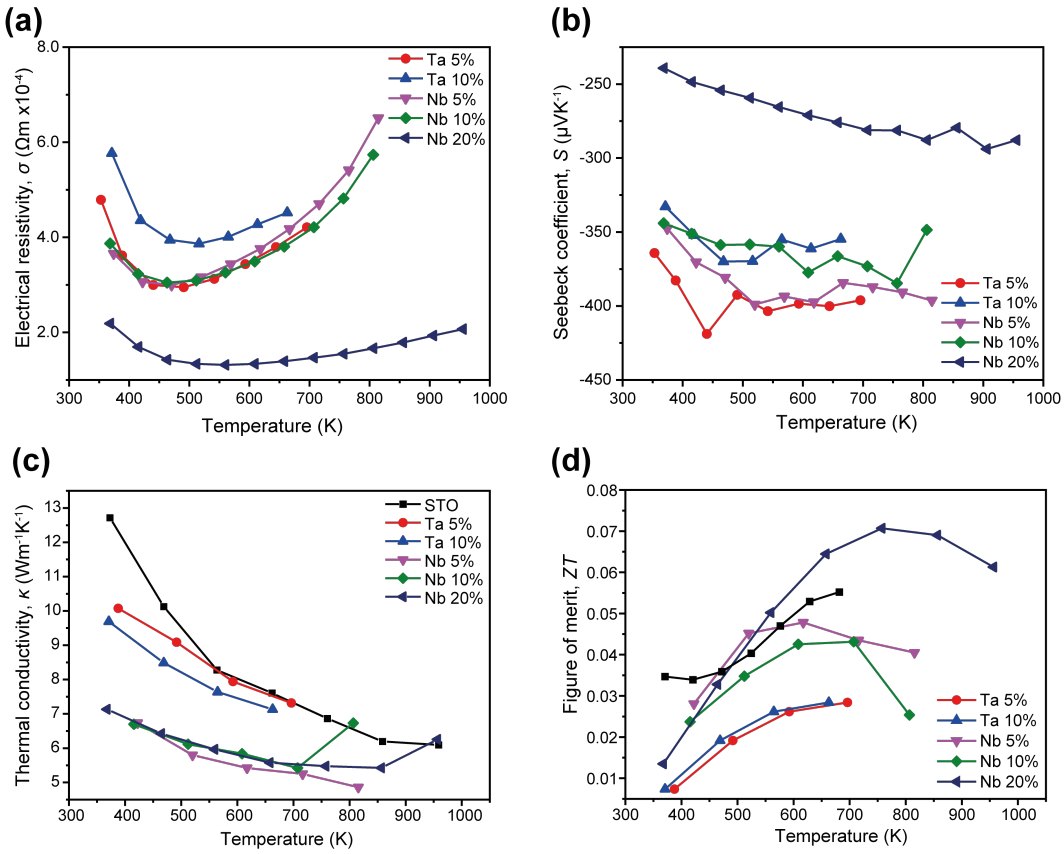

Figure 5.10: Temperature dependence of the (a) electrical resistivity (σ), (b) Seebeck coefficient (S), (c) thermal conductivity (κ) and (d) the thermoelectric figure of merit (ZT) across the temperature range 350-950 K. Pellets for measurements were formed by the spark plasma sintering method.

therefore no measurement was recorded. Given the dependence of the Seebeck coefficient (S) on the carrier concentration, the electrical conductivity temperature dependences dominate the trends observed for S in Nb doped systems; where 20 mol% Nb exhibits the highest coefficient and 5 mol% Nb the lowest (Figure 5.10(b)). However, for the Ta doped samples the electrical conductivity does not seem to dominate S because of the heavier effective mass. The S of these A-site deficient Nb or Ta doped $SrTiO_3$ ceramics are higher than those found in other stoichiometric carrier-doped $SrTiO_3$ materials found in the literature. [121, 143]

The temperature dependence of the thermal conductivity for $SrTiO_3$ and its doped counterparts are shown in Figure 5.10(c). The Ta doped sam-

ples exhibit a higher thermal conductivity close to the values achieved by $SrTiO_3$, whereas the Nb doped analogues demonstrate a much lower thermal conductivity. However, there is no obvious thermal conductivity dependency on the Nb/Ta concentration. The formation of niobia nanoclusters within the $Sr_{1-x/2}Ti_{1-x}Nb_xO_3$ structure could hinder the thermal transport properties acting as stoppages, resulting in lower thermal conductivities. Combining thermal conductivity progressions with electrical conductivities and Seebeck coefficients for each material, the calculated change in ZT with respect to temperature is presented in Figure 5.10(d). Nb doped $SrTiO_3$ samples show a far greater ZT factor than their Ta doped counterparts due to significantly lower thermal conductivities, despite generally comparable electrical resistivity and Seebeck coefficients. Furthermore, $Sr_{0.9}Ti_{0.8}Nb_{0.2}O_3$ achieved the highest ZT value of 0.07 obtained at 757 K.

5.4 Conclusions

Multiple techniques have been employed to extensively explore structural changes contributing to the enhanced thermoelectric performance for Nb and Ta B site dopants in $SrTiO_3$. Initially implementing neutron diffraction and elemental analysis, an A site deficiency in the doped analogues was confirmed despite maintaining the long range periodicity of the cubic ($Pm\bar{3}m$) lattice. XPS data has shown that Nb^{5+} and Ta^{5+} do not reduce and remain in the 5+ oxidation state, signifying the need to balance the excess cationic charge through the formation of Sr vacancies. Furthermore, the appearance of first order forbidden modes in the Raman spectra of doped structures also provided evidence for localised structural distortions.

Due to its sensitivity to local distortions, both ^{93}Nb and ^{87}Sr solid state MAS NMR showed the formation of multiple distinct Nb and Sr sites. Three sites were observed in ^{93}Nb spectra alluding to Nb directly substituted into the octahedral Ti B site, two distorted NbO_6 octahedra along the <110> and <111> planes about a Sr vacancy and a clustering of Sr vacancies forming disordered nanodomains of niobia. These structural realizations were confirmed using theoretical ^{93}Nb NMR parameters determined from structural models. It was also found that Nb dimers preferentially form along a <111> unit cell

plane. From ^{87}Sr spectra, two sites are observed showing Sr in a relatively undistorted position surrounded by TiO_6 octahedra and Sr sites next to A site vacancies causing significant disorder.

Large improvements in ZT were seen for doping analogues of $SrTiO_3$ with Nb doped samples, which achieved much higher ZT values than their Ta counterparts due to comparatively lower thermal conductivities. The formation of disordered niobia nanodomains is thought to hinder the thermal transport properties of Nb doped samples, whereas for Ta doped samples clustering may not occur. Improvements in the electrical conductivities were attributed to the formation of distorted MO_6 (M = Nb, Ta) <110> and <111> dimers allowing for a greater overlap of the electronic orbitals. The highest ZT factor obtained was 0.07 at 757 K for the sample $Sr_{0.9}Ti_{0.8}Nb_{0.2}O_3$ which, at high temperatures, outperformed all other dopant levels discussed here due to its significantly lower electrical resistivity.

Chapter 6

Structural Elucidation of Metal Cation (Bi^{3+}, Na^{+} and K^{+}) Incorporated $Cs_2AgInCl_6$ Double Perovskite Nanocrystals

This Chapter has been published as Parth Vashishtha, Benjamin E. Griffith, Albert P. Bartok, Yanan Fang, Ankit Jaiswal, Gautam V. Nutan, Tim White, and John V. Hanna. Elucidation of Structural and Optical Properties of Metal Cation (Na^{+}, K^{+}, and Bi^{3+}) Incorporated $Cs_2AgInCl_6$ Double Perovskite Nanocrystals, *Journal of Materials Chemistry A*, **10**, 3562-3578, 2022. This paper is co-first authored by Parth Vashishtha and Benjamin E. Griffith.

6.1 Introduction

6.1.1 Background

Alternative materials for optoelectronic and solar cell applications are of significant interest due to the time consuming and costly nature of currently produced semiconductor materials. Therefore, many perovskite materials have been looked to as potentially cheaper alternatives. Lead-based perovskite nanocrystals have shown immense promise in recent years due to their tunable narrow emission widths, high photo luminescence quantum yield

and due to the presence of passivating organic ligands, structural stability. [177–180] Lead containing perovksites of interest include $CsPbX_3$ (X = Cl, Br, I), $FAPbX_3$ (FA=formamidinium), $MAPbX_3$ (MA=methyl ammonium) and $Cs_{0.05}(FA_{0.83}MA_{0.17})_{0.95}PbX_3$ which have demonstrated emission throughout the visible range (400 - 760 nm). [181–183] However, these promising halide perovskites contain the toxic element lead which limits the commercial viability due to possible negative environmental impacts. [184] Therefore, the development of lead-free alternatives is of paramount importance and has been extensive; however the performance of these materials is inferior to the lead based counterparts. [185, 186] One such alternative is $CsSnX_3$ (X = Cl, Br, I), although, due to the tendency of Sn^{2+} to oxidise and turn into Sn^{4+}, these systems are highly unstable. [187] As a result, these nanocrystals contain many structural defects which lower the quantum yield. [188] Further developments of lead-free alternatives have led to the inclusion of many other metal cations such as Sb, Bi and Cu, although device integration of these materials has yet to be fully explored. [189–191]

Another focus of research for lead-free alternatives is pure inorganic double perovskites such as the direct band gap $Cs_2AgInCl_6$ and indirect band gap $Cs_2AgBiCl_6$, that have high structural stability under ambient conditions. [192–194] Due to the indirect band gap in $Cs_2AgBiCl_6$ caused by the cell symmetry, the double perovskite produces a low photo luminescence quantum yield. [195, 196] However, the direct band gap analogue $Cs_2AgInCl_6$ has shown greater promise for application in optoelectronics. [197, 198] The primitive unit cell is shown in Figure 6.1, where Cs^+, Ag^+ and In^{3+} occupy the A, B'(I) and B"(III) sites, respectively. The bulk structure of $Cs_2AgInCl_6$ was first reported in 2017 by Volonakis *et al.* and since then Locardi *et al.* has reported the synthesis of quantum confined $Cs_2AgInCl_6$ colliodal nanocrystals using a hot-injection route. [194,197] A cubic $Fm\bar{3}m$ structure was determined for both the nanocrystal and its bulk counterpart. Doping the cubic structure with bismuth has indicated a reduction in surface defects which leads to an increase in the material's broad band emission. [192,193] The broad band emission is attributed to the Jahn-teller distortion of $[AgCl_6]^{5-}$ in the excited state or due to the presence of self-trapped excitons. [192,199] The inclusion of Bi^{3+} has led to a suite of different metal dopants on both B'(I) and B"(III) sites,

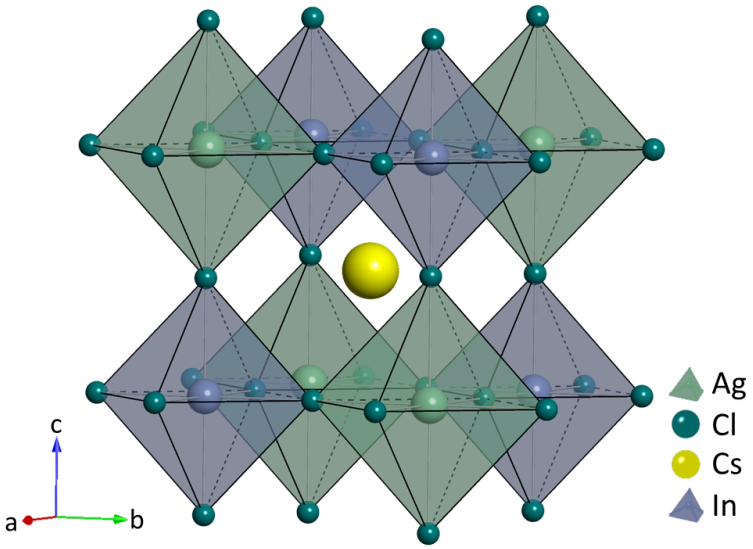

Figure 6.1: Primitive unit cell structure of bulk $Cs_2AgBiCl_6$ showing Cs^+, Ag^+ and In^{3+} located on A, B'(I) and B"(III) sites, respectively.

such as Ga^+, Na^+, Cr^{3+}, Ce^{3+} and Sb^{3+} in attempts to improve the photo luminescence properties. [200–203] Notably, Na^+ doping in $Cs_2AgInCl_6$:Bi bulk thin-films and nanocrystals have led to increases of up to 85 and 22%, respectively. [201, 202] However, a structural understanding is still required in order to precisely tune the optical properties upon metal cation inclusion.

6.1.2 NMR Studies on Perovskite Nanocrystals and Double Perovskites

In recent years, solid state NMR has shown great functionality in determining the local structure and surface speciation of perovskite NCs. Despite this, the main focus of studies has been on lead based systems, in particular $CsPbX_3$ (X = Cl, Br and I) based nanocrystals. Initial studies by Brown *et al.* and Vashishtha *et al.* utilised solid state NMR extensively to study $CsPbBr_3$ where the passivating ligands octylphosphonic acid, oleylamine and oleic acid were used to stabilized the nanocrystal structure. [179,181] With the use of ^{133}Cs it was possible to observe distinct core, sub-surface and surface layers of the nanocrystal. In addition to this, the use of ^{1}H, ^{13}C and ^{31}P two dimensional double quantum measurements demonstrated the ligand surface

bonding. Over the past two years, many studies have adopted solid state NMR as a primary characterisation tool for lead-based nanocrystals to analyse the effects of metal cation doping, halide mixing, particle sizes and the usage of different ligands. [204–207]

The use of solid state NMR to analyse lead-free double perovskite structures has thus far been limited. However, Karmakar *et al.* has employed the use of ^{133}Cs, ^{209}Bi and ^{115}In NMR to characterise the bulk structures of $Cs_2AgIn_xBi_{1-x}Cl_6$:Sb and correlated them to the photoluminescent performance. [208] A more recent study by Karmakar *et al.* has shown the use of solid state NMR in identifying vancancies and structural dynamics of Cs_2SnX_6 (X = Cl, Br and I) and mixed halide systems. [209] Kubicki *et al.* has also recently used ^{133}Cs NMR to look at the effects of halide mixing and phase segregation phenomena in bulk Cs_2AgBiX_6 (X = Cl, Br and I) and the correlation to material performance. [210] The inclusion of I in large quantities (>3mol%) causes impure phases to form which are detrimental to the PL emission intensity and charge carrier lifetimes. Whereas there has been a few studies focusing on the bulk structures, there has yet to be any reports which utilise solid state NMR to characterise the double perovskite nanocrystal counterparts.

Here, structural elucidation of $Cs_2AgInCl_6$ nanocrystals with inclusion of the metal cations Bi^{3+}, Na^+ and K^+, synthesised using a colloidal hot-injection route have been investigated. Initially, structural properties of $Cs_2AgIn_xBi_{1-x}Cl_6$ (x = 0 - 1) are looked at as a baseline material. Following this, a systematic characterisation of B'(I) site foreign cation inclusion for series with the nominal formula $Cs_2Ag_{1-x}Na_xInCl_6$:Bi and $Cs_2Ag_{1-x}K_xInCl_6$:Bi (x = 0 - 1) was carried out. Both ^{23}Na and ^{133}Cs solid state NMR have been utlised to examine the short range localised structures. This is combined with XRD methods pertaining to the long range periodicity to provide a complete structural picture.

6.2 Experimental

6.2.1 Synthesis

The reagents cesium carbonate (ReagentPlus, 99%), oleic acid (90%), silver acetate (99.99% trace metals basis), indium(III) acetate (99.99% trace metals basis), bismuth(III) acetate (≥99.99% trace metals basis), sodium acetate (99.0% Aldrich), potassium acetate (99.0%, Aldrich), diphenyl ether (ReagentPlus, 99%), benzoyl chloride (ReagentPlus, ≥99%), oleylamine (Olam, technical grade, 70%), and hexane (anhydrous, 95%) were all purchased from Sigma-Aldrich.

A 0.5 M Cesium-oleate solution was synthesised by mixing cesium carbonate (4075 mg) with OAc (50 mL) loaded in a 3-neck round-bottom flask under inert atmosphere. The reaction mixture was degassed under vacuum at 100 ^{o}C for about half an hour followed by heating in nitrogen atmosphere at 150 ^{o}C for 3 hours, until the solution becomes clear. The prepared solution was cooled to room temperature, then stored in a vial and kept inside a nitrogen-filled glovebox.

For the synthesis of $Cs_2AgInCl_6$ samples, Ag(ac) (0.96 mmol), $In(ac)_3$ (1 mmol), 16 mL of diphenyl ether, 4 mL of the Cs-oleate solution, and 2 mL of Olam were loaded in a three-neck flask and degassed under vacuum for 60 min at 80 ^{o}C. Simultaneously, 2 mL of diphenyl ether was dried under vacuum at 50 ^{o}C. Subsequently, the system was flushed under N_2, the temperature was slowly increased to 115 ^{o}C, and, at this temperature, 800 μL of Bz-Cl (6.89 mmol), mixed with 2 mL of degassed DPE, was swiftly injected into the flask. The reaction was quenched after 5 s by cooling with an ice-water bath. Bi-doped $Cs_2AgInCl_6$ samples were prepared using the same protocol, but loading the starting reaction mixture with 1 mmol of $In(ac)_3$ and $Bi(ac)_3$ salts in complementary amounts according to the desired percentages. Six different Bi-doped samples were prepared by using the Bi precursor in 0.5, 10, 25, 50, 75 and 90%.

For the synthesis of $Cs_2Ag_{1-x}A_xInCl_6$ (A = Na, K), the total amount of Na(ac)/K(ac) and Ag(ac) must be 0.96 mmol. Na(ac) or K(ac) (x mmol; x = 0, 0.2, 0.4, 0.6, 0.8, and 1), Ag(ac) (1-x mmol), $In(ac)_3$ (1 mmol), $Bi(ac)_3$ (0.05 mmol) 16 mL of diphenyl ether, 4 mL of the Cs-oleate solution, and 2 mL of

Olam were loaded in a three-neck flask and degassed under vacuum for 60 min at 80 ^{o}C. Simultaneously, 2 mL of diphenyl ether was dried under vacuum at 50 ^{o}C. Subsequently, the system was flushed under N_2, the temperature was slowly increased to 115 ^{o}C, and, at this temperature, 800 μL of Bz-Cl (6.89 mmol), mixed with 2 mL of degassed DPE, was swiftly injected into the flask. The reaction was quenched after 5 s by cooling with an ice-water bath.

All nanocrystals were purified using the same method. The growth solution was first centrifuged at 10,000 rpm for 10 min. The supernatant was discarded and required amounts of the solids were dispersed in 4 mL of anhydrous hexane for optical characterization, whereas remaining solids were stored under inert atmosphere for other characterizations.

6.2.2 XRD

XRD measurement was carried out using a PANalytical X-ray diffractometer equipped with a 1.8 kW Cu Kα X-ray tube and operating at 45 kV and 30 mA. The diffraction patterns were collected in air at room temperature using Bragg-Brentano geometry. All XRD samples were prepared by drop casting a concentrated solution on a zero diffraction silicon holder.

6.2.3 Transmission Electron Microscopy

A JEOL 2100F was utilized for the HR-TEM and energy dispersive X-ray spectroscopy (EDXS) measurements at an accelerating voltage of 200 kV and beam current of 146 μA. Samples were prepared by dispersing nanocrystals in hexane solvent followed by sonication for 1 min and collection on Cu-200 mesh on a forvar grid.

6.2.4 UV-Vis and PL Measurements

Samples for optical measurements were prepared by diluting the purified solution in 2.5 mL hexane in 1 cm path length quartz cuvettes. A Cary 5000 UV-vis-NIR spectrophotometer and a Cary Eclipse spectrophotometer (slit width = 1 nm, λex = 365 nm) were used. PLQY measurements were conducted using

an Ocean Optics QEPro spectrometer and a HAMAMATSU Quantaurus-QY Plus UV–NIR absolute PL quantum yield spectrometer.

6.2.5 Solid State NMR

All ^{133}Cs MAS NMR data were acquired at 14.1 and 9.4 T using Bruker Avance II-600 (Larmor frequency $\nu_o = 78.72$ MHz) and Bruker Avance III-400 (Larmor frequency $\nu_o = 52.47$ MHz) spectrometers, respectively, and Bruker 4 mm HX probes operating at a MAS frequency of 12 kHz. At each field, the pulse time calibration was undertaken using solid CsCl where a non-selective ('solution') $\pi/2$ pulse time of 12 μs was measured corresponding to a selective ('solids') $\pi/2$ pulse time 3 μs for the $I = 7/2$ nucleus (calculated using $\tau_{solids} = \tau_{solution}/(I + 1/2)$). All single pulse ^{133}Cs MAS NMR data were measured using a $\pi/6$ pulse of 1 μs and a recycle delay of 300 s. Each spectrum was simulated using the DMFit programme. [8] The solid CsCl sample was also used as a secondary chemical shift reference ($\delta_{iso} = 223.2$ ppm) against the 0.1 M $CsNO_3$ solution IUPAC primary reference ($\delta_{iso} = 0.0$ ppm). [9] The corresponding ^{133}Cs T_1 measurements were performed using the saturation-recovery pulse technique which utilised a saturation pulse train of 300 $\pi/2$ pulses of 3 μs duration, a 1 μs delay between pulses, and a variable τ delay spanning a 0.01 - 1600 s range.

The ^{23}Na MAS NMR data from the $Cs_2Na_xAg_{1-x}In_xCl_6$:Bi ($x = 0.2$ - 1) nanocrystal series were acquired at 14.1 and 9.4 T using Bruker Avance II-600 (Larmor frequency $\nu_o = 158.76$ MHz) and Bruker Avance III-400 (Larmor frequency $\nu_o = 105.81$ MHz) spectrometers, respectively, and Bruker 4 mm HX probes operating at a MAS frequency of 12 kHz. The pulse time calibration at each field was undertaken using solid NaCl where a non-selective ('solution') $\pi/2$ pulse time of 4 μs was measured corresponding to a selective ('solids') $\pi/2$ pulse time of 2 μs for the $I = 3/2$ nucleus (calculated using $\tau_{solids} = \tau_{solution}/(I + 1/2)$). All single pulse ^{23}Na MAS NMR data were measured using a selective $\pi/4$ pulse of 1 μs and a recycle delay of 30 s. The solid NaCl sample was also used as a secondary chemical shift reference ($\delta_{iso} = 7.0$ ppm) against the 0.1 M NaCl solution IUPAC primary reference ($\delta_{iso} = 0.0$ ppm). [9] Accompanying ^{23}Na T_1 measurements were performed using the saturation-recovery pulse technique which utilised a saturation pulse train of 300 $\pi/2$ pulses of 2 μs

duration, a 1 μs delay between pulses, and a variable τ delay spanning a 0.001 - 50 s range.

The ^{39}K MAS NMR data from the $Cs_2K_xAg_{1-x}In_xCl_6$:Bi (x = 0 - 1) nanocrystal series were acquired at 20.0 T using a Bruker Avance HD-850 (Larmor frequency ν_o = 39.67 MHz) spectrometer and a Bruker 4 mm HX probe operating at a MAS frequency of 12 kHz. Pulse time and chemical shift calibration were undertaken using solid KBr, where a non-selective ('solution') $\pi/2$ pulse time of 10 μs was measured corresponding to a selective ('solids') $\pi/2$ pulse time 5 μs for the $I = 3/2$ nucleus, and where the secondary solid KBr shift (δ_{iso} = 55.1 ppm) is standardised against the 0.1 M KCl solution IUPAC primary reference (δ_{iso} = 0.0 ppm). [9] All ^{39}K MAS NMR data was acquired using a rotor-synchronised Hahn-echo ($\pi/2$-τ-π-τ-acq.) experiment using a $\pi/2/\pi$ pulse pair of 5 and 10 μs, respectively, a recycle delay of 5 s, and a rotor-synchronised τ delay of 83.33 μs. The ^{39}K T_1 measurements were performed using the saturation-recovery pulse technique which utilised a saturation pulse train of 300 $\pi/2$ pulses of 5 μs duration, a 10 μs delay between pulses, and a variable τ delay spanning a 0.001 - 10 s range.

6.2.6 DFT Calculations and Materials Modelling

Ab initio calculations were performed using the CASTEP density functional theory (DFT) package which employs planewave basis set and ultrasoft pseudopotentials. [163] Each input file was generated using the cif2cell package [164] and the Atomic Simulation Environment. [165] The regularised SCAN exchange-correlation functional [166] has been used throughout with consistent, on-the-fly ultrasoft pseudopotential generation. [167] SCAN has been shown to accurately describe the electronic and geometrical structure of perovskite materials. [168] Geometry optimisation were performed on all systems, with atomic position and lattice parameter relaxation being permitted; in these adjustments the 'FINE' basis precision setting in CASTEP and k-point grids that correspond to cubic supercells of approximately 20 $\AA$ lattice parameters were used. All NMR parameters were calculated using the GIPAW method using a 600 eV planewave cut-off for all compounds. [170,171] The accuracy of the calculated chemical shieldings against the experimentally measured chem-

ical shifts was established by comparison with NMR parameters from previously measured reference compounds. As demonstrated by the ^{133}Cs chemical shift calibration in Figure C.1(a), an excellent linear relationship for the $CsCl/CsClO_4/Cs_2SO_4$ series was established; however, for the perovskite materials studied in this work it was necessary to include an additional shift to align the experimental and computed values. Hence, a small recalibration using the experimental and calculated NMR parameters from the $Cs_2AgInCl_6$ and $Cs_2AgBiCl_6$ systems was introduced (see Figure C.1(a)) A similar ^{39}K chemical shift calibration was undertaken using the $KF/KCl/KBr/KI/KClO_4/KIO_4$ series as shown in Figure C.1(b). [211]

To model the effect of K^+ cation incorporation on the structural speciation and order, and the implications for the interpretation of the measured ^{133}Cs and ^{39}K MAS NMR data, a constrained variation of the Ab Initio Random Structure Search (AIRSS) method was introduced to generate ensembles of perturbed initial configurations by applying random rotations on the $[InCl_6]^{3-}$ and $[BiCl_6]^{3-}$ octahedra. [212] This was followed by subsequent geometry relaxation. This method has been successfully used to discover novel phases of materials. [213] Atomic structures were visualised using the AtomEye package. [214]

6.3 Results and Discussion

6.3.1 Bi^{3+} Incorporated $Cs_2AgInCl_6$Nanocrystals

Initially, double perovskite nanocrystals with the stoichiometric formula $Cs_2AgIn_xBi_{1-x}Cl_6$ (x = 0 - 1) were investigated as baseline materials to optimise Bi incorporation. X-ray diffraction patterns shown in Figure 6.2(a) confirms the formation of the cubic $Cs_2AgInCl_6$ perovskite phase. As expected from Vegard's law, the inclusion of Bi^{3+} expands the lattice, thus inducing a monotonic shift to lower angles in observed reflections (Figure 6.2(a) and 6.2(b)). [215] From TEM micrographs of $Cs_2AgIn_{0.9}Bi_{0.1}Cl_6$ and $Cs_2AgIn_{0.5}Bi_{0.5}Cl_6$ shown in Figures 6.2(d) and, a cubic morphology is observed for these nanocrystals with average particle size diameters of ∼17 nm and ∼15 nm, respectively. High resolution TEM micrographs in Figure 6.2(e)

show resolved lattice fringes and the fast Fourier transform (FFT) of cubic nanocrystals corresponding to the (022) crystal plane of the perovskite structure. Overall, the nanocrystals crystal structure is validated by the matching of FFT and lattice spacing d with the (022) plane of the XRD plane.

Figures 6.2(f) and 6.2(g) illustrate the absorption and PL characteristics from the $Cs_2AgIn_xBi_{1-x}Cl_6$ ($x = 0$ - 1) suite of nanocrystals, with the observed excitonic peak at 367 - 368 nm observed in all absorption spectra resulting from direct s-p transitions as has been previously reported. [192,216] However, pure $Cs_2AgInCl_6$ exhibits a weak absorption at ∼430 nm along with a strong absorption at <300 nm caused by parity-forbidden direct transitions, characteristic in $Cs_2AgInCl_6$ systems. [189] In contrast, pure $Cs_2AgBiCl_6$ nanocrystals display a very weak emission at ∼715 nm, which is attributed to an indirect band gap transition associated with this system (Figure 6.2(f)). [195] Pure $Cs_2AgInCl_6$ shows a blue emission near 400 nm, however the inclusion of Bi^{3+} even at low dopant levels of 0.5 mol% induces an orange emission at ∼581 nm which systematically becomes more red-shifted with increasing Bi^{3+} content. It was measured that the nanocrystal with 90 mol% In/10 mol% Bi content achieved the highest PLQY of 8 %, whereas the 99.5 mol% In/0.5 mol% Bi exhibited the second highest PLQY of 6 %. Whilst it has been shown that dopant level inclusion of Bi^{3+} improves the performance, it should be noted that the overall crystal structure and lattice parameters characterising the $Cs_2AgInCl_6$ system are not perturbed. Based on these characteristics, doping levels of Bi^{3+} have been adopted for further compositional engineering of nanocrystal systems. Previous reports have suggested that improvements in optical properties from Bi^{3+} incorporation could be due to improved short range crystalline order and excitonic localisation, therefore ^{133}Cs solid state NMR has been adopted to probe the short range structural effects upon Bi^{3+} inclusion. [193, 217]

^{133}Cs solid state MAS NMR data characterising $Cs_2AgIn_xBi_{1-x}Cl_6$ ($x =$ 0 - 1) nanocrystals are presented in Figures 6.3(a-c), Figure C.2 and Table C.1. The spectra of $Cs_2AgInCl_6$ nanocrystal systems acquired here exhibit similarities to data recently reported for their bulk counterparts by Karmakar *et al.*; these assignments were adopted to assign the Cs speciation in these nanocrystalline materials. [208] Each Cs^+ cation in the $Cs_2AgIn_xBi_{1-x}Cl_6$ structure is located in a cubooctahedral environment surrounded by four $[AgCl_6]^{5-}$ octahe-

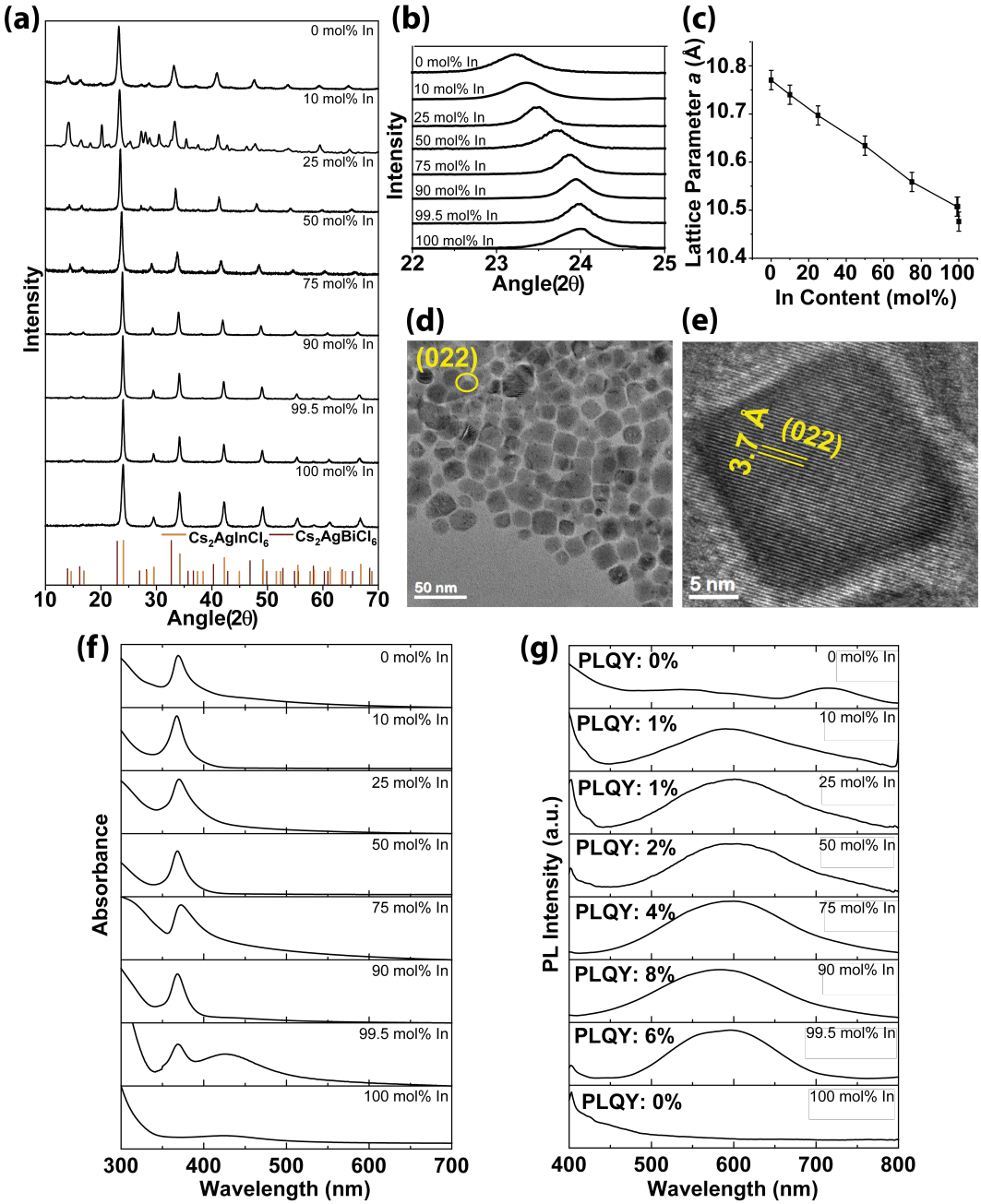

Figure 6.2: Characterisation data of $Cs_2AgIn_xBi_{1-x}Cl_6$ x = 0 - 1) nanocrystal series including, (a) X-ray diffraction data, (b) an expansion of the (022) reflection showing the peak shift as a function of In composition, (c) the changing lattice parameter (a) with In content, (d) a TEM micrographs of $Cs_2AgIn_{0.90}Bi_{0.10}Cl_6$ nanocrystals, (e) a high-resolution TEM image depicting the lattice fringes and fast Fourier transform (FFT), (f) absorption and (g) photoluminescence (PL) spectra of $Cs_2AgIn_xBi_{1-x}Cl_6$ nanocrystals dispersed in hexane.

dra, alternating with $[InCl_6]^{3-}$ or $[BiCl_6]^{3-}$ octahedra. The narrow ^{133}Cs resonances characterising these data reflect the high point symmetry defining the Cs^+ nearest-neighbour environments. In Figure 6.3(a), the single resonances observed at $\delta\sim$128 ppm and 82 ppm for the pure $Cs_2AgInCl_6$ and $Cs_2AgBiCl_6$ end members are assigned to Cs surrounded by four $[InCl_6]^{3-}$ octahedra and four $[BiCl_6]^{3-}$ octahedra on the B"(III) site, respectively. Throughout the intermediate compositional range (x = 0.1 - 0.995), a series of $[InCl_6]^{3-}$ and $[BiCl_6]^{3-}$ octahedral combinations are seen surrounding the Cs^+ centre. At 50 mol% Bi^{3+} substitution, five discrete Cs position are observed. While the resonances at $\delta\sim$87 and 118 ppm are shifted derivatives of the $Cs_2AgBiCl_6$ and $Cs_2AgInCl_6$ end members, the three remaining ^{133}Cs resonances at $\delta\sim$109, 102 and 96 are attributed to the four $[InCl_6]^{3-}$ octahedra being substituted by one, two and three $[BiCl_6]^{3-}$ octahedra, respectively. The measured ^{133}Cs chemical shift are directly influenced by the varying quantities of Bi^{3+} substituents on the In position, i.e. as the Bi^{3+} concentration increases the ^{133}Cs chemical shift becomes increasingly deshielded, moving linearly to lower ppm due to the decreasing electron density at the Cs^+ positions governed by the concomitant lattice expansion. This corroborates the structural evolution observed from XRD in Figure 6.2. It should be noted that the ^{133}Cs resonance linewidths presented in Figures 6.3(a) and C.2 broaden significantly at intermediate Bi^{3+} contents due to the increased local structural disorder induced by the variation in next-nearest neighbour environments.

The mobility of each Cs environment was investigated through the measurement of ^{133}Cs spin-lattice (T_1) relaxation times, shown in Figures 6.3(b) and 6.3(c) as a function of In^{3+}. The insignificant quadrupolar nature of the I = 7/2 ^{133}Cs nucleus is reflected in ^{133}Cs MAS spectra (Figures C.2 and Table C.1) through the abscence of chemical shift variation with change of external field, and the apparent increase in ^{133}Cs linewidths collectively indicate the ^{133}Cs linewidths are dominated by chemical shift dispersion. Furthermore, the $1/B_0$ dependance of measured T_1 values suggests the logitudinal relaxation is governed by a dipolar relaxation mechanism, which reflects the dynamics and mobility characterising each Cs^+ cation position. It is important to note that the resonances assigned to $Cs_2AgBiCl_6$ and $Cs_2AgInCl_6$ end members in Bi^{3+} or In^{3+} rich compositions exhibit ^{133}Cs T_1 values which are 2-3 orders of mag-

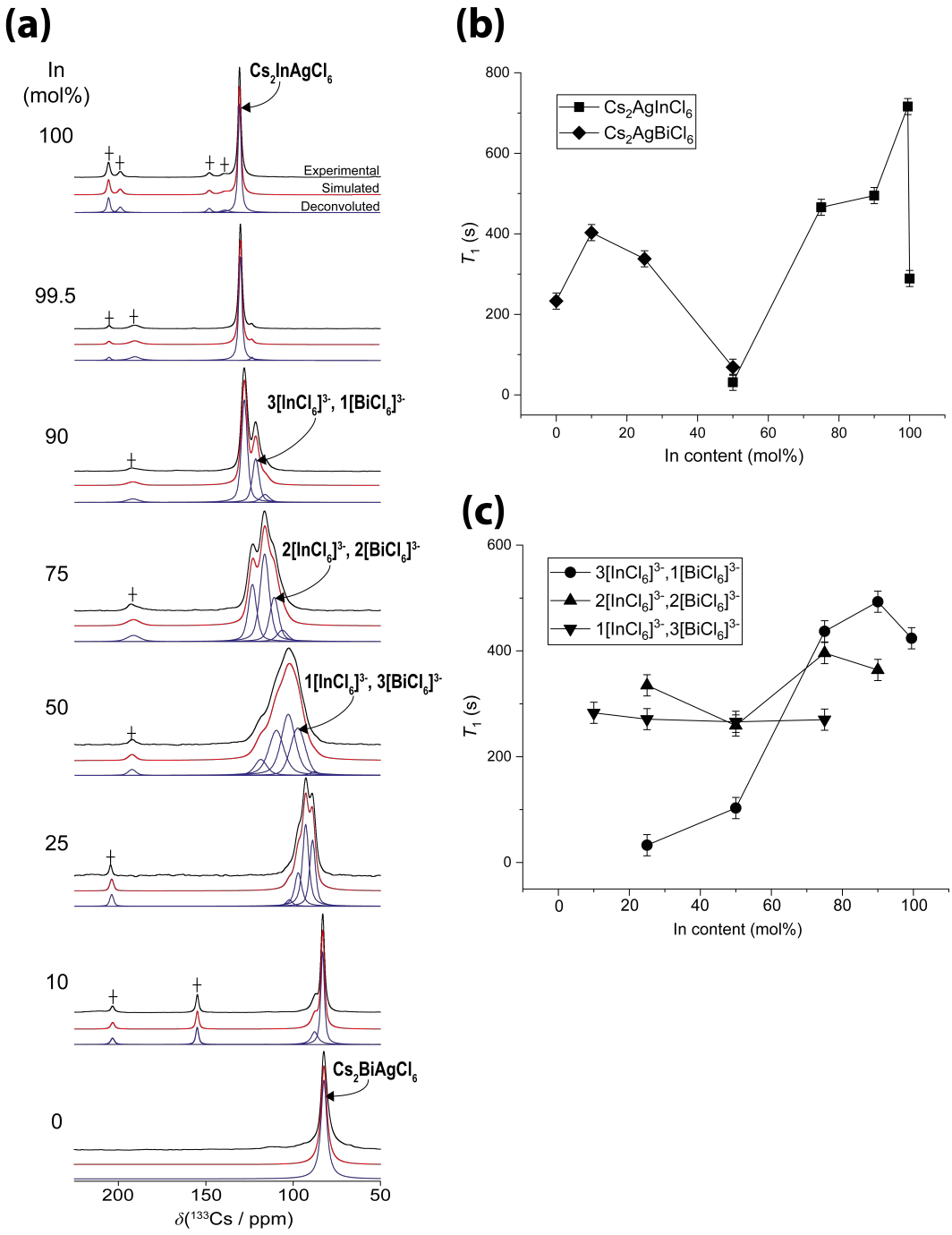

Figure 6.3: ^{133}Cs MAS NMR data (B_0 = 14.1 T, ν_r = 12 kHz) for the $Cs_2AgIn_xBi_{1-x}Cl_6$ (x = 0 - 1) nanocrystal series showing (a) the deconvolutions, spectral simulations and resonance assignments indicating the different octahedral substitutions comprising each Cs environment (impurities are indicated by '†'). (b) and (c) The progression of T_1 relaxation times for each Cs environment determined via saturation recovery experiments.

nitude greater than those across the intermediate compositional range. This demonstrates the far greater Cs^+ mobility facilitated by the structural disorder which dominates the mid-range compositions. The larger ^{133}Cs T_1 values observed for $Cs_2AgBiCl_6$ and $Cs_2AgInCl_6$ resonances at dopant levels of In^{3+} and Bi^{3+} implies that a passivation effect takes place within these structures. In particular, dopant level incorporation of ∼0.5 mol% Bi^{3+} is required to stimulate an increase in T_1 from ∼290 to 720 s, thus highlighting the efficiency of this species in passivating structural defects and vacancies and restricting Cs^+ mobility. This effect is correlated with the strong orange emission at ∼580 nm which dominates the PL properties up to a composition of 99.5 mol% In^{3+} and subsequently disappears at 100 mol%.

The ^{133}Cs T_1 data spanning the intermediate compositional range (i.e. 25 - 75 mol% In^{3+}) suggests that the Cs speciation is dominated by structural disorder defined by the relative nearest-neighbour octahedral substitutions surrounding each Cs^+ cation position (i.e. $1[InCl_6]^{3-}$,$3[BiCl_6]^{3-}$, $2[InCl_6]^{3-}$,$2[BiCl_6]^{3-}$ and $3[InCl_6]^{3-}$,$1[BiCl_6]^{3-}$). Figure 6.3(c) indicates that the Cs^+ mobility and response to compositional change is inhomogeneous and complex; these data show the ^{133}Cs T_1 of the $1[InCl_6]^{3-}$,$3[BiCl_6]^{3-}$ environment to be invariant over the compositional range, the $2[InCl_6]^{3-}$,$2[BiCl_6]^{3-}$ environment varies marginally with composition, whilst the $3[InCl_6]^{3-}$,$1[BiCl_6]^{3-}$ environment exhibits a significant T_1 variation of 460 s over the 25 - 90 mol% In^{3+} range. Like the passivation phenomenon demonstrated in the 99.5 mol% In^{3+} preparation, this behaviour suggests that Cs^+ cation mobility is actively reduced (i.e. T_1s increase) with optimum passivation occuring when Bi^{3+} concentrations are substantially reduced.

6.3.2 Na^+ Incorporated $Cs_2AgInCl_6$:Bi Nanocrystals

Since the inclusion of dopant levels (∼0.5 mol%) Bi^{3+} into the nominal $Cs_2AgInCl_6$ structure optimises the photophysical performance of the nanocrystals without inducing major structural alterations, this strategy is adopted for further exploration of B'(I) site substituted double perovskite nanocrystals. Recent reports have indicated that Na^+ cation incorporation improves the PLQY in bulk preparations of double perovskite systems, [201]

hence a logical progression has been made to investigate nanocrystals with the stoichiometric formula $Cs_2Na_xAg_{1-x}InCl_6$:Bi (x = 0.2 - 1). Figures 6.4(a) and 6.4(b) show the XRD patterns for $Cs_2AgInCl_6$:Bi and $Cs_2NaInCl_6$:Bi nanocrystals where both exhibit a cubic $Fm\bar{3}m$ space group, whereas Figure 6.4(c) shows the corresponding expansion of the lattice parameter a with respect Na^+ content. The TEM micrographs of $Cs_2Na_{0.4}Ag_{0.6}InCl_6$:Bi nanocrystals is shown in Figure 6.4(d), exhibiting a cubic morphology with an average particle diameter of 14 nm. The associated high-resolution TEM image in Figure 6.4(e) indicates a lattice spacing of 3.7 $\mathring{A}$, corresponding to the (022) lattice plane which closely matches that found from XRD data.

Figure 6.5(a) and 6.5(b) show ^{23}Na and ^{133}Cs solid state MAS NMR data, respectively, for the $Cs_2Na_xAg_{1-x}InCl_6$:Bi (x = 0.2 - 1) series of nanocrystals. The ^{23}Na MAS NMR spectra exhibit a single narrow resonance which is assigned to the single highly symmetric octahedral $[NaCl_6]^{5-}$ environment in the cubic structure, as was highlighted from the XRD study. This narrow resonance progressively becomes more shielded, shifting from $\delta\sim$2.0 to 2.5 ppm, whilst increasing Na^+ inclusion. Similarly, a single narrow resonance is observed in the corresponding ^{133}Cs MAS NMR spectra, providing further verification of the highly symmetric cubooctahedral $[CsCl_6]^{5-}$ environments. However, this ^{133}Cs shifts from $\delta\sim$128 to 121 ppm, thus becoming more deshielded with increasing Na^+ content. The opposing shift trends between ^{23}Na and ^{133}Cs NMR data correlate with the emerging disorder in nearest-neighbour octahedra upon increasing Na^+ substitution, which subsequently induces a lattice expansion. From the ^{23}Na and ^{133}Cs T_1 relaxation time behaviour presented in Figures 6.5(c) and 6.5(d), respectively, there exists $\sim$2-3 orders of magnitude difference between each nucleus' respective relaxation time. This indicates a far greater comparative mobility of Na^+ cations within this structure which is consistent with its much smaller ionic radius ($\sim$1.02 $\mathring{A}$ for Na^+, $\sim$1.67 $\mathring{A}$ for Cs^+) and propensity to avoid chemical/covalent interaction. Despite ^{23}Na nuclei possessing a much larger quadrupole moment than ^{133}Cs, the high cubic point symmetry ensures that the average ^{23}Na quadrupole parameters are negligible, as is evident from the invariant chemical shifts with change in B_0 (Table C.3). Therefore, it can be inferred that a dipolar relaxation mechanism is also dominant for this nucleus. Within experimental error,

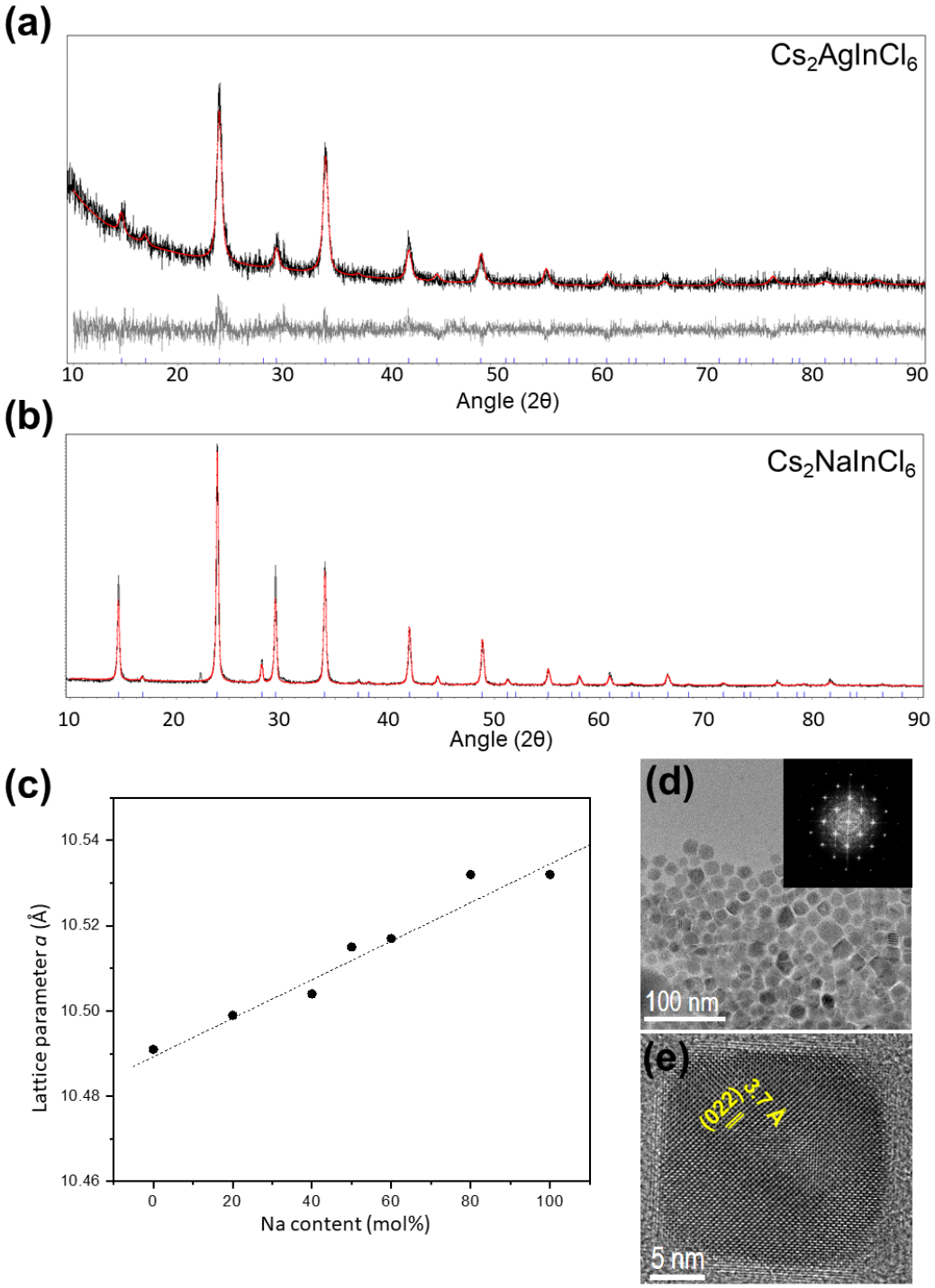

Figure 6.4: X-ray diffraction patterns of (a) $Cs_2AgInCl_6$:Bi and (b) $Cs_2NaInCl_6$:Bi nanocrystals. (c) The corresponding change in lattice parameter a with Na content as determined via XRD refinement. (d) TEM micrographs of $Cs_2Na_{0.4}Ag_{0.6}InCl_6$:Bi nanocrystals with FFT and (e) a high-resolution TEM image showing the lattice fringes of the cubic nanocrystal.

the ^{23}Na T_1 times appear largely invariant over the entire compositional range. In contrast, the ^{133}Cs T_1 times are invariant up to 60 mol% Na, however the >60 mol% Na range exhibits a significant decrease in T_1 of ∼300 s. This is attributed to an increase in the Cs vacancy formation that is characterised by more rapid Cs^+ cation mobility and reduced T_1 relaxation times. A blue shift in the absorption peak from ∼370 nm to 324 nm is observed as the Na^+ content increases.

Figure 6.6 shows the absorption and PL data obtained from the $Cs_2Na_xAg_{1-x}InCl_6$:Bi (x = 0.2 - 1) nanocrystal series. It has been established that Na does not contribute to the valence band maxima or conduction band minima of the double perovskite band gap, [197] hence only minor changes in the PL characteristics are observed with changing Na content (Figure 6.6(b)). From Figure 6.6(b) it is evident that Na inclusion enhances the emission of these nanocrystals; this phenomenon has been previously reported for the bulk perovskite. [201] Luo *et al.* revealed that the increase in PLQY is due to the break in inversion symmetry of $Cs_2AgInCl_6$ by formation of $NaCl_6$ octahedra, allowing electron-hole overlap and subsequent radiative recombination. [201] The emission mechanism is attributed to previously reported self-trapped exciton (STE) phenomena originating from Jahn-Teller distortion of $[AgCl_6]^{5-}$ octahedra in the excited state. [201, 202] Figure 6.6(b) also shows that the 100 mol% Na sample is not emissive, whereas at 60 mol% Na and 40 mol% Na concentrations, the highest PLQY values of 21% and 16% are achieved, respectively. A decrease in the PLQY for nanocrystal compositions >60 mol% Na is attributed to an onset of significant Cs vacancy formation and greater Cs^+ mobility which directly correlates with a significant decrease in the ^{133}Cs T_1 values of ∼300 s.

6.3.3 K^+ Incorporated $Cs_2AgInCl_6$:Bi Nanocrystals

Although Na^+ incorporation into the double perovskite system improves the optical and structural properties, other B'(I) possible cation substitutions can be realised to create alloys. Due to its compatible ionic radius, the K^+ cation can be considered as a viable candidate for incorporation into the $Cs_2AgInCl_6$:Bi framework on the Ag^+ position. A K^+-substituted composi-

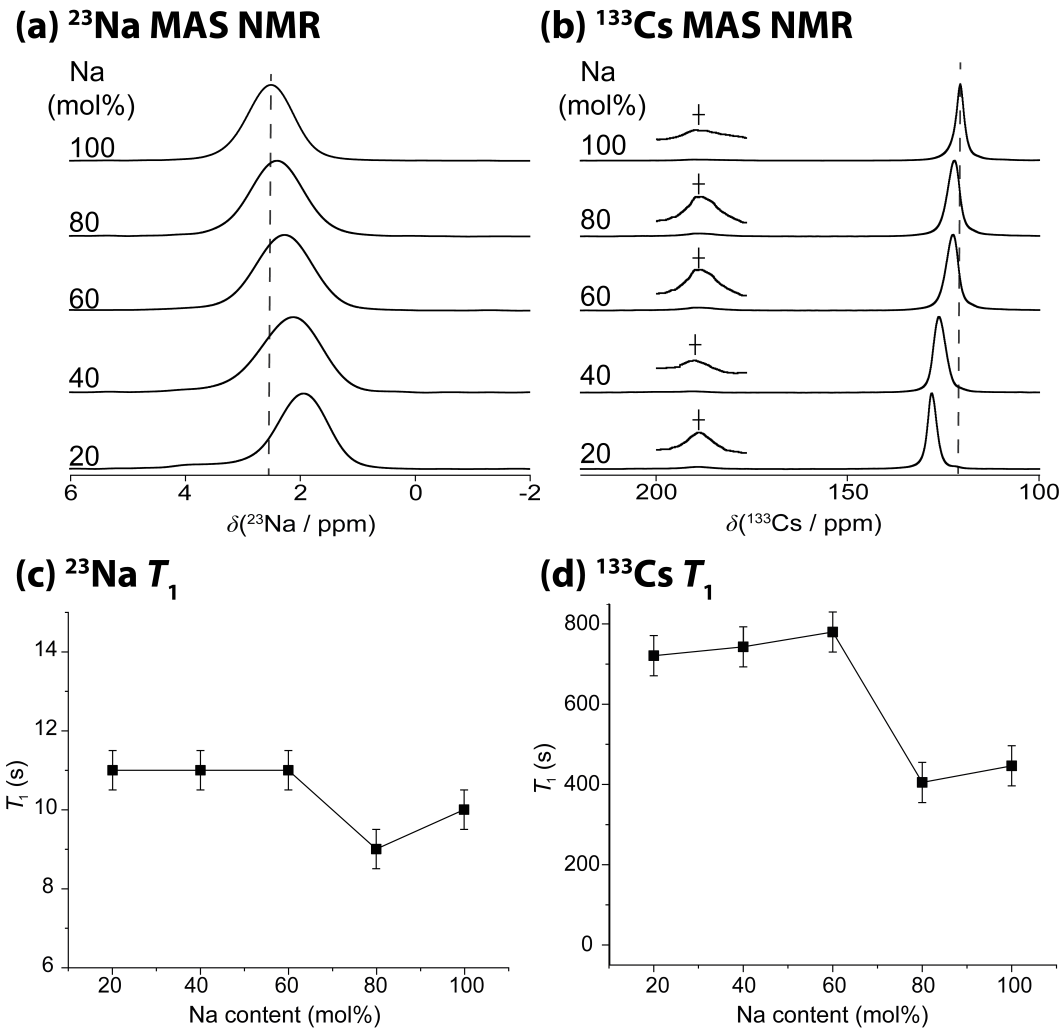

Figure 6.5: (a) ^{23}Na and (b) ^{133}Cs solid state MAS NMR spectra (B_0 = 14.1 T, ν_r = 12 kHz) for the $Cs_2Na_xAg_{1-x}InCl_6$:Bi (x = 0.2 - 1) nanocrystal series. (c) ^{23}Na T_1 data, and (d) ^{133}Cs T_1 data acquired using the saturation-recovery technique. Impurities are marked by a '†'.

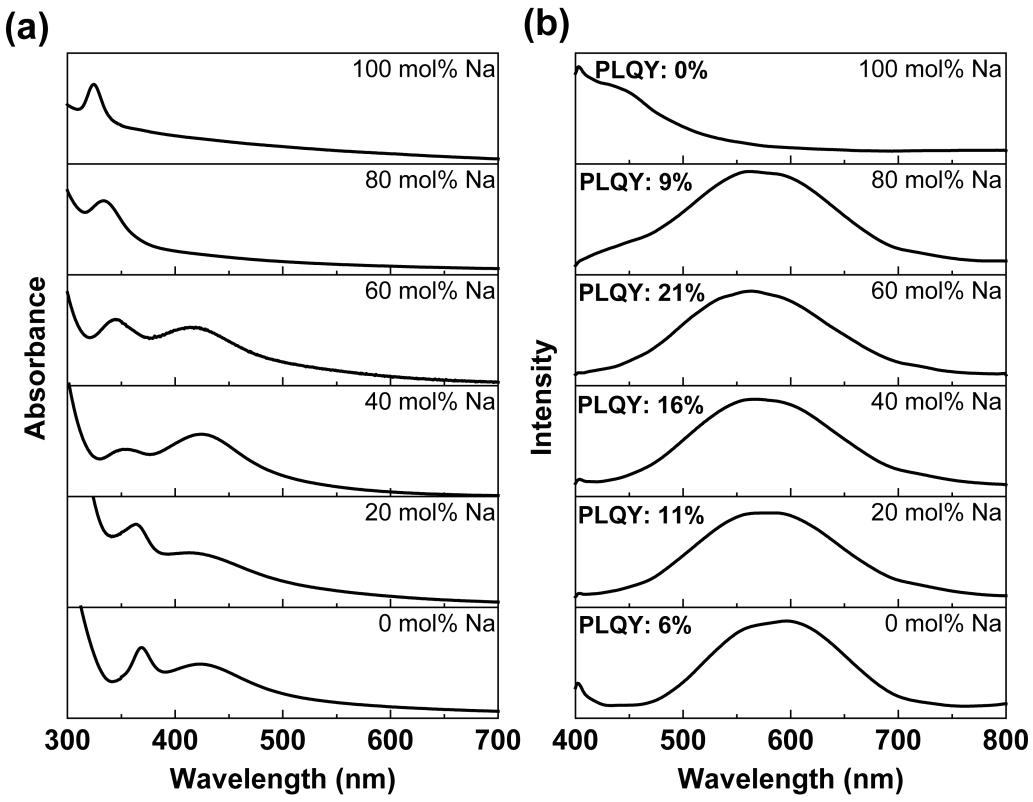

Figure 6.6: (a) Absorption and (b) photoluminescence (PL) data for the $Cs_2Na_xAg_{1-x}InCl_6$:Bi (x = 0.2 - 1) nanocrystal series suspended in hexane. The achieved photoluminescence quantum yields (PLQY) are indicated in each spectrum.

tional series of the form of $Cs_2K_xAg_{1-x}InCl_6$:Bi (x = 0.2 - 1) was synthesized with a stoichiometry mirroring the Na^+ series. In comparison to the $Cs_2In_xBi_{1-x}AgCl_6$ (x = 0 - 1) and the $Cs_2Na_xAg_{1-x}InCl_6$:Bi (x = 0.2 - 1) nanocrystal series which represent direct substitutional systems, the powder XRD data of Figure 6.7 and the ^{133}Cs and ^{39}K MAS NMR data of Figure 6.8 demonstrate that the $Cs_2K_xAg_{1-x}InCl_6$:Bi (x = 0.2 - 1) system is more complex where the formation of other similar phases competes for components of the K^+ inventory.

The powder XRD data of Figures 6.7(a) characterising the $Cs_2K_xAg_{1-x}InCl_6$:Bi (x = 0.2 - 1) nanocrystal series are refined as two similar crystal types consisting of a cubic perovskite phase (space group $Fm\bar{3}m$) and a monoclinic phase (space group C12/cl) similar to the CsK_2BiCl_6 structure type. [218,219] The appearance of reflections at 29^o and 34^o 2θ in the 40 mol% K (see Figure 6.7(a)) indicate the onset of a monoclinic phase; this phase assumes greater prominence with increasing mol% K^+ (particularly at the 80 and 100 mol% K^+ levels). Furthermore, Figure 6.7(b) also shows that the cubic perovskite $Fm\bar{3}m$ phase is described by a decreasing a lattice parameter with increasing mol% K^+. As the ionic radius of K^+ (1.38 $\mathring{A}$) is larger than Ag^+ (1.15 $\mathring{A}$), the a lattice parameter of this cubic phase is expected to increase proportionally with K content as per Vegard's law. [215] However, Figure 6.7(b) demonstrates that the lattice parameter a decreases as the 20 mol% K level is exceeded, suggesting that the K^+ cation is incorporated on both the Cs^+ (A) and Ag^+ (B'(I)) sites in this cubic structure. Additional confirmation of this behaviour is provided by the TEM micrographs of the $Cs_2K_{0.6}Ag_{0.4}InCl_6$:Bi and $Cs_2K_{0.6}Ag_{0.4}InCl_6$:Bi nanocrystals in Figure 6.7(c) reveal faceted particles of ∼4 nm and ∼6 nm diameter, respectively, while the HRTEM micrograph of Figure 6.7(d) exhibit the lattice fringes and lattice spacing of 2.3 $\mathring{A}$ corroborating the (224) crystal plane associated with the cubic double perovskite structure. The smaller particle size characterising the K^+ substituted nanocrystals is attributed to the comparatively slower reaction dynamics in the synthesis mixture.

From the TEM images of Figures 6.7(c) and (d), the small nanocrystal size of ∼4-6 nm characterising the $Cs_2K_xAg_{1-x}InCl_6$:Bi (x = 0.2 - 1) series induces lower resolution XRD data (Figures 6.7(a)). While the XRD data

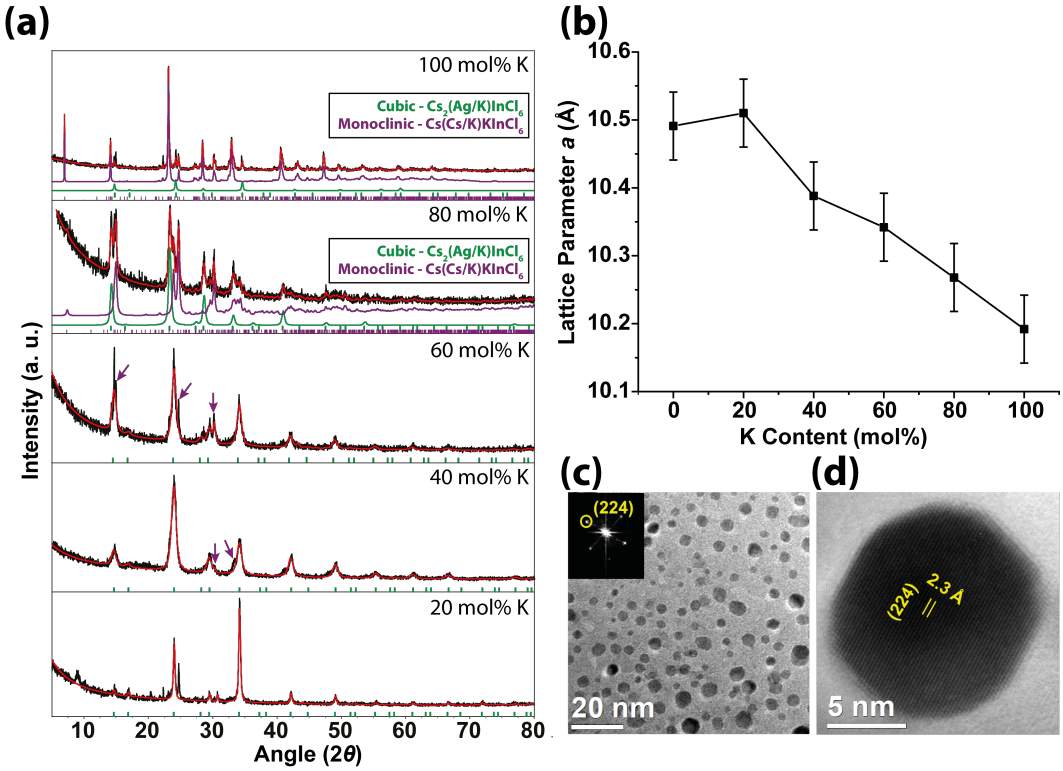

Figure 6.7: Structural characterisation data from the $Cs_2K_xAg_{1-x}InCl_6$:Bi (x = 0.2 - 1) nanocrystal series including: (a) X-ray diffraction data with arrows in the 40 mol% K and 60 mol% K pattern indicating the onset of monoclinic phases, (b) changes to the cubic structure lattice parameter a with increasing mol% K, (c) TEM micrograph of $Cs_2K_{0.60}Ag_{0.40}InCl_6$:Bi nanocrystals with FFT, and (d) a HRTEM image of a $Cs_2K_{0.60}Ag_{0.40}InCl_6$:Bi nanocrystal depicting lattice fringes associated with the cubic components of the overall structure.

provides indications of the structural polytypes formed throughput this series, the short range information afforded by the solid state ^{133}Cs and ^{39}K MAS NMR data (Figures 6.8(a-d)), and the associated AIRSS materials modelling provide greater specificity to the evolving phases stimulated by the changing stoichiometry. As observed in Figure 6.9, based on varying amounts of K^+ cation substitution into the parent $Cs_2AgInCl_6$ structure, a broad range of crystalline structures were generated that exhibited considerable differences in the rigidity of the perovskite framework. [220] In all these substituted systems, AIRSS modelling initiated a series of random $InCl_6$ octahedra rotations and geometry relaxations to arrive at structural realisations representing lower energies in the potential energy surface than the original $Fm\bar{3}m$ structure. From Figure 6.9, the resultant families of cubic and monoclinic crystalline structures accommodate various degrees of octahedral tilting and distortion within each lattice. The parent structure $Cs_2AgInCl_6$ was found to be the most rigid, with the perfect $Fm\bar{3}m$ structure defined as the ground state in these relaxation experiments. Substituting K^+ atoms for Cs^+ on the A site results in distorted structures that are energetically more favourable than the perfect cubic crystal, although the energy differences are not more than 15 meV/formula unit, thus indicating a flat potential energy landscape where the $InCl_6$ octahedra have considerable rotational flexibility at finite temperatures. This phenomenon is emphasised upon inspection of the relaxed monoclinic $Cs_{2-x}K_{1+x}InCl_6$ structure (A and B site K^+ occupancy) which exhibits significant long-range disorder while preserving the overall local pseudo-cubic structure of the metal cations, thus corroborating the XRD data reported above.

The partial density of states (DoS) calculated from the AIRSS generated structures shown in Figure 6.9 are presented in Figures 6.10(a-f). From the evolution of the B site substituted cubic structures with increasing K^+ incorporation depicted on the right side of Figure 6.9, the calculated DoS progressing from the parent $Cs_2AgInCl_6$ system, to the partially substituted $Cs_2K_yAg_{1-y}InCl_6$ (B site occupancy, $y = 0.5$) through to the fully substituted Cs_2KInCl_6 (B site occupancy, $y = 1$) reveals a reduction and an eventual loss of covalent bonding character between the anionic Cl^- and the B'(I) cations upon K^+ incorporation (see Figures 6.10(a-c)). This rationalises the increased flexibility and ionic character of the system with increasing mol% K^+ by high-

lighting that the isoenergetic relationship between the Cl^- p electrons and the Ag^+ d electrons (spanning ∼1.5 - 4.5 eV) underpinning $Cs_2AgInCl_6$ is replaced by a large energy displacement between the Cl^- p electrons and the K^+ p electrons in Cs_2KInCl_6 of ∼10 eV. Similarly, the DoS for the evolution of the A and B site substituted systems on the left side of Figure 6.9 to the cubic $Cs_{2-x}K_{x+y}Ag_{1-y}InCl_6$ and eventually the monoclinic $Cs_{2-x}K_{1+x}InCl_6$ systems (see Figures 6.10(e) and (f)) reflects the same loss of covalency and structural rigidity.

Calculation of the lattice parameters from the generalised cubic $Cs_{2-x}K_{x+y}Ag_{1-y}InCl_6$ AIRSS realisation demonstrates that K^+ substitution can be partitioned in two competing scenarios (see Figure 6.10(g)). The lattice parameter changes from both A and B site substitution are represented as change to the average edge length of the (pseudo)cubic sublattice for monoclinic $Cs_{2-x}K_{1+x}InCl_6$ and cubic $Cs_{2-x}K_xAgInCl_6$. Observation of the orange curves show that by keeping the B site occupancy constant (i.e. $y = 0.0$, 0.5, 1.0) and varying the A site substitution, the lattice contracts in agreement with the XRD data of Figures 6.7(a) and (b). This contraction is accompanied by structural distortion which ultimately destabilises the cubic structure at high A site substitution levels. Conversely, the blue curves demonstrate that by keeping the A site occupancy constant (i.e. $x = 0.0$, 0.5) B site variation induces lattice expansion.

The ^{133}Cs and ^{39}K MAS NMR data measured from the $Cs_2K_xAg_{1-x}InCl_6$:Bi (x = 0.2 - 1) nanocrystal series is shown in Figures 6.8(a) and (b), while assignment of these complex spectra is assisted by GIPAW DFT calculation of the chemical shift distributions calculated from the AIRSS modelled structures of Figure 6.9 (Figures 6.8(c) and (d)). It is important to note from both the ^{133}Cs and ^{39}K MAS NMR data that the parent cubic $Cs_2AgInCl_6$ and cubic (B site substituted) $Cs_2K_yAg_{1-y}InCl_6$ structures exhibit confined chemical shifts ranges at δ∼128 ppm and δ∼50 ppm, respectively, while all other systems display marked chemical shift distributions commensurate with the structural disorder. From the ^{133}Cs MAS NMR data in Figure 6.8(a), the lower substitution levels of 20 - 60 mol% K^+ are dominated by the cubic (B site substituted) $Cs_2K_yAg_{1-y}InCl_6$ species, although evidence of the cubic (A and B site substituted) $Cs_{2-x}K_{x+y}Ag_{1-y}InCl_6$

and cubic (A site substituted) $Cs_{2-x}K_xAgInCl_6$ systems is observed to emerge. Figures 6.8(a) and (c) demonstrate that the substitution of K^+ onto the Cs^+ A site introduces significant structural disorder as reflected by the large GIPAW DFT predicted chemical shift dispersion spanning ∼80 - 100 ppm. The clearest experimental evidence of these disordered species is via the very broad, partially resolved (bimodal) resonance distributions centred at δ∼150 ppm and δ∼120 ppm (Figure 6.8(c)). At the higher 80 and 100 mol% K^+ substitution levels the cubic (B site substituted) $Cs_2K_yAg_{1-y}InCl_6$ structure disappears and the speciation is dominated by the less cubic (B site substituted) Cs_2KInCl_6 and monoclinic (A and B site substituted) $Cs_{2-x}K_{1+x}InCl_6$ systems, in addition to the cubic (A and B site substituted) $Cs_{2-x}K_{x+y}Ag_{1-y}InCl_6$ and (A site substituted) $Cs_{2-x}K_xAgInCl_6$ systems mentioned above. The newly emergent cubic (B site substituted) Cs_2KInCl_6 and monoclinic (A and B site substituted) $Cs_{2-x}K_{1+x}InCl_6$ systems are also characterised by complex disorder and broad predicted chemical shift ranges of ∼50 ppm and ∼80 ppm, respectively, which are thus partially resolved in the experimental data.

Unlike the Cs^+ cation which only occupies the A site in this series of structures, the incorporation of the K^+ cation on both the A and B positions introduces more profound affects to the observed ^{39}K MAS NMR data of Figure 6.8(b). The A site and B site ^{39}K shifts are partitioned into distinctly resolved chemical shift ranges, with the K speciation occupying the cuboctahedral A sites displaying ^{39}K shifts in the δ∼−50 - 20 ppm range, while the octahedral B site substitution is comparatively less shielded exhibiting ^{39}K shifts in the δ∼50 - 80 ppm range. The component of the K inventory entering the rigid cubic $Cs_2K_yAg_{1-y}InCl_6$ structure (B site occupancy) is confined to a very narrow ^{39}K chemical shift range around δ∼50 ppm. It is important to note that the lower level (20 mol% K^+) of incorporation does not introduce K^+ cation speciation into B site of the cubic $Cs_2K_yAg_{1-y}InCl_6$ system; i.e., there is no evidence of a narrow resonance at δ∼48 ppm, however, a broad distributed resonance centred around δ∼20 ppm is observed. From the GIPAW DFT calculated ^{39}K chemical shift ranges presented in Figure 6.8(d), it is apparent that the absence of a bimodal (A and B site distributed) chemical shift range suggests that this chemical shift distribution is restricted to

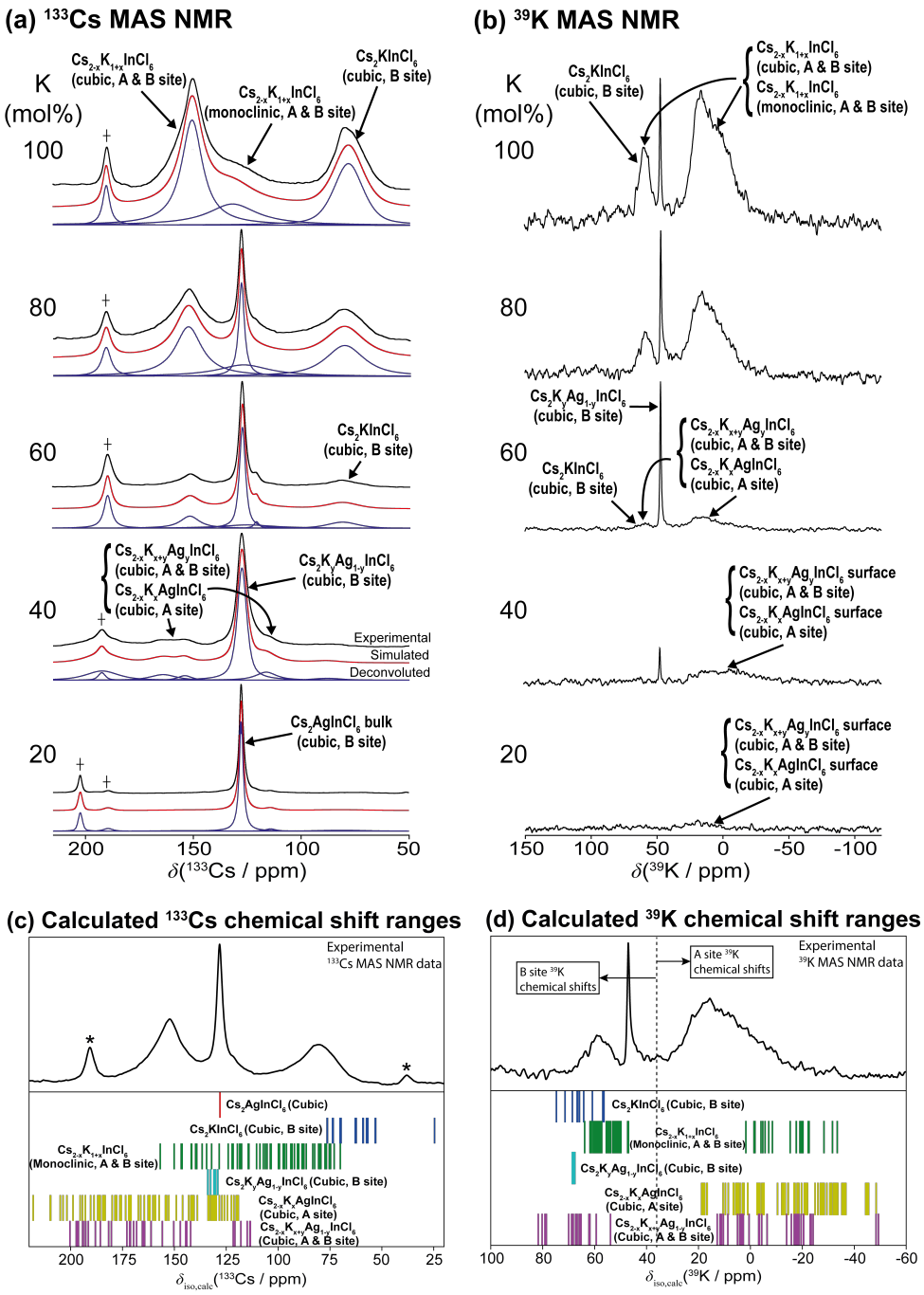

Figure 6.8: Solid state NMR study of the $Cs_2K_xAg_{1-x}InCl_6$:Bi (x = 0.2 - 1) nanocrystal series showing (a) ^{133}Cs MAS NMR data (B_0 = 14.1 T, ν_r = 12 kHz), (b) ^{39}K MAS NMR data (B_0 = 20.0 T, ν_r = 12 kHz), (c) GIPAW DFT calculated ^{133}Cs chemical shifts, and (d) GIPAW DFT calculated ^{39}K chemical shifts from across the compositional range.

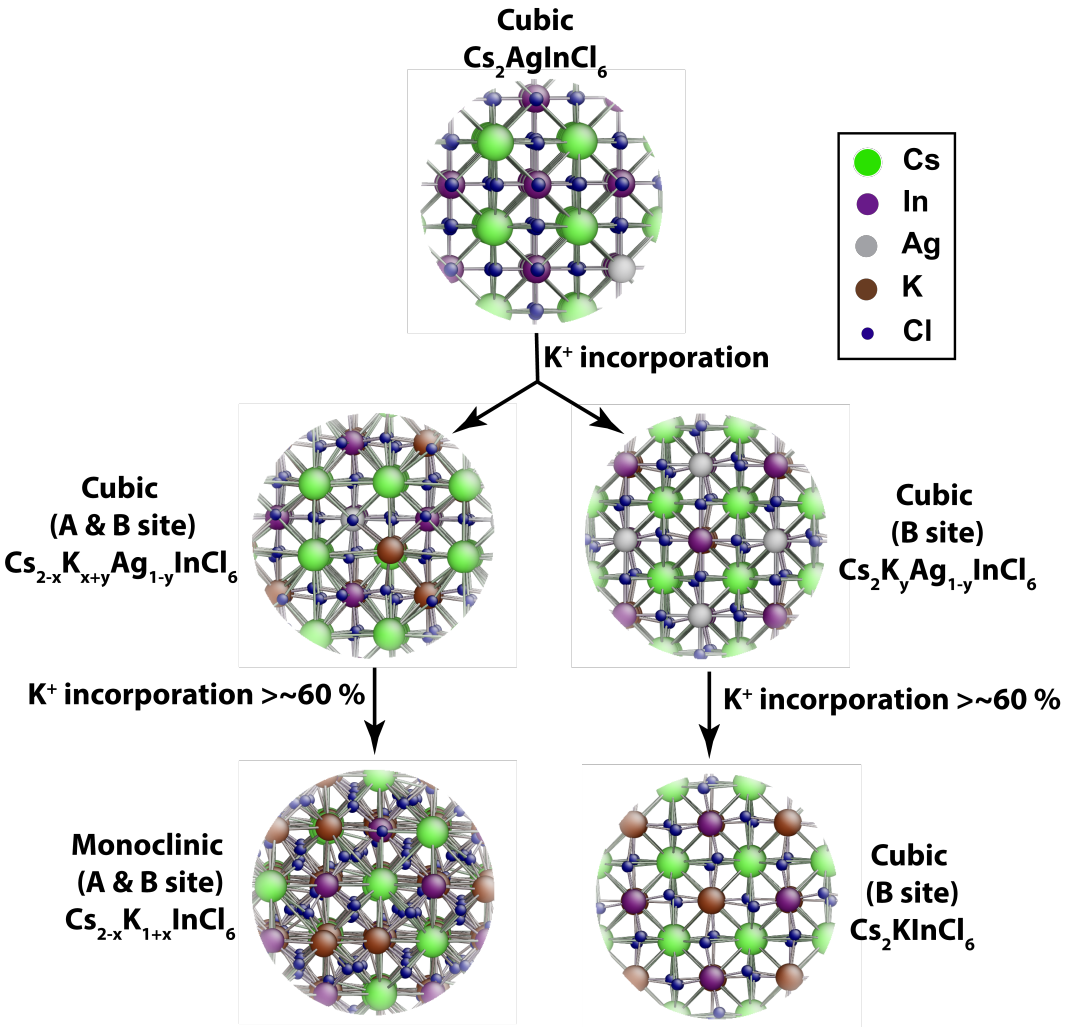

Figure 6.9: Structural realisation determined from Ab Initio Random Structure Search (AIRSS) DFT CASTEP calculation for $Cs_2AgInCl_6$ upon K^+ incorporation onto the A (Cs) site and B'(I) (Ag) site at different K^+ concentrations.

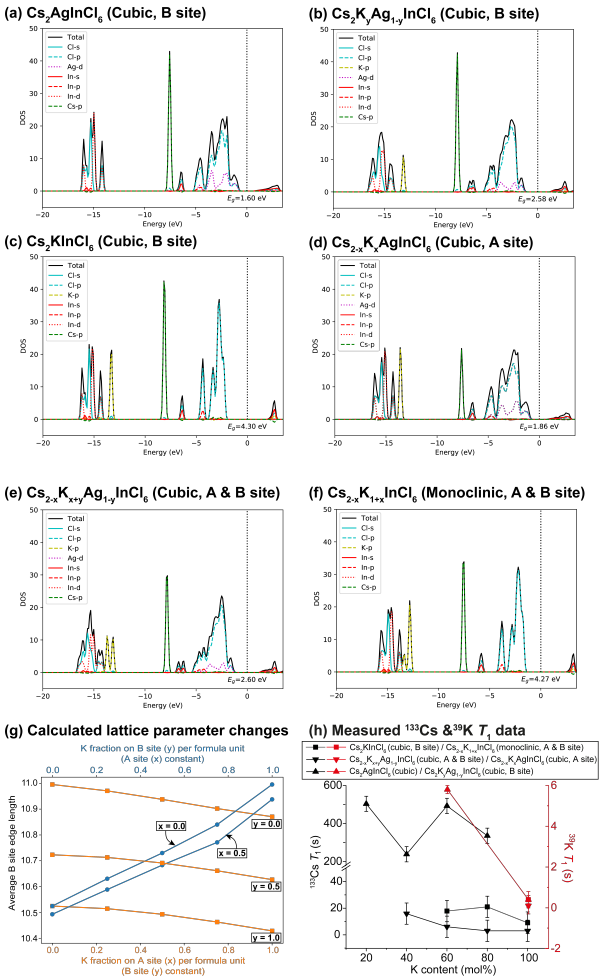

Figure 6.10: The calculated partial density of states (DoS) for (a) cubic $Cs_2AgInCl_6$, (b) cubic (B site substituted) $Cs_2K_yAg_{1-y}InCl_6$ (y = 0.5), (c) cubic (fully B site substituted) Cs_2KInCl_6, (d) to cubic (A site substituted) $Cs_{2-x}K_xAgInCl_6$ (x = 0.5), (e) cubic (A and B site substituted) $Cs_{2-x}K_{x+y}Ag_{1-y}InCl_6$ (x = 0.5, y = 0.5), (f) monoclinic (A and B site substituted) $Cs_{2-x}K_{1+x}InCl_6$ (x = 0.25), with (g) the calculated lattice parameter changes and (h) the measured ^{133}Cs and ^{39}K T_1 data acquired using the saturation-recovery technique.

cubic (A site substituted) $Cs_{2-x}K_xAgInCl_6$ that is passivating the surface of the parent cubic $Cs_2AgInCl_6$ nanocrystals, with the corresponding ^{133}Cs MAS NMR data of the 20 mol% K^+ system representing the $Cs_2AgInCl_6$ nanocrystal bulk. This observation is consistent with recent reports of the surface passivation of $Cs_2AgInCl_6$ and $Cs_2In_{0.9}Bi_{0.1}AgCl_6$ nanocrystals using low levels of K^+ cations introduced as KBr. [221] The GIPAW DFT calculated ^{39}K chemical shift distributions shown in Figures 6.8(d) suggest that significant overlap influences both the A and B site shift ranges, precluding chemical resolution of the constituent cubic and monoclinic phases in each case. However, more importantly, the distinct resolution between the A and B site chemical shift ranges demonstrates that the K^+ substitution levels into this nanocrystal series (particularly at the higher incorporation levels) is dominated by A site occupancy by a factor of ∼2 - 4:1.

Despite the large ^{133}Cs and ^{39}K linewidths and lack of resolution that characterises the structural disorder within K^+ substituted nanocrystal series, valuable information can be obtained from the T_1 relaxation data from those resonances that can be isolated. From the ^{133}Cs MAS NMR data, three distinct resonances at δ∼128 ppm (cubic (B site substituted) $Cs_2AgInCl_6/Cs_2K_yAg_{1-y}InCl_6$ phases), δ∼152 ppm (convoluted cubic (A site substituted) $Cs_{2-x}K_xAgInCl_6$ and cubic (A and B site substituted) $Cs_{2-x}K_{x+y}Ag_{1-y}InCl_6$ phases) and δ∼82 ppm (convoluted cubic (fully B site substituted) Cs_2KInCl_6 and monoclinic (A and B site substituted) $Cs_{2-x}K_{1+x}InCl_6$ phases) exhibit sufficient resolution for a T_1 relaxation analysis. The measured ^{133}Cs T_1 relaxation data is reported as a function of mol% K^+ incorporation in Figure 6.10(b) and Table C.4. These data highlight differences of over two orders of magnitude exists between the ^{133}Cs T_1s characterising the cubic (B site substituted) $Cs_2AgInCl_6/Cs_2K_yAg_{1-y}InCl_6$ phases, (T_1s of ∼250 - 500 s) and the more disordered structures represented by broader resonance linewidths (T_1s of ∼5 - 20 s), thus corroborating the DoS data presented in Figures 6.10(a-f). Figure 6.10(h) displays a noticeable decrease in the ^{133}Cs T_1s at the 40 mol% K^+ incorporation level. As the 20 mol% K incorporation level probably only represents a surface passivation event (see the ^{39}K MAS NMR data above), the T_1 measurement of ∼500 s from this sample represents Cs^+ cations in the bulk $Cs_2AgInCl_6$ structure. Hence, the reduced T_1 of ∼250 s

at 40 mol% K represents the initial K^+ cation introduction into the $Cs_2AgInCl_6$ framework, which is probably distributed inhomogeneously throughout quasi-stable surface, sub-surface and near-surface environments of the nanocrystal (see the ^{39}K MAS NMR data of Figure 6.8(b)). As evidenced by the ^{39}K MAS NMR data of the 60 mol% K preparation, the increase of the ^{133}Cs T_1 back to ∼500 s is accompanied by the maximum proliferation of K^+ into the bulk $Cs_2AgInCl_6$ framework (producing the B site substituted $Cs_2K_yAg_{1-y}InCl_6$ phase), thus suggesting that the substituted $Cs_2K_{0.60}Ag_{0.40}InCl_6$ phase represents an important balance between the disordered structures, restricted Cs^+ mobility and K^+ incorporation (see Figure 6.8(b)).

Figures 6.11(a) and (b) show the absorption and emission data from the $Cs_2K_xAg_{1-x}InCl_6$:Bi (x = 0.2 - 1) nanocrystal series. From Figure 6.11(a), a blue shift in the excitonic peak spanning 370 nm to 328 nm is observed across this compositional range; however, there is no apparent shift in the PL peak as K^+ cations do not perturb the valence band maxima or conduction band minima of the double perovskite band gap (Figure 6.11(b)). [197] Figure 6.11(c) shows the relative PL performance from the $Cs_2AgIn_{0.90}Bi_{0.10}Cl_6$, $Cs_2Na_{0.60}Ag_{0.40}InCl_6$:Bi, and $Cs_2K_{0.60}Ag_{0.40}InCl_6$:Bi nanocrystal samples that present the highest PLQY within each compositional series, demonstrating that the K^+ substituted $Cs_2K_{0.60}Ag_{0.40}InCl_6$:Bi nanocrystals represent the best performing systems by a factor of ∼100%. More importantly, Figure 6.11(d) indicates that K^+ incorporation induces significant improvements to the optical properties specifically at the 60 mol% K level where the PLQY increases from 11% to 38%. Indeed, Figures 6.11(d) and (e) shows that the increasing PLQY performance of the K^+ substituted series correlates directly with amount of the cubic (B site substituted) $Cs_2K_yAg_{1-y}InCl_6$ phase present which is maximized at the 60 mol% K level. Although the XRD, MAS NMR and materials modelling studies reveal that compositions supporting >20 mol% K accommodate simultaneous K^+ substitution on both the A (Cs) and B'(I) (Ag) double perovskite positions, Figures 6.11(d) and (e) emphasize that the 60 mol% K preparation optimises the presence of the cubic (B site substituted) $Cs_2K_yAg_{1-y}InCl_6$ phase that shows the most effective passivation of the Cs^+ bulk and surface defects as indicated by the longest ^{133}Cs and ^{39}K T_1 values (Figure 6.10(h)), attenuated cation mobility and enhanced PLQY

performance. From the XRD data of Figures 6.7(a), and the ^{133}Cs and ^{39}K MAS NMR of Figures 6.8(a) and (b), respectively, increased K^+ incorporation of >60 mol% K induces the formation of large quantities of disordered cubic and monoclinic phases, where A site substitution dominates the K speciation. These more disordered phases are characterised by greatly reduced T_1s, increased cation mobility and much reduced PLQY function.

Similar improvements to the optical properties by surface passivation have been reported from the incorporation of K^+ cations into other ABX_3 perovskite systems. [222] It is important to note that a measured PLQY of 38% for the 60 mol% K system represents a maximum theoretical threshold as the uncoordinated Cl^- ions on the nanocrystals surface limit the emission efficiency in double perovskite structure. [223] While further developments are necessary to improve the PLQY in these nanocrystal systems, this XRD/MAS NMR/materials modelling approach has demonstrated that K^+ cation incorporation induces the evolution of multiple phases associated with simultaneous A and B site passivation. Furthermore, while higher K^+ cation substitution levels show a clear dominance of the A site substitution phenomenon, the PLQY performance is maximized when the cubic (B site substituted) $Cs_2K_yAg_{1-y}InCl_6$ is the predominant nanocrystal phase.

6.4 Conclusions

Three series of nanocrystals samples, $Cs_2In_xBi_{1-x}AgCl_6$, $Cs_2Na_xAg_{1-x}InCl_6$:Bi, and $Cs_2K_xAg_{1-x}InCl_6$:Bi, were synthesised using a colloidal hot-injection procedure. $Cs_2In_xBi_{1-x}AgCl_6$ nanocrystals were synthesised as a baseline system, with the 0.5% Bi doped sample ($Cs_2AgInCl_6$:Bi) being taken forward for investigations of the Na^+ and K^+ cation incorporation into these double perovskite nanocrystalline materials. A combined XRD, TEM and solid state MAS NMR approach demonstrated that clear structural and functional trends were observed for the $Cs_2In_xBi_{1-x}AgCl_6$ (x = 0 - 1) and $Cs_2Na_xAg_{1-x}InCl_6$:Bi (x = 0.2 - 1) substitutional series. The $Cs_2In_xBi_{1-x}AgCl_6$ (x = 0 - 1) series exhibited ^{133}Cs T_1 values that are 2 - 3 orders of magnitude greater than the those representing the mid-range ~50 mol% In^{3+} compositions, thus reflecting increased Cs^+ mobility where

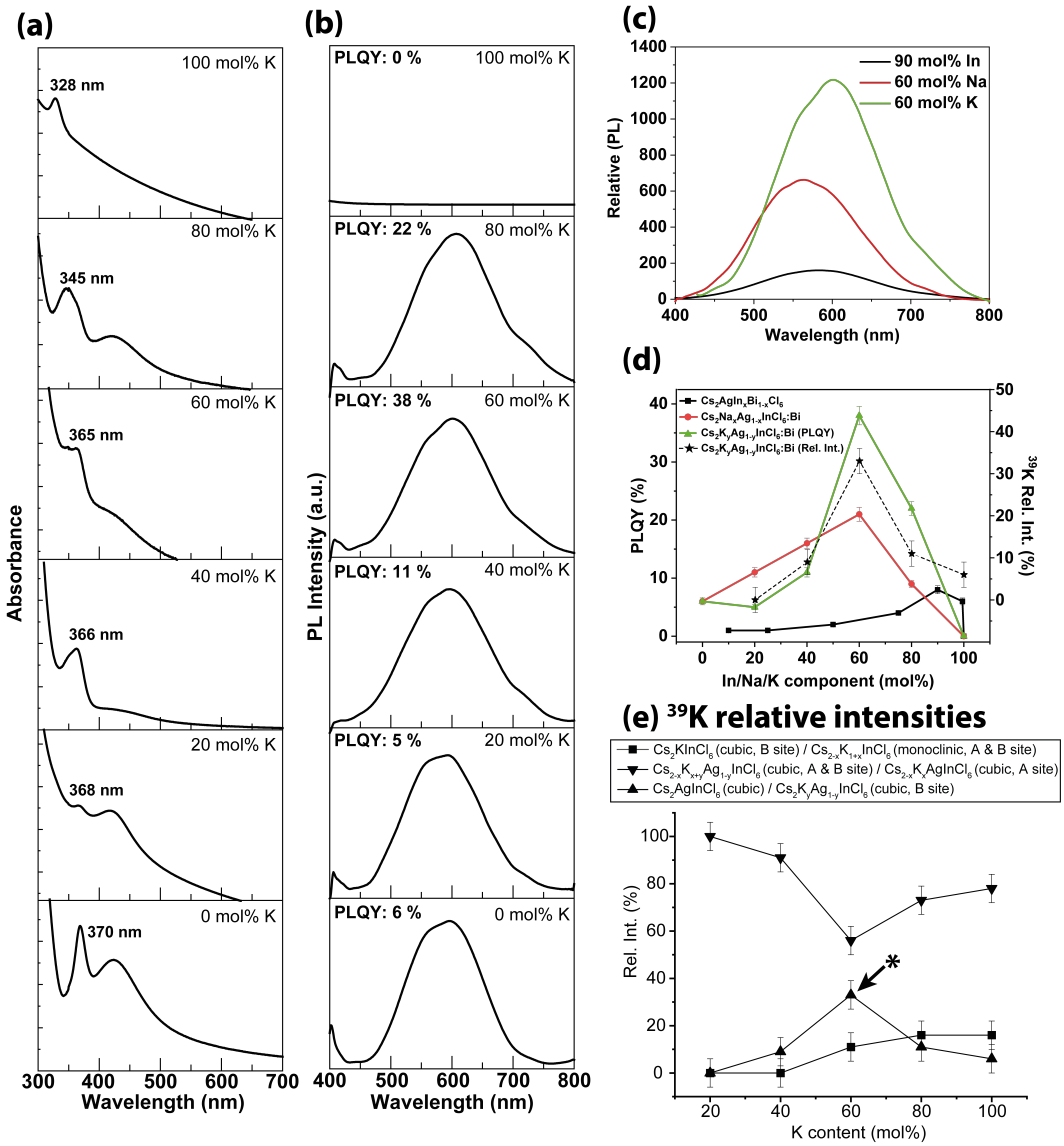

Figure 6.11: Optoelectronic data from the $Cs_2K_xAg_{1-x}InCl_6$:Bi (x = 0.2 - 1) nanocrystal series displaying (a) absorption spectra and (b) photoluminescence (PL) spectra from nanocrystal solutions dispersed in hexane, (c) the relative PL data from the $Cs_2AgIn_{0.90}Bi_{0.10}Cl_6$, $Cs_2Na_{0.60}Ag_{0.40}InCl_6$:Bi, and $Cs_2K_{0.60}Ag_{0.40}InCl_6$:Bi systems yielding the highest PLQY in each nanocrystal series, (d) the trend in PLQY vs mol% Na/mol% K/mol% In, and (e) the relative intensity of the K speciation measured from the ^{39}K MAS NMR data. The PLQY behaviour demonstrated by the K substituted series in (d) directly correlates with the amount of cubic $Cs_2K_yAg_{1-y}In_xCl_6$ phase represented by the δ 48 ppm resonance from the ^{39}K MAS NMR data in (e) and in Figure 6.8(b) (maximum indicated with an asterisk *).

maximum structural disorder is present. In contrast, the maximum measured ^{133}Cs T_1 values were evident for compositions close to (but not directly at) the end member $Cs_2BiAgCl_6$ and $Cs_2InAgCl_6$ compositions, suggesting that minor substituted amounts of In^{3+} in the $Cs_2BiAgCl_6$ system, and Bi^{3+} within the $Cs_2InAgCl_6$ system, induce marked passivation effects within this system. This phenomenon is highlighted by the strong orange emission at ∼580 nm dominating the PL properties up to a composition of 99.5 mol% In^{3+}, but which subsequently disappears at 100 mol% In^{3+}. For the $Cs_2Na_xAg_{1-x}InCl_6$:Bi (x = 0.2 - 1) nanocrystal series the reduction in the ^{133}Cs T_1 relaxation times at >60 mol% Na^+ relates to increased Cs^+ vacancy formation, more rapid Cs^+ cation mobility and the maximum PLQY of 21% for the 60 mol% Na^+ composition.

In contrast, the $Cs_2K_xAg_{1-x}InCl_6$:Bi (x = 0.2 - 1) nanocrystal series produced a complex array of closely related K^+ cation substituted phases. XRD studies demonstrated that cubic and monoclinic phases co-exist in the nanocrystal structure, while solid state ^{133}Cs and ^{39}K MAS NMR studies, AIRSS materials modelling and GIPAW DFT chemical shift calculations verified the specific cubic and monoclinic phases present. All of these studies conclusively proved that K^+ incorporation in these nanocrystals can occur on both A and B'(I) positions of the double perovskite structure, and the DFT DoS calculations identified that varying degrees of covalent/ionic character and structural rigidity characterise the resultant phases. Optimum PL and PLQY behaviour was observed with maximum amounts of the structurally rigid 60 mol% K^+ $Cs_2K_yAg_{1-y}InCl_6$ phase that supports only B site occupancy.

Chapter 7

Summary and Outlook

7.1 Solid State NMR Investigations of Heterogenous Catalysts on Metal Oxide Supports

The effectiveness of ^{17}O enrichment and solid state NMR as a method to study PGM oxide materials for heterogeneous catalysis was explored. From this, the first reported ^{17}O solid state NMR spectra of each PGM oxide has been achieved and characterised. Enrichment of PtO_2 was found to largely reduce to Pt metal under the enrichment conditions as was identified from PXRD and static ^{195}Pt solid state NMR results. However, this still allowed the identification of PtO_2 and PtO ^{17}O NMR resonances.

Furthermore, the enrichment of PdO was carried out at multiple temperatures because at $\sim$500 ^oC it was observed to develop into nanoparticles. Despite this morphological change taking place, excellent enrichment was achieved. A core-shell model described the ^{17}O NMR spectra of PdO nanoparticles due to the different Knight shift strengths at each nanoparticle layer. The core and bulk PdO ^{17}O were located at ~-408 ppm, way outside of the usual ^{17}O chemical shift range due to the large Knight shift generated by the Pd nucleus.

Enrichment of Pt and Pd catalyst on the commonly used metal oxide supports, γ-Al_2O_3, TiO_2 and SiO_2 were also carried out. However, no indication of the strong metal support interaction was observed for SiO_2 and TiO_2

supports. On the other hand, for γ-Al_2O_3 a broad disordered resonance was seen for both Pt and Pd catalysts at weightings of 1 and 10%. This resonance was the direct observation of the catalyst bonding to the metal oxide support. Moreover, these results have shown ^{17}O to be a viable technique in the characterisation of PGM containing materials.

In the future, the application of ^{17}O solid state NMR could be taken further to look at complex PGM containing systems. Given the sensitivity of the ^{17}O nucleus, it could be used to identify details of strong metal support interactions which are unobtainable from other experimental techniques. Furthermore, the exploration of NMR calculations on PGM ^{17}O species could provide a new avenue for structural characterisation in heterogeneous catalysis. Additionally, different enrichment methods could be compared and tested such as using enriched water in a liquid assisted grinding technique or heating with water vapour in order to find more non-destructive methods of enrichment. To further investigate changes in the surface speciation of alumina supports, Al-Pt and Al-H rotational-echo, double-resonance (REDOR) or Al-H heteronuclear correlation (HETCOR) experiments could elucidate catalyst surface bonding. For titania supports, $^{47,49}Ti$ NMR could be performed. However, there is usually significant peak overlap from both Ti isotopes, making spectra convoluted and difficult to simulate. Analysis of these spectra could be assisted through GIPAW DFT calculations.

7.2 Quadrupolar Solid State NMR Investigation of High Temperature Thermoelectric Materials

Solid state NMR was implemented for the first time in the area of thermoelectric materials and has been proven to be an essential tool in identifying the local structures and disorder manifested within these functional materials. The application of both ^{93}Nb and ^{87}Sr MAS NMR in combination with DFT calculations to Nb doped $SrTiO_3$ systems have provided detailed descriptions of Sr vacancy formation, octahedral distortion and niobia clustering unbeknownst from previously reported diffraction based methods.

The application of elemental analysis and neutron diffraction refinements enabled the detection of Sr vacancies with the doped $SrTiO_3$ analogues. Furthermore, the presence of first order forbidden modes in Raman spectra of both Ta and Nb doped $SrTiO_3$ indicate the presence of structural distortions within the structure. Further explanation of the structural distortions is provided by solid state NMR and DFT calculations. Combining quadrupolar experimental ^{93}Nb solid state NMR parameters to those calculated from material modelling CASTEP DFT calculations, NbO_6 dimers along <110> and <111> planes are found to form about a Sr vacancy. The distortion from the original cubic $SrTiO_3$ caused by the dimers is thought to contribute to an increase in the Seebeck coefficient. Comparatively the relatively constant S for Ta doped $SrTiO_3$ indicates that structural distortions in these systems may not be advantageous. Moreover, the clustering of disordered niobia nanodomains are detected within structures at high levels of Nb doping ($>$ 5 mol% Nb). These nanodomains are thought to hinder the thermal transport properties, thus lowering the thermal conductivity and improving the material's ZT value.

The acquisition of ^{17}O NMR spectra on these doped $SrTiO_3$ structures could potentially provide a further insight into the nature of tilting and vacancies forming. However, given the high stability and solid state synthesis requiring temperatures $\sim$1250 ^{o}C, sufficient and isotopic enrichment could be difficult to achieve. A ^{87}Sr 2D MQMAS could be performed to further look at the disorder and sites found in the 1D spectra. However, ^{87}Sr enrichment would be required to provide sufficient signal. Here only B site cation dopants have been considered, therefore further exploration on A site doped systems as well as dual doped A and B site systems structures could be probed. Furthermore, theoretical calculations of the electrical conductivity and Seebeck coefficients from different structural realisations could allow for an improved understanding of structural intricacies which have positive and negative effects on the thermoelectric performance. Thus far, structural characterisation experiments have only been performed prior to ZT measurements. Therefore, a future study which investigates the changes which occur after performance measurements will provide insight into the durability of these materials.

7.3 Structural Elucidation of Metal Cation Incorporated Double Perovskite Nanocrystals

Through the use of ^{133}Cs, ^{23}Na and ^{39}K NMR, the structure of Bi^{3+}, Na^+ and K^+ incorporated $Cs_2AgInCl_6$ NCs were analysed and correlated to their PL performance. The use of ^{133}Cs MAS NMR on Bi integrated $Cs_2AgInCl_6$ samples identified different substitutions of $[InCl_6]^{3-}$ and $[BiCl_6]^{3-}$ octahedra surrounding the Cs nucleus. Measurements of the spin-lattice relaxation times were related to the PLQY by way of structural defect formation causing both T_1 and the PLQY to decrease. The same effect on a material's performance and relaxation time was observed when introducing Na^+ on the B'(I) site.

For K^+ samples, a multitude of different structural evolutions occurred upon increasing the K^+ content. Disordered cubic and monoclinic Cs_2KInCl_6 phases were both identified from ^{133}Cs and ^{39}K MAS NMR. However, these phases are thought to not enhance the PL properties of the materials since only minor amounts are seen in the best performing sample (60 mol% K). Furthermore, from XRD measurements, a decrease in the refined lattice parameter above 40 mol% is detected, indicating K begins to occupy both A (Cs^+) and B'(I) (Ag^+) sites in the double perovskite lattice.

The development of lead-free alternative optoelectronic materials has gained a significant amount of interest in recent years. The ability of solid state NMR to probe the local structures of nanocrystals has been shown to provide great insight into the structures of these perovskite based materials and is becoming a popularised technique for the study of many similar systems to those studied here. Interesting future studies could entail the inclusion of different foreign cations into the system. Additionally, ^{1}H and ^{13}C single and double quantum experiments (e.g. HETCOR, NOESY, BABA) could be used to look at the bonding of organic ligand, and how the nanocrystal is stabilised using ligands of different chain length. Furthermore, ^{35}Cl NMR could be performed at multiple fields to detect the formation of vacancies. The highly quadrupolar nature of the ^{35}Cl nucleus makes it very sensitive to structural changes.

Bibliography

[1] T. F. Kemp and M. E. Smith. Quadfit—a new cross-platform computer program for simulation of nmr line shapes from solids with distributions of interaction parameters. *Solid state nuclear magnetic resonance*, 35(4):243–252, 2009.

[2] E. L. Hahn. Spin echoes. *Physical Review*, 80(4):580, 1950.

[3] E. R. Andrew, A. Bradbury, and R. G. Eades. Removal of dipolar broadening of nuclear magnetic resonance spectra of solids by specimen rotation. *Nature*, 183(4678):1802–1803, 1959.

[4] M. H. Levitt. *Spin Dynamics: Basics of Nuclear Magnetic Resonance*. Wiley, England, 2013.

[5] K. J. D. MacKenzie and M. E. Smith. *Multinuclear Solid State NMR of Inorganic Materials*. Pergamon Press, Oxford, 2002.

[6] M. J. Duer. *Introduction to Solid-State NMR Spectroscopy*. Wiley, Oxford, 2005.

[7] Michael Mehring. *Principles of high resolution NMR in solids*. Springer Science & Business Media, Berlin, 2012.

[8] D. Massiot, F. Fayon, M. Capron, I. King, S.e Le Calvé, B. Alonso, J.-O. Durand, B. Bujoli, Z. Gan, and G. Hoatson. Modelling one- and two-dimensional solid-state NMR spectra. *Magnetic Resonance in Chemistry*, 40(1):70–76, 2002.

[9] R. K. Harris, E. D. Becker, S. M. Cabral de Menezes, P. Granger, R. E. Hoffman, and K. W. Zilm. Further conventions for nmr shielding and

chemical shifts (iupac recommendations 2008). *Pure and Applied Chemistry*, 80(1):59–84, 2008.

[10] D. C. Apperley, R. K. Harris, and P. Hodgkinson. *Solid-state NMR: Basic principles and practice*. Momentum Press, New York, 2012.

[11] S. E. Ashbrook and M. J. Duer. Structural information from quadrupolar nuclei in solid state NMR. *Concepts in Magnetic Resonance Part A: An Educational Journal*, 28(3):183–248, 2006.

[12] R. E. Wasylishen, S. E. Ashbrook, and S. Wimperis. *Man, P. P. in Chapter 1: NMR of quadrupolar nuclei in solid materials*. John Wiley & Sons, United Kingdom, 2012.

[13] W. D. Knight and S. I. Kobayashi. *Knight Shift*. American Cancer Society, 2007.

[14] J. J. van der Klink and H. B. Brom. NMR in metals, metal particles and metal cluster compounds. *Progress in Nuclear Magnetic Resonance Spectroscopy*, 36(2):89–201, 2000.

[15] I. Bertini, C. Luchinat, G. Parigi, and E. Ravera. *NMR of paramagnetic molecules: applications to metallobiomolecules and models*. Elsevier, Germany, 2016.

[16] M. Bertmer. Paramagnetic solid-state NMR of materials. *Solid State Nuclear Magnetic Resonance*, 81:1–7, 2017.

[17] G. Pintacuda, G.and Kervern. *Paramagnetic Solid-State Magic-Angle Spinning NMR Spectroscopy*. Springer Berlin Heidelberg, Berlin, Heidelberg, 2013.

[18] G. Czjzek, J. Fink, F. Götz, H. Schmidt, J. M. D. Coey, J-P. Rebouillat, and A. Liénard. Atomic coordination and the distribution of electric field gradients in amorphous solids. *Physical Review B*, 23(6):2513, 1981.

[19] J. Keeler. *Understanding NMR spectroscopy*. John Wiley & Sons, United Kingdom, 2011.

[20] D. Freude and J. Haase. Quadrupole effects in solid-state nuclear magnetic resonance. In *Special Applications*, pages 1–90. Springer, 1993.

[21] F. Bloch. Nuclear induction. *Physical Review*, 70(7-8):460, 1946.

[22] A. Narayanan, S. J. Hartman, and A. D. Bain. Characterizing non-exponential spin-lattice relaxation in solid-state NMR by fitting to the stretched exponential. *Journal of Magnetic Resonance, Series A*, 112(1):58–65, 1995.

[23] J. P. Yesinowski. Finding the true spin–lattice relaxation time for half-integral nuclei with non-zero quadrupole couplings. *Journal of Magnetic Resonance*, 252:135–144, 2015.

[24] J. Korringa. Nuclear magnetic relaxation and resonnance line shift in metals. *Physica*, 16(7-8):601–610, 1950.

[25] A. E. Bennett, C. M. Rienstra, M. Auger, K. V. Lakshmi, and R. G. Griffin. Heteronuclear decoupling in rotating solids. *The Journal of Chemical Physics*, 103(16):6951–6958, 1995.

[26] S. R. Hartmann and E. L. Hahn. Nuclear double resonance in the rotating frame. *Physical Review*, 128(5):2042, 1962.

[27] H. Y. Carr and E. M. Purcell. Effects of diffusion on free precession in nuclear magnetic resonance experiments. *Physical Review*, 94(3):630, 1954.

[28] R. W. Schurko. Acquisition of wideline solid-state NMR spectra of quadrupolar nuclei. *eMagRes*, 2007.

[29] R. W. Schurko. Ultra-wideline solid-state NMR spectroscopy. *Accounts of Chemical Research*, 46(9):1985–1995, 2013.

[30] Y. Wu, B. Q. Sun, A. Pines, A. Samoson, and E. Lippmaa. NMR experiments with a new double rotor. *Journal of Magnetic Resonance (1969)*, 89(2):297–309, 1990.

[31] K. T. Mueller, G. C. Chingas, and A. Pines. NMR probe for dynamic-angle spinning. *Review of Scientific Instruments*, 62(6):1445–1452, 1991.

[32] L. Frydman and J. S. Harwood. Isotropic spectra of half-integer quadrupolar spins from bidimensional magic-angle spinning NMR. *Journal of the American Chemical Society*, 117(19):5367–5368, 1995.

[33] J-P. Amoureux and C. Fernandez. Triple, quintuple and higher order multiple quantum MAS NMR of quadrupolar nuclei. *Solid State Nuclear Magnetic Resonance*, 10(4):211–223, 1998.

[34] S. P. Brown and S. Wimperis. Two-dimensional multiple-quantum MAS NMR of quadrupolar nuclei: a comparison of methods. *Journal of Magnetic Resonance*, 128(1):42–61, 1997.

[35] B. E. Warren. *X-ray Diffraction*. Courier Corporation, 1990.

[36] H. M. Rietveld. A profile refinement method for nuclear and magnetic structures. *Journal of Applied Crystallography*, 2(2):65–71, 1969.

[37] A. L. Patterson. The scherrer formula for X-ray particle size determination. *Physical Review*, 56(10):978, 1939.

[38] B. Chen, U. Dingerdissen, J. G. E. Krauter, H. G. J. L. Rotgerink, K. Möbus, D. J. Ostgard, P. Panster, T. H. Riermeier, S. Seebald, T. Tacke, and H. Trauthwein. New developments in hydrogenation catalysis particularly in synthesis of fine and intermediate chemicals. *Applied Catalysis A: General*, 280(1):17–46, 2005.

[39] T. Tsubogo, H. Oyamada, and S. Kobayashi. Multistep continuous-flow synthesis of (R)-and (S)-rolipram using heterogeneous catalysts. *Nature*, 520(7547):329–332, 2015.

[40] U. Shah, A. R. Patel, D. Van de Walle, P. S. Rajarethinem, A. Proctor, and K. Dewettinck. CLA-rich soy oil margarine production and characterization. *Journal of the American Oil Chemists' Society*, 91(2):309–316, 2014.

[41] I. Yakoumis, A. M. Moschovi, I. Giannopoulou, and D. Panias. Real life experimental determination of platinum group metals content in automotive catalytic converters. In *IOP Conference Series: Materials Science and Engineering*, volume 329, page 012009. IOP Publishing, 2018.

[42] J. Heveling. Heterogeneous catalytic chemistry by example of industrial applications. *Journal of Chemical Education*, 89(12):1530–1536, 2012.

[43] M. Seehra and A. Bristow. *Noble and Precious Metals: Properties, Nanoscale Effects and Applications*. BoD–Books on Demand, United Kingdom, 2018.

[44] S. Seetharaman. *Treatise on process metallurgy, volume 3: industrial processes*, volume 3. Newnes, Netherlands, 2013.

[45] D. S. Cameron, S. J. Cooper, I. L. Dodgson, B. Harrison, and J. W. Jenkins. Carbons as supports for precious metal catalysts. *Catalysis Today*, 7(2):113–137, 1990.

[46] T.-S. Nguyen, F. Morfin, M. Aouine, F. Bosselet, J.-L. Rousset, and L. Piccolo. Trends in the CO oxidation and PROX performances of the platinum-group metals supported on ceria. *Catalysis Today*, 253:106–114, 2015.

[47] M. Skoglundh, L. O. Löwendahl, and J.-E. Otterated. Combinations of platinum and palladium on alumina supports as oxidation catalysts. *Applied Catalysis*, 77(1):9–20, 1991.

[48] J. A. Horsley. A molecular orbital study of strong metal-support interaction between platinum and titanium dioxide. *Journal of the American Chemical Society*, 101(11):2870–2874, 1979.

[49] C. Prado-Burguete, A. Linares-Solano, F. Rodriguez-Reinoso, and C. Salinas-Martinez De Lecea. The effect of oxygen surface groups of the support on platinum dispersion in Pt/carbon catalysts. *Journal of Catalysis*, 115(1):98–106, 1989.

[50] S. J. Tauster, S. C. Fung, R. T. K. Baker, and J. A. Horsley. Strong interactions in supported-metal catalysts. *Science*, 211(4487):1121–1125, 1981.

[51] S. J. Tauster, S. C. Fung, and R. l. L. Garten. Strong metal-support interactions. group 8 noble metals supported on titanium dioxide. *Journal of the American Chemical Society*, 100(1):170–175, 1978.

[52] W. D. Goodman. Model studies in catalysis using surface science probes. *Chemical Reviews*, 95(3):523–536, 1995.

[53] N. Lopez, J. K. Nørskov, T. V. W. Janssens, A. Carlsson, A. Puig-Molina, B. S. Clausen, and J.-D. Grunwaldt. The adhesion and shape of nanosized Au particles in a Au/TiO_2 catalyst. *Journal of Catalysis*, 225(1):86–94, 2004.

[54] M. S. Chen and D. W. Goodman. The structure of catalytically active gold on titania. *Science*, 306(5694):252–255, 2004.

[55] M. G. Sanchez and J. L. Gazquez. Oxygen vacancy model in strong metal-support interaction. *Journal of Catalysis*, 104(1):120–135, 1987.

[56] A. Bruix, J. A. Rodriguez, P. J. Ramírez, S. D. Senanayake, J. Evans, J. B. Park, D. Stacchiola, P. Liu, J. Hrbek, and F. Illas. A new type of strong metal–support interaction and the production of H_2 through the transformation of water on Pt/CeO_2 (111) and $Pt/CeO_x/TiO_2$ (110) catalysts. *Journal of the American Chemical Society*, 134(21):8968–8974, 2012.

[57] M. Cargnello, V. V. T. Doan-Nguyen, T. R. Gordon, R. E. Diaz, E. A. Stach, R. J. Gorte, P. Fornasiero, and C. B. Murray. Control of metal nanocrystal size reveals metal-support interface role for ceria catalysts. *Science*, 341(6147):771–773, 2013.

[58] R. Burch and P. J. Millington. Selective reduction of NO_x by hydrocarbons in excess oxygen by alumina-and silica-supported catalysts. *Catalysis Today*, 29(1-4):37–42, 1996.

[59] S. N Rashkeev, D. M. Ginosar, L. M. Petkovic, and H. H. Farrell. Catalytic activity of supported metal particles for sulfuric acid decomposition reaction. *Catalysis Today*, 139(4):291–298, 2009.

[60] C. Morterra and G. Magnacca. A case study: surface chemistry and surface structure of catalytic aluminas, as studied by vibrational spectroscopy of adsorbed species. *Catalysis Today*, 27(3-4):497–532, 1996.

[61] E. C. DeCanio, J. C. Edwards, and J. W. Bruno. Solid-state ^{1}H MAS NMR characterization of γ-alumina and modified γ-aluminas. *Journal of Catalysis*, 148(1):76–83, 1994.

[62] G. Paglia, C. E. Buckley, A. L. Rohl, R. D. Hart, K. Winter, A. J. Studer, B. A. Hunter, and J. V. Hanna. Boehmite derived γ-alumina system. 1. structural evolution with temperature, with the identification and structural determination of a new transition phase, γ-alumina. *Chemistry of Materials*, 16(2):220–236, 2004.

[63] R. Lizárraga, E. Holmström, S. C. Parker, and C. Arrouvel. Structural characterization of amorphous alumina and its polymorphs from first-principles XPS and NMR calculations. *Physical Review B*, 83(9):094201, 2011.

[64] G. Paglia, A. L. Rohl, C. E. Buckley, and J. D. Gale. Determination of the structure of γ-alumina from interatomic potential and first-principles calculations: The requirement of significant numbers of nonspinel positions to achieve an accurate structural model. *Physical Review B*, 71(22):224115, 2005.

[65] J. A. Wang, X. Bokhimi, A. Morales, O. Novaro, T. Lopez, and R. Gomez. Aluminum local environment and defects in the crystalline structure of sol- gel alumina catalyst. *The Journal of Physical Chemistry B*, 103(2):299–303, 1999.

[66] Y. G. Wang, P. M. Bronsveld, J. T. M. DeHosson, B. Djuričić, D. McGarry, and S. Pickering. Ordering of octahedral vacancies in transition aluminas. *Journal of the American Ceramic Society*, 81(6):1655–1660, 1998.

[67] C. Pecharroman, I. Sobrados, J. E. Iglesias, T. Gonzalez-Carreno, and J. Sanz. Thermal evolution of transitional aluminas followed by NMR and IR spectroscopies. *The Journal of Physical Chemistry B*, 103(30):6160–6170, 1999.

[68] S. J. Wilson. The dehydration of boehmite, γ-AlOOH, to γ-Al_2O_3. *Journal of Solid State Chemistry*, 30(2):247–255, 1979.

[69] A. R. Ferreira, E. Küçükbenli, S. De Gironcoli, W. F. Souza, S. S. X. Chiaro, E. Konstantinova, and A. A. Leitão. Structural models of activated γ-alumina surfaces revisited: Thermodynamics, NMR and IR spectroscopies from ab initio calculations. *Chemical Physics*, 423:62–72, 2013.

[70] D. Dou, D-J. Liu, W. B. Williamson, K. C. Kharas, and H. J. Robota. Structure and chemical properties of Pt nitrate and application in three-way automotive emission catalysts. *Applied Catalysis B: Environmental*, 30(1-2):11–24, 2001.

[71] S-J. Hwang, D. O. Uner, T. S. King, M. Pruski, and B. C. Gerstein. Characterization of silica catalyst supports by single and multiple quantum proton NMR spectroscopy. *The Journal of Physical Chemistry*, 99(11):3697–3703, 1995.

[72] A. M. Saib, M. Claeys, and E. Van Steen. Silica supported cobalt fischer–tropsch catalysts: effect of pore diameter of support. *Catalysis today*, 71(3-4):395–402, 2002.

[73] R. Filipović, Z. Obrenović, I. Stijepović, L. M. Nikolić, and V. V. Srdić. Synthesis of mesoporous silica particles with controlled pore structure. *Ceramics International*, 35(8):3347–3353, 2009.

[74] M-Y. Kim, J-H. Park, C-H. Shin, S-W. Han, and G. Seo. Dispersion improvement of platinum catalysts supported on silica, silica-alumina and alumina by titania incorporation and ph adjustment. *Catalysis Letters*, 133(3):288–297, 2009.

[75] R. Van Grieken, G. Calleja, D. Serrano, C. Martos, A. Melgares, and I. Suarez. The role of the hydroxyl groups on the silica surface when supporting metallocene/MAO catalysts. *Polymer Reaction Engineering*, 11(1):17–32, 2003.

[76] S. Bagheri, N. Muhd Julkapli, and S. Bee Abd Hamid. Titanium dioxide as a catalyst support in heterogeneous catalysis. *The Scientific World Journal*, 727496, 2014.

[77] M. Nolan. Modifying ceria (111) with a TiO_2 nanocluster for enhanced reactivity. *The Journal of Chemical Physics*, 139(18):184710, 2013.

[78] R. Palcheva, L. Dimitrov, G. Tyuliev, A. Spojakina, and K. Jiratova. TiO_2 nanotubes supported NiW hydrodesulphurization catalysts: characterization and activity. *Applied Surface Science*, 265:309–316, 2013.

[79] W. Yan, B. Chen, S. M. Mahurin, V. Schwartz, D. R. Mullins, A. R. Lupini, S. J. Pennycook, S. Dai, and S. H. Overbury. Preparation and comparison of supported gold nanocatalysts on anatase, brookite, rutile, and P_{25} polymorphs of TiO_2 for catalytic oxidation of CO. *The Journal of Physical Chemistry B*, 109(21):10676–10685, 2005.

[80] C. P. Slichter. NMR study of platinum catalysts. *Surface Science*, 106(1-3):382–396, 1981.

[81] R. K. Harris, P. Reams, and K. J. Packer. High-resolution solid-state platinum-195 nuclear magnetic resonance. *Journal of the Chemical Society, Dalton Transactions*, (5):1015–1020, 1986.

[82] J. P. Bucher, J. Buttet, J. J. Van Der Klink, M. Graetzel, E. Newson, and T. B. Truong. ^{195}Pt NMR studies of supported catalysts. *Colloids and Surfaces*, 36(2):155–167, 1989.

[83] G. J. Rees, S. T. Orr, L. O. Barrett, J. M. Fisher, J. Houghton, G. H. Spikes, B. R. C. Theobald, D. Thompsett, M. E. Smith, and J. V. Hanna. Characterisation of platinum-based fuel cell catalyst materials using ^{195}Pt wideline solid state NMR. *Physical Chemistry Chemical Physics*, 15(40):17195–17207, 2013.

[84] T. J. N. Hooper, T. A. Partridge, G. J. Rees, D. S. Keeble, N. A. Powell, M. E. Smith, I. P. Mikheenko, L. E. Macaskie, P. T. Bishop, and J. V. Hanna. Direct solid state NMR observation of the ^{105}Pd nucleus in inorganic compounds and palladium metal systems. *Physical Chemistry Chemical Physics*, 20(41):26734–26743, 2018.

[85] H. Mukuda, K. Ishida, Y. Kitaoka, K. Asayama, R. Kanno, and M. Takano. Spin fluctuations in the ruthenium oxides RuO_2, $SrRuO_3$,

$CaRuO_3$, and Sr_2RuO_4 probed by Ru NMR. *Physical Review B*, 60(17):12279, 1999.

[86] H. Mukuda, K. Ishida, Y. Kitaoka, R. Kanno, and M. Takano. Spin fluctuations in ruthenium oxides probed by Ru – NMR. *Physica B: Condensed Matter*, 284:1467–1468, 2000.

[87] J. H. Kwak, J. Z. Hu, D. H. Kim, J. Szanyi, and C. H. F. Peden. Penta-coordinated Al^{3+} ions as preferential nucleation sites for BaO on γ-Al_2O_3: An ultra-high-magnetic field ^{27}Al MAS NMR study. *Journal of Catalysis*, 251(1):189–194, 2007.

[88] J. H. Kwak, J. Hu, D. Mei, C-W. Yi, D. H. Kim, C. H. F. Peden, L. F. Allard, and J. Szanyi. Coordinatively unsaturated Al^{3+} centers as binding sites for active catalyst phases of platinum on γ-Al_2O_3. *Science*, 325(5948):1670–1673, 2009.

[89] H. Zhao, Q. Chen, and S. Zhang. A novel scheme for quantitative characterization of the structures of mesoporous silica by solid-state ^{29}Si NMR. *Microporous and Mesoporous Materials*, 155:240–244, 2012.

[90] T. Kobayashi, D. Singappuli-Arachchige, Z. Wang, I. I. Slowing, and M. Pruski. Spatial distribution of organic functional groups supported on mesoporous silica nanoparticles: A study by conventional and DNP-enhanced ^{29}Si solid-state NMR. *Physical Chemistry Chemical Physics*, 19(3):1781–1789, 2017.

[91] E. Raine, A. H. Clark, G. Smales, A. Smith, D. Gianolio, T. Li, J. Zheng, B. E. Griffith, T. I. Hyde, M. Feaviour, P. Collier, J. V. Hanna, G. Sankar, and S. C. E. Tsang. Synthesis and characterization of platinum nanoparticle catalysts capped with isolated zinc species in SBA-15 cchannels: The wall effect. *ACS Applied Nano Materials*, 1(12):6603–6612, 2018.

[92] J. M. Griffin, L. Clark, V. R. Seymour, D. W. Aldous, D. M. Dawson, D. Iuga, R. E. Morris, and S. E. Ashbrook. Ionothermal ^{17}O enrichment of oxides using microlitre quantities of labelled water. *Chemical Science*, 3(7):2293–2300, 2012.

[93] R. Dervicoğlu, D. S. Middlemiss, F. Blanc, L. A. Holmes, Y-L. Lee, D. Morgan, and C. P. Grey. Joint experimental and computational ^{17}O solid state NMR study of brownmillerite $Ba_2In_2O_5$. *Physical Chemistry Chemical Physics*, 16(6):2597–2606, 2014.

[94] B. C. Schmidt, F. Gaillard, and M. E. Smith. Characterisation of ^{17}O-enriched alumina from a new hydrothermal preparation. *Solid State Nuclear Magnetic Resonance*, 26(3-4):197–202, 2004.

[95] C-H. Chen, E. Gaillard, F. Mentink-Vigier, K. Chen, Z. Gan, P. Gaveau, B. Rebière, R. Berthelot, P. Florian, C. Bonhomme, M. E. Smith, T-X. Métro, B. Alonso, and D. Laurencin. Direct ^{17}O isotopic labeling of oxides using mechanochemistry. *Inorganic Chemistry*, 59(18):13050–13066, 2020.

[96] M. Wang, X-P. Wu, S. Zheng, L. Zhao, L. Li, L. Shen, Y. Gao, N. Xue, X. Guo, W. Huang, Z. Gan, F. Blanc, Z. Yu, X. Ke, W. Ding, X-Q. Gong, C. P. Grey, and L. Peng. Identification of different oxygen species in oxide nanostructures with ^{17}O solid-state NMR spectroscopy. *Science advances*, 1(1):e1400133, 2015.

[97] C. A. Klug, S. Kroeker, P. M. Aguiar, M. Zhou, D. F. Stec, and I. E. Wachs. Insights into oxygen exchange between gaseous O_2 and supported vanadium oxide catalysts via ^{17}O NMR. *Chemistry of Materials*, 21(18):4127–4134, 2009.

[98] G. Ertl, H. Knözinger, and J. Weitkamp. *Preparation of solid catalysts*. John Wiley & Sons, Germany, 2008.

[99] R. Wu and W. H. Weber. The mechanism of the rutile-to-$CaCl_2$ phase transition:RuO_2 and β-PtO_2. *Journal of Physics: Condensed Matter*, 12(30):6725, 2000.

[100] D. R. Lide. *CRC handbook of chemistry and physics*, volume 85. CRC press, United States, 2004.

[101] M. Taoufik, K. C. Szeto, N. Merle, I. D. Rosal, L. Maron, J. Trébosc, G. Tricot, R. M. Gauvin, and L. Delevoye. Heteronuclear NMR spec-

troscopy as a surface-selective technique: A unique look at the hydroxyl groups of γ-alumina. *Chemistry–A European Journal*, 20(14):4038–4046, 2014.

[102] M. Delgado, F. Delbecq, C. Santini, F. Lefebvre, S. Norsic, P. Putaj, P. Sautet, and J-M. Basset. Evolution of structure and of grafting properties of γ-alumina with pretreatment temperature. *The Journal of Physical Chemistry C*, 116(1):834–843, 2012.

[103] W. Li, Q. Wang, J. Xu, F. Aussenac, G. Qi, X. Zhao, P. Gao, C. Wang, and F. Deng. Probing the surface of γ-Al_2O_3 by oxygen-17 dynamic nuclear polarization enhanced solid-state nmr spectroscopy. *Physical Chemistry Chemical Physics*, 20(25):17218–17225, 2018.

[104] X. Li and I-M. Hsing. The effect of the Pt deposition method and the support on Pt dispersion on carbon nanotubes. *Electrochimica Acta*, 51(25):5250–5258, 2006.

[105] S. L. Greasley, S. J. Page, S. Sirovica, S. Chen, R. A. Martin, A. Riveiro, J. V. Hanna, A. E. Porter, and J. R. Jones. Controlling particle size in the Stöber process and incorporation of calcium. *Journal of Colloid and Interface Science*, 469:213–223, 2016.

[106] H.-K. Ting, S. J. Page, G. Poologasundarampillai, S. Chen, B. Yu, J. V Hanna, and J. R. Jones. Phosphate content affects structure and bioactivity of sol-gel silicate bioactive glasses. *International Journal of Applied Glass Science*, 8(4):372–382, 2017.

[107] J. Trébosc, J. W. Wiench, S. Huh, V. S-Y. Lin, and M. Pruski. Solid-state NMR study of MCM-41-type mesoporous silica nanoparticles. *Journal of the American Chemical Society*, 127(9):3057–3068, 2005.

[108] N. Merle, J. Trebosc, A. Baudouin, I. D. Rosal, L. Maron, K. Szeto, M. Genelot, A. Mortreux, M. Taoufik, L. Delevoye, and R. M. Gauvin. ^{17}O NMR gives unprecedented insights into the structure of supported catalysts and their interaction with the silica carrier. *Journal of the American Chemical Society*, 134(22):9263–9275, 2012.

[109] K. V. R. Chary, V. Vijayakumar, P. K. Rao, A. V. Nosov, and V. M. Mastikhin. Characterization of MoO_3TiO_2 catalysts by ^1H magic-angle-spinning NMR spectroscopy. *Journal of Molecular Catalysis A: Chemical*, 96(1):L5–L8, 1995.

[110] M. Crocker, H. M. Ruud, A. E. Wilson, M. Mackay, C. A. Emeis, and A. M. Hoogendoorn. ^1H NMR spectroscopy of titania. chemical shift assignments for hydroxy groups in crystalline and amorphous forms of TiO_2. *Journal of the Chemical Society, Faraday Transactions*, 92(15):2791–2798, 1996.

[111] X. Sun, M. Dyballa, J. Yan, L. Li, N. Guan, and M. Hunger. Solid-state nmr investigation of the $^{16/17}O$ isotope exchange of oxygen species in pure-anatase and mixed-phase TiO_2. *Chemical Physics Letters*, 594:34–40, 2014.

[112] T. J. Bastow, A. F. Moodie, M. E. Smith, and H. J. Whitfield. Characterisation of titania gels by ^{17}O nuclear magnetic resonance and electron diffraction. *Journal of Materials Chemistry*, 3(7):697–702, 1993.

[113] Y. Rao, T. F. Kemp, M. Trudeau, M. E. Smith, and D. M. Antonelli. ^{17}O and ^{15}N solid state NMR studies on ligand-assisted templating and oxygen coordination in the walls of mesoporous Nb, Ta and Ti oxides. *Journal of the American Chemical Society*, 130(46):15726–15731, 2008.

[114] H. Lu, L. Price, and Q. Zhang. Capturing the invisible resource: Analysis of waste heat potential in chinese industry. *Applied energy*, 161:497–511, 2016.

[115] D. M. Rowe. *CRC handbook of thermoelectrics*. CRC press, United Kingdom, 2018.

[116] Y. Feng, X. Jiang, E. Ghafari, B. Kucukgok, C. Zhang, I. Ferguson, and N. Lu. Metal oxides for thermoelectric power generation and beyond. *Advanced Composites and Hybrid Materials*, 1(1):114–126, 2018.

[117] M. N. Hasan, H. Wahid, N. Nayan, and M. S. Mohamed Ali. Inorganic thermoelectric materials: A review. *International Journal of Energy Research*, 44(8):6170–6222, 2020.

[118] G. Chen, M. S. Dresselhaus, G. Dresselhaus, J-P. Fleurial, and T. Caillat. Recent developments in thermoelectric materials. *International Materials Reviews*, 48(1):45–66, 2003.

[119] Y. Pei, X. Shi, A. LaLonde, H. Wang, L. Chen, and G. J. Snyder. Convergence of electronic bands for high performance bulk thermoelectrics. *Nature*, 473(7345):66–69, 2011.

[120] D. Lindley. The energy should always work twice. *Nature News*, 458(7235):138–141, 2009.

[121] X-L. Shi, H. Wu, Q. Liu, W. Zhou, S. Lu, Z. Shao, M. Dargusch, and Z-G. Chen. $SrTiO_3$-based thermoelectrics: Progress and challenges. *Nano Energy*, 78:105195, 2020.

[122] D. Bao, J. Chen, Y. Yu, W. Liu, L. Huang, G. Han, J. Tang, D. Zhou, L. Yang, and Z-G. Chen. Texture-dependent thermoelectric properties of nano-structured Bi_2Te_3. *Chemical Engineering Journal*, 388:124295, 2020.

[123] T. Chen, K. Zhang, H. Wang, W. Su, F. Mehmood, T. Wang, J. Zhai, X. Wang, T. Huo, and C. Wang. The high thermoelectric performance of slightly Sb doped PbTe alloys. *Journal of Materials Chemistry C*, 8(5):1679–1685, 2020.

[124] X-L. Shi, X. Tao, J. Zou, and Z-G. Chen. High-performance thermoelectric SnSe: aqueous synthesis, innovations, and challenges. *Advanced Science*, 7(7):1902923, 2020.

[125] L. Xie, Y. Chen, R. Liu, E. Song, T. Xing, T. Deng, Q. Song, J. Liu, R. Zheng, X. Gao, S. Bai, and L. Chen. Stacking faults modulation for scattering optimization in GeTe-based thermoelectric materials. *Nano Energy*, 68:104347, 2020.

[126] W-D. Liu, L. Yang, and Z-G. Chen. Cu_2Se thermoelectrics: property, methodology, and device. *Nano Today*, 35:100938, 2020.

[127] R. Prasad and S. D. Bhame. Review on texturization effects in thermoelectric oxides. *Materials for Renewable and Sustainable Energy*, 9(1):1–22, 2020.

[128] M. Ito and D. Furumoto. Microstructure and thermoelectric properties of $Na_xCo_2O_{4/}Ag$ composite synthesized by the polymerized complex method. *Journal of alloys and compounds*, 450(1-2):517–520, 2008.

[129] W. J. Weber, C. W. Griffin, and J. L. Bates. Effects of cation substitution on electrical and thermal transport properties of $YCrO_3$ and $LaCrO_3$. *Journal of the American Ceramic Society*, 70(4):265–270, 1987.

[130] N. Van Nong, N. Pryds, S. Linderoth, and M. Ohtaki. Enhancement of the thermoelectric performance of p-type layered oxide $Ca_3Co_4O_{9+\delta}$ through heavy doping and metallic nanoinclusions. *Advanced Materials*, 23(21):2484–2490, 2011.

[131] M. Mikami, E. Guilmeau, R. Funahashi, K. Chong, and D. Chateigner. Enhancement of electrical properties of the thermoelectric compound $Ca_3Co_4O_9$ through use of large-grained powder. *Journal of Materials Research*, 20(9):2491–2497, 2005.

[132] Y. Wang, Y. Sui, H. Fan, X. Wang, Y. Su, W. Su, and X. Liu. High temperature thermoelectric response of electron-doped $CaMnO_3$. *Chemistry of Materials*, 21(19):4653–4660, 2009.

[133] L. Brockway, V. Vasiraju, M. K. Sunkara, and S. Vaddiraju. Engineering efficient thermoelectrics from large-scale assemblies of doped ZnO nanowires: nanoscale effects and resonant-level scattering. *ACS Applied Materials & Interfaces*, 6(17):14923–14930, 2014.

[134] H. Ohta, K. Sugiura, and K. Koumoto. Recent progress in oxide thermoelectric materials: p-type $Ca_3Co_4O_9$ and n-type $SrTiO_3$. *Inorganic Chemistry*, 47(19):8429–8436, 2008.

[135] J. Sun and D. J. Singh. Thermoelectric properties of n-type $SrTiO_3$. *APL Materials*, 4(10):104803, 2016.

[136] Y. Cui, J. R. Salvador, J. Yang, H. Wang, G. Amow, and H. Kleinke. Thermoelectric properties of heavily doped n-type $SrTiO_3$ bulk materials. *Journal of Electronic Materials*, 38(7), 2009.

[137] Y. Li, Q-Y. Hou, X-H. Wang, H-J. Kang, X. Yaer, J-B. Li, T-M. Wang, L. Miao, and J. Wang. First-principles calculations and high thermoelectric performance of La–Nb doped $SrTiO_3$ ceramics. *Journal of Materials Chemistry A*, 7(1):236–247, 2019.

[138] B. Zhang, J. Wang, T. Zou, S. Zhang, X. Yaer, N. Ding, C. Liu, L. Miao, Y. Li, and Y. Wu. High thermoelectric performance of Nb-doped $SrTiO_3$ bulk materials with different doping levels. *Journal of Materials Chemistry C*, 3(43):11406–11411, 2015.

[139] A. V. Kovalevsky, A. A. Yaremchenko, S. Populoh, A. Weidenkaff, and J. R. Frade. Effect of A-site cation deficiency on the thermoelectric performance of donor-substituted strontium titanate. *The Journal of Physical Chemistry C*, 118(9):4596–4606, 2014.

[140] J. Liu, C. L. Wang, W. B. Su, H. C. Wang, J. C. Li, J. L. Zhang, and L. M. Mei. Thermoelectric properties of $Sr_{1-x}Nd_xTiO_3$ ceramics. *Journal of Alloys and Compounds*, 492(1-2):54–56, 2010.

[141] S. R. Popuri, A. J. M. Scott, R. A. Downie, M. A. Hall, E. Suard, R. Decourt, M. Pollet, and J-W. G. Bos. Glass-like thermal conductivity in $SrTiO_3$ thermoelectrics induced by A-site vacancies. *RSC Advances*, 4(64):33720–33723, 2014.

[142] H. C. Wang, C. L. Wang, W. B. Su, J. Liu, Y. Sun, H. Peng, and L. M. Mei. Doping effect of La and Dy on the thermoelectric properties of $SrTiO_3$. *Journal of the American Ceramic Society*, 94(3):838–842, 2011.

[143] Z. Lu, H. Zhang, W. Lei, D. C. Sinclair, and I. M. Reaney. High-figure-of-merit thermoelectric La-doped A-site-deficient $SrTiO_3$ ceramics. *Chemistry of Materials*, 28(3):925–935, 2016.

[144] A. A. Yaremchenko, S. Populoh, S. G. Patricio, J. Macias, P. Thiel, D. P. Fagg, A. Weidenkaff, J. R. Frade, and A. V. Kovalevsky. Boosting thermoelectric performance by controlled defect chemistry engineering in Ta-substituted strontium titanate. *Chemistry of Materials*, 27(14):4995–5006, 2015.

[145] A. V. Kovalevsky, S. Populoh, S. G. Patricio, P. Thiel, M. C. Ferro, D. P. Fagg, J. R. Frade, and A. Weidenkaff. Design of $SrTiO_3$-based thermoelectrics by tungsten substitution. *The Journal of Physical Chemistry C*, 119(9):4466–4478, 2015.

[146] A. Spinelli, M. A. Torija, C. Liu, C. Jan, and C. Leighton. Electronic transport in doped $SrTiO_3$: Conduction mechanisms and potential applications. *Phys. Rev. B*, 81:155110, Apr 2010.

[147] H. Muta, K. Kurosaki, and S. Yamanaka. Thermoelectric properties of reduced and La-doped single-crystalline $SrTiO_3$. *Journal of Alloys and Compounds*, 392(1):306–309, 2005.

[148] U. S. Shenoy and D. Krishna Bhat. Enhanced thermoelectric properties of vanadium doped $SrTiO_3$: A resonant dopant approach. *Journal of Alloys and Compounds*, 832:154958, 2020.

[149] K. Muthamilselvam, M. Mayarani, G. M. Muralikrishna, M. Battabyal, and R. Gopalan. Tuning the optical and thermoelectric properties of $SrTi_{0.8-x}Sn_{0.2}Fe_xO_3$. *Materials Research Express*, 6(4):045905, jan 2019.

[150] P. Blennow, A. Hagen, K. K. Hansen, L. R. Wallenberg, and M. Mogensen. Defect and electrical transport properties of Nb-doped $SrTiO_3$. *Solid State Ionics*, 179(35):2047–2058, 2008.

[151] F. Azough, S. S. Jackson, D. Ekren, R. Freer, M. Molinari, S. R. Yeandel, P. M. Panchmatia, S. C. Parker, D. H. Maldonado, D. M. Kepaptsoglou, and Q. M. Ramasse. Concurrent La and A-site vacancy doping modulates the thermoelectric response of $SrTiO_3$: Experimental and computational evidence. *ACS Applied Materials & Interfaces*, 9(48):41988–42000, 2017.

[152] S. P. Singh, N. Kanas, T. D. Desissa, M. Johnsson, M-A. Einarsrud, T. Norby, and Wiik. K. Thermoelectric properties of A-site deficient La-doped $SrTiO_3$ at 100-900 ^oC under reducing conditions. *Journal of the European Ceramic Society*, 40(2):401–407, 2020.

[153] D. Srivastava, C. Norman, F. Azough, M. C. Schäfer, E. Guilmeau, D. Kepaptsoglou, Q. M. Ramasse, G. Nicotra, and R. Freer. Tuning the thermoelectric properties of A-site deficient $SrTiO_3$ ceramics by vacancies and carrier concentration. *Phys. Chem. Chem. Phys.*, 18:26475–26486, 2016.

[154] T. Zhao, L. M. Daniels, B. Slater, M. J. Rosseinsky, and F. Corà. Effects of octahedral tilting on band structure and thermoelectric power factor of titanate perovskites: A first-principles study on $SrTiO_3$. *The Journal of Physical Chemistry C*, 124(24):13045–13052, 2020.

[155] S. Ohta, T. Nomura, H. Ohta, M. Hirano, H. Hosono, and K. Koumoto. Large thermoelectric performance of heavily Nb-doped $SrTiO_3$ epitaxial film at high temperature. *Applied Physics Letters*, 87(9):092108, 2005.

[156] N. Wang, L. Han, H. He, Y. Ba, and K. Koumoto. Effects of mesoporous silica addition on thermoelectric properties of Nb-doped $SrTiO_3$. *Journal of Alloys and Compounds*, 497(1):308–311, 2010.

[157] K. H. Lee, A. Ishizaki, S. W. Kim, H. Ohta, and K. Koumoto. Preparation and thermoelectric properties of heavily Nb-doped $SrO(SrTiO_3)1$ epitaxial films. *Journal of Applied Physics*, 102(3):033702, 2007.

[158] A. Kinaci, C. Sevik, and T. Çağin. Electronic transport properties of $SrTiO_3$ and its alloys: $Sr_{1-x}La_xTiO_3$ and $SrTi_{1-x}M_xO_3$ (M=Nb, Ta). *Physical Review B*, 82:155114, 2010.

[159] J. Ravichandran, W. Siemons, D-W. Oh, J. T. Kardel, A. Chari, H. Heijmerikx, M. L. Scullin, A. Majumdar, R. Ramesh, and D. G. Cahill. High-temperature thermoelectric response of double-doped $srtio_3$ epitaxial films. *Physical Review B*, 82:165126, 2010.

[160] H. Muta, K. Kurosaki, and S. Yamanaka. Thermoelectric properties of rare earth doped $SrTiO_3$. *Journal of Alloys and Compounds*, 350(1):292–295, 2003.

[161] H.C. Wang, C.L. Wang, W.B. Su, J. Liu, Y. Zhao, H. Peng, J.L. Zhang, M.L. Zhao, J.C. Li, N. Yin, and L.M. Mei. Enhancement of thermoelectric figure of merit by doping Dy in $La_{0.1}Sr_{0.9}TiO_3$ ceramic. *Materials Research Bulletin*, 45(7):809–812, 2010.

[162] Bruker. *TOPAS, version 4.1.* Bruker AXS Inc., Madison, Wisconsin, USA, 2008.

[163] S. J. Clark, M. D. Segall, C. J. Pickard, P. J. Hasnip, M. I. J. Probert, K. Refson, and M. C. Payne. First principles methods using CASTEP. *Zeitschrift für Kristallographie-Crystalline Materials*, 220(5-6):567–570, 2005.

[164] T. Björkman. Cif2cell: Generating geometries for electronic structure programs. *Computer Physics Communications*, 182(5):1183–1186, 2011.

[165] A. H. Larsen, J. J. Mortensen, J. Blomqvist, I. E. Castelli, R. Christensen, M. Dułak, J. Friis, M. N. Groves, B. Hammer, C. Hargus, et al. The atomic simulation environment—a python library for working with atoms. *Journal of Physics: Condensed Matter*, 29(27):273002, 2017.

[166] A. P. Bartók and J. R. Yates. Regularized scan functional. *The Journal of Chemical Physics*, 150(16):161101, 2019.

[167] A. P. Bartók and J. R. Yates. Ultrasoft pseudopotentials with kinetic energy density support: Implementing the tran-blaha potential. *Physical Review B*, 99(23):235103, 2019.

[168] M. Bokdam, J. Lahnsteiner, B. Ramberger, T. Schäfer, and G. Kresse. Assessing density functionals using many body theory for hybrid perovskites. *Physical Review Letters*, 119(14):145501, 2017.

[169] L. B. Pártay, A. P. Bartók, and G. Csányi. Efficient sampling of atomic configurational spaces. *The Journal of Physical Chemistry B*, 114(32):10502–10512, 2010.

[170] C. J. Pickard and F. Mauri. All-electron magnetic response with pseudopotentials: NMR chemical shifts. *Physical Review B*, 63(24):245101, 2001.

[171] J. R. Yates, C. J. Pickard, and F. Mauri. Calculation of nmr chemical shifts for extended systems using ultrasoft pseudopotentials. *Physical Review B*, 76(2):024401, 2007.

[172] V. K. Veerapandiyan, S. Khosravi, G. Canu, A. Feteira, V. Buscaglia, K. Reichmann, and M. Deluca. *b*-site vacancy induced *r*aman scattering in $batio_3$-based ferroelectric ceramics. *Journal of the European Ceramic Society*, 40(13):4684–4688, 2020.

[173] K. C. B. Naidu, T. S. Sarmash, M. Maddaiah, A. G. Kumar, D. J. Rani, V. S. Samyuktha, L. Obulapathi, and T. Subbarao. Structural and electrical properties of *pbo*-doped $srtio_3$ ceramics. *Journal of Ovonic Research*, 11:79–84, 2015.

[174] C. Bonhomme, C. Gervais, N. Folliet, F. Pourpoint, C. Coelho Diogo, J. Lao, E. Jallot, J. Lacroix, J-M. Nedelec, D. Iuga, J. V. Hanna, M. E. Smith, Y. Xiang, J. Du, and D. Laurencin. ^{87}Sr solid-state NMR as a structurally sensitive tool for the investigation of materials: Antiosteoporotic pharmaceuticals and bioactive glasses. *Journal of the American Chemical Society*, 134(30):12611–12628, 2012.

[175] H. T. Kreissl, M. M. J. Li, Y-K. Peng, K. Nakagawa, T. J. N. Hooper, J. V. Hanna, A. Shepherd, T-S. Wu, Y-L. Soo, and S. C. E. Tsang. Structural studies of bulk to nanosize niobium oxides with correlation to their acidity. *Journal of the American Chemical Society*, 139(36):12670–12680, 2017.

[176] J. V. Hanna, K. J. Pike, T. Charpentier, T. F. Kemp, M. E. Smith, B. E. G. Lucier, R. W. Schurko, and L. S. Cahill. A ^{93}Nb solid-state nmr and density functional theory study of four- and six-coordinate niobate systems. *Chemistry – A European Journal*, 16(10):3222–3239, 2010.

[177] L. Protesescu, S. Yakunin, M. I. Bodnarchuk, F. Krieg, R. Caputo, C. H. Hendon, R. X. Yang, A. Walsh, and M. V. Kovalenko. Nanocrystals

of cesium lead halide perovskites ($CsPbX_3$, X= Cl, Br, and I): novel optoelectronic materials showing bright emission with wide color gamut. *Nano Letters*, 15(6):3692–3696, 2015.

[178] J. Butkus, P. Vashishtha, K. Chen, J. K. Gallaher, S. K. K. Prasad, D. Z. Metin, G. Laufersky, N. Gaston, J. E. Halpert, and J. M. Hodgkiss. The evolution of quantum confinement in $CsPbBr_3$ perovskite nanocrystals. *Chemistry of Materials*, 29(8):3644–3652, 2017.

[179] A. A. M. Brown, T.J. N. Hooper, S. A. Veldhuis, X. Y. Chin, A. Bruno, P. Vashishtha, J. N. Tey, L. Jiang, B. Damodaran, S. H. Pu, S. G. Mhaisalkar, and N. Mathews. Self-assembly of a robust hydrogen-bonded octylphosphonate network on cesium lead bromide perovskite nanocrystals for light-emitting diodes. *Nanoscale*, 11(25):12370–12380, 2019.

[180] M. V. Kovalenko, L. Protesescu, and M. I. Bodnarchuk. Properties and potential optoelectronic applications of lead halide perovskite nanocrystals. *Science*, 358(6364):745–750, 2017.

[181] P. Vashishtha, S. A. Veldhuis, S. S. H. Dintakurti, N. L. Kelly, B. E. Griffith, A. A. M. Brown, M. S. Ansari, A. Bruno, N. Mathews, Y. Fang, T. White, S. G. Mhaisalkar, and J. V. Hanna. Investigating the structure–function relationship in triple cation perovskite nanocrystals for light-emitting diode applications. *Journal of Materials Chemistry C*, 8(34):11805–11821, 2020.

[182] Y. Zhou, J. Chen, O. M. Bakr, and H-T. Sun. Metal-doped lead halide perovskites: synthesis, properties, and optoelectronic applications. *Chemistry of Materials*, 30(19):6589–6613, 2018.

[183] S. T. Ha, X. Liu, Q. Zhang, D. Giovanni, T. C. Sum, and Q. Xiong. Synthesis of organic–inorganic lead halide perovskite nanoplatelets: towards high-performance perovskite solar cells and optoelectronic devices. *Advanced Optical Materials*, 2(9):838–844, 2014.

[184] M. Jeong, I. W. Choi, E. M. Go, Y. Cho, M. Kim, B. Lee, S. Jeong, Y. Jo, H. W. Choi, J. Lee, J-H. Bae, S. K. Kwak, D. S. Kim, and

C. Yang. Stable perovskite solar cells with efficiency exceeding 24.8% and 0.3−V voltage loss. *Science*, 369(6511):1615–1620, 2020.

[185] L. Peedikakkandy and P. Bhargava. Composition dependent optical, structural and photoluminescence characteristics of cesium tin halide perovskites. *RSC Advances*, 6(24):19857–19860, 2016.

[186] H. Siddiqui. Lead-free perovskite quantum structures towards the efficient solar cell. *Materials Letters*, 249:99–103, 2019.

[187] R. X. Yang, J. M. Skelton, E. L. Da Silva, J. M. Frost, and A. Walsh. Spontaneous octahedral tilting in the cubic inorganic cesium halide perovskites $CsSnX_3$ and $CsPbX_3$ (X= F, Cl, Br, I). *The Journal of Physical Chemistry Letters*, 8(19):4720–4726, 2017.

[188] T. C. Jellicoe, J. M. Richter, H. F. J. Glass, M. Tabachnyk, R. Brady, S. E. Dutton, A. Rao, R. H. Friend, D. Credgington, N. C. Greenham, and M. L. Bohm. Synthesis and optical properties of lead-free cesium tin halide perovskite nanocrystals. *Journal of the American Chemical Society*, 138(9):2941–2944, 2016.

[189] J. Zhang, Y. Yang, H. Deng, U. Farooq, X. Yang, J. Khan, J. Tang, and H. Song. High quantum yield blue emission from lead-free inorganic antimony halide perovskite colloidal quantum dots. *ACS Nano*, 11(9):9294–9302, 2017.

[190] B. Yang, J. Chen, F. Hong, X. Mao, K. Zheng, S. Yang, Y. Li, T. Pullerits, W. Deng, and K. Han. Lead-free, air-stable all-inorganic cesium bismuth halide perovskite nanocrystals. *Angewandte Chemie*, 129(41):12645–12649, 2017.

[191] P. Vashishtha, G. V. Nutan, B. E. Griffith, Y. Fang, D. Giovanni, M. Jagadeeswararao, T. C. Sum, N. Mathews, S. G. Mhaisalkar, J. V. Hanna, and T. White. Cesium copper iodide tailored nanoplates and nanorods for blue, yellow, and white emission. *Chemistry of Materials*, 31(21):9003–9011, 2019.

[192] B. Yang, X. Mao, F. Hong, W. Meng, Y. Tang, X. Xia, S. Yang, W. Deng, and K. Han. Lead-free direct band gap double-perovskite nanocrystals with bright dual-color emission. *Journal of the American Chemical Society*, 140(49):17001–17006, 2018.

[193] Y. Liu, Y. Jing, J. Zhao, Q. Liu, and Z. Xia. Design optimization of lead-free perovskite $Cs_2AgInCl_6$:Bi nanocrystals with 11.4% photoluminescence quantum yield. *Chemistry of Materials*, 31(9):3333–3339, 2019.

[194] F. Locardi, M. Cirignano, D. Baranov, Z. Dang, M. Prato, F. Drago, M. Ferretti, V. Pinchetti, M. Fanciulli, S. Brovelli, L. D. Trizio, and L. Manna. Colloidal synthesis of double perovskite $Cs_2AgInCl_6$ and Mn-doped $Cs_2AgInCl_6$ nanocrystals. *Journal of the American Chemical Society*, 140(40):12989–12995, 2018.

[195] N. Chen, T. Cai, W. Li, K. Hills-Kimball, H. Yang, M. Que, Y. Nagaoka, Z. Liu, D. Yang, A. Dong, C-Y. Xu, R. Zia, and O. Chen. Yb-and Mn-doped lead-free double perovskite Cs_2AgBiX_6 (X= Cl, Br) nanocrystals. *ACS Applied Materials & Interfaces*, 11(18):16855–16863, 2019.

[196] M. R. Filip, S. Hillman, A. A. Haghighirad, H. J. Snaith, and F. Giustino. Band gaps of the lead-free halide double perovskites $Cs_2BiAgCl_6$ and $Cs_2BiAgBr_6$ from theory and experiment. *The Journal of Physical Chemistry Letters*, 7(13):2579–2585, 2016.

[197] G. Volonakis, A. A. Haghighirad, R. L. Milot, W. H. Sio, M. R. Filip, B. Wenger, M. B. Johnston, L. M. Herz, H. J. Snaith, and F. Giustino. $Cs_2InAgCl_6$: a new lead-free halide double perovskite with direct band gap. *The Journal of Physical Chemistry Letters*, 8(4):772–778, 2017.

[198] J. Zhou, Z. Xia, M. S. Molokeev, X. Zhang, D. Peng, and Q. Liu. Composition design, optical gap and stability investigations of lead-free halide double perovskite $Cs_2AgInCl_6$. *Journal of Materials Chemistry A*, 5(29):15031–15037, 2017.

[199] T. Hu, M. D. Smith, E. R. Dohner, M-J. Sher, X. Wu, M. T. Trinh, A. Fisher, J. Corbett, X-Y. Zhu, H. I. Karunadasa, and A. M. Lin-

denberg. Mechanism for broadband white-light emission from two-dimensional (110) hybrid perovskites. *The Journal of Physical Chemistry Letters*, 7(12):2258–2263, 2016.

[200] J. C. Dahl, W. T. Osowiecki, Y. Cai, J. K. Swabeck, Y. Bekenstein, M. Asta, E. M. Chan, and A. P. Alivisatos. Probing the stability and band gaps of $Cs_2AgInCl_6$ and $Cs_2AgSbCl_6$ lead-free double perovskite nanocrystals. *Chemistry of Materials*, 31(9):3134–3143, 2019.

[201] J. Luo, X. Wang, S. Li, J. Liu, Y. Guo, G. Niu, L. Yao, Y. Fu, L. Gao, Q. Dong, C. Zhao, M. Leng, F. Ma, W. Liang, L. Wang, S. Jin, J. Han, L. Zhang, J. Etheridge, J. Wang, Y. Yan, E. H. Sargent, and J. Tang. Efficient and stable emission of warm-white light from lead-free halide double perovskites. *Nature*, 563(7732):541–545, 2018.

[202] F. Locardi, E. Sartori, J. Buha, J. Zito, M. Prato, V. Pinchetti, M. L. Zaffalon, M. Ferretti, S. Brovelli, I. Infante, L. D. Trizio, and L. Manna. Emissive Bi-doped double perovskite $Cs_2Ag_{1--x}Na_xInCl_6$ nanocrystals. *ACS Energy Letters*, 4(8):1976–1982, 2019.

[203] C-Y. Wang, P. Liang, R-J. Xie, Y. Yao, P. Liu, Y. Yang, J. Hu, L. Shao, X. W. Sun, F. Kang, and G. Wei. Highly efficient lead-free (Bi, Ce)-codoped $Cs_2Ag_{0.4}Na_{0.6}InCl_6$ double perovskites for white light-emitting diodes. *Chemistry of Materials*, 32(18):7814–7821, 2020.

[204] P. Vashishtha, B. E. Griffith, A. A. M. Brown, T. J. N. Hooper, Y. Fang, M. S. Ansari, A. Bruno, S. H. Pu, S. G. Mhaisalkar, T. White, and J. V. Hanna. Performance enhanced light-emitting diodes fabricated from nanocrystalline $CsPbBr_3$ with in situ Zn^{2+} addition. *ACS Applied Electronic Materials*, 2020.

[205] M. Aebli, L. Piveteau, O. Nazarenko, B. M. Benin, F. Krieg, R. Verel, and M. V. Kovalenko. Lead-halide scalar couplings in ^{207}Pb NMR of $APbX_3$ perovskites (A= Cs, methylammonium, formamidinium; X= Cl, Br, I). *Scientific Reports*, 10(1):1–9, 2020.

[206] D. J. Kubicki, D. Prochowicz, A. Pinon, G. Stevanato, A. Hofstetter, S. M. Zakeeruddin, M. Grätzel, and L. Emsley. Doping and phase segre-

gation in Mn^{2+} and Co^{2+} doped lead halide perovskites from ^{133}Cs and ^{1}H NMR relaxation enhancement. *Journal of Materials Chemistry A*, 7(5):2326–2333, 2019.

[207] A. A. M. Brown, P. Vashishtha, T. J. N. Hooper, Y. F. Ng, G. V. Nutan, Y. Fang, D. Giovanni, J. N. Tey, L. Jiang, B. Damodaran, T. C. Sum, S. H. Pu, S. G. Mhaisalkar, and N. Mathews. Precise control of $CsPbBr_3$ perovskite nanocrystal growth at room temperature: Size tunability and synthetic insights. *Chemistry of Materials*, 2021.

[208] A. Karmakar, G. M. Bernard, A. Meldrum, A. O. Oliynyk, and V. K. Michaelis. Tailorable indirect to direct band-gap double perovskites with bright white-light emission: Decoding chemical structure using solid-state NMR. *Journal of the American Chemical Society*, 142(24):10780–10793, 2020.

[209] A. Karmakar, A. Bhattacharya, G. M. Bernard, A. Mar, and V. K. Michaelis. Revealing the local Sn and Pb arrangements in $CsSn_xPb_{1-x}Br_3$ perovskites with solid-state NMR spectroscopy. *ACS Materials Letters*, 3(3):261–267, 2021.

[210] D. J. Kubicki, M. Saski, S. MacPherson, K. Galkowski, J. Lewinski, D. Prochowicz, J. J. Titman, and S. D. Stranks. Halide mixing and phase segregation in Cs_2AgBiX_6 (X= Cl, Br, and I) double perovskites from cesium-133 solid-state NMR and optical spectroscopy. *Chemistry of Materials*, 32(19):8129–8138, 2020.

[211] I. L. Moudrakovski and J. A. Ripmeester. ^{39}K NMR of solid potassium salts at 21 T: effect of quadrupolar and chemical shift tensors. *The Journal of Physical Chemistry B*, 111(3):491–495, 2007.

[212] C. J. Pickard and R. J. Needs. Ab initio random structure searching. *Journal of Physics: Condensed Matter*, 23(5):053201, 2011.

[213] C. J. Pickard and R. J. Needs. Structure of phase iii of solid hydrogen. *Nature Physics*, 3(7):473–476, 2007.

[214] J. Li. Atomeye: an efficient atomistic configuration viewer. *Modelling and Simulation in Materials Science and Engineering*, 11(2):173, 2003.

[215] A. R. Denton and N. W. Ashcroft. Vegard's law. *Physical Review A*, 43(6):3161, 1991.

[216] Y. Bekenstein, J. C. Dahl, J. Huang, W. T. Osowiecki, J. K. Swabeck, E. M. Chan, P. Yang, and A. P. Alivisatos. The making and breaking of lead-free double perovskite nanocrystals of cesium silver–bismuth halide compositions. *Nano Letters*, 18(6):3502–3508, 2018.

[217] F. Moser and S. Lyu. Luminescence in pure and I-doped AgBr crystals. *Journal of Luminescence*, 3(6):447–458, 1971.

[218] F. Benachenhou, G. Mairesse, G. Nowogrocki, and D. Thomas. Structural studies of Cs-K-Bi mixed chlorides relation to the crystal structures of A_2BMX_6, A_3MX_6, and A_2MX_6. *Journal of Solid State Chemistry*, 65(1):13–26, 1986.

[219] T. Guedira, J. P. Wignacourt, M. Drache, A. Lorriaux-Rubbens, and F. Wallart. Phase transition in a chloro-elpasolite, Cs_2KInCl_6. *Phase Transitions*, 13(1-4):81–85, 1988.

[220] J. Zhou, Z. Xia, M. S. Molokeev, X. Zhang, D. Peng, and Q. Liu. Composition design, optical gap and stability investigations of lead-free halide double perovskite $Cs_2AgInCl_6$. *Journal of Materials Chemistry A*, 5(29):15031–15037, 2017.

[221] Q. Liao, Q. Meng, L. Jing, J. Pang, Q. Pang, and J. Z. Zhang. Highly emissive and stable $Cs_2AgInCl_6$ double perovskite nanocrystals by Bi^{3+} doping and potassium bromide surface passivation. *The Journal of Physical Chemistry C*, 2021.

[222] A. Kanwat, N. Yantara, Y. F. Ng, T. J. N. Hooper, P. J. S. Rana, B. Febriansyah, P. C. Harikesh, T. Salim, P. Vashishtha, S. G. Mhaisalkar, et al. Stabilizing the electroluminescence of halide perovskites with potassium passivation. *ACS Energy Letters*, 5(6):1804–1813, 2020.

[223] B. Zhang, M. Wang, M. Ghini, A. E. M. Melcherts, J. Zito, L. Goldoni, I. Infante, M. Guizzardi, F. Scotognella, I. Kriegel, et al. Colloidal Bi-doped $Cs_2Ag_{1-x}Na_xInCl_6$ nanocrystals: Undercoordinated surface Cl ions limit their light emission efficiency. *ACS Materials Letters*, 2(11):1442–1449, 2020.

Appendix A

Solid State NMR Investigations of Heterogenous Catalysts on Metal Oxide Supports

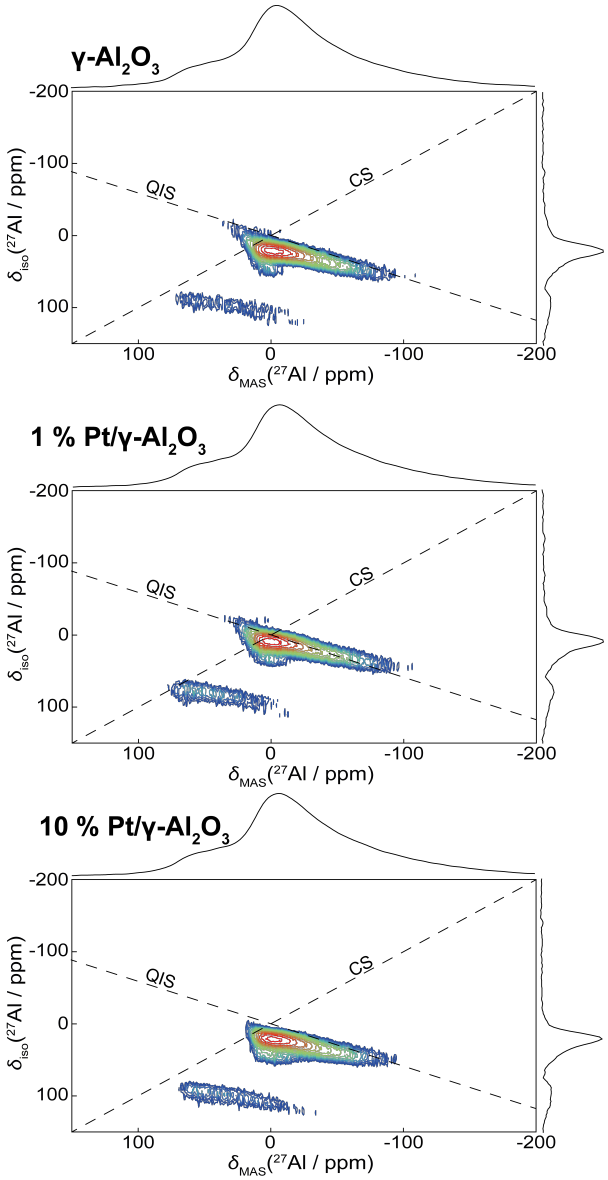

Figure A.1: Sheared solid state ^{27}Al 3QMAS NMR spectra (B_0 = 4.7 T, ν_r = 20 kHz) of γ-Al_2O_3, 1 and 10 % weighted Pt/γ-Al_2O_3 synthesised via a co-precipitation method and subsequently calcined at 500 ^{o}C.

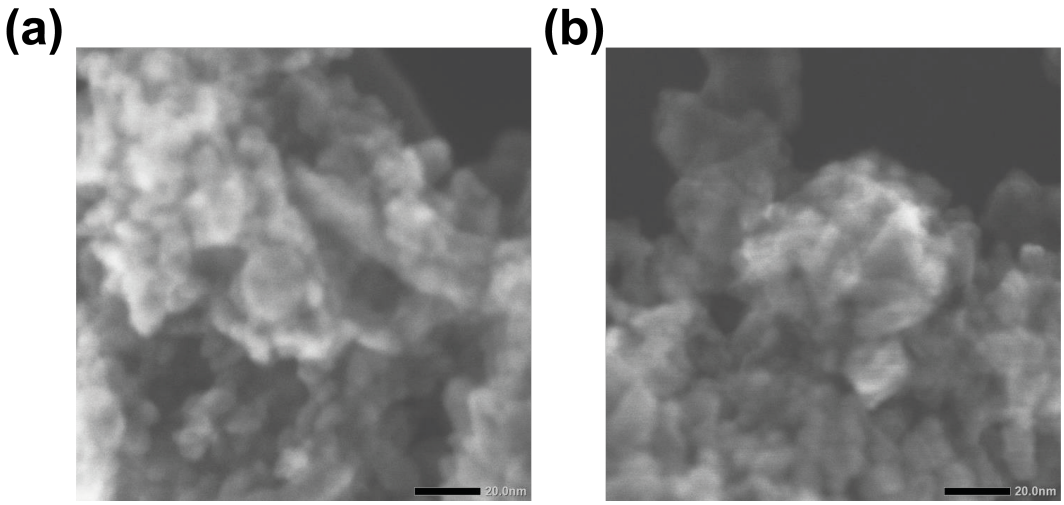

Figure A.2: STEM images of (a) 1 % and (b) 10 % weighted Pt/γ-Al_2O_3 synthesised using a precipitation deposition method and calcined at 500 ^{o}C.

Table A.1: ^{17}O solid state MAS NMR parameters obtained from linear graphical fits of γ-Al_2O_3, 10 wt% Pt/γ-Al_2O_3 and 10 wt% Ni/γ-Al_2O_3 determined from spectra in Figure 4.12.

Sample	Site	δ_{iso} (± 4 ppm)	P_Q (± 0.5 MHz)	R.I. (± 5 %)
γ-Al_2O_3	-OH	43	4.4	46
	AlO_3	68	3.5	38
	AlO_4	79	2.1	16
10% Pt/γ-Al_2O_3	Al-O-Pt	−1	-	28
	-OH	33	5.4	16
	AlO_3	64	3.6	40
	AlO_4	77	2.0	16
10% Ni/γ-Al_2O_3	-OH	30	4.0	46
	AlO_3	64	3.8	33
	AlO_4	75	1.8	21

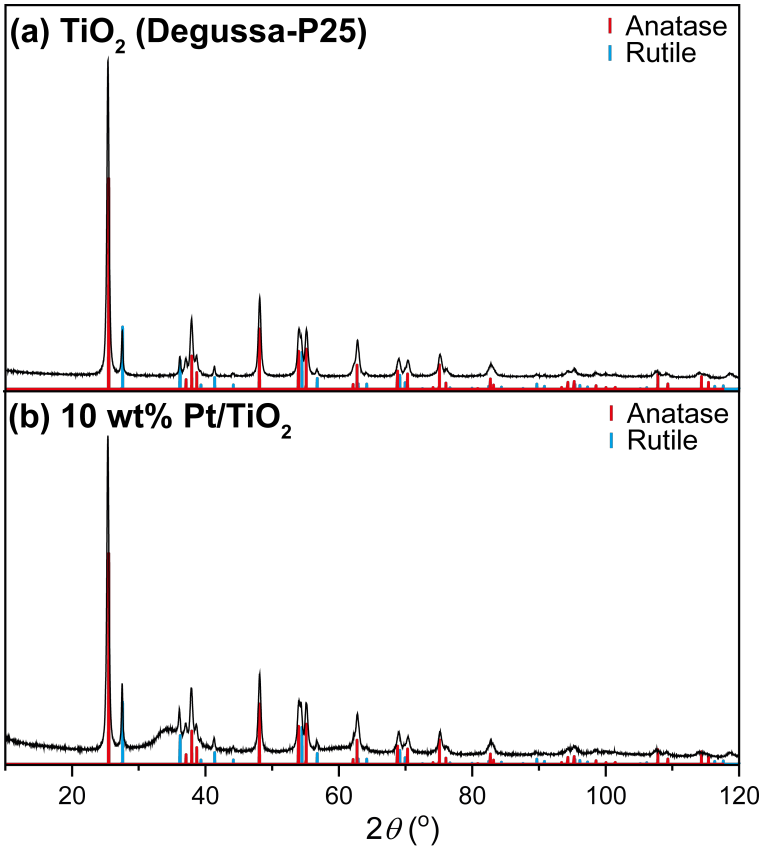

Figure A.3: PXRD patterns of (a) TiO_2 and (b) 10 % Pt/TiO_2 showing the presence of anatase (red) and rutile (blue).

Table A.2: Solid state ^{17}O and ^{1}H MAS NMR parameters obtained from spectral deconvolutions of TiO_2 and 10 wt% Pt/TiO_2. ^{17}O parameters were determined from the fitting of data across three fields showing isotropic chemical shifts (δ_{iso}), quadrupolar coupling constants (C_Q) and assymetry (η_Q).

Sample	Site	^{17}O MAS NMR				^{1}H MAS NMR	
		δ_{iso} (± 2 ppm)	C_Q (± 0.2 MHz)	η_Q (± 0.1)	Rel. Int. (± 3 %)	δ_{iso} (± 0.2 ppm)	Rel. Int. (± 2 %)
TiO_2	Distorted OTi_3/surface OTi_4	520	1.7	0.8	7	1.0	56
	Distorted OTi_3/surface OTi_4	547	1.6	0.6	9	4.0	9
	OTi_3 (Anatase)	562	1.1	0.6	60	6.3	35
	OTi_3 in low-ordered TiO_2	577	1.5	0.2	7		
	OTi_3 (Rutile)	600	1.8	0.6	17		
10 % Pt/TiO_2	Distorted OTi_3/surface OTi_4	522	1.8	0.8	5	1.2	13
	Distorted OTi_3/surface OTi_4	549	1.6	0.6	8	2.0	17
	OTi_3 (Anatase)	562	1.1	0.6	51	5.7	70
	OTi_3 in low-ordered TiO_2	575	1.6	0.2	8		
	OTi_3 (Rutile)	600	1.8	0.6	28		

Appendix B

Quadrupolar Solid State NMR Investigations of High Temperature Thermoelectric Materials

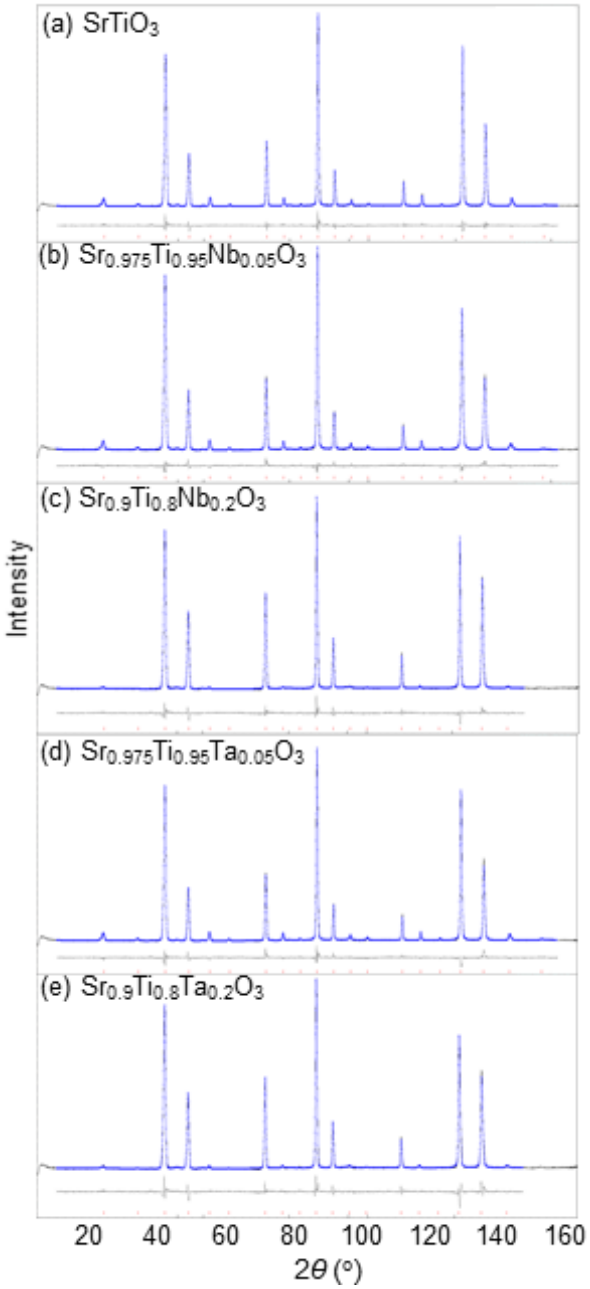

Figure B.1: Neutron diffraction Rietveld refinements of (a) $SrTiO_3$, $Sr_{(1-x/2)}Ti_{(1-x)}Nb_xO_3$ for (b) $x = 0.05$ and (c) $x = 0.2$ and $Sr_{(1-x/2)}Ti_{(1-x)}Ta_xO_3$ for (d) $x = 0.05$ and (e) $x = 0.2$. The content of Cu is from the Cu foil covered outside the neutron sample holder. The differences (grey line) between observed (black line) and calculated pattern (blue dots) are shown.

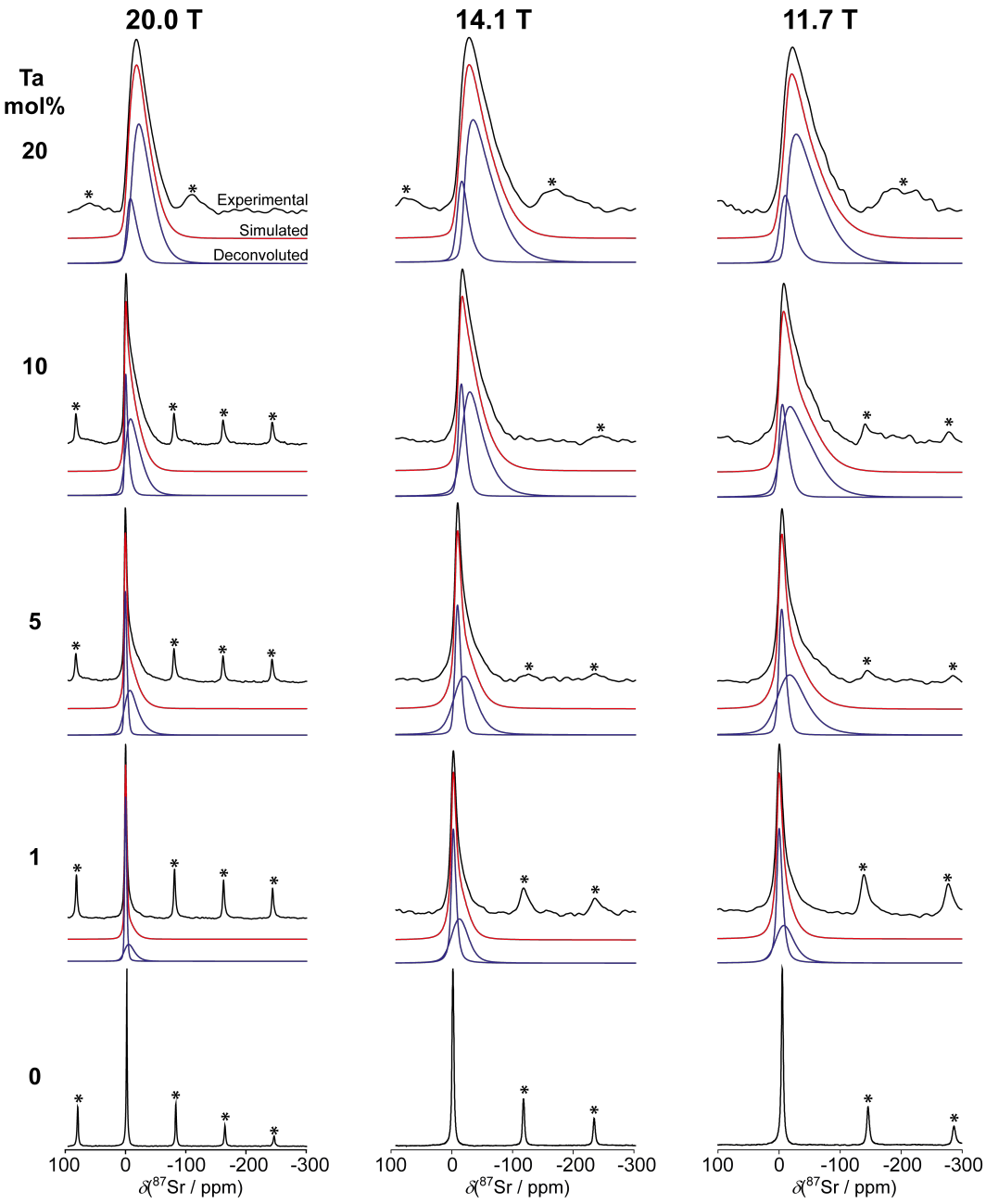

Figure B.2: Solid state ^{87}Sr MAS NMR (ν_r = 3 kHz) spectra of (a) $Sr_{(1-x/2)}Ti_{(1-x)}Ta_xO_3$ for x = 0, 0.01, 0.05, 0.1 and 0.2. Spectra are acquired at 20.0, 14.1 and 11.7 T and are shown together with their corresponding simulated (red) and deconvoluted fits (blue). Spinning sidebands are marked using an $*$.

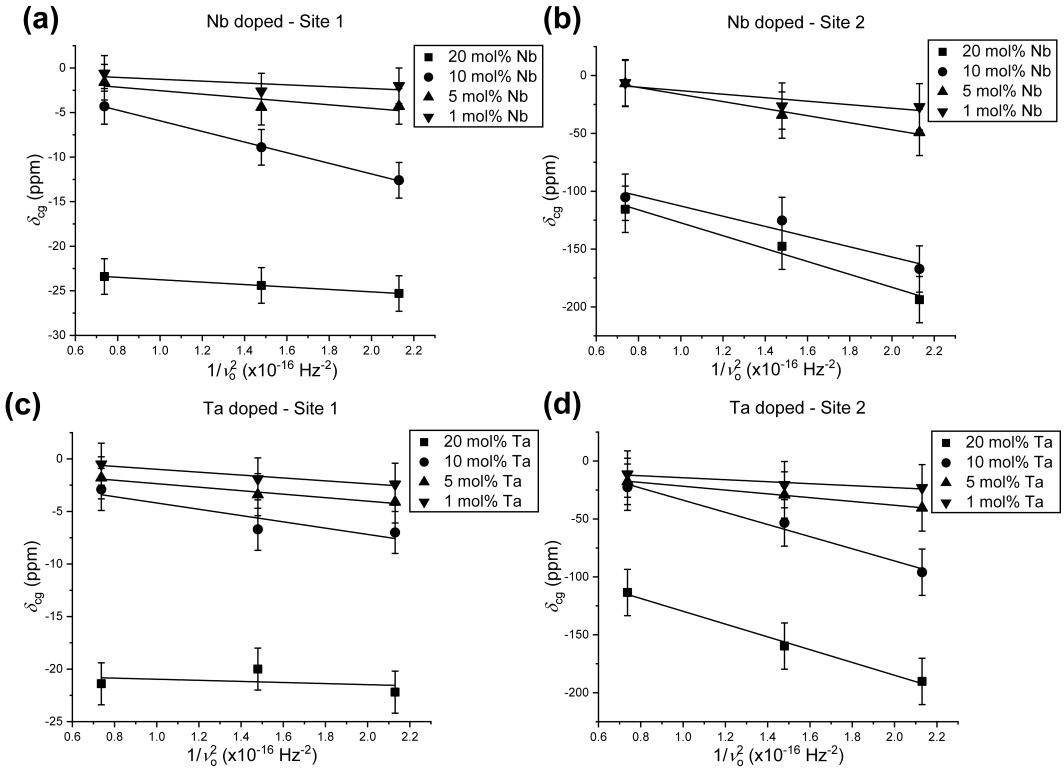

Figure B.3: Centre of gravity chemical shifts plotted against the $1/\nu_o^2$ for corresponding ^{87}Sr solid state MAS NMR spectra of $Sr_{(1-x/2)}Ti_{(1-x)}Nb_xO_3$ shown in (a) for site 1 and (b) for site 2 as well as fits for $Sr_{(1-x/2)}Ti_{(1-x)}Ta_xO_3$ in (c) and (d) for sites 1 and 2 respectively.

Table B.1: Solid state ^{87}Sr MAS NMR parameters obtained from spectral disordered quadrupolar lineshape simulations using QuadFit and graphical linear fit plots of δ_{cg} against $1/\nu_o^2$ from MAS ^{87}Sr data.

Dopant	mol%	Site	Averaged Parameters - QuadFit					Graphical fit	
			δ_{iso} (± 4 ppm)	η_Q (± 0.1)	C_Q (±3 MHz)	C_Q dist. (±2 MHz)	R.I. (±4 %)	δ_{iso} (± 4 ppm)	P_Q (±2 MHz)
Nb	20	1	−5	0.2	2	2	14	−10	1
		2	−6	0.3	4	2	86	−35	4
	10	1	−1	0.1	2	1	24	−5	1
		2	−6	0.1	4	2	76	−21	3
	5	1	−5	0	1	1	39	−1	1
		2	−6	0	3	2	61	−9	4
	1	1	−5	0	1	1	47	0	1
		2	−6	0	2	2	53	−1	3
Ta	20	1	−5	0.2	2	2	14	−10	1
		2	−6	0.3	4	2	86	−35	4
	10	1	−1	0.1	2	1	24	−5	1
		2	−6	0.1	4	2	76	−21	3
	5	1	−5	0	1	1	39	−1	1
		2	−6	0	3	2	61	−9	4
	1	1	−5	0	1	1	47	0	1
		2	−6	0	2	2	53	−1	3

Appendix C

Structural Elucidation of Metal Cation Incorporated Double Perovskite Nanocrystals

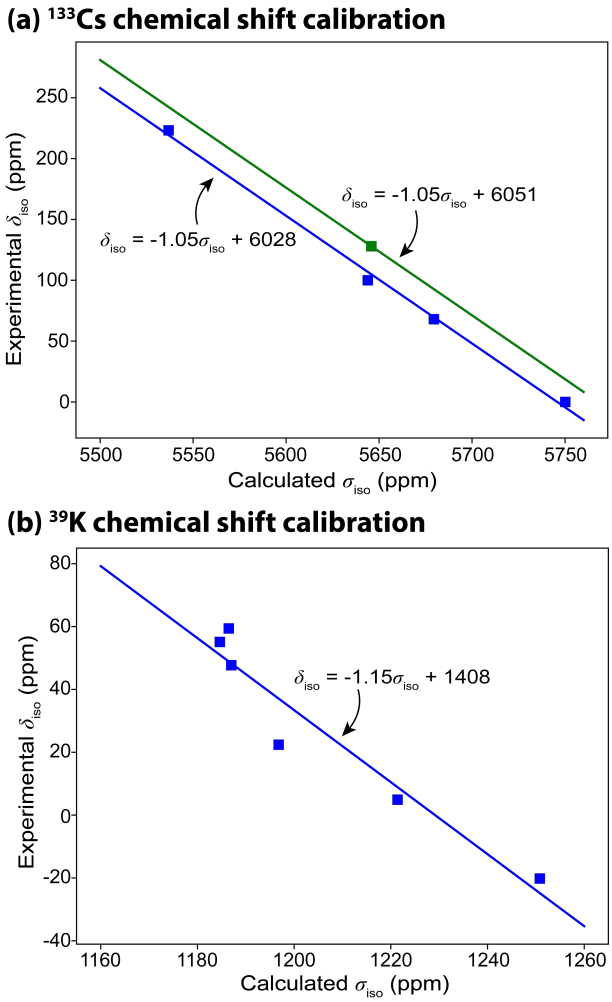

Figure C.1: Calculated σ_{iso}/experimental δ_{iso} calibration curves relating, (a) the experimentally measured ^{133}Cs shifts and DFT calculated shieldings, and (b) the experimentally measured ^{39}K shifts and DFT calculated shieldings.

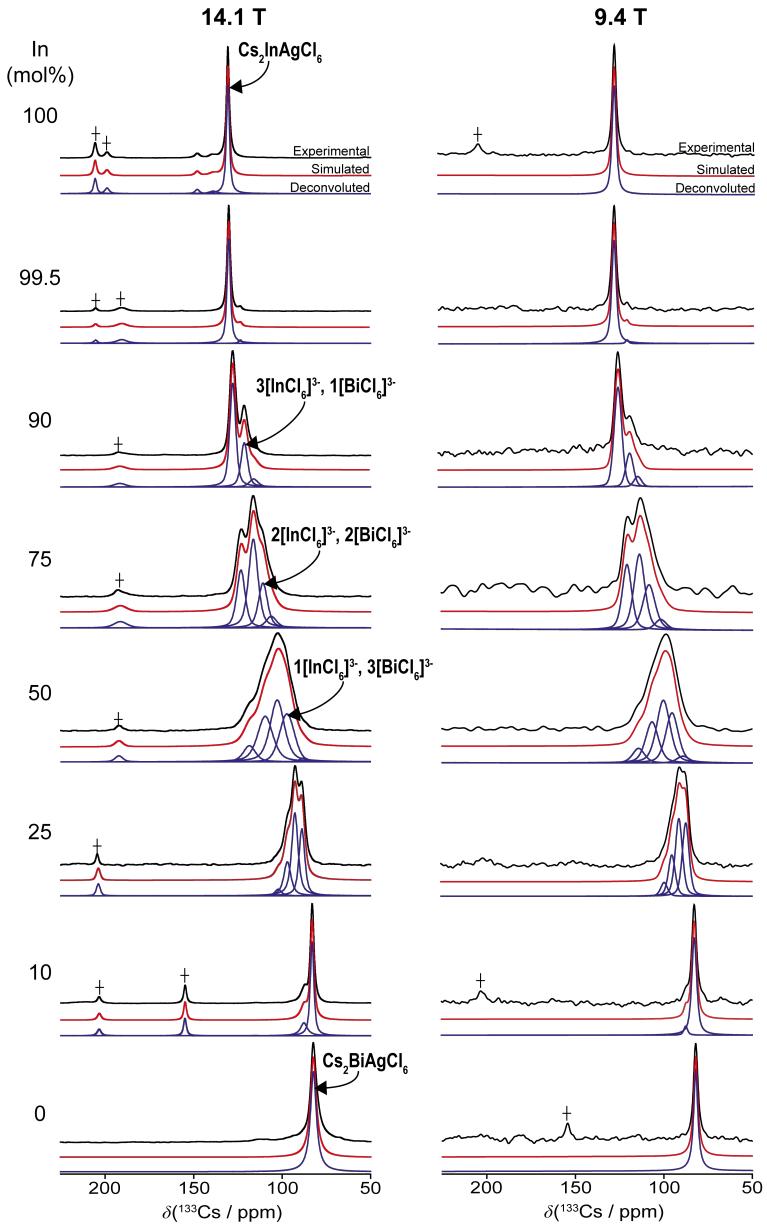

Figure C.2: ^{133}Cs MAS NMR data (ν_r = 12 kHz) from the $Cs_2In_xBi_{1-x}AgCl_6$ (x = 0 - 1) nanocrystal series measured at magnetic field strengths of 14.1 and 9.4 T. Spectral simulations and deconvolutions are shown together with resonance assignments for the different octahedral substitution arrangements about each Cs position. The resonances attributed to impurities are indicated with a '†'.

Table C.1: The ^{133}Cs isotropic chemical shifts (δ_{iso}), relative intensities, full-width-half-maximum (FWHM) and T_1 relaxation time data from the $Cs_2In_xBi_{1-x}AgCl_6$ (x = 0 - 1) nanocrystal compositional series measured at magnetic field strengths of 14.1 and 9.4 T (see Figure C.2). The T_1 values were determined using the saturation-recovery technique.

In content (%)	Site	14.1 T δ_{iso} (± 1 ppm)	14.1 T Rel. Int. (± 2 %)	14.1 T FWHM (± 20 Hz)	14.1 T T_1 (± 20 s)	9.4 T δ_{iso} (± 1 ppm)	9.4 T Rel. Int. (± 2 %)	9.4 T FWHM (± 20 Hz)	9.4 T T_1 (± 20 s)
100	$Cs_2InAgCl_6$	128	100	160	290	128	100	150	200
99.5	$3[InCl_6]^{3-}$,$1[BiCl_6]^{3-}$	121	3	170	420	121	2	110	350
	$Cs_2InAgCl_6$	128	97	170	720	127	98	160	500
90	$2[InCl_6]^{3-}$,$2[BiCl_6]^{3-}$	114	7	360	360	114	7	260	320
	$3[InCl_6]^{3-}$,$1[BiCl_6]^{3-}$	119	30	350	490	119	23	260	440
	$Cs_2InAgCl_6$	126	63	310	500	125	70	260	400
75	$1[InCl_6]^{3-}$,$3[BiCl_6]^{3-}$	104	7	560	270	102	6	400	230
	$2[InCl_6]^{3-}$,$2[BiCl_6]^{3-}$	109	22	480	400	108	26	430	260
	$3[InCl_6]^{3-}$,$1[BiCl_6]^{3-}$	114	45	490	440	114	39	380	270
	$Cs_2InAgCl_6$	121	26	440	470	121	29	430	290
50	$Cs_2BiAgCl_6$	87	1	780	70	89	4	440	20
	$1[InCl_6]^{3-}$,$3[BiCl_6]^{3-}$	96	26	780	270	95	28	440	80
	$2[InCl_6]^{3-}$,$2[BiCl_6]^{3-}$	102	36	750	260	100	37	470	110
	$3[InCl_6]^{3-}$,$1[BiCl_6]^{3-}$	109	29	800	100	107	23	450	60
	$Cs_2InAgCl_6$	118	8	740	30	114	8	420	30
25	$Cs_2BiAgCl_6$	88	32	300	340	88	34	240	200
	$1[InCl_6]^{3-}$,$3[BiCl_6]^{3-}$	92	44	330	270	91	39	250	200
	$2[InCl_6]^{3-}$,$2[BiCl_6]^{3-}$	96	20	330	340	95	20	240	210
	$3[InCl_6]^{3-}$,$1[BiCl_6]^{3-}$	102	4	270	30	100	7	240	170
10	$Cs_2BiAgCl_6$	83	77	190	400	83	93	170	300
	$1[InCl_6]^{3-}$,$3[BiCl_6]^{3-}$	87	23	170	280	88	7	130	220
0	$Cs_2BiAgCl_6$	82	100	170	220	82	100	150	200

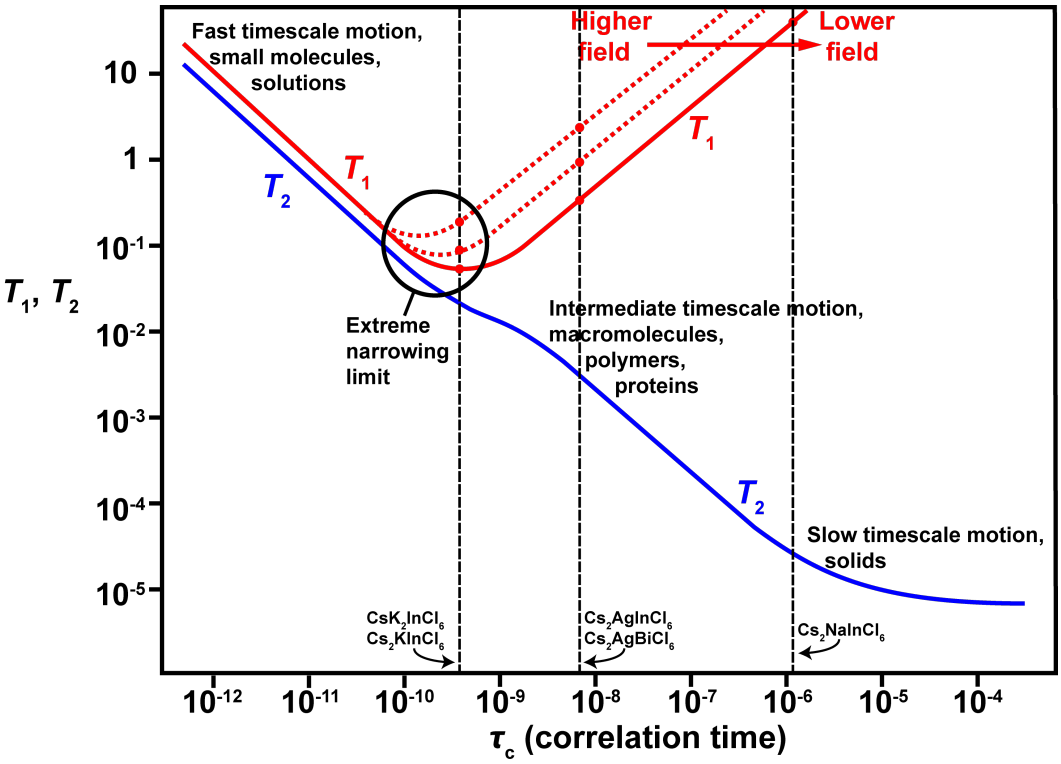

Figure C.3: A diagrammatic representation showing the variation in longitudinal (T_1) and transverse (T_2) relaxation times with correlation time of motion (τ_c) under the influence of a dipolar relaxation mechanism. The approximate location of ^{133}Cs T_1 relaxation times from the Cs_2AInCl_6 (A = Na, K) and Cs_2AgBCl_6 (B = In, Bi) systems determined from saturation-recovery experiments are indicated, highlighting the large variations in reported T_1 values and Cs^+ mobility within these materials.

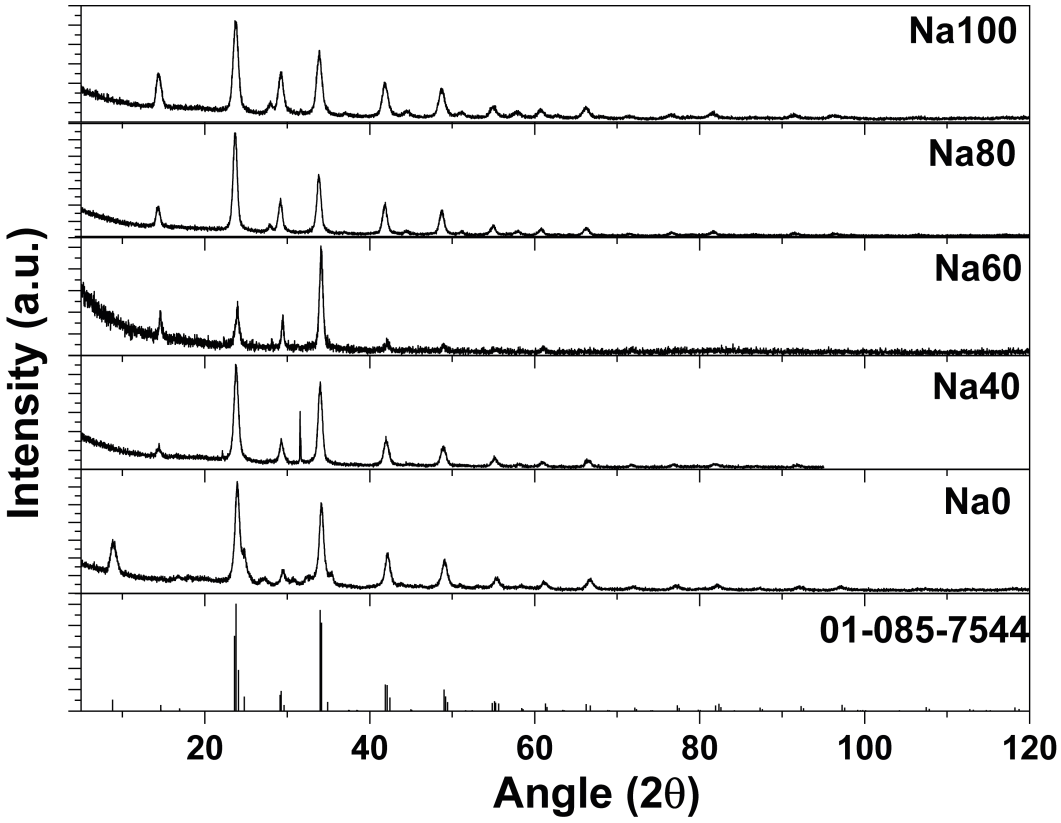

Figure C.4: Powder X-ray diffraction data from the $Cs_2Na_xAg_{1-x}InCl_6$:Bi (x = 0 - 1) nanocrystal series. All diffraction peaks were matched against a standard $Cs_2AgInCl_6$ cubic perovskite phase (PDF: 01-085-7544).

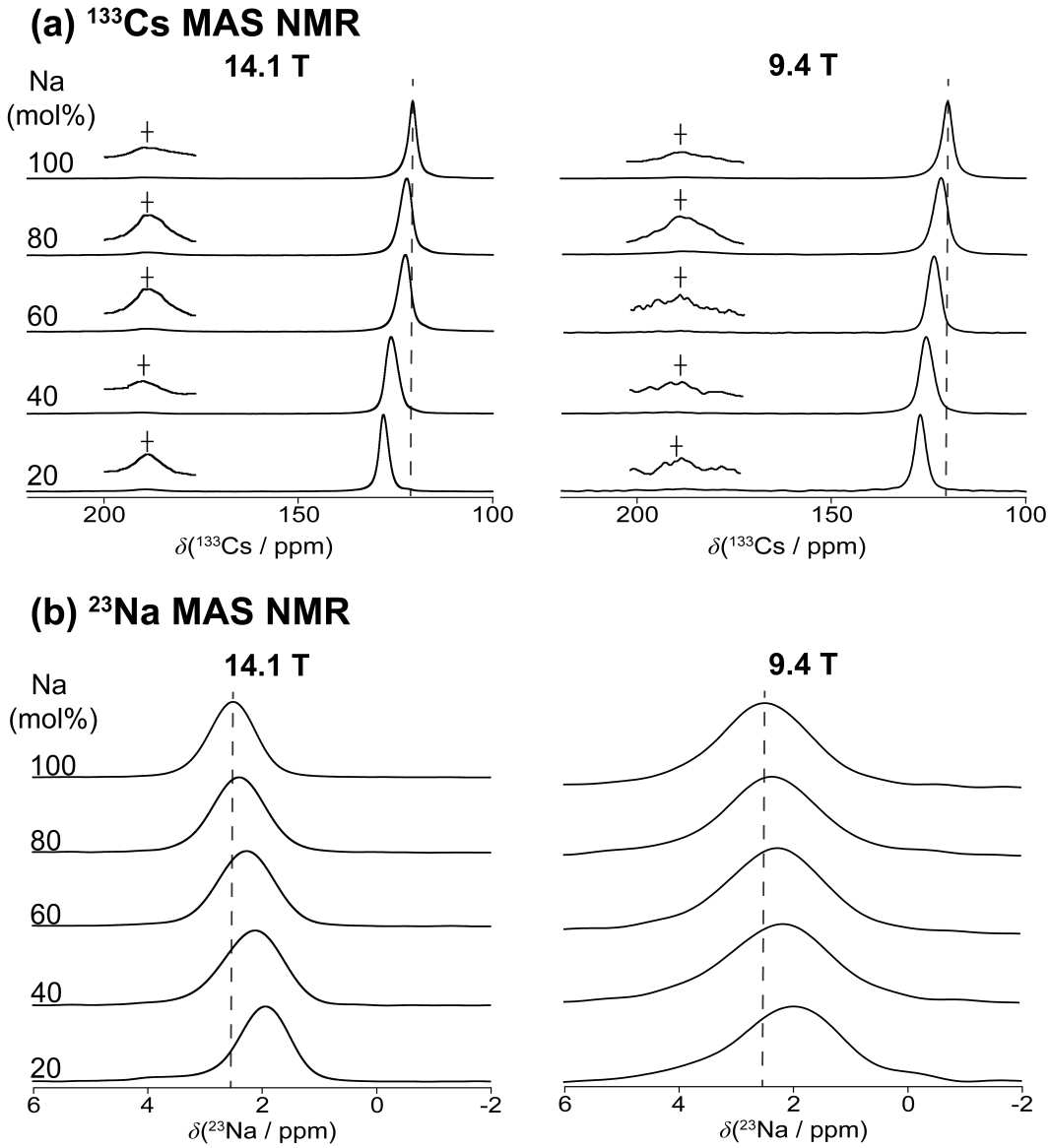

Figure C.5: Solid state NMR study of the $Cs_2Na_xAg_{1-x}InCl_6$:Bi (x = 0.2 - 1) nanocrystal series showing (a) ^{133}Cs MAS NMR data (B_0 = 14.1 & 9.4 T, ν_r = 12 kHz), (b) ^{23}Na MAS NMR data (B_0 = 14.1 & 9.4 T, ν_r = 12 kHz). The low-intensity resonance in the ^{133}Cs MAS NMR data at $\delta\sim$190 ppm denoted with a '†' indicates the presence of a minor $CsInCl_4$ impurity.

Table C.2: The ^{133}Cs NMR parameters, including isotropic chemical shifts (δ_{iso}), full-width-half-maximum (FWHM) and T_1 relaxation time data from the $Cs_2Na_xAg_{1-x}InCl_6$:Bi (x = 0.2 - 1) nanocrystal series measured at magnetic field strengths of 14.1 and 9.4 T (see Figure C.5). The T_1 values were determined using the saturation-recovery technique.

Na content (%)	Site	14.1 δ_{iso} (± 0.5 ppm)	14.1 T_1 (± 10 s)	14.1 FWHM (± 10 Hz)	9.4 δ_{iso} (± 0.5 ppm)	9.4 T_1 (± 1 s)	9.4 FWHM (± 10 Hz)
100	$Cs_2InNaCl_6$/ $Cs_2InAgCl_6$	120.9	200	450	120.2	190	380
80	$Cs_2InNaCl_6$/ $Cs_2InAgCl_6$	122.6	290	410	122.2	190	390
60	$Cs_2InNaCl_6$/ $Cs_2InAgCl_6$	124.5	300	780	123.8	200	470
40	$Cs_2InNaCl_6$/ $Cs_2InAgCl_6$	126.5	270	740	125.8	220	590
20	$Cs_2InNaCl_6$/ $Cs_2InAgCl_6$	128.0	230	720	127.3	180	450

Table C.3: The ^{23}Na NMR parameters, including isotropic chemical shifts (δ_{iso}), full-width-half-maximum (FWHM) and T_1 relaxation time data from the $Cs_2Na_xAg_{1-x}InCl_6$:Bi (x = 0.2 - 1) nanocrystal series measured at magnetic field strengths of 14.1 and 9.4 T (see Figure C.5). The T_1 values were determined using the saturation-recovery technique.

Na content (%)	Site	14.1 δ_{iso} (± 0.2 ppm)	14.1 T_1 (± 1 s)	14.1 FWHM (± 10 Hz)	9.4 δ_{iso} (± 0.2 ppm)	9.4 T_1 (± 1 s)	9.4 FWHM (± 10 Hz)
100	$Cs_2InNaCl_6$	2.5	10	180	2.5	9	220
80	$Cs_2InNaCl_6$	2.4	9	190	2.4	10	210
60	$Cs_2InNaCl_6$	2.3	11	210	2.3	10	230
40	$Cs_2InNaCl_6$	2.1	11	200	2.2	9	230
20	$Cs_2InNaCl_6$	2.0	11	180	2.0	10	230

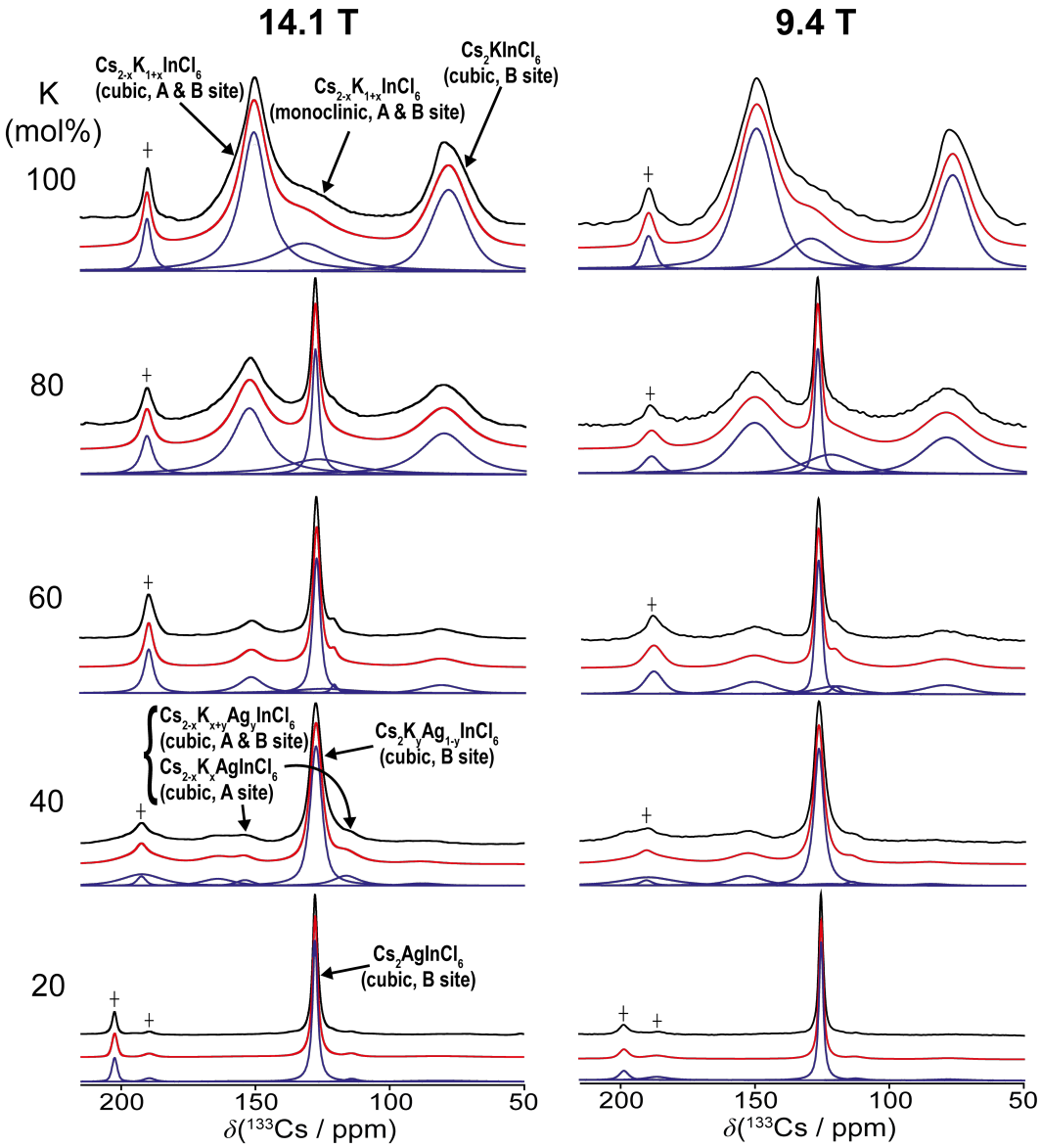

Figure C.6: ^{133}Cs MAS NMR data ($\nu_r = 12$ kHz) from the $Cs_2K_xAg_{1-x}InCl_6$:Bi ($x = 0.2$ - 1) nanocrystal series measured at magnetic field strengths of 14.1 and 9.4 T. Spectral simulations and deconvolutions are shown together with resonance assignments for the different octahedral substitution arrangements about each Cs position. The low-intensity resonance at $\delta\sim$190 ppm denoted with a '†' indicates the presence of a minor $CsInCl_4$ impurity.

Table C.4: The ^{133}Cs isotropic chemical shifts (δ_{iso}), relative intensities, full-width-half-maximum (FWHM) and T_1 relaxation time data from the $Cs_2K_xAg_{1-x}InCl_6$:Bi (x = 0.2 - 1) nanocrystal series measured at magnetic field strengths of 14.1 and 9.4 T (see Figure C.6). The T_1 values were determined using the saturation-recovery technique.

K content (%)	Site	14.1 T δ (± 4 ppm)	14.1 T T_1 (s)	14.1 T FWHM (Hz, ±10%)	9.4 T δ (± 4 ppm)	9.4 T T_1 (s)	9.4 T FWHM (Hz, ±10%)
100	Cs_2KInCl_6 (cubic, B site)	78	9 ± 3	1270	77	5 ± 3	800
	$Cs_{2-x}K_{1+x}InCl_6$ (monoclinic, A & B site)	132	6 ± 3	2160	129	5 ± 3	1180
	$Cs_{2-x}K_{1+x}InCl_6$ (cubic, A & B site)	151	3 ± 1	930	150	2 ± 1	880
80	Cs_2KInCl_6 (cubic, B site)	80	21 ± 3	1660	80	6 ± 3	1110
	$Cs_2AgInCl_6$ (cubic, B site) / $Cs_2K_yAg_{1-y}InCl_6$ (cubic, B site)	128	340 ± 20	240	127	220 ± 20	150
	$Cs_{2-x}K_xAgInCl_6$ (cubic, A site) / $Cs_{2-x}K_{x+y}Ag_yInCl_6$ (cubic, A & B site)	153	3 ± 1	1170	151	3 ± 1	1030
60	Cs_2KInCl_6 (cubic, B site)	82	18 ± 3	1420	80	8 ± 3	1010
	$Cs_2AgInCl_6$ (cubic, B site) / $Cs_2K_yAg_{1-y}InCl_6$ (cubic, B site)	128	490 ± 20	250	127	370 ± 20	160
	$Cs_{2-x}K_xAgInCl_6$ (cubic, A site) / $Cs_{2-x}K_{x+y}Ag_yInCl_6$ (cubic, A & B site)	152	6 ± 2	950	151	4 ± 2	900
40	$Cs_2AgInCl_6$ (cubic, B site) / $Cs_2K_yAg_{1-y}InCl_6$ (cubic, B site)	128	240 ± 20	410	127	160 ± 20	230
	$Cs_{2-x}K_xAgInCl_6$ (cubic, A site) / $Cs_{2-x}K_{x+y}Ag_yInCl_6$ (cubic, A & B site)	153	16 ± 3	590	154	12 ± 3	550
20	$Cs_2AgInCl_6$ bulk (cubic, B site)	128	500 ± 20	180	128	410 ± 20	100

Table C.5: The ^{39}K isotropic chemical shifts (δ_{iso}), and T_1 relaxation time data from the $Cs_2K_xAg_{1-x}InCl_6$:Bi (x = 0.2 - 1) nanocrystal series measured at a magnetic field strength of 20.0 T (see Figure 6.8 in the main text). The T_1 values were determined using the saturation-recovery technique.

K content (%)	Site	20.0 T δ (± 5 ppm)	20.0 T T_1 (± 0.1 s)	Rel. Int. (± 3 %)
100	$Cs_{2-x}K_{1+x}InCl_6$ (cubic, A & B site) / $Cs_{2-x}K_{1+x}InCl_6$ (monoclinic, A & B site)	9	0.4	78
	$Cs_2K_yAg_{1-y}InCl_6$ (cubic, B site)	47	0.4	6
	Cs_2KInCl_6 (cubic, B site)/ $Cs_{2-x}K_{1+x}InCl_6$ (cubic, A & B site) / $Cs_{2-x}K_{1+x}InCl_6$ (monoclinic, A & B site)	59	0.1	16
80	$Cs_{2-x}K_xAgInCl_6$ (cubic, A site) / $Cs_{2-x}K_{x+y}Ag_yInCl_6$ (cubic, A & B site)	14	-	73
	$Cs_2K_yAg_{1-y}InCl_6$ (cubic, B site)	47	-	11
	Cs_2KInCl_6 (cubic, B site) / $Cs_{2-x}K_{1+x}InCl_6$ (cubic, A & B site) / $Cs_{2-x}K_{1+x}InCl_6$ (monoclinic, A & B site)	59	-	16
60	$Cs_{2-x}K_xAgInCl_6$ (cubic, A site) / $Cs_{2-x}K_{x+y}Ag_yInCl_6$ (cubic, A & B site)	15	-	56
	$Cs_2K_yAg_{1-y}InCl_6$ (cubic, B site)	48	5.8	33
	Cs_2KInCl_6 (cubic, B site) / $Cs_{2-x}K_{1+x}InCl_6$ (cubic, A & B site) / $Cs_{2-x}K_{1+x}InCl_6$ (monoclinic, A & B site)	60	-	11
40	$Cs_{2-x}K_xAgInCl_6$ (cubic, A site) / $Cs_{2-x}K_{x+y}Ag_yInCl_6$ (cubic, A & B site)	15	-	56
	$Cs_2K_yAg_{1-y}InCl_6$ (cubic, B site)	48	5.8	33
20	$Cs_{2-x}K_xAgInCl_6$ (cubic, A site) / $Cs_{2-x}K_{x+y}Ag_yInCl_6$ (cubic, A & B site)	15	-	56